Ultrarelativistic Particle Acceleration in Collisionless Shock Waves

Yukiharu Ohsawa

Department of Physics, Nagoya University, Nagoya 464-8602, Japan

ohsawa@nagoya-u.jp

Internal Report of

Institute for Fusion Studies, The University of Texas at Austin

IFSR 1433

1 September 2012

Abstract

This paper describes the theory and particle simulations of ultrarelativistic particle acceleration caused by shock waves in a collisionless magnetized plasma.

Since knowledge of field strengths and structures is necessary for the analysis of particle motions, theories of magnetosonic waves are reviewed first: (1) linear and nonlinear magnetosonic waves in a single-ion-species plasma, (2) those in a two-ion-species plasma, (3) those in an electron-positron-ion (EPI) plasma, and (4) parallel electric field. The first topic contains a general introduction to the magnetosonic wave. The second and third topics are concerned with three-component plasmas, in which the magnetosonic wave is split into two modes; the plasma behavior can thus be considerably different from that in a single-ion-species plasma. The fourth topic is the electric field parallel to the magnetic field, $E_\parallel$, in a nonlinear magnetosonic wave. It is shown that $E_\parallel$ can be strong even in low frequency, magnetohydrodynamic phenomena.

Next, nonstochastic particle acceleration caused by the intense electric and magnetic fields formed in a shock wave is studied with theory and with fully kinetic, fully relativistic, electromagnetic, particle simulations. The subjects include (1) electron trapping and acceleration, (2) energization of thermal and relativistic ions, (3) heavy-ion acceleration and resultant damping of nonlinear pulses in a multi-ion-species plasma, and (4) positron acceleration due to $E_\parallel$ in the shock transition region in an EPI plasma. In addition to these processes near a shock front, (5) the evolution of large-amplitude Alfvén waves generated behind a shock front and acceleration of electrons in the Alfvén wave region are examined.

Simulations demonstrate particle acceleration caused by these nonlinear magnetohydrodynamic waves to ultrarelativistic energies much higher than those of solar energetic particles. The acceleration theory based on the investigation of nonlinear waves quantitatively accounts for these simulation results.

Keywords

particle acceleration, cosmic ray, collisionless shock wave, solitary wave, magnetosonic wave, Alfvén wave, single-ion-species plasma, multi-ion-species plasma, electron-positron-ion plasma, particle simulation

Acknowledgments

With the personnel exchange program of the Joint Institute for Fusion Theory (JIFT), the author visited the Institute for Fusion Studies (IFS), The University of Texas at Austin, several times to collaborate on the subject of this IFS Report. Without the JIFT and the support of IFS members, this review would not have been written. He is particularly grateful to Dr. J. W. Van Dam (former Director of the IFS, currently Director of Research Division, Fusion Energy Sciences, Office of Science, US Department of Energy), Dr. F. L. Waelbroeck (Director), Dr. C. W. Horton, Jr., and Dr. H. L. Berk for their stimulating discussions, encouragement, and warm hospitality during his visits to the IFS. Large part of this article is based on the work conducted in collaboration with graduate students of the plasma theory group in the Department of Physics, Nagoya University; cooperation of Dr. M. Toida (now assistant professor) for two decades is especially acknowledged. The computational work shown in this article has been carried out through the collaboration programs of the National Institute for Fusion Science and of the Solar-Terrestrial Environment Laboratory.

Contents

Chapter 1

Introduction

Cosmic rays have been investigated for nearly a century and are still attracting increasing attention from plasma, particle, and astrophysics communities [1]- [13]. Their acceleration mechanism, however, remains unresolved. Unlike the studies of plasma-based accelerators initiated by John Dawson *et al.* in the late 1970's [14, 15], in which detailed comparisons between the experiments, theories, and simulations are possible, it is quite difficult to directly observe the acceleration processes of cosmic rays produced in the distance, although we have a huge amount of experimental data, such as time variations of x-ray and gamma-ray emission associated with solar flares [3].

Because of the rapid increase in the power of computers, however, we can now perform simulations that solve large-scale plasma behavior and individual relativistic particle motions in a self-consistent manner. Their precise information about particle motions and electromagnetic fields would enable us to create new theories for particle acceleration and to test existing theories. With use of relativistic particle simulations, in fact, several distinct nonstochastic particle acceleration mechanisms caused by shock waves in a magnetized collisionless plasma have been found and analyzed in the past few decades [16]- [30]. Furthermore, to account for the field structures that lead to energization of particles, nonlinear wave theory has been developed [31]- [36]: A coherent theory for nonlinear waves and particle acceleration mechanisms has thus been constructed. This paper reviews these studies.

Before looking at detailed theories, however, we briefly describe in this chapter some fundamental properties of cosmic rays for the readers who are not familiar with them and then outline the structure of this paper.

1.1 Cosmic rays

The origin of the research of cosmic rays may date far back to 1912, when Hess revealed that radiation causing ionization in the atmosphere comes from the sky. In 1930's, it was recognized that the main component of the cosmic radiation is high-energy particles. For several decades since then, their observations were the major experimental way to analyze elementary particles. For instance, mesons predicted by Yukawa and positrons predicted by Dirac were both discovered through observations of cosmic rays. We now know that cosmic rays contain protons, heavy ions such as He, C, and Fe, neutrons, electrons, and positrons.

Although cosmic rays are still investigated from the viewpoint of particle physics, the main concern has shifted to the mechanism of cosmic-ray acceleration: How and where do they gain energies, and what is their highest energy?

To explore cosmic rays, we analyze the data of particles and photons arriving at the earth from the space. High-energy particles emit electromagnetic waves (or photons) with a wide range of frequencies: from radio to gamma rays generated by bremsstrahlung, synchrotron radiation, and various nuclear reactions such as

$$p + p \to p + p + \pi^0, \tag{1.1}$$

$$\pi^0 \to 2\gamma, \tag{1.2}$$

i.e., a neutral pion (π^0) with a rest mass energy of 135 MeV produced by a collision of two protons (p) quickly decays into two photons (γ). Besides these processes, by scattering low-energy photons such as cosmic microwave background, energetic particles can also create high-energy photons; this process is called the inverse Compton scattering. These radiations, as well as particles, give information concerning cosmic rays [1]- [13]. For instance, comparison of the time variations of

photon fluxes with several different energy levels has revealed that the solar energetic particles are promptly accelerated, within a few seconds [1]- [4], which was a surprise because many people had believed that acceleration of solar energetic particle was a slow stochastic process in a turbulent plasma. Another simpler example is that we can determine the locations (or directions) of the sources of cosmic rays from photons, which, unlike charged particles, propagate straight even in the presence of magnetic fields. (Extremely high-energy particles have gyroradii greater than the size of our Galaxy [13]. Their orbits can be viewed as nearly straight within our Galaxy.)

1.1.1 Sources and energies of cosmic rays

The sun is the nearest cosmic-ray source. In association with solar flares, in which the energy of coronal magnetic tubes is rapidly released, shock waves are generated, electromagnetic waves from radio waves to gamma rays are emitted, and solar energetic particles are promptly produced. Protons reach energy $1 - 10$ GeV (in terms of the Lorentz factor, $\gamma \lesssim 10$), and electrons several tens of MeV ($\gamma \sim 100$) [1]- [4]. Energetic heavy ions are also detected near the earth; their elemental compositions are, on average, nearly the same as that of the solar corona, i.e., the background plasma of the acceleration site [5, 6].

Supernova explosions create shock waves that expand in the interstellar medium, producing a vast high-temperature plasma region inside the spherical shock front. These shock waves are one of the sources of cosmic rays: From the observations of x rays (due to synchrotron radiation) and gamma rays (due to inverse Compton scattering), high-energy electrons with $\sim 10^{14}$ eV have been found near the shock fronts of supernova remnants [37–39].

Pulsars are rapidly rotating neutron stars with spin periods $\lesssim 1$ s, having extremely intense magnetic fields ($\sim 10^{12}$ G) [40, 41]. Because of their strong electromagnetic fields, pulsars are thought to be an origin of cosmic rays [42]; indeed, TeV gamma rays from the directions of pulsars have been detected [43]. Another pecu-

liar point of pulsars is that they could create positrons in their magnetospheres [44].

1.1.2 Extremely high energy cosmic rays

The observed energy spectrum of cosmic rays extends up to $\sim 10^{19}$ eV with nearly a power law distribution. However, it shows a sharp suppression at an energy of $\sim 6 \times 10^{19}$ eV, which is consistent with the GZK cutoff, a theoretical prediction made by Greisen, Zatsepin, and Kuz'min: Particles with energies higher than this cutoff traveling over distances greater than ∼160 million year length should not be detected on the earth because they continue to lose their energies through interactions with the cosmic microwave background radiation until their energies go down below this threshold. The observed spectrum thus implies that the sources of extremely high energy cosmic rays are extragalactic [7–10].

Furthermore, recent experiments have revealed that the arrival directions of cosmic rays with energies above 6×10^{19} eV are anisotropic and correlated with the locations of active galactic nuclei, where massive black holes are supposed to exist [12, 13].

1.2 Acceleration models

1.2.1 Stochastic acceleration models

The Fermi acceleration model, in which particles are assumed to be energized through collisions with "magnetic clouds," was proposed in 1949 [45]; its modified models such as "diffusive shock acceleration" were also presented later [46]. As far as the author knows, however, the verification of these models with particle simulations has not been made yet.

Counter-streaming instabilities [47–50] could possibly be a cause of cosmic rays: Turbulent electromagnetic fields arising from those instabilities might boost energies of some particles. Despite a great number of such simulations, however, ultrarelativistic acceleration such that $\gamma > 100$ has not been demonstrated. For example, in the simulations in Ref. [49] to investigate cosmic-ray acceleration in the

vicinity of a supernova remnant shock wave, instabilities due to two proton beams perpendicular to a magnetic field were examined. Even with a large relative speed of the two beams, 12 v_{Te} where v_{Te} is the electron thermal velocity, the observed highest speed of accelerated electrons was nonrelativistic, $\sim 20 v_{Te}$.

1.2.2 Nonstochastic acceleration due to shock waves

Collisionless magnetosonic shock waves are frequently observed in space plasmas in association with strong disturbances such as solar flares and supernova explosions; these disturbances are often accompanied also by the production of high-energy particles [1–4,37–39]. Shock waves are thought to be related to particle acceleration as well as to plasma heating in these phenomena.

Indeed, particle simulations have clearly demonstrated that shock waves cause ultrarelativistic acceleration of particles to energies $\gamma > 100$, which are comparable to or higher than the level of solar energetic particles [16, 17, 22–30]. The strong electric and magnetic fields formed in a shock wave directly and promptly accelerate some fraction of particles to high energies with nonstochastic mechanisms. Various kinds of particles have been found to suffer such processes: protons, electrons, heavy ions, and positrons.

These studies have the following features:

1) The acceleration mechanisms are nonstochastic.

2) The theories for particle acceleration and for nonlinear waves have been developed from the first principles. These theories are consistent each other.

3) The acceleration and wave theories have been verified with fully kinetic, relativistic, electromagnetic simulations.

It is expected that extremely intense electric and magnetic fields are generated around pulsars, in the sites of supernova explosions, and in active galactic nuclei. The results of the above studies suggest that rapid, nonstochastic particle acceleration would take place in those rather small, localized regions, as well as in solar flares and in interstellar shock waves. Observations of gamma-ray emission

with fine time (or space) resolution are therefore desirable: They would provide us with important information on the acceleration mechanisms as they did for solar flares [3].

This type of acceleration is intriguing also from the viewpoint of energy dissipation in collisionless shock waves. There has been a widely accepted view on it [47] that "some instabilities grow in collisionless shock waves, and resultant turbulent electromagnetic fluctuations randomly scatter particles; thereby wave energies are converted to thermal energies." The nonstochastic acceleration, in which part of the wave energy is directly converted to rather a small number of particles, is an energy dissipation mechanism that is obviously different from those processes.

1.3 Structure of this paper

Theory and particle simulations of shock waves and nonstochastic particle acceleration are described in this article, which consists of seven chapters including this one for introduction.

Chapter 2 is devoted to the theory of nonlinear magnetosonic waves [31]- [36]. We first outline linear and nonlinear magnetosonic waves in a two-component plasma consisting of electrons and ions. Field structures and strengths in solitary waves and in shock waves are discussed. The next subject is the effect of the presence of multiple ion species. In a two-ion-species plasma, the magnetosonic wave is split into two modes; we derive their nonlinear evolution equations and investigate the wave properties of the two modes. Similarly, we have two magnetosonic modes in an electron-positron-ion (EPI) plasma. Their wave properties, such as the dependence of the linear dispersion relation on the positron density, are examined. The final section of Chap. 2 shows that the electric field parallel to the magnetic field can be much stronger in nonlinear magnetosonic waves than was generally thought.

These studies provide a basis for the development of particle acceleration theory. The readers who are not very interested in the details of the wave theory, however,

could skip Chap. 2 and proceed to the subsequent chapters on particle acceleration.

Chapter 3 describes ultrarelativistic acceleration of electrons to energies $\gamma > 100$ [16, 17]. Some electrons are trapped near a shock front and then absorb a great amount of energy there. This acceleration is strong in a rather intense external magnetic field $\boldsymbol{B}_0$ such that $|\Omega_e| \gtrsim \omega_{pe}$, where Ω_e (< 0) and ω_{pe} are the electron gyrofrequency and plasma frequency, respectively.

Chapter 4 presents three types of ion acceleration [18]- [23]: energization due to one reflection from the shock front, surfatron acceleration caused by multiple reflections, and incessant acceleration of relativistic ions. The third one can occur in relativistic particles if the shock speed $v_{\rm sh}$ is close to $c\cos\theta$, where c is the speed of light and θ is the angle between the wave normal and $\boldsymbol{B}_0$; in this situation particles with their speeds close to c can move with the shock wave for long periods of time and repeatedly gain energy from the transverse electric field of the shock wave in association with their gyromotions. An example will be shown that the Lorentz factor of an ion goes up stepwise to $\gamma \sim 160$.

Chapter 5 shows that all the heavy ions that pass through a shock front are accelerated by the transverse electric field in a multi-ion-species plasma with protons being the major ion constituent. Furthermore, their final speeds are nearly the same, independent of particle species [24]. This surprisingly simple result is consistent with the observations that the elemental compositions of energetic heavy ions are similar to that of the background plasma of the acceleration site [5, 6].

Chapter 6 treats positron acceleration [25–27]. In an EPI plasma, positrons can be persistently accelerated along the magnetic field near the shock transition region. We will show a simulation in which positron γ's reach $\sim 10^4$ by the end of the run ($\omega_{pe}t = 7000$). Since the acceleration is not saturated, γ's would further rise if one carries out a longer simulation with a larger system size.

Unlike Chapters 2–6, which focus on the phenomena near a shock front, the theme of Chapter 7 is wave evolution and particle acceleration behind a shock front [28–30]. A strong explosion in a plasma creates forward and backward shock waves.

Furthermore, large-amplitude Alfvén waves are generated behind them. In the Alfvén wave region, three types of electron acceleration have been observed. They occur in weak magnetic fields ($|\Omega_e| \lesssim \omega_{pe}$) as well as in strong ones. These processes could therefore be found in shock waves in interstellar space with $B_0 \sim 10^{-6}$ G and in coronal magnetic flux tubes with $\sim 10^3$ G.

In these chapters, calculations that are too lengthy for the main text are omitted. Important ones are, however, given in Appendices.

Bibliography

[1] D. J. Forrest and E. L. Chupp, Nature (London) **305**, 291 (1983).

[2] H. Nakajima, T. Kosugi, K. Kai, and S. Enome, Nature (London) **305**, 292 (1983).

[3] S. R. Kane, E. L. Chupp, D. J. Forrest, G. H. Share, and E. Rieger, Astrophys. J. Lett. **300**, L95 (1986).

[4] E. L. Chupp, H. Debrunner, E. Flückiger *et al.*, Astrophys. J. **318**, 913 (1987).

[5] J. P. Meyer, Astrophys. J. Suppl. **57**, 151 (1985).

[6] J. P. Meyer, Astrophys. J. Suppl. **57**, 173 (1985).

[7] R. U. Abbasi *et al.* (High Resolution Fly's Eye Collaboration), Phys. Rev. Lett. **100**, 101101 (2008).

[8] J. Abraham *et al.* (The Pierre Auger Collaboration), Phys. Rev. Lett. **101**, 061101 (2008).

[9] K. Greisen, Phys. Rev. Lett. **16**, 748 (1966).

[10] G. T. Zatsepin and V. A. Kuz'min, JETP Lett. **4**, 78 (1966).

[11] J. Abraham *et al.* (The Pierre Auger Collaboration), Astropart. Phys. **27**, 244 (2007).

[12] The Pierre Auger Collaboration, Science **318**, 938 (2007).

[13] J. Abraham *et al.* (The Pierre Auger Collaboration), Astropart. Phys. **29**, 188 (2008).

[14] T. Tajima and J. M. Dawson, Phys. Rev. Lett. **43**, 267 (1979).

[15] C. Joshi and T. Katsouleas, Physics Today **56**, No. 6, 47 (2003).

[16] N. Bessho and Y. Ohsawa, Phys. Plasmas **6**, 3076 (1999).

[17] N. Bessho and Y. Ohsawa, Phys. Plasmas **9**, 979 (2002).

[18] D. Biskamp and H. Welter, Nuclear Fusion **12**, 663 (1972).

[19] D. W. Forslund, K. B. Quest, J. U. Brackbill, and K. Lee, J. Geophys. Res. [Space Physics] **89**, 2142 (1984).

[20] R. Z. Sagdeev and V. D. Shapiro, JETP Lett. **17**, 279 (1973).

[21] T. Katsouleas and J. M. Dawson, Phys. Rev. Lett. **51**, 392 (1983).

[22] Y. Ohsawa, J. Phys. Soc. Jpn. **59**, 2782 (1990).

[23] S. Usami and Y. Ohsawa, Phys. Plasmas **9**, 1069 (2002).

[24] M. Toida and Y. Ohsawa, Solar Physics **171**, 161 (1997).

[25] H. Hasegawa, S. Usami, and Y. Ohsawa, Phys. Plasmas **10**, 3455 (2003).

[26] H. Hasegawa, K. Kato, and Y. Ohsawa, Phys. Plasmas **12**, 082306 (2005).

[27] T. Iwata, S. Takahashi, and Y. Ohsawa, Phys. Plasmas **19**, 022302 (2012).

[28] M. Sato, S. Miyahara, and Y. Ohsawa, Phys. Plasmas **12**, 052308 (2005).

[29] M. Sato and Y. Ohsawa, Phys. Plasmas **13**, 063110 (2006).

[30] Y. Takeyama, S. Nakayama, and Y. Ohsawa, Phys. Plasmas **18**, 092307 (2011).

[31] Y. Ohsawa, Phys. Fluids **29**, 1844 (1986).

[32] Y. Ohsawa, Phys. Fluids **29**, 2474 (1986).

[33] M. Toida, Y. Ohsawa, and T. Jyounouchi, Phys. Plasmas **2**, 3329 (1995).

[34] S. Takahashi and Y. Ohsawa, Phys. Plasmas **14**, 112305 (2007).

[35] S. Takahashi, M. Sato, and Y. Ohsawa, Phys. Plasmas **15**, 082309 (2008).

[36] S. Takahashi and Y. Ohsawa, J. Plasma Fusion Res. Series **8**, 238 (2009).

[37] K. Koyama, R. Petre, E. V. Gotthelf, U. Hwang, M. Matsuura, M. Ozaki, and S. S. Holt, Nature (London) **378**, 255 (1995).

[38] F. A. Aharonian, A. G. Akhperjanian, K.-M. Aye, A. R. Bazer-Bachi, M. Beilicke *et al.*, Nature (London) **432**, 75 (2002).

[39] T. Takahashi, T. Tanaka, Y. Uchiyama, J. S. Hiraga, K. Nakazawa *et al.*, Publ. Astron. Soc. Japan **60**, S131 (2008).

[40] T. Gold, Nature **218**, 731 (1968).

[41] P. Goldreich and W. H. Julian, Astrophys. J. **157**, 869 (1969).

[42] S. Hayakawa, K. Ito, and Y. Terashima, Prog. Theor. Phys. Suppl. **6**, 1 (1958).

[43] F. A. Aharonian, A. G. Akhperjanian, J. A. Barrio, K. Bernlohr, H. Bojahr *et al.*, Astrophys. J. **539**, 317 (2000).

[44] P. A. Sturrock, Astrophys. J. **164**, 529 (1971).

[45] E. Fermi, Phys. Rev. **75**, 1169 (1949).

[46] R. D. Blandford and D. Eichler, Phys. Rep. **154**, 1 (1987).

[47] N. Krall and P. Liewer, Phys. Rev. A **4**, 2094 (1971).

[48] E. Ott, J. B. McBride, J. H. Orens, and J. P. Boris, Phys. Rev. Lett. **28**, 88 (1972).

[49] M. E. Dieckmann, K. G. McClements, S. C. Chapman, R. O. Dendy, and L. O'C. Drury, Astron. Astrophys. **356**, 377 (2000).

[50] M. E. Dieckmann, A. Bret, and P. K. Shukla, Plasma Physics and Controlled Fusion, **49**, 1989 (2007).

Chapter 2

Structure of nonlinear magnetosonic waves

For the analysis of the motion of charged particles in a wave, information of the electric and magnetic fields is needed. This chapter therefore describes some fundamental properties of low-frequency waves such that $\omega \lesssim \Omega_i$ in magnetized plasmas and examine their field structures, where ω is the wave frequency and Ω_i is the ion gyrofrequency.

First, we give an introductory outline of linear and nonlinear magnetohydrodynamic (MHD) waves in a single-ion-species plasma [1]- [20]. The field structures of nonlinear magnetosonic waves are discussed based on the theory of finite-amplitude, stationary, perpendicular waves and on the Korteweg-de Vries (KdV) equation that is applicable to small-amplitude waves with arbitrary angles θ between the wave normal and the external magnetic field $\boldsymbol{B}_0$. Besides, we obtain the field strengths in a large-amplitude shock wave in a heuristic way.

Second, effects of multiple ion species are studied. In a two-ion-species plasma, the magnetosonic wave is split into two modes [21, 22], which are referred to as the high- and low-frequency modes in this paper. Although the former has a finite cutoff frequency of the order of Ω_i, the KdV equation is derived for each mode [23–25]. Furthermore, simulations show that a long-wavelength, large-amplitude, low-frequency-mode pulse quickly steepens and emits many short-wavelength, high-frequency-mode solitons; the original low-frequency-mode pulse is thus damped.

Third, the theory is extended to an EPI plasma, which also has the high- and low-frequency modes. Their frequency domains, nonlinear evolution equations, and field structures are examined [26, 27].

Fourth, the electric field parallel to the magnetic field, $E_\parallel = \boldsymbol{E}\cdot\boldsymbol{B}/B$, is studied. Although it was generally thought that $E_\parallel$ was quite weak in low-frequency, long-wavelength phenomena in a high-temperature plasma, it is shown that $E_\parallel$ can be strong in nonlinear magnetosonic waves [28, 29].

2.1 Linear magnetosonic and Alfvén waves

This section gives an introduction to the theory of low-frequency, long-wavelength waves in one- and two-fluid models.

2.1.1 One-fluid MHD theory

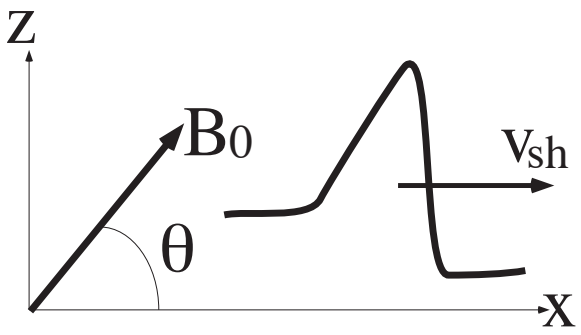

Fig. 1

Figure 2.1: Schematic diagram of wave propagation and external magnetic field. The waves are supposed to propagate in the x direction in an external magnetic field $\boldsymbol{B}_0$ in the (x, z) plane. The propagation speed of a shock wave is denoted by $v_{\rm sh}$.

In the ideal MHD, there are three kinds of waves in a homogeneous plasma: Alfvén wave, and fast and slow magnetosonic waves [1–3]. The Alfvén wave is an

incompressible mode, propagating along the magnetic field. If we assume that the external magnetic field is in the (x, z) plane, as shown in Fig. 2.1,

$$\boldsymbol{B}_0 = B_0(\cos\theta, 0, \sin\theta) = (B_{x0}, 0, B_{z0}), \tag{2.1}$$

(for definiteness, both B_{x0} and B_{z0} are taken to be positive), and that infinitely small-amplitude waves propagate in the x direction, such that

$$\boldsymbol{B} = \boldsymbol{B}_0 + \boldsymbol{B}_1 \exp[i(kx - \omega t)], \tag{2.2}$$

then the linear dispersion relation of the Alfvén wave is given as

$$\omega = k v_{\rm A} \cos\theta, \tag{2.3}$$

where $v_{\rm A}$ is the Alfvén speed

$$v_{\rm A} = \frac{B_0}{(4\pi\rho_0)^{1/2}}, \tag{2.4}$$

with ρ_0 being the equilibrium mass density. With use of $v_{\rm A}$ and the sound speed

$$c_s = \left(\frac{\Gamma p_0}{\rho_0}\right)^{1/2}, \tag{2.5}$$

where Γ is the specific heat ratio and p_0 is the thermal pressure, the dispersion relation of the magnetosonic waves is given as

$$\omega^2/k^2 = (1/2)\left\{(v_{\rm A}^2 + c_s^2) \pm \left[(v_{\rm A}^2 + c_s^2)^2 - 4v_{\rm A}^2 c_s^2 \cos^2\theta\right]^{1/2}\right\}, \tag{2.6}$$

where the upper (plus) and lower (minus) signs, respectively, correspond to the fast and slow waves. The linear slow wave is usually heavily damped [4]. In the following, the term "magnetosonic wave" indicates the fast wave, unless otherwise stated.

In the MHD theory, the three modes have no dispersion: The frequency ω is proportional to the wavenumber k. As shown below, however, dispersion appears in the two-fluid model.

2.1.2 Two-fluid theory

The basic equations for the two-fluid model may read as

$$\frac{\partial n_j}{\partial t} + \nabla \cdot (n_j \boldsymbol{v}_j) = 0, \tag{2.7}$$

$$m_j \left(\frac{\partial}{\partial t} + (\boldsymbol{v}_j \cdot \nabla) \right) \boldsymbol{v}_j = q_j \boldsymbol{E} + \frac{q_j}{c} \boldsymbol{v}_j \times \boldsymbol{B} - \frac{\nabla p_j}{n_j}, \tag{2.8}$$

$$\left(\frac{\partial}{\partial t} + (\boldsymbol{v}_j \cdot \nabla) \right) p_j = -\Gamma_j p_j \nabla \cdot \boldsymbol{v}_j, \tag{2.9}$$

$$\frac{1}{c} \frac{\partial \boldsymbol{B}}{\partial t} = -\nabla \times \boldsymbol{E}, \tag{2.10}$$

$$\frac{1}{c} \frac{\partial \boldsymbol{E}}{\partial t} = \nabla \times \boldsymbol{B} - \frac{4\pi}{c} \sum_j n_j q_j \boldsymbol{v}_j, \tag{2.11}$$

$$\nabla \cdot \boldsymbol{E} = 4\pi \sum_j n_j q_j, \tag{2.12}$$

$$\nabla \cdot \boldsymbol{B} = 0, \tag{2.13}$$

where the subscript j refers to ions ($j = i$) or electrons ($j = e$), m_j is the mass, q_j is the charge, n_j is the number density, $\boldsymbol{v}_j$ is the velocity, p_j is the pressure, and Γ_j is the specific heat ratio.

From the cold ($p_j = 0$), two-fluid model with no displacement current, one obtains the dispersion relation for waves with propagation angle θ as [5]

$$c^2 k^2 [c^2 k^2 \sin^2\theta + \omega_p^2 (1 + \cos^2\theta)] \sum_j \frac{\omega_{pj}^2 \omega^2}{\omega^2 - \Omega_j^2}$$
$$+ (c^2 k^2 \sin^2\theta + \omega_p^2) \left(\sum_j \frac{\omega_{pj}^2}{\omega - \Omega_j} \right) \left(\sum_j \frac{\omega_{pj}^2}{\omega + \Omega_j} \right) \omega^2 + c^4 k^4 \omega_p^2 \cos^2\theta = 0, \tag{2.14}$$

where Ω_j is the gyrofrequency,

$$\Omega_j = q_j B_0 / (m_j c), \tag{2.15}$$

(Ω_j includes the sign of the charge q_j), ω_{pj} is the plasma frequency,

$$\omega_{pj} = (4\pi n_{j0} q_j^2 / m_j)^{1/2}, \tag{2.16}$$

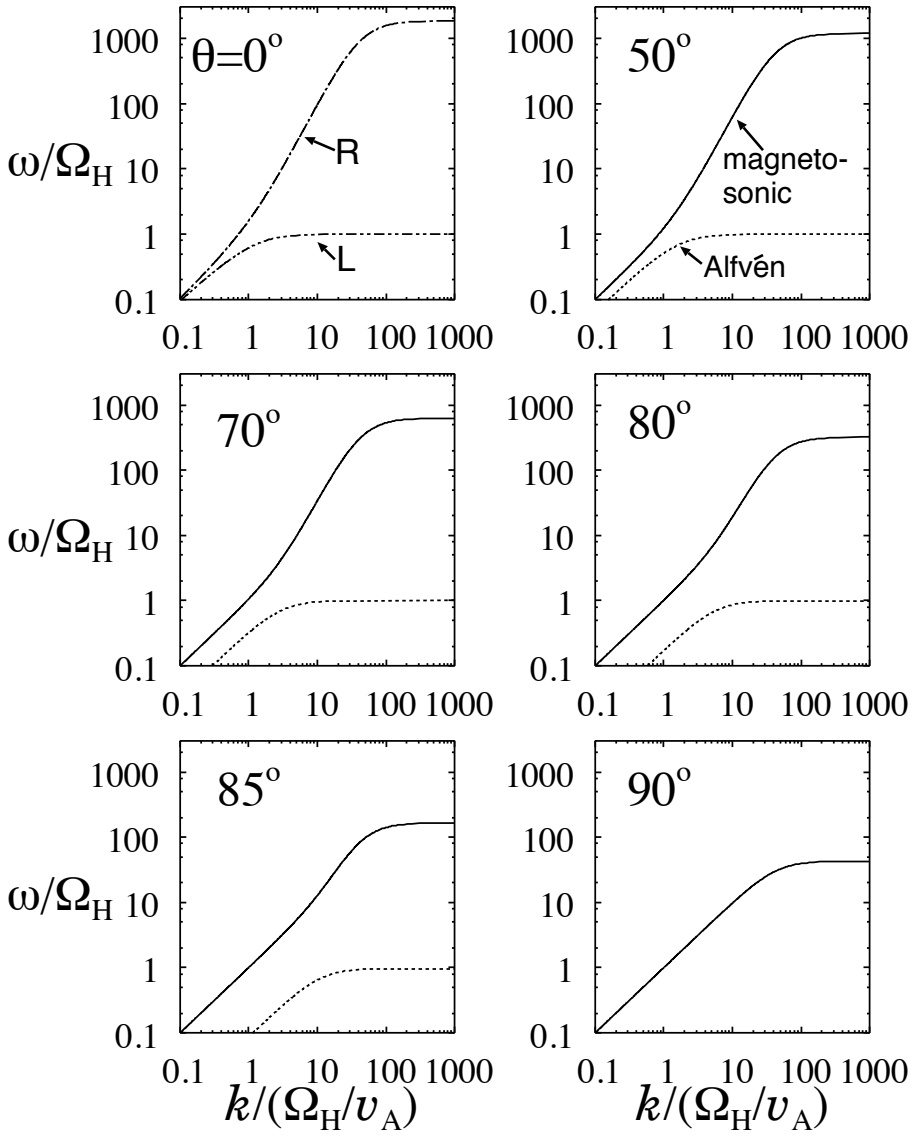

Figure 2.2: Linear dispersion relations of magnetosonic and Alfvén waves for various propagation angles θ. Because the cold plasma model is used, the slow magnetosonic wave does not appear. The displacement current is ignored.

and ω_p^2 is the sum of ω_{pj}^2,

$$\omega_p^2 = \sum_j \omega_{pj}^2. \tag{2.17}$$

Figure 2.2 displays the dispersion curves of the modes in the frequency regime $\omega \lesssim |\Omega_e|$, for which we have magnetosonic and Alfvén waves. Since the cold plasma model is used, the slow magnetosonic wave is not present. The frequencies of the perpendicular magnetosonic wave are given as

$$\frac{\omega^2}{k^2} = \frac{v_{\rm A}^2}{1 + c^2 k^2/\omega_{pe}^2}, \tag{2.18}$$

where c/ω_{pe} is the electron skin depth. In the limit of $k \to \infty$, the perpendicular magnetosonic wave has the lower-hybrid-resonance frequency,

$$\omega_{\rm LH} = (\Omega_i |\Omega_e|)^{1/2}. \tag{2.19}$$

At $\theta = 0$, the Alfvén and magnetosonic waves become left- and right-circularly polarized, respectively, with the dispersion relation

$$c^2 k^2 = -\frac{\omega_{pi}^2 \omega}{\omega \mp \Omega_i} - \frac{\omega_{pe}^2 \omega}{\omega \mp \Omega_e}. \tag{2.20}$$

Here, the upper and lower signs, respectively, correspond to the left- and right-circularly polarized waves. The rotation sense of the latter is the same as that of the electron gyromotion.

With use of the quantity χ defined as [6]

$$\chi = \frac{\cos\theta}{1 + (c^2 k^2/\omega_p^2)\sin^2\theta} \left[\left(c^2 k^2 + \sum_j \frac{\omega_{pj}^2 \omega^2}{\omega^2 - \Omega_j^2} \right) \Big/ \sum_j \frac{\omega_{pj}^2 \Omega_j \omega}{\omega^2 - \Omega_j^2} \right], \tag{2.21}$$

the perturbed transverse fields are related through

$$E_{z1} = i\chi E_{y1}, \tag{2.22}$$

$$B_{y1} = -i\chi B_{z1}, \tag{2.23}$$

with

$$B_{z1} = \frac{ck}{\omega} E_{y1}. \tag{2.24}$$

The longitudinal electric field and density perturbation can be written as

$$E_{x1} = -i\left(1 + \frac{c^2k^2}{\omega_p^2}\right)\frac{\sin\theta}{\cos\theta}\chi E_{y1}, \tag{2.25}$$

$$\frac{n_{j1}}{n_{j0}} = \left[\left(\frac{\Omega_j\omega}{\omega^2-\Omega_j^2} + \frac{\Omega_j}{\omega}\frac{c^2k^2}{\omega_p^2}\cdot\frac{\cos^2\theta}{1+(c^2k^2/\omega_p^2)\sin^2\theta}\right)\right.$$
$$\left.\times\left(c^2k^2 + \sum_{j'}\frac{\omega_{pj'}^2\omega^2}{\omega^2-\Omega_{j'}^2}\right)\Big/\left(\sum_{j'}\frac{\omega_{pj'}^2\Omega_{j'}\omega}{\omega^2-\Omega_{j'}^2}\right) - \frac{\Omega_j^2}{\omega^2-\Omega_j^2}\right]\frac{k\sin\theta}{\omega}\frac{cE_{y1}}{B_0}. \tag{2.26}$$

In the parallel propagation ($\theta = 0$), $E_{x1} = 0$, $n_{j1} = 0$, and $\chi = \pm 1$; the waves with $\chi = 1$ are right circularly polarized, while the ones with $\chi = -1$ are left circularly polarized. In the oblique and perpendicular propagation ($0 < \theta \leq 90°$), E_{x1} and n_{j1} are finite.

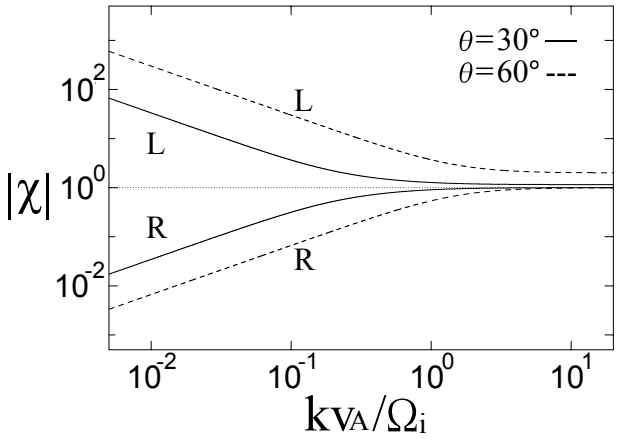

Figure 2.3: Magnitudes of χ for L- and R-modes as functions of k. Here, $\chi = -iE_{z1}/E_{y1} = iB_{y1}/B_{z1}$. The rotation sense of the transverse fields of the R-mode is the same as electron gyromotion. In the long-wavelength regime, $|\chi| \gg 1$ or $|\chi| \ll 1$, while in the short-wavelength regime, $|\chi| \sim 1$.

Figure 2.3 shows the magnitudes of χ for R-mode [magnetosonic (or whistler) wave with $\chi > 0$, with its transverse fields with right-handed rotation] and for L-mode (Alfvén wave with $\chi < 0$) as functions of the normalized wavenumber $kv_{\rm A}/\Omega_i$ for $\theta = 30°$ (thick lines) and for $\theta = 60°$ (dashed lines). In the long-wavelength regime, the R- and L-modes, respectively, are close to the magnetosonic

and Alfvén waves described in the MHD; i.e., E_{y1} and B_{z1} are the dominant field components in the R-mode while E_{z1} and B_{y1} are dominant in the L-mode. In short-wavelength waves with $kv_{\rm A}/\Omega_i \sim O(1)$, however, E_{y1} and E_{z1} are of the same order of magnitude, and so are B_{y1} and B_{z1}.

2.1.3 Long-wavelength magnetosonic wave

In the long-wavelength regime, the dispersion of the magnetosonic wave is weak and the relation between ω and k can be written in the form [7–11]

$$\omega/k = v_{p0}(1 + \mu k^2). \tag{2.27}$$

Here, the phase velocity v_{p0} in the limit of $k = 0$ is given by Eq. (2.6) with the upper (plus) sign, with c_s now defined as

$$c_s = \left(\frac{\sum_j \Gamma_j p_{j0}}{\sum_j n_{j0} m_j} \right)^{1/2}, \tag{2.28}$$

and the dispersion coefficient μ is

$$\mu = -\frac{c^2}{4\omega_{pe}^2} \frac{(v_{p0}^2 - c_s^2)}{[v_{p0}^2 - (v_{\rm A}^2 + c_s^2)/2]} \left(1 - \frac{(m_i - m_e)^2 v_{\rm A}^2 \cos^2\theta}{m_i m_e (v_{p0}^2 - v_{\rm A}^2 \cos^2\theta)} \right). \tag{2.29}$$

This coefficient strongly depends on the propagation angle θ. Let θ_c designate the critical angle at which μ becomes zero [9–11]:

$$1 - \frac{(m_i - m_e)^2 v_{\rm A}^2 \cos^2\theta_c}{m_i m_e (v_{p0}^2 - v_{\rm A}^2 \cos^2\theta_c)} = 0, \tag{2.30}$$

from which one sees that θ_c is close to 90°,

$$\cos\theta_c \simeq (m_e/m_i)^{1/2}. \tag{2.31}$$

For the angles $\theta_c < \theta \leq 90°$, the dispersion coefficient is negative, $\partial^2\omega/\partial k^2 < 0$, and approximated as

$$\mu \sim -c^2/\omega_{pe}^2, \tag{2.32}$$

while for the angles $\theta < \theta_c$, the coefficient is positive, $\partial^2\omega/\partial k^2 > 0$, and much larger:

$$\mu \sim c^2/\omega_{pi}^2. \tag{2.33}$$

The ion inertial length c/ω_{pi} is identical to the quantity $v_{\rm A}/\Omega_i$.

If the displacement current is included and the pressures are ignored in the two-fluid model, the phase velocity of the linear magnetosonic wave in the long-wavelength limit becomes equal to the modified Alfvén speed [26, 27],

$$\tilde{v}_{\rm A} = \frac{v_{\rm A}}{[1 + (v_{\rm A}/c)^2]^{1/2}}. \tag{2.34}$$

For a high density plasma in a weak magnetic field, the Alfvén speed $v_{\rm A}$ is much lower than the speed of light, and thus $\tilde{v}_{\rm A} \simeq v_{\rm A}$; in which the displacement current is unimportant in the magnetosonic wave.

2.2 Nonlinear waves

Nonlinear magnetosonic waves have been extensively investigated by many authors since the early days of plasma physics, and these studies, mainly for a single-ion-species plasma, have been reviewed in several textbooks [12–14]. The subjects of this section are related to the central part of such studies: field structures in a finite-amplitude, stationary, perpendicular magnetosonic wave; KdV equation for small-amplitude waves; and field strengths in a large-amplitude shock wave.

2.2.1 Finite-amplitude stationary waves

With use of the cold two-fluid model, finite-amplitude-wave solutions were obtained in 1958 for magnetosonic waves steadily propagating perpendicular to a magnetic field [15, 16]; later, this theory was extended to a weakly relativistic case [17]. We here describe some important results of this theory, giving its detailed calculations in Appendix A.

Basic properties

These solutions contain wavetrains and solitary waves. The solitary wave solutions exist in the range of Alfvén Mach numbers

$$1 \leq M \leq 2, \tag{2.35}$$

with the maximum value of the magnetic field

$$B_m = (2M - 1)B_0. \tag{2.36}$$

The plasma density, transverse electric field E_y, and electric potential ϕ are proportional to $(B_z - B_0)$, with $E_z = 0$ and $B_y = 0$.

The electron skin depth c/ω_{pe} gives a measure of the characteristic soliton width,

$$D \sim \frac{c}{\omega_{pe}(M-1)^{1/2}}. \tag{2.37}$$

Charge neutrality, which is assumed in the theory, makes the ion and electron velocities in the x direction equal, $v_{ix} = v_{ex} = v_x$. Then, from the fluid equation of motion (2.8) with $p_j = 0$, it follows that

$$m_i v_{iy} + m_e v_{ey} = \text{constant}, \tag{2.38}$$

along the characteristics of the plasma, indicating that the change in v_{ey} is m_i/m_e times as large as that of v_{iy}. As a result, the magnetic structure of a perpendicular magnetosonic wave is determined by the electron current, although this wave is a low frequency phenomenon.

Electric potential

The longitudinal electric field E_x arises from charge separation. The magnitude of the electric potential ($E_x = -\partial\phi/\partial x$) is

$$e\phi = 2m_i v_{\rm A}^2 (M-1), \tag{2.39}$$

which is of the same order of magnitude as the ion kinetic energy: In the wave frame, where the y component of the electric field is constant, $E_y = E_{y0}$ (< 0) (see Sec. 2.2.3), the plasma flows in the negative x direction; its velocity is $v_x = -Mv_{\rm A} = cE_{y0}/B_0$ in the upstream region. If there is a region where the magnetic field B_z sharply rises, then the speed of electrons, which move with the $\boldsymbol{E}\times\boldsymbol{B}$ drift velocity $cE_{y0}/B_z(x)$, would slow down there, while the ions with a much greater gyroradius would penetrate there nearly keeping the same speed $v_x = -Mv_{\rm A}$.

This difference produces the electric potential (2.39) that is comparable to the ion kinetic energy $m_i(Mv_{\rm A})^2/2$; the ions are then substantially decelerated to maintain charge neutrality $n_i \simeq n_e$. The potential, however, remains smaller than the kinetic energy,

$$\frac{e\phi}{m_i(Mv_{\rm A})^2/2} = \frac{4(M-1)}{M^2} \leq 1. \tag{2.40}$$

Thus, the ions with the fluid speed $v_x = -Mv_{\rm A}$ are not reflected by the electric potential [18].

Charge neutrality and pulse width in a strong magnetic field

If the magnetic field is rather strong,

$$\frac{|\Omega_e|}{\omega_{pe}} \gtrsim 1, \tag{2.41}$$

charge neutrality ($|n_i - n_e|/n_0 \ll 1$) breaks down in large-amplitude magnetosonic waves with $M - 1 \sim O(1)$. In fact, from Gauss's law, it follows that

$$\frac{e\phi}{m_e D^2} \sim \omega_{pe}^2 \frac{(n_i - n_e)}{n_0}. \tag{2.42}$$

Substituting Eqs. (2.37) and (2.39) in Eq. (2.42) yields

$$\frac{(n_i - n_e)}{n_0} \sim 2\left(\frac{\Omega_e}{\omega_{pe}}(M-1)\right)^2, \tag{2.43}$$

indicating that $(n_i - n_e)/n_0 \sim O(1)$.

Furthermore, relativistic effects become important under these circumstances. With the help of Eqs. (2.37) and (2.39), one can estimate the $\boldsymbol{E} \times \boldsymbol{B}$ drift velocity as

$$\frac{v_{ey}}{c} \simeq -\frac{E_x}{B} \simeq -\frac{\phi}{DB} \sim -\frac{|\Omega_e|}{\omega_{pe}}(M-1)^{3/2}. \tag{2.44}$$

This nonrelativistic estimate suggests that the electron fluid velocity in the pulse region becomes relativistic if $|\Omega_e|/\omega_{pe} \gtrsim 1$ and $(M-1) \gtrsim 1$. In such a case, the pulse width is given as

$$D \sim \frac{c}{\omega_{pe}} \frac{|\Omega_e|}{\omega_{pe}}(M-1), \tag{2.45}$$

which we find from Ampère's law, $\partial B_z/\partial x = (4\pi/c)n_e e v_{ey}$, by noting that the current is approximately estimated as $n_e ec$ because $v_{ey} \sim -c$ and that $(B_m - B_0)/B_0 \sim (M-1)$, which is obtained from Eq. (2.36). The relativistic pulse width, in contrast to the nonrelativistic one (2.37), increases with the wave amplitude [17].

2.2.2 KdV equation for small-amplitude waves

For the magnetosonic waves with small-but-finite amplitudes, one can derive from the original set of equations, (2.7)–(2.13), a single nonlinear evolution equation: KdV equation for arbitrary propagation angles θ [7–11, 19, 20]. The reductive perturbation method developed by Taniuti *et al.* [8,30,31] enables us to do this without mathematical ambiguities for weakly dispersive waves with their frequencies given by Eq. (2.27).

This method considers wave evolution in the stretched coordinates

$$\xi = \epsilon^{1/2}(x - v_{p0}t), \tag{2.46}$$

$$\tau = \epsilon^{3/2}t, \tag{2.47}$$

where ϵ is the smallness parameter representing the wave amplitude. This transformation can be related to the phase of a linear monochromatic wave with weak dispersion of the form (2.27) with the following equation:

$$kx - \omega t = k(x - v_{p0}t) - v_{p0}\mu k^3 t. \tag{2.48}$$

If $k \sim \epsilon^{1/2}$, the first and the second terms on the right-hand side of Eq. (2.48) are, respectively, of the same forms as Eqs. (2.46) and (2.47). The time variation of the wave profile with small k would be quite slow in the frame moving with the velocity v_{p0}. The relation $k \sim \epsilon^{1/2}$, where k is now viewed as the characteristic wavenumber of nonlinear pulses in the KdV equation, may be expected from Eq. (2.37) and will be directly shown below by Eqs. (2.56) and (2.57).

Physical quantities are then expanded as, for instance,

$$B_{z1} = B_{z0} + \epsilon B_{z1} + \epsilon^2 B_{z2} + \cdots, \tag{2.49}$$

$$E_x = \epsilon^{3/2} E_{x1} + \epsilon^{5/2} E_{x2} + \cdots . \tag{2.50}$$

Charge neutrality $n_i \simeq n_e$ is assumed; hence, from the continuity equation it follows that

$$v_{ix} = v_{ex} = v_x. \tag{2.51}$$

Applying the above transformation, (2.46) and (2.47), and expansion to the two-fluid model, (2.7)–(2.13), we obtain, after some algebra (see Appendix B), the KdV equation as

$$\frac{\partial B_{z1}}{\partial \tau} + v_{p0}\alpha \frac{B_{z1}}{B_0}\frac{\partial B_{z1}}{\partial \xi} - v_{p0}\mu \frac{\partial^3 B_{z1}}{\partial \xi^3} = 0, \tag{2.52}$$

where μ is the dispersion coefficient (2.29) and α is given by

$$\alpha = \frac{v_{\rm A}^2 \sin\theta \left[3v_{\rm A}^2(v_{p0}^2 - c_s^2\cos^2\theta) + (c_s^2 + \Gamma_i c_i^2 + \Gamma_e c_e^2)\,(v_{p0}^2 - v_{\rm A}^2\cos^2\theta)\right]}{4v_{p0}^2(v_{p0}^2 - c_s^2)[v_{p0}^2 - (v_{\rm A}^2 + c_s^2)/2]}, \tag{2.53}$$

where $c_j^2 = \Gamma_j p_{j0}/[n_0(m_i + m_e)]$ with $j = i$ or e [11]. The second and third terms in Eq. (2.52), respectively, represent nonlinear and dispersion effects.

If the phase velocity given by Eq. (2.6) with the upper (plus) sign is used for v_{p0} in these equations, then Eq. (2.52) represents the KdV equation for the fast magnetosonic waves. On the other hand, the phase velocity with the lower (minus) sign gives the KdV equation for slow magnetosonic waves. Each KdV equation with these coefficients is valid for finite pressure plasmas and for arbitrary angles $0 < \theta \leq 90°$. In a cold plasma model with $\theta = 90°$, in which the slow wave does not propagate, these coefficients reduce to $\alpha = 3/2$ and $\mu = -c^2/(2\omega_{pe}^2)$, with $v_{p0} = v_{\rm A}$.

Equation (2.52) also has a stationary, solitary wave solution:

$$\frac{B_{z1}}{B_0} = \sigma B_{\rm n}\ {\rm sech}^2\left(\frac{\xi - \sigma\alpha B_{\rm n}\tau/3}{D}\right), \tag{2.54}$$

where $\sigma = 1$ for $\mu < 0$ and $\sigma = -1$ for $\mu > 0$, $B_{\rm n}$ (> 0) is the normalized amplitude, and D is the soliton width given by

$$D = \left(\frac{12|\mu|}{\alpha B_{\rm n}}\right)^{1/2}. \tag{2.55}$$

The profile of a solitary wave is symmetric.

The initial value problem for the KdV equation was solved numerically [32] and analytically [33]. These studies have shown that the solitary waves are stable and keep their identities in their space-time evolution, like individual particles; they are therefore called solitons.

We now again restrict ourselves to the fast magnetosonic wave.

Because the dispersion coefficient μ strongly depends on the propagation angle θ, the structure of the solitary wave also has strong dependence on θ. Quasi-perpendicular pulses in the angles $\theta_c < \theta \leq 90°$, for which $\mu \sim -c^2/\omega_{pe}^2$, are compressive (they have high plasma densities and magnetic fields), with their characteristic pulse width $D \sim (c/\omega_{pe})/B_{\rm n}^{1/2}$. For the angles $\theta < \theta_c$, on the other hand, $\mu \sim c^2/\omega_{pi}^2$, and thus the coefficient of the third term in Eq. (2.52), $-v_{p0}\mu$, becomes negative. The solitary waves are rarefactive (low plasma densities and magnetic fields), with $D \sim (c/\omega_{pi})/B_{\rm n}^{1/2}$.

The longitudinal electric field E_x ($\sim \phi/D$) is thus much weaker in oblique waves than in quasi-perpendicular ones (the dependence of the potential ϕ on θ is rather weak [11]). The $E_x \times B_z$ drift of electrons along a nonlinear pulse is thus slower in the oblique case.

Since $\epsilon \sim B_{\rm n}$ and the characteristic wavenumber k is related to D as $k \sim 1/D$, we have

$$\frac{ck}{\omega_{pi}} \sim \epsilon^{1/2}, \tag{2.56}$$

for oblique waves and

$$\frac{ck}{\omega_{pe}} \sim \epsilon^{1/2}, \tag{2.57}$$

for quasi-perpendicular waves.

2.2.3 Shock waves

Field profiles

In large-amplitude pulses with $\epsilon \sim O(1)$, energy dissipation can occur even in a collisionless plasma: Part of the wave energy is transferred to particles owing to instabilities and particle acceleration. Such large-amplitude magnetosonic pulses

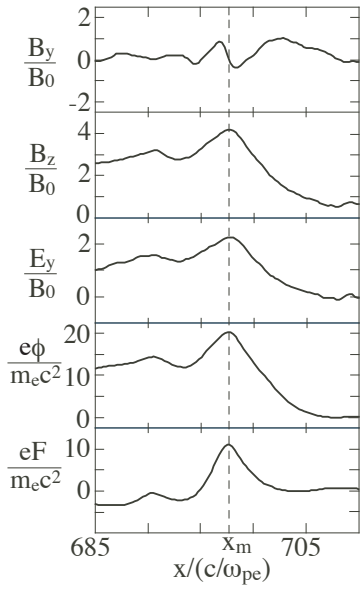

Figure 2.4: Field profiles of an oblique shock wave with $\theta = 45°$ obtained from a particle simulation. The fields B_z, E_y, ϕ, and F have similar profiles, while B_y is approximately proportional to $\partial B_z/\partial x$. The quantity F in the bottom panel is defined as $F = -\int E_\parallel ds$.

have asymmetric field profiles and are called collisionless shock waves. Their profile could be approximated by a train of solitons of decreasing amplitude [12].

Figure 2.4 displays the field profiles of an oblique shock wave with a propagation angle $\theta = 45°$ obtained by a particle simulation [34] (the method of shock simulation is described in Sec. 3.1.1). It clearly shows that B_z, E_y, and ϕ have similar profiles, while B_y is nearly proportional to $\partial B_z/\partial x$; E_x and E_z, which are not shown here, are also proportional to $\partial B_z/\partial x$. These relations are mathematically proved for small-amplitude waves [8–11] [perturbations are expressed in terms of B_{z1} in Eqs. (B.28)–(B.37) in Appendix B], and simulations show that these relations approximately hold also in large-amplitude magnetosonic waves. The quantity F in the bottom panel is the integral of the parallel electric field, $E_\parallel = (\boldsymbol{E}\cdot\boldsymbol{B})/B$, along the magnetic field, $F = -\int E_\parallel ds$, which will be examined in Sec. 2.5.1.

Quantities in the wave frame

The profiles of the electric fields $E_{\mathrm{w}y}$ and $E_{\mathrm{w}z}$, where the subscript w refers to quantities in the wave frame, are completely different from those in the laboratory frame: In this paper, the term "laboratory frame" means the system where the upstream plasma is at rest: The wave frame moves with the shock speed v_{sh} in the x direction relative to the laboratory frame. Since the time derivatives in the fluid equations are zero in the wave frame, $\partial/\partial t = 0$, it follows from Faraday's law that both $E_{\mathrm{w}y}$ and $E_{\mathrm{w}z}$ are constant in time and space. Because the plasma velocity in the upstream region is $\boldsymbol{v}_{\mathrm{w}0} = (-v_{\mathrm{sh}}, 0, 0)$, from the macroscopic relation $\boldsymbol{E}_{\mathrm{w}} + \boldsymbol{v}_{\mathrm{w}} \times \boldsymbol{B}_{\mathrm{w}}/c = 0$ and the assumption for the external magnetic field that $\boldsymbol{B}_{\mathrm{w}0} = (B_{\mathrm{w}x0}, 0, B_{\mathrm{w}z0})$, we find that

$$E_{\mathrm{w}y} = E_{\mathrm{w}y0} = -\frac{v_{\mathrm{sh}} B_{\mathrm{w}z0}}{c}, \tag{2.58}$$

$$E_{\mathrm{w}z} = 0. \tag{2.59}$$

For one-dimensional propagation with $\partial/\partial y = \partial/\partial z = 0$, the x component of the magnetic field is constant,

$$B_{\mathrm{w}x} = B_{\mathrm{w}x0} = B_{\mathrm{l}x0}, \tag{2.60}$$

where the subscript l denotes the laboratory frame. Also, we have the relation

$$B_{\mathrm{w}z0} = \gamma_{\mathrm{sh}} B_{\mathrm{l}z0}, \tag{2.61}$$

where γ_{sh} is the Lorentz factor corresponding to the shock speed v_{sh},

$$\gamma_{\mathrm{sh}} = \left(1 - v_{\mathrm{sh}}^2/c^2\right)^{-1/2}. \tag{2.62}$$

Field strengths in a large-amplitude shock wave

We here compute field strengths in a large-amplitude shock wave such that $M > 2$. In this calculation, we make use of the fact that the plasma density, magnetic field B_z, and electric potential ϕ sharply rise in the shock transition region and take their maximum values at the same point, say $x = x_m$, while the fields E_x and B_y become

zero there. This analysis was first made for perpendicular waves [35]. Then, since its theoretical predictions were confirmed to be consistent with simulation results, this investigation has been extended to oblique waves [36], as described below.

We start from the cold, two-fluid model, Eqs. (2.7)–(2.13) with $p_j = 0$. Instead of Eq. (2.8) though, we adopt a relativistic equation of motion:

$$m_j \left(\frac{\partial}{\partial t} + (\boldsymbol{v}_j \cdot \nabla) \right) (\gamma_j \boldsymbol{v}_j) = q_j \boldsymbol{E} + \frac{q_j}{c} \boldsymbol{v}_j \times \boldsymbol{B}, \tag{2.63}$$

where γ_j is the Lorentz factor for the fluid velocity $\boldsymbol{v}_j$, i.e., $\gamma_j = (1 - v_j^2/c^2)^{-1/2}$. This allows us to treat high-speed fluids: The Alfvén speed can be of the order of c in a strong magnetic field.

Since the time derivatives are zero in the wave frame, the continuity equation, (2.7), gives

$$n_{\mathrm{w}j}(x_{\mathrm{w}}) v_{\mathrm{w}jx}(x_{\mathrm{w}}) = -n_{\mathrm{w}j0} v_{\mathrm{sh}}, \tag{2.64}$$

where $n_{\mathrm{w}j0}$ is the upstream density. We multiply the x component of Eq. (2.63) by $n_{\mathrm{w}j}$ and sum over particle species to have

$$\sum_j m_j n_{\mathrm{w}j} v_{\mathrm{w}jx} \frac{d(\gamma_{\mathrm{w}j} v_{\mathrm{w}jx})}{dx} = \sum_j q_j n_{\mathrm{w}j} \left(E_{\mathrm{w}x} + \frac{v_{\mathrm{w}jy}}{c} B_{\mathrm{w}z} - \frac{v_{\mathrm{w}jz}}{c} B_{\mathrm{w}y} \right). \tag{2.65}$$

Combining Eqs. (2.11), (2.64), (2.65), and Gauss's law, we find that

$$\frac{d}{dx} \left(-\sum_j m_j n_{\mathrm{w}0} v_{\mathrm{sh}} \gamma_{\mathrm{w}j} v_{\mathrm{w}jx} + \frac{B_{\mathrm{w}y}^2 + B_{\mathrm{w}z}^2 - E_{\mathrm{w}x}^2}{8\pi} \right) = 0, \tag{2.66}$$

which is integrated to give

$$\frac{B_{\mathrm{w}y}^2 + B_{\mathrm{w}z}^2 - B_{\mathrm{w}z0}^2 - E_{\mathrm{w}x}^2}{8\pi} = \sum_j m_j n_{\mathrm{w}0} v_{\mathrm{sh}} (\gamma_{\mathrm{sh}} v_{\mathrm{sh}} + \gamma_{\mathrm{w}j} v_{\mathrm{w}jx}). \tag{2.67}$$

As mentioned above, both $B_{\mathrm{w}y}$ and $E_{\mathrm{w}x}$ are small near x_{wm}. Furthermore, $v_{\mathrm{w}jx}$ is small in magnitude compared with the far upstream speed v_{sh}, because the plasma density is high at $x_{\mathrm{w}} = x_{\mathrm{wm}}$ in a large-amplitude shock wave. Hence we obtain the maximum value of $B_{\mathrm{w}z}$ as

$$\frac{B_{\mathrm{w}z\mathrm{m}}}{B_{\mathrm{w}z0}} = \left(1 + \frac{m_i n_{\mathrm{w}0} \gamma_{\mathrm{sh}} v_{\mathrm{sh}}^2}{B_{\mathrm{w}z0}^2/(8\pi)} \right)^{1/2}, \tag{2.68}$$

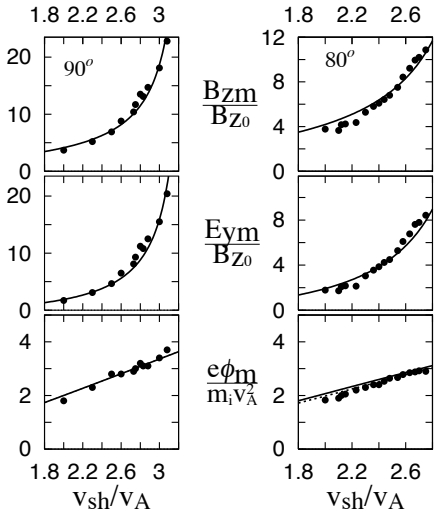

Figure 2.5: Field strengths versus Alfvén Mach number for $\theta = 90°$ and for $\theta = 80°$. Theory (solid lines) and simulations (dots) for B_z, E_y, and ϕ are shown.

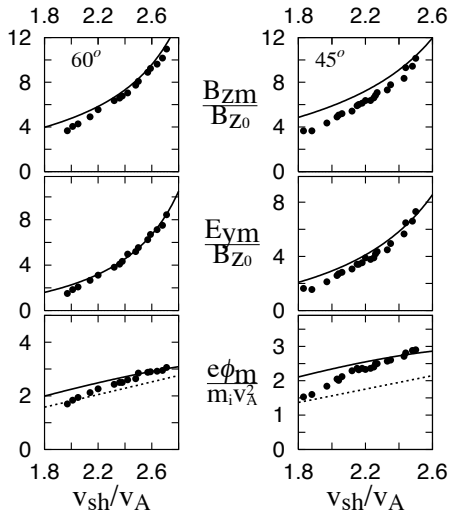

Figure 2.6: Field strengths versus Alfvén Mach number for $\theta = 60°$ and for $\theta = 45°$. The dotted lines show $\phi_{\rm lCmd}$, the potential due to the $\boldsymbol{E} \times \boldsymbol{B}$ drift motion.

where the electron term in Eq. (2.67) has been ignored.

We can then calculate field strengths in the laboratory frame. From Eqs. (2.58), (2.61), and the relation

$$B_{\rm lz} = \gamma_{\rm sh}[B_{\rm wz} + (v_{\rm sh}/c)E_{\rm wy0}], \tag{2.69}$$

it follows that

$$\frac{B_{\rm lzm}}{B_{\rm lz0}} = 1 + \gamma_{\rm sh}^2 \left(\frac{B_{\rm wzm}}{B_{\rm wz0}} - 1 \right). \tag{2.70}$$

Substituting Eq. (2.68) in Eq. (2.70) and then using Eq. (2.61) and the relation $n_{\rm w0} = \gamma_{\rm sh} n_{\rm l0}$, we find the maximum value of $B_{\rm lz}$ as

$$\frac{B_{\rm lzm}}{B_{\rm lz0}} = 1 + \gamma_{\rm sh}^2 \left[\left(1 + \frac{2v_{\rm sh}^2}{v_{\rm A}^2 \sin^2\theta} \right)^{1/2} - 1 \right], \tag{2.71}$$

where $v_{\rm A}$ and θ are the quantities defined in the laboratory frame. The maximum value of the transverse electric field $E_{\rm ly}$ is related to the magnetic field through

$$E_{\rm lym} = (v_{\rm sh}/c)(B_{\rm lzm} - B_{\rm lz0}). \tag{2.72}$$

Substitution of Eq. (2.71) in (2.72) yields

$$\frac{E_{\rm lym}}{B_{\rm lz0}} = \frac{\gamma_{\rm sh}^2 v_{\rm sh}}{c} \left[\left(1 + \frac{2v_{\rm sh}^2}{v_{\rm A}^2 \sin^2\theta} \right)^{1/2} - 1 \right]. \tag{2.73}$$

Although the calculation for the electric potential is more lengthy, one obtains its maximum value in a similar way under the assumption that $B_{\rm wz0}/B_{\rm wx0} \gtrsim 1$ ($\theta \gtrsim 45°$) [36]:

$$e\phi_{\rm lCm} = m_i v_{\rm A}^2 \left(\sin^2\theta + \frac{\sin\theta\cos\theta}{\gamma_{\rm sh}(1+\gamma_{\rm sh}^2\tan^2\theta)^{1/2}} \right) \left[\left(1 + \frac{2v_{\rm sh}^2}{v_{\rm A}^2 \sin^2\theta} \right)^{1/2} - 1 \right], \tag{2.74}$$

where the subscript C indicates that the potential is expressed in the Coulomb gauge. The term proportional to $1/(1+\gamma_{\rm sh}^2\tan^2\theta)^{1/2}$ in Eq. (2.74) arises from the electron motion parallel to the magnetic field. The rest is due to the $\boldsymbol{E} \times \boldsymbol{B}$ drift,

$$e\phi_{\rm lCmd} = m_i v_{\rm A}^2 \sin^2\theta \left[\left(1 + \frac{2v_{\rm sh}^2}{v_{\rm A}^2 \sin^2\theta} \right)^{1/2} - 1 \right], \tag{2.75}$$

which is the main part of the potential. In the limit of $\theta = 90°$, Eqs. (2.71), (2.73), and (2.74) reduce to the results for perpendicular waves obtained in Ref. [35].

Figures 2.5 and 2.6 compare the theory (solid lines) and particle simulations (dots) with $m_i/m_e = 100$ and $|\Omega_e|/\omega_{pe} = 3$ for four different propagation angles [36]: $\theta = 90°$, 80°, 60°, and 45°. The dotted lines in the bottom panels show the contribution from the drift motions, Eq. (2.75). The theory and simulations have quite close values, particularly for large angles and for large Mach numbers. (In addition to the assumption $B_{wz0}/B_{wx0} \gtrsim 1$ in the theory, we note the simulation result that wavetrains with noticeable amplitudes appear in front of a shock wave in the case that θ is small, in which short-wavelength waves have higher propagation speeds than long-wavelength waves.) The contribution of the parallel particle motion to the potential becomes appreciable [the difference $(\phi - \phi_{\rm lCmd})$ increases] as the propagation angle θ decreases.

2.3 Waves in a multi-ion-species plasma

Although the above wave theories have been constructed for single-ion-species plasmas, ionized gases usually contain multiple ion species. In space plasmas, there are a small fraction of heavy ions, such as He, C, O, and Fe, in addition to the major ion constituent H. The density ratio of He and H is $n_{\rm He}/n_{\rm H} \simeq 0.1$, with the densities of other heavy ions much lower than $n_{\rm He}$. Fusion plasmas will contain D, T, and fusion products He (neutrons will quickly go out of the plasma region). This section concerns wave properties in multi-ion-species plasmas. For simplicity, we use a cold plasma model, $T_j = 0$.

2.3.1 Perpendicular waves in a two-ion-species plasma

Linear dispersion relation

In a two-ion-species plasma, the magnetosonic wave is split into two modes: high- and low-frequency modes [21–24]. Figure 2.7 shows the dispersion curves for these modes in a H-He plasma. As in space plasmas, the density ratio is $n_{\rm He}/n_{\rm H} = 0.1$;

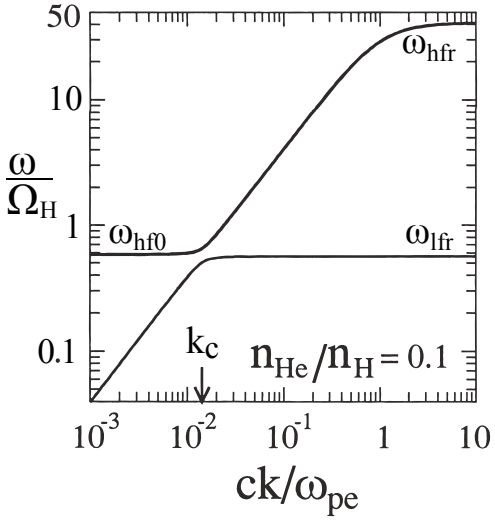

Figure 2.7: Linear dispersion curves of perpendicular magnetosonic waves in a H-He plasma. In a two-ion-species plasma, there is a frequency domain near the ion gyrofrequencies where the magnetosonic wave cannot propagate.

this ratio is used in all the figures for H-He plasmas in this section. The dispersion curves of these two modes have large curvatures near the wavenumber $k = k_c$, which is quantitatively given below by Eq. (2.91).

Let "a" and "b" designate two different ion species with $\Omega_a > \Omega_b$. Then, for a plasma consisting of electrons and these ions, the cutoff frequency $\omega_{\rm hf0}$ of the high-frequency mode is given as

$$\omega_{\rm hf0}^2 = \left(\frac{\omega_{pa}^2}{\Omega_a^2} + \frac{\omega_{pb}^2}{\Omega_b^2} \right)^2 \frac{\Omega_a^2 \Omega_b^2 \Omega_e^2}{\omega_{pe}^4}, \tag{2.76}$$

and the resonance frequency $\omega_{\rm hfr}$ at $k = \infty$ is

$$\omega_{\rm hfr}^2 = (\omega_{pa}^2 + \omega_{pb}^2)\Omega_e^2/\omega_{pe}^2. \tag{2.77}$$

The frequency of the low-frequency mode approaches the ion-ion hybrid resonance frequency $\omega_{\rm lfr}$ as $k \to \infty$ [21, 22],

$$\omega_{\rm lfr}^2 = \left(\frac{\omega_{pa}^2}{\Omega_a^2} + \frac{\omega_{pb}^2}{\Omega_b^2} \right) \frac{\Omega_a^2 \Omega_b^2}{(\omega_{pa}^2 + \omega_{pb}^2)}. \tag{2.78}$$

The following relation holds among these frequencies:

$$\Omega_b < \omega_{\rm lfr} < \omega_{\rm hf0} < \Omega_a. \tag{2.79}$$

The magnetosonic wave cannot propagate in the frequency range $\omega_{\rm lfr} < \omega < \omega_{\rm hf0}$.

The expressions for the resonance frequencies are valid for $\omega_{pe}/|\Omega_e| \gtrsim 1$. If the plasma density is quite low, $\omega_{pe}/|\Omega_e| \ll 1$, one must include the effect of the displacement current in Maxwell's equations. In the low density limit, i.e., $\omega_{pe}/|\Omega_e| \ll (m_e/m_i)^{1/2}$, these resonance frequencies are given by $\omega_{\rm hfr} = \Omega_a$ and $\omega_{\rm lfr} = \Omega_b$ [21]. Here, we are concerned with the case in which the plasma densities are not too low, $\omega_{pe}/|\Omega_e| > (m_e/m_i)^{1/2}$.

The dispersion relation for the high- and low-frequency modes reads as

$$\frac{k^2}{\omega^2} = \frac{\omega_{pe}^2(\omega^2 - \omega_{\rm hf0}^2)}{c^2(\omega_{\rm hfr}^2\omega^2 - \omega_{\rm hfr}^2\omega_{\rm lfr}^2 - \omega^4)}. \tag{2.80}$$

In the long-wavelength region such that

$$c^2k^2/\omega_{pe}^2 \ll m_e/m_i, \tag{2.81}$$

the low-frequency mode is approximated as [23]

$$\omega \simeq v_{\rm A}k\ (1 + \mu k^2), \tag{2.82}$$

with

$$\begin{aligned} \mu &= -\frac{c^3}{2v_{\rm A}}\left(\frac{\omega_{pa}^2}{\Omega_a^2} + \frac{\omega_{pb}^2}{\Omega_b^2} + \frac{\omega_{pe}^2}{\Omega_e^2}\right)^{-7/2}\left[\frac{\omega_{pa}^2\omega_{pb}^2}{\Omega_a^2\Omega_b^2}\left(\frac{1}{\Omega_a} - \frac{1}{\Omega_b}\right)^2\right. \\ &+ \left.\frac{\omega_{pb}^2\omega_{pe}^2}{\Omega_b^2\Omega_e^2}\left(\frac{1}{\Omega_b} - \frac{1}{\Omega_e}\right)^2 + \frac{\omega_{pe}^2\omega_{pa}^2}{\Omega_e^2\Omega_a^2}\left(\frac{1}{\Omega_e} - \frac{1}{\Omega_a}\right)^2\right], \end{aligned} \tag{2.83}$$

where the Alfvén speed, $v_{\rm A} = B_0/(4\pi\rho_0)^{1/2}$, is defined with use of the average mass density,

$$\rho_0 = n_{a0}m_a + n_{b0}m_b. \tag{2.84}$$

For a two-ion-species plasma, the first term in the square brackets, which is proportional to $(\Omega_a^{-1} - \Omega_b^{-1})^2$, is the dominant term, and μ is approximated as

$$\mu \simeq -\frac{c^2}{2\omega_{pa}\omega_{pb}}\left(\frac{n_{a0}m_an_{b0}m_b}{\rho_0^2}\right)^{3/2}\frac{(\Omega_a - \Omega_b)^2}{\Omega_a\Omega_b} \sim -\frac{c^2}{\omega_{pa}\omega_{pb}}. \tag{2.85}$$

For a single-ion-species plasma, however, this term vanishes, and Eq. (2.83) reduces to Eq. (2.32), i.e., $\mu \simeq -c^2/\omega_{pe}^2$. The dispersion in a two-ion-species plasma is $\sim m_i/m_e$ times as large as that in a single-ion-species plasma.

In the range of wavenumbers

$$(m_e/m_i)^{1/2} \ll c^2k^2/\omega_{pe}^2 \ll 1, \tag{2.86}$$

the high-frequency mode is given by

$$\omega = v_{\rm h}k\ [1 - c^2k^2/(2\omega_{pe}^2)], \tag{2.87}$$

where $v_{\rm h}$ is the characteristic phase velocity of this mode in the wavenumber range (2.86),

$$v_{\rm h} = \frac{(\omega_{pa}^2 + \omega_{pb}^2)^{1/2}|\Omega_e|c}{\omega_{pe}^2} = v_{\rm A}\left[1 + \frac{\omega_{pa}^2\omega_{pb}^2}{\omega_{pe}^4}\Omega_e^2\left(\frac{1}{\Omega_a} - \frac{1}{\Omega_b}\right)^2\right]^{1/2}. \tag{2.88}$$

The speed $v_{\rm h}$ is slightly higher than the Alfvén speed $v_{\rm A}$, and in a single-ion-species plasma it reduces to $v_{\rm A}$.

Noting the relation

$$v_{\rm A} = c\left(\frac{\omega_{pa}^2}{\Omega_a^2} + \frac{\omega_{pb}^2}{\Omega_b^2}\right)^{-1/2}, \tag{2.89}$$

one can show the identity

$$\omega_{\rm hf0}/v_{\rm h} = \omega_{\rm lfr}/v_{\rm A}. \tag{2.90}$$

Around the wavenumber k_c defined by

$$k_c = \omega_{\rm lfr}/v_{\rm A}, \tag{2.91}$$

the dispersion curves of the high- and low-frequency modes both have large curvatures (Fig. 2.7). Furthermore, the following relation holds:

$$(2|\mu|)^{1/2}k_c = (1 - v_{\rm A}^2/v_{\rm h}^2)^{1/2}, \tag{2.92}$$

where the terms proportional to ω_{pe}/Ω_e in μ, Eq.(2.83), have been ignored.

KdV equation for the low-frequency mode

As expected from the dispersion relation (2.82), the KdV equation for the low-frequency mode [22, 23] is obtained with the conventional reductive perturbation method [8–11]; it has the same form as Eq. (2.52) with $v_{p0} = v_{\rm A}$, $\alpha = 3/2$, and μ given by (2.83). The soliton width D is now

$$D = (8|\mu|/B_{\rm n})^{1/2}\,. \tag{2.93}$$

The characteristic wavenumber k and the amplitude ϵ have a relation similar to Eq. (2.57),

$$(|\mu|)^{1/2}k \sim \epsilon^{1/2}. \tag{2.94}$$

Since the magnitude of the dispersion coefficient μ is large, its characteristic soliton width ($\sim c/\omega_{pi}$) is $\sim (m_i/m_e)^{1/2}$ times as large as that of perpendicular pulses ($\sim c/\omega_{pe}$) in a single-ion-species plasma.

KdV equation for the high-frequency mode

Even though the high-frequency mode has a finite cutoff frequency, one can derive the KdV equation for this mode [5, 23] as shown in Appendix C, with an expansion scheme slightly different from the conventional reductive perturbation scheme. Noting that the relation between ω and k of the high-frequency mode is approximated by a weak dispersion type, Eq. (2.87), in a large frequency domain [the resonance frequency of the low-frequency mode is nearly $(m_e/m_i)^{1/2}$ times as small as that of the high-frequency mode], we suppose that

$$ck/\omega_{pe} \sim \epsilon^{1/2}, \tag{2.95}$$

and that the wave amplitude is in the range

$$(m_e/m_i)^{1/2} \ll \epsilon \ll 1. \tag{2.96}$$

This ordering avoids the frequency domain of the low-frequency mode and focuses on the wavenumber range (2.86) of the high-frequency mode, for which the dispersion relation (2.87) takes the same form as that of the magnetosonic wave in a

single-ion-species plasma. The KdV equation obtained in this way has the same form as Eq. (2.52) with $v_{p0} = v_{\rm h}$, $\mu = -c^2/(2\omega_{pe}^2)$, and

$$\alpha = \frac{3}{2}\left(1 + \frac{\omega_{pa}^2\omega_{pb}^2(\Omega_a - \Omega_b)^2}{(\omega_{pa}^2 + \omega_{pb}^2)^2\Omega_a\Omega_b}\right). \tag{2.97}$$

The characteristic soliton width of the high-frequency mode is given by the electron skin depth c/ω_{pe}, which is $\sim (m_e/m_i)^{1/2}$ times as small as that of the low-frequency mode. The nonlinear properties of the high-frequency mode resemble those of the magnetosonic wave in a single-ion-species plasma.

Three-fluid simulation

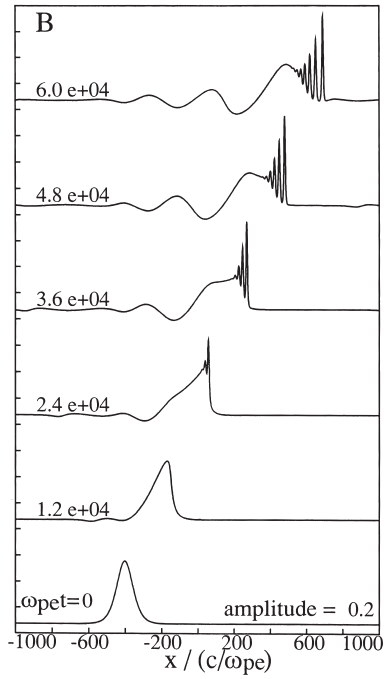

Figure 2.8: Evolution of nonlinear magnetosonic wave. The low-frequency-mode pulse with a width $\sim c/\omega_{pi}$ with rather a large initial amplitude, $\epsilon = 0.2$, quickly steepens and emits short-wavelength ($\sim c/\omega_{pe}$) pulses of the high-frequency mode. This occurs if the initial amplitude of the low-frequency mode is large.

Nonlinear evolution of the magnetosonic wave has also been investigated with one-dimensional, three-fluid simulations with full Maxwell equations [5, 23, 24, 26]. If small-amplitude, solitary wave solutions are used for initial wave profiles, these

pulses propagate steadily as the theory predicts. If their amplitudes are large, however, the high- and low-frequency modes are coupled.

Figure 2.8 shows the evolution of a perpendicular solitary wave of the low-frequency mode, with its initial amplitude being rather large, $\epsilon = B_{z1}/B_0 = 0.2$, where B_{z1} is the perturbed magnetic field [23]. Other simulation parameters are as follows: $m_a/m_e = 1000$, $m_b/m_a = 4$, $q_a/q_e = -1$, $q_b/q_a = 2$, and $n_{b0}/n_{a0} = 0.1$. The magnetic-field strength is $|\Omega_e|/\omega_{pe} = 0.5$, so that $c/v_{\rm A} = 68.3$ and $v_{\rm A}/v_h = 0.967$. The pulse quickly steepens, despite the fact that its initial profile is a solitary wave solution of the low-frequency mode with a width $\sim c/\omega_{pi}$. Short-wavelength ($\sim c/\omega_{pe}$) pulses are then generated and go ahead of the original long-wavelength pulse. Measurements of their propagation speeds and amplitudes indicate that these short-wavelength pulses are solitary waves of the high-frequency mode.

This result shows that if a large-amplitude, low-frequency-mode pulse (or periodic wave) is generated in a plasma, then large part of its energy is converted to the high-frequency mode. Although linear magnetosonic waves cannot propagate in the frequency domain $\omega_{\rm lfr} < \omega < \omega_{\rm hf0}$, steepening of the low-frequency-mode pulse produces higher harmonics with $\omega > \omega_{\rm hf0}$ along the dispersion line of the high-frequency mode.

The condition for the nonlinear coupling is related to the amplitude ϵ and the frequency gap ($\omega_{\rm hf0} - \omega_{\rm lfr}$). The weak-dispersion approximation of the low-frequency mode, Eq. (2.82), is valid in the long-wavelength regime, $k < k_c$; if the characteristic wavenumber of the pulse satisfies this, it will propagate steadily. By virtue of Eqs. (2.90)-(2.92) and (2.94), one can prove [23, 25] that the inequality $k < k_c$ is equivalent to the relation $\epsilon < 2\Delta_\omega$, where Δ_ω is the normalized frequency gap,

$$\begin{aligned} \Delta_\omega &\equiv \frac{\omega_{\rm hf0} - \omega_{\rm lfr}}{\omega_{\rm hf0}} \\ &= 1 - \frac{[1 + n_{b0}q_b/(n_{a0}q_a)]}{[\Omega_b/\Omega_a + n_{b0}q_b/(n_{a0}q_a)]^{1/2}[\Omega_a/\Omega_b + n_{b0}q_b/(n_{a0}q_a)]^{1/2}}. \end{aligned} \quad (2.98)$$

If the pulse amplitude of the low-frequency mode is greater than the normalized

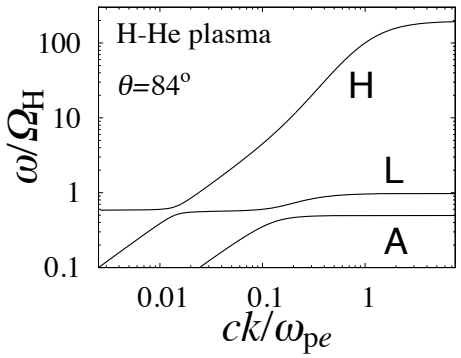

Figure 2.9: Dispersion curves for the high- and low-frequency modes and Alfvén wave for $\theta = 84°$ in a H-He plasma with $n_{\rm He}/n_{\rm H} = 0.1$.

frequency gap,

$$\epsilon > 2\Delta_\omega, \tag{2.99}$$

the perturbation scheme for the KdV equation breaks down. In this case, the nonlinear coupling can occur; for the simulation parameters of Fig. 2.8, $\Delta_\omega \simeq 0.03$, and thus ϵ $(= 0.2)$ is much greater than $2\Delta_\omega$.

2.3.2 Oblique waves in a two-ion-species plasma

In addition to the high- and low-frequency modes, we have the Alfvén wave in the oblique case $0 < \theta < 90°$. Their linear dispersion relations in a cold plasma can be obtained from Eqs. (2.14)–(2.17), which are applicable also to multi-ion-species plasmas if the summation $\sum_j$ is taken over all particle species. We show in Fig. 2.9 the dispersion curves of these three modes for propagation angle $\theta = 84°$ in a H-He plasma with the density ratio $n_{\rm He}/n_{\rm H} = 0.1$, where the lines H, L, and A represent the high- and low-frequency modes and Alfvén wave, respectively [5]. The gyrofrequencies are taken to be $\Omega_{\rm H}/\Omega_{\rm He} = 2$ and $|\Omega_e|/\Omega_{\rm H} = 1836$. The resonance frequency of the Alfvén wave is equal to the gyrofrequency of the heavier ions: $\Omega_{\rm He}$ in the present case.

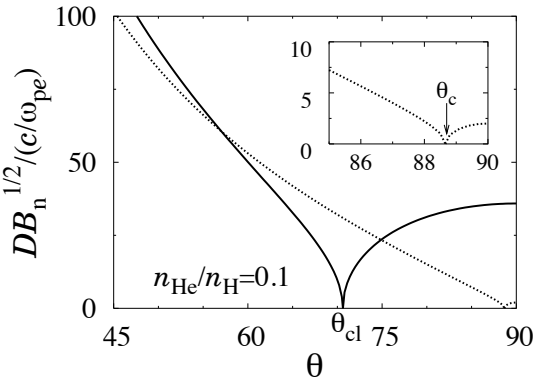

Figure 2.10: Normalized soliton width $DB_{\rm n}^{1/2}/(c/\omega_{pe})$ for the low-frequency mode in a H-He plasma. For comparison, the width in a single-ion-species plasma is also plotted with the dotted line; the small panel shows an expanded view near $\theta = \theta_c$.

Oblique low-frequency mode

In the low-frequency region, $\omega \ll \Omega_j$, the low-frequency mode is approximated as

$$\omega \simeq v_{\rm A} k(1 + \mu_{\rm l} k^2), \tag{2.100}$$

with

$$\mu_{\rm l} = -\frac{v_{\rm A}^2}{2}\left[\frac{v_{\rm A}^2}{c^2}\sum_j \frac{\omega_{pj}^2}{\Omega_j^4} - \frac{v_{\rm A}^4}{c^4 \sin^2\theta}\left(\sum_j \frac{\omega_{pj}^2}{\Omega_j^3}\right)^2\right]. \tag{2.101}$$

At the critical angle $\theta_{\rm cl}$,

$$\theta_{\rm cl} = \arcsin\left[\frac{v_{\rm A}}{c}\left(\sum_j \frac{\omega_{pj}^2}{\Omega_j^3}\right) \Big/ \left(\sum_j \frac{\omega_{pj}^2}{\Omega_j^4}\right)^{1/2}\right], \tag{2.102}$$

$\mu_{\rm l}$ vanishes. The dispersion coefficient $\mu_{\rm l}$ is negative for $\theta_{\rm cl} < \theta < 90^\circ$ and is positive for $0 < \theta < \theta_{\rm cl}$. The critical angle $\theta_{\rm cl}$ in a multi-ion-species plasma is considerably smaller than θ_c in a single-ion-species plasma. It is $\theta_{\rm cl} \simeq 70^\circ$ in a H-He plasma.

Nonlinear behavior of the low-frequency mode is governed by the KdV equation (2.52) with $v_{p0} = v_{\rm A}$, $\alpha = (3/2)\sin\theta$, and $\mu = \mu_{\rm l}$. Figure 2.10 shows the soliton width D normalized to $(c/\omega_{pe})/B_{\rm n}^{1/2}$, where $B_{\rm n}$ is the normalized amplitude $|B_{z1}|/B_0$ [5]. The solid and dotted lines, respectively, the soliton widths in H-He and in single-ion-species plasmas. As mentioned above, $\theta_{\rm cl} < \theta_c$. Furthermore, the

normalized soliton width $DB_{\rm n}^{1/2}/(c/\omega_{pe})$ is ~ 40 even at $\theta = 90^\circ$ in a H-He plasma, while it is order unity in a single-ion-species plasma.

Oblique high-frequency mode

The linear dispersion relation of quasi-perpendicular high-frequency waves for the range of wavenumbers

$$m_e/m_i \ll c^2k^2/\omega_{pe}^2 \ll 1, \tag{2.103}$$

(the corresponding frequency range is $\Omega_i^2 \ll \omega^2 \ll |\Omega_e|\Omega_i$) is approximated as

$$\omega = v_{\rm h}k(1 + \mu_{\rm h}k^2 + \bar{\mu}_{\rm h}k^{-2}), \tag{2.104}$$

where $\mu_{\rm h}$ and $\bar{\mu}_{\rm h}$ are defined to be

$$\mu_{\rm h} = -\frac{c^2}{2\omega_{pe}^2}\left(1 - \frac{\cos^2\theta}{\eta^2}\right), \tag{2.105}$$

$$\bar{\mu}_{\rm h} = \frac{\omega_{pe}^2\eta^2}{2c^2}\left(1 - 2\sum_i \frac{\omega_{pi}^2\Omega_i}{\omega_{pe}^2|\Omega_e|\eta^4} + \sum_i \frac{\omega_{pi}^2\Omega_i^2}{\omega_{pe}^2\Omega_e^2\eta^6}\right), \tag{2.106}$$

with η being the small quantity $[\sim (m_e/m_i)^{1/2}]$ given by

$$\eta = \left(\sum_i \omega_{pi}^2\right)^{1/2} \Big/ \omega_{pe}. \tag{2.107}$$

Here, $\sum_i$ denotes the summation over ion species. We obtain Eq. (2.104) from Eq. (2.14) ignoring small terms of the order of m_e/m_i compared with the others.

Equation (2.105) indicates that at the critical angle $\theta_{\rm ch}$ defined by

$$\cos\theta_{\rm ch} = \eta, \tag{2.108}$$

the dispersion is extremely weak. Numerical calculations show that $\theta_{\rm ch} \simeq 89^\circ$ for a H-He plasma; $\theta_{\rm ch}$ is close to θ_c of a single-ion-species plasma and considerably greater than $\theta_{\rm cl}$ of the low-frequency mode. Indeed, if we take c_s to be zero and θ to be close to 90° in Eq. (2.29), and if we apply Eq. (2.105) to a single-ion-species plasma, then we find they are identical.

Figure 2.11 shows the dispersion coefficients $\mu_{\rm l}$ and $\mu_{\rm h}$ as functions of θ near $\theta = 90^\circ$ for a H-He plasma [5]. The solid and dotted lines indicate that the values

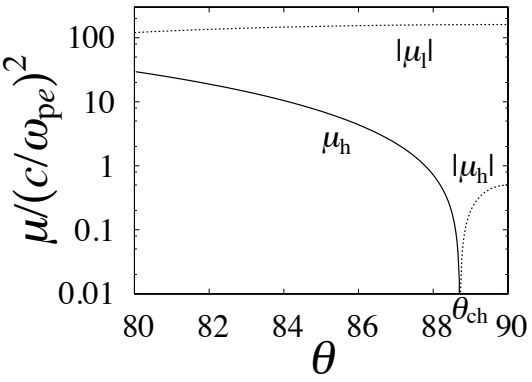

Figure 2.11: Dispersion coefficients $\mu_{\rm h}$ and $\mu_{\rm l}$ as functions of θ. The dashed lines indicate that the values are negative. The critical angle for $\mu_{\rm l}$ is at $\theta = 70°$, which is out of the region of the figure.

are positive and negative, respectively. At $\theta = 90°$, $|\mu_{\rm h}|$ is $\sim m_e/m_i$ times as small as $|\mu_{\rm l}|$. As θ decreases from 90°, $\mu_{\rm h}$ changes from negative to positive values at the critical angle $\theta_{\rm ch}$. The sign of $\mu_{\rm l}$ also changes at the critical angle for the low-frequency mode, $\theta_{\rm cl} = 70°$, as was shown in Fig. 2.10.

The third term on the right-hand side of Eq. (2.104) is negligibly small for $\eta < c^2k^2/\omega_{pe}^2 < 1$. That is, for these wavenumbers, $|\mu_{\rm h}k^2| \gg \bar{\mu}_{\rm h}k^{-2}$ except for the vicinity of $\theta = \theta_{\rm ch}$.

For the wavenumbers such that

$$c^2k^2/\omega_{pe}^2 \gg (m_e/m_i)^{1/2}, \tag{2.109}$$

[i.e., for frequencies $\omega^2 \gg \Omega_i^2(m_i/m_e)^{1/2}$], ignoring small terms of the order of m_e/m_i compared with the others, we can reduce the dispersion relation (2.14) to

$$\omega = |\Omega_e| \left(\eta^2 \frac{c^2k^2}{c^2k^2 + \omega_{pe}^2} + \frac{c^4k^4\cos^2\theta}{(c^2k^2 + \omega_{pe}^2)^2} \right)^{1/2}, \tag{2.110}$$

which can be further approximated as

$$\omega = |\Omega_e|(\eta^2 + \cos^2\theta)^{1/2} \left(1 - \frac{1}{2} \frac{(\eta^2 + 2\cos^2\theta)}{(\eta^2 + \cos^2\theta)} \frac{\omega_{pe}^2}{c^2k^2} \right), \tag{2.111}$$

for large wavenumbers

$$c^2k^2/\omega_{pe}^2 \gg 1. \tag{2.112}$$

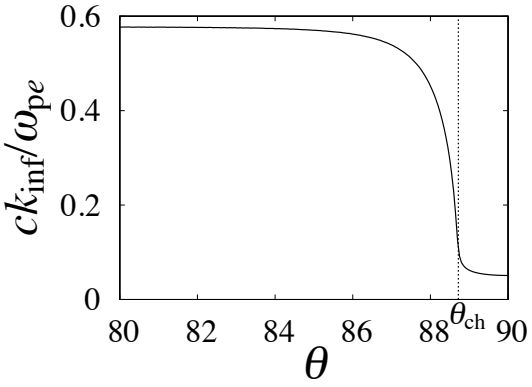

Figure 2.12: Wavenumber at the inflection point, $k_{\rm inf}$, as a function of θ for a H-He plasma. The magnitude of $k_{\rm inf}$ sharply changes near $\theta = \theta_{\rm ch}$.

The dispersion curve has an inflection point, the wavenumber of which is denoted by $k_{\rm inf}$. The second derivative $\partial^2\omega/\partial k^2$ is positive for $k < k_{\rm inf}$ and is negative for $k > k_{\rm inf}$. By applying the condition $\partial^2\omega/\partial k^2 = 0$ to Eq. (2.14), we can numerically calculate $k_{\rm inf}$ as a function of θ (Fig. 2.12). The wavenumber $k_{\rm inf}$ sharply changes around the critical angle $\theta_{\rm ch}$; in other regions, $k_{\rm inf}$ is almost constant.

We can analytically obtain $k_{\rm inf}$ outside the small region around $\theta = \theta_{\rm ch}$. From Eq. (2.104), one finds $k_{\rm inf}$ as

$$\frac{ck_{\rm inf}}{\omega_{pe}} \simeq \left(\frac{\bar{\mu}_{\rm h}}{3|\mu_{\rm h}|}\right)^{1/4} \frac{c}{\omega_{pe}} \sim \left(\frac{m_e}{m_i}\right)^{1/4}, \tag{2.113}$$

for $\theta_{\rm ch} < \theta \leq 90^\circ$. For $\theta < \theta_{\rm ch}$, Eq. (2.110) gives

$$\frac{ck_{\rm inf}}{\omega_{pe}} \simeq \left(\frac{(12\eta^4 + 12\eta^2\cos^2\theta + \cos^4\theta)^{1/2}\cos^2\theta - (3\eta^4 + 3\eta^2\cos^2\theta - \cos^4\theta)}{3(\eta^2 + \cos^2\theta)(\eta^2 + 2\cos^2\theta)}\right)^{1/2}, \tag{2.114}$$

which indicates that $ck_{\rm inf}/\omega_{pe} \sim O(1)$. If $\theta < \theta_{\rm ch}$, $\partial^2\omega/\partial k^2$ is positive in large part of the wavenumber region (2.103), while, in the case $\theta_{\rm ch} < \theta \leq 90^\circ$, it is negative in most part of that region.

We can now show the wavenumber region in which the magnitude of $\bar{\mu}_{\rm h}k^{-2}$ is much smaller than that of $\mu_{\rm h}k^2$ so that the dispersion relation (2.104) is written as

$$\omega = v_{\rm h}k(1 + \mu_{\rm h}k^2). \tag{2.115}$$

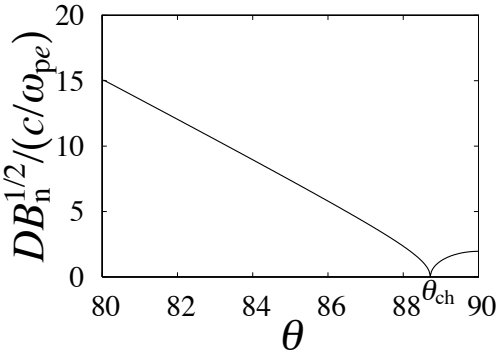

Figure 2.13: Normalized soliton width $DB_{\rm n}^{1/2}/(c/\omega_{pe})$ for high-frequency mode in a H-He plasma.

The relation $|\mu_{\rm h}k^2| = \bar{\mu}_{\rm h}k^{-2}$ holds at the wavenumber

$$\frac{ck_{\rm min}}{\omega_{pe}} = \left(\frac{\bar{\mu}_{\rm h}}{|\mu_{\rm h}|}\right)^{1/4}\frac{c}{\omega_{pe}} \sim \left(\frac{m_e}{m_i}\right)^{1/4}. \tag{2.116}$$

Hence, for $0 < \theta < \theta_{\rm ch}$, where $c^2{k_{\rm inf}}^2/\omega_{pe}^2 \sim O(1)$, Eq. (2.115) is valid in the range of wavenumbers

$$c^2{k_{\rm min}}^2/\omega_{pe}^2 \ll c^2k^2/\omega_{pe}^2 \ll c^2{k_{\rm inf}}^2/\omega_{pe}^2. \tag{2.117}$$

For $\theta_{\rm ch} < \theta < 90^\circ$, where $c^2{k_{\rm inf}}^2/\omega_{pe}^2 \sim (m_e/m_i)^{1/2}$, we have Eq. (2.115) in the wavenumber region

$$c^2{k_{\rm inf}}^2/\omega_{pe}^2 \ll c^2k^2/\omega_{pe}^2 \ll 1. \tag{2.118}$$

For the wavenumber regions (2.117) and (2.118), the dispersion form becomes similar to that of long-wavelength magnetosonic waves in a single-ion-species plasma.

The KdV equation for the oblique high-frequency mode has therefore been derived [5]. As shown in Appendix C, it is given by Eq. (2.52) with the coefficients $v_{p0} = v_{\rm h}$, $\mu = \mu_{\rm h}$, and

$$\alpha = (3\sum_i \omega_{pi}^2\Omega_i)/(2\omega_{pe}^2|\Omega_e|\eta^4). \tag{2.119}$$

With use of the normalized amplitude $B_{\rm n} = B_{z1}/B_0$, the soliton width can be written as $D = [12|\mu_{\rm h}|/(\alpha B_{\rm n})]^{1/2}$. The normalized soliton width $DB_{\rm n}^{1/2}/(c/\omega_{pe})$ is depicted in Fig. 2.13 as a function of θ for a H-He plasma [5]. The pulses are

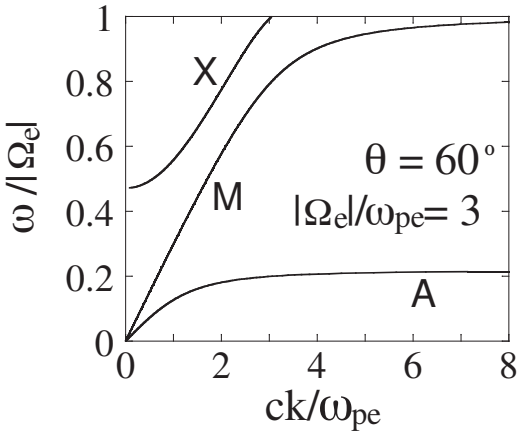

Figure 2.14: Dispersion relation of magnetohydrodynamic waves in a pure electron-positron plasma. The lines M and A represent magnetosonic and Alfvén waves, respectively. Here, $\theta = 60^\circ$ and $|\Omega_e|/\omega_{pe} = 3$.

compressive with the characteristic width $\sim c/\omega_{pe}$ for $\theta_{\rm ch} < \theta < 90^\circ$, while they are rarefactive with $D \sim c/\omega_{pi}$ for angles smaller than $\theta_{\rm ch}$.

2.4 Waves in an EPI plasma

2.4.1 Waves in a pure electron-positron plasma

Before discussing electron-positron-ion (EPI) plasmas, we look at the linear dispersion relation in a pure electron-positron plasma, where there are waves similar to magnetosonic and Alfvén waves in an ordinary electron-ion plasma. From the cold, two-fluid model, Eqs. (2.7)–(2.13) with $p_j = 0$ with the subscript j referring to electrons ($j = e$) or positrons ($j = p$), one obtains linear dispersion relations [37]:

$$\frac{c^2k^2}{\omega^2} = 1 - \frac{2\omega_{pe}^2}{\omega^2 - \Omega_e^2}, \tag{2.120}$$

$$\frac{c^2k^2}{\omega^2} = \frac{(\omega^2 - 2\omega_{pe}^2)(\omega^2 - \Omega_e^2 - 2\omega_{pe}^2)}{(\omega^2 - 2\omega_{pe}^2)(\omega^2 - \Omega_e^2) - 2\omega_{pe}^2\Omega_e^2\sin^2\theta}. \tag{2.121}$$

Figure 2.14 shows the dispersion relation of oblique waves with $\theta = 60^\circ$ in the frequency domain $\omega < |\Omega_e|$.

Line M in Fig. 2.14 represents the magnetosonic wave obtained from Eq. (2.120), which is independent of θ. This mode is linearly polarized, with its electric field

parallel to the y direction, i.e., parallel to $\boldsymbol{k}\times\boldsymbol{B}_0$. Since the positrons and electrons have the same mass, the longitudinal electric field is not created [38].

From Eq. (2.120), one finds the dispersion relation of the magnetosonic wave as

$$\frac{\omega}{k} = \tilde{v}_{\rm A}\left(1+\frac{\tilde{v}_{\rm A}^4}{v_{\rm A}^4}\frac{c^2k^2}{\omega_{pep}^2}\right)^{-1/2}, \tag{2.122}$$

where

$$\omega_{pep} = (\omega_{pe}^2+\omega_{pp}^2)^{1/2}, \tag{2.123}$$

$v_{\rm A}$ is the Alfvén speed in an electron-positron plasma,

$$v_{\rm A} = \frac{B_0}{(8\pi n_{e0}m_e)^{1/2}} = \frac{c|\Omega_e|}{\omega_{pep}}, \tag{2.124}$$

and $\tilde{v}_{\rm A}$ is defined by Eq. (2.34). In the long-wavelength regime such that $ck/\omega_{pe} \ll 1$, the dispersion relation is approximated as

$$\frac{\omega}{k} = \tilde{v}_{\rm A}\left(1-\frac{\tilde{v}_{\rm A}^4}{2v_{\rm A}^4}\frac{c^2k^2}{\omega_{pep}^2}\right). \tag{2.125}$$

The density perturbation n_{j1} is related to the magnetic perturbation B_{z1} through

$$n_{j1} \simeq n_{j0}(B_{z1}/B_0)\sin\theta, \tag{2.126}$$

indicating that this wave is a compressional mode with n_{j1}/n_{j0} being of the same order of magnitude as B_{z1}/B_0.

Line A in Fig. 2.14 represents the shear Alfvén wave, which disappears at $\theta = 90^\circ$ and becomes linearly polarized at $\theta = 0^\circ$. Both X and A are obtained from Eq. (2.121), and their electric fields are in the (x,z) plane. The dispersion relation of the Alfvén wave in the long-wavelength regime is given as

$$\frac{\omega}{k} = \tilde{v}_{\rm A}\cos\theta\left(1-\frac{[1+(1+v_{\rm A}^2/c^2)(v_{\rm A}^2/c^2)\sin^2\theta]}{2(1+v_{\rm A}^2/c^2)^2}\frac{c^2k^2}{\omega_{pep}^2}\right). \tag{2.127}$$

Its density perturbation is

$$\frac{n_{j1}}{n_{j0}} \simeq i\,\frac{\Omega_e^2}{\omega_{pep}^2}\frac{\tilde{v}_{\rm A}k\sin\theta}{\Omega_j}\frac{B_{y1}}{B_0}, \tag{2.128}$$

from which one sees that $n_{j1}/n_{j0} \sim (\omega/\Omega_j)(B_{y1}/B_0)$. The density perturbation of the Alfvén wave is small in the low-frequency regime, $\omega/\Omega_j \ll 1$.

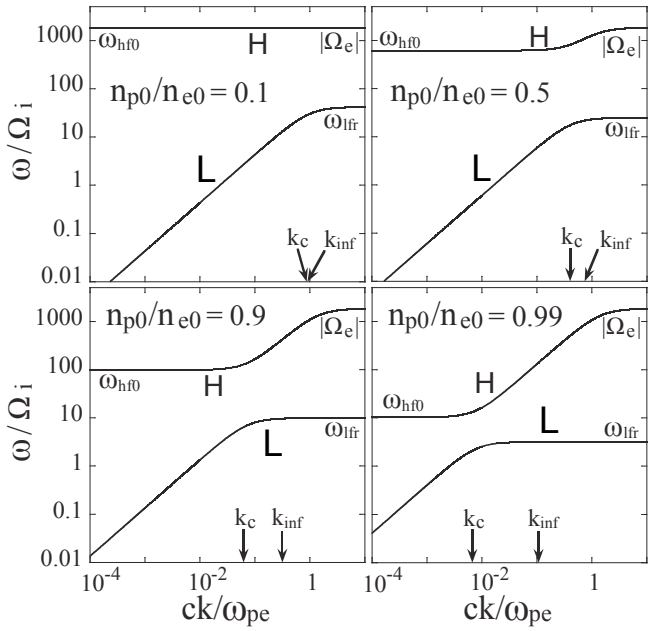

Figure 2.15: Dispersion relations of perpendicular magnetosonic waves in EPI plasmas. Lines H and L show, respectively, the high- and low-frequency modes. Here, the mass ratio is $m_i/m_e = 1836$. The definitions of k_c and $k_{\rm inf}$ are given by Eqs. (2.140) and (2.146), respectively.

2.4.2 Perpendicular waves in an EPI plasma

If a plasma contains a single species of ions as well as electrons and positrons, the magnetosonic wave is split into the high- and low-frequency modes. The linear dispersion relation for perpendicular waves may be written as

$$\left(\sum_j \frac{\omega_{pj}^2}{\omega^2-\Omega_j^2}\right)\left(\sum_j \frac{\omega_{pj}^2}{\omega^2-\Omega_j^2}+\frac{c^2k^2}{\omega^2}\right)-\left(\sum_j \frac{\omega_{pj}^2}{(\omega^2-\Omega_j^2)}\frac{\Omega_j}{\omega}\right)^2=0, \quad (2.129)$$

where the displacement current has been ignored, and the subscript j refers to electrons ($j = e$), positrons ($j = p$), or ions ($j = i$). The details of the calculations are found in Refs. [26, 27]. Inspection of Eq. (2.129) indicates that ω/Ω_i does not depend on magnetic-field strength; it is a function of k, densities, and particle masses and charges.

The dispersion relation of the high- and low-frequency magnetosonic modes is plotted in Fig. 2.15 for four different values of n_{p0}/n_{e0}. Line M in Fig. 2.14 is split

into lines H and L in Fig. 2.15: the high- and low-frequency modes. The structure of the dispersion curves is similar to that of two-ion-species plasmas discussed in Sec. 2.3, although there are some significant quantitative differences between them.

The frequency of the low-frequency mode goes from zero to the resonance frequency

$$\omega_{\rm lfr} = \left(\frac{r_{ei} + \nu}{1 + r_{ei}\nu} \right)^{1/2} \omega_{\rm LH}, \tag{2.130}$$

as the wavenumber k increases from zero to ∞, where

$$r_{ei} = m_e/m_i, \tag{2.131}$$

$$\nu = n_{i0}/(n_{e0} + n_{p0}), \tag{2.132}$$

and $\omega_{\rm LH}$ is the lower hybrid frequency defined by Eq. (2.19). The high-frequency mode has a cutoff frequency

$$\omega_{\rm hf0} = \frac{r_{ei} + \nu}{1 + r_{ei}\nu} |\Omega_e| = \frac{\omega_{\rm lfr}^2}{\Omega_i}, \tag{2.133}$$

and, as $k \to \infty$, approaches the resonance frequency

$$\omega_{\rm hfr} = |\Omega_e|. \tag{2.134}$$

The following relation holds among these frequencies and gyrofrequencies:

$$\Omega_i < \omega_{\rm lfr} < \omega_{\rm hf0} < \Omega_p = |\Omega_e|. \tag{2.135}$$

This relation resembles Eq. (2.79); note that the gyrofrequency of light ions, Ω_a, has been replaced by the positron gyrofrequency, which is equal to $|\Omega_e|$ and much greater than Ω_i.

As the positron density n_{p0} increases (namely, as n_{i0} and ν decrease), the difference $(\omega_{\rm hf0} - \omega_{\rm lfr})$ decreases; i.e., $\omega_{\rm hf0}$ goes down more rapidly than $\omega_{\rm lfr}$. In addition, because $\omega_{\rm hfr}$ is unchanged, the frequency range of the high-frequency mode, $(\omega_{\rm hfr} - \omega_{\rm hf0})$, expands. In the limit of $\nu \to 1$, i.e., $n_{p0} \to 0$ and $n_{i0} \to n_{e0}$, we have

$$\omega_{\rm lfr} = \omega_{\rm LH}, \tag{2.136}$$

$$\omega_{\rm hf0} = |\Omega_e|, \tag{2.137}$$

while in the limit of $\nu \to 0$, i.e., $n_{i0} = 0$,

$$\omega_{\rm lfr} = \omega_{\rm hf0} = \Omega_i. \tag{2.138}$$

With use of the Alfvén speed in an EPI plasma,

$$v_{\rm A} = \left(\frac{B_0}{4\pi \sum_j n_{j0} m_j} \right)^{1/2} = \frac{B_0}{(8\pi n_{e0} m_e)^{1/2}} \left(\frac{1+\nu}{1+\nu/r_{ei}} \right)^{1/2}, \tag{2.139}$$

the wavenumber $k_{\rm c}$ appearing in Fig. 2.15 is given by

$$k_{\rm c} = \omega_{\rm lfr}/v_{\rm A}, \tag{2.140}$$

which is in terms of ν and r_{ei}

$$\frac{ck_{\rm c}}{\omega_{pep}} = \frac{r_{ei}+\nu}{(1+r_{ei}\nu)^{1/2}}. \tag{2.141}$$

As in the case of two-ion-species plasmas, the dispersion curves of the low- and high-frequency modes have large curvatures around k_c.

Using these quantities, we can express approximate dispersion relations. In the long-wavelength domain such that $k \ll k_{\rm c}$, the high-frequency mode can be given as

$$\begin{aligned} \omega^2 &= \omega_{\rm hf0}^2 \left\{ 1 + \left(1 - \frac{\omega_{\rm hf0}^2}{\Omega_e^2} \right) \left(1 - \frac{\omega_{\rm lfr}^2}{\omega_{\rm hf0}^2} \right) \frac{k^2}{k_c^2} \right. \\ &\quad \left. + \left[\frac{\omega_{\rm lfr}^2}{\omega_{\rm hf0}^2} \left(1 - \frac{\omega_{\rm lfr}^2}{\omega_{\rm hf0}^2} + \frac{\omega_{\rm lfr}^2}{\Omega_e^2} \right) - \frac{\omega_{\rm hf0}^2}{\Omega_e^2} \left(1 + \frac{\omega_{\rm lfr}^2}{\Omega_e^2} \right) \right] \frac{k^4}{k_c^4} \right\}, \end{aligned} \tag{2.142}$$

while the low-frequency mode is

$$\frac{\omega}{k} = v_{\rm A} \left[1 - \frac{1}{2} \left(1 - \frac{\omega_{\rm lfr}^2}{\omega_{\rm hf0}^2} + \frac{\omega_{\rm lfr}^2}{\Omega_e^2} \right) \frac{k^2}{k_c^2} \right]. \tag{2.143}$$

If we ignore r_{ei} compared with unity, then, from Eqs. (2.130) and (2.133), we have

$$1 - \frac{\omega_{\rm lfr}^2}{\omega_{\rm hf0}^2} + \frac{\omega_{\rm lfr}^2}{\Omega_e^2} = \frac{\nu}{r_{ei}+\nu}, \tag{2.144}$$

for the case $\nu \gg r_{ei}^3$.

In the short-wavelength region such that $k \gg k_c$, the high-frequency mode is given as

$$\omega^2 = \omega_{\rm hf0}^2 \left(\frac{1 + k^2/k_c^2}{1 + c^2 k^2/\omega_{pep}^2} - \frac{(\omega_{\rm lfr}^2/\omega_{\rm hf0}^2)(k^2/k_c^2)}{1 + k^2/k_c^2} \right), \tag{2.145}$$

where we have used the relation $r_{ei} \ll 1$. The dispersion curve has an inflection point ($\partial^2\omega/\partial k^2 = 0$) at

$$k_{\rm inf} = \frac{1}{3^{1/4}} \left(1 - \frac{\omega_{\rm lfr}^2}{\omega_{\rm hf0}^2} \right)^{1/4} \frac{\omega_{pep}}{c} (r_{ei} + \nu)^{1/2} = \left(\frac{\nu}{3(r_{ei} + \nu)^3} \right)^{1/4} k_{\rm c}, \tag{2.146}$$

where we have assumed that $c^2 k^2/\omega_{pep}^2 \ll 1$. It is evident that $k_{\rm inf} \gg k_{\rm c}$ if $\nu \ll 1$. In the wavenumber domain such that $k \gg k_{\rm inf}$, the high-frequency mode is given by

$$\omega = \frac{v_{\rm h} k}{(1 + c^2 k^2/\omega_{pep}^2)^{1/2}}. \tag{2.147}$$

Here, $v_{\rm h}$ is defined as

$$v_{\rm h} = |\Omega_e| c/\omega_{pep}, \tag{2.148}$$

giving a measure of the propagation speed of the high-frequency mode. The ratio of $v_{\rm A}$ to $v_{\rm h}$ can be written as

$$\frac{v_{\rm A}}{v_{\rm h}} = \left(\frac{r_{ei}}{r_{ei} + \nu} \right)^{1/2}, \tag{2.149}$$

which indicates that $v_{\rm h}$ is always greater than $v_{\rm A}$. By virtue of the relations $\omega_{\rm hf0} = \omega_{\rm lfr}^2/\Omega_i$ and (2.149), k_c given by Eq. (2.140) is found to be equal to $\omega_{\rm hf0}/v_{\rm h}$ if m_e/m_i is ignored. For the wavenumber domain

$$k_{\rm inf} \ll k \ll \omega_{pep}/c, \tag{2.150}$$

the high-frequency mode can be approximated as

$$\frac{\omega}{k} = v_{\rm h} \left(1 - \frac{c^2 k^2}{2\omega_{pep}^2} \right). \tag{2.151}$$

Effects of the displacement current

The Alfvén speed $v_{\rm A}$ can be quite fast if $\boldsymbol{B}_0$ is strong, the plasma density is low, or n_{p0}/n_{e0} is close to unity, for which full Maxwell equations should be used. If

the displacement current is included in Ampère's law, then Eq. (2.129) for the dispersion relation of perpendicular waves is modified as follows:

$$\left(1-\sum_j \frac{\omega_{pj}^2}{\omega^2-\Omega_j^2}\right)\left(1-\sum_j \frac{\omega_{pj}^2}{\omega^2-\Omega_j^2}-\frac{c^2k^2}{\omega^2}\right)-\left(\sum_j \frac{\omega_{pj}^2}{(\omega^2-\Omega_j^2)}\frac{\Omega_j}{\omega}\right)^2=0. \tag{2.152}$$

In the long-wavelength regime $k \ll k_c$, the low-frequency mode can be written as

$$\frac{\omega}{k}=\tilde{v}_{\rm A}(1+\mu k^2), \tag{2.153}$$

with

$$\begin{aligned}\mu &= -\frac{1}{2}\frac{\tilde{v}_{\rm A}^4}{c^2}\left[\sum_j \frac{\omega_{pj}^2}{\Omega_j^4}-\frac{\tilde{v}_{\rm A}^2}{c^2}\left(\sum_j \frac{\omega_{pj}^2}{\Omega_j^3}\right)^2\right]\\ &= -\frac{1}{2}\frac{(\tilde{v}_{\rm A}/v_{\rm A})^6}{(r_{ei}+\nu)^3}\left[\left(\frac{\Omega_e^2}{2\omega_{pe}^2}+2r_{ei}-r_{ei}^3\right)\nu^2\right.\\ &\quad\left.+\left(1+\frac{\Omega_e^2}{2\omega_{pe}^2}(1+r_{ei}^3)+r_{ei}^2\right)\nu+\left(1+\frac{\Omega_e^2}{2\omega_{pe}^2}\right)r_{ei}^3\right]\frac{c^2}{\omega_{pep}^2}.\end{aligned} \tag{2.154}$$

The high-frequency mode in the wavenumber region (2.150) is approximated as

$$\frac{\omega}{k}=\tilde{v}_{\rm h}\left(1-\frac{1}{2}\frac{\tilde{v}_{\rm h}^4}{v_{\rm h}^4}\frac{c^2k^2}{\omega_{pep}^2}\right), \tag{2.155}$$

with

$$\tilde{v}_{\rm h}=\frac{v_{\rm h}}{(1+v_{\rm h}^2/c^2)^{1/2}}. \tag{2.156}$$

In the rest of Sec. 2.4.2 and in Sec. 2.4.3, the displacement current is included.

Nonlinear perpendicular low-frequency mode

As expected from the dispersion relation, the KdV equation for the low-frequency mode is derived [26] with the conventional reductive perturbation method [8,9]: It takes the form of Eq. (2.52) with $v_{p0}=\tilde{v}_{\rm A}$, $\alpha=(3/2)(\tilde{v}_{\rm A}/v_{\rm A})^2$, and μ given by Eq. (2.154).

From Eq. (2.55), one obtains the soliton width $D_{\rm lf}$, which is plotted in the top panel of Fig. 2.16 as a function of $\nu=n_{i0}/(n_{e0}+n_{p0})$ for a Mach number $M_{\rm lf}=1.25$ [26]. The width $D_{\rm lf}$ goes up as ν goes down from $\nu=1$ to $\nu\sim m_e/m_i$.

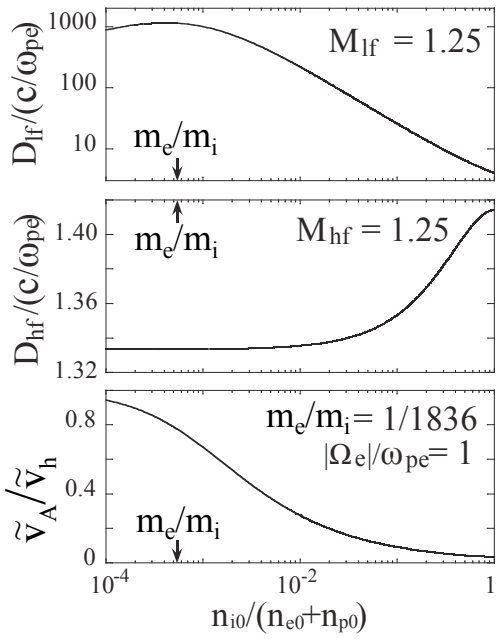

Figure 2.16: Soliton widths and speed ratio $\tilde{v}_{\rm A}/\tilde{v}_{\rm h}$ as functions of $\nu = n_{i0}/(n_{e0} + n_{p0})$. The Mach numbers are taken to be 1.25. The mass ratio is $m_i/m_e = 1836$. The top and second panels show the widths of the low- and high-frequency modes, respectively.

This is due to the fact that the current density parallel to the wave front decreases with increasing positron density and thus the pulse width increases to keep the same magnitude of magnetic perturbation. In the low-frequency mode in an EPI plasma, electrons and positrons both move mainly with the $\boldsymbol{E} \times \boldsymbol{B}$ drift. Their currents and the one due to the ion $\boldsymbol{E} \times \boldsymbol{B}$ drift cancel out. Consequently, the current in a pulse region is created primarily by the ion polarization drift parallel to the wave front. On the other hand, in a perpendicular nonlinear magnetosonic wave in an electron-ion plasma, the electron current is much greater than the ion current and determines the magnetic structure, as mentioned in Sec. 2.2.1.

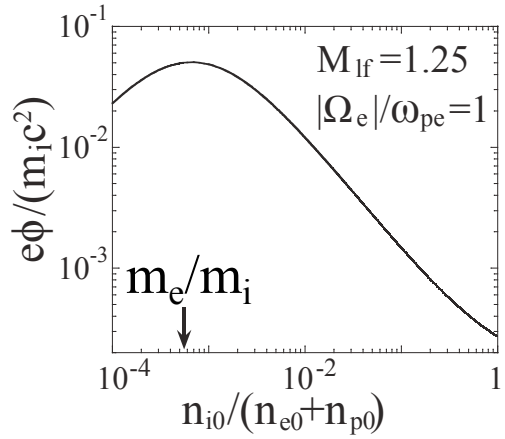

Figure 2.17: Magnitude of potential as a function of $\nu = n_{i0}/(n_{e0} + n_{p0})$.

The magnitude of the potential formed in a solitary wave is given as

$$e\phi = 2m_i\tilde{v}_{\rm A}^2 \frac{(1 - r_{ei}^2)\nu}{r_{ei} + \nu}(M_{\rm lf} - 1). \tag{2.157}$$

In the limit of $\nu \to 1$ (no positrons), this reduces to

$$e\phi = 2m_i\tilde{v}_{\rm A}^2(M_{\rm lf} - 1), \tag{2.158}$$

which is identical to the potential in a cold, electron-ion plasma. Figure 2.17 shows the magnitude of potential as a function of ν for $M_{\rm lf} = 1.25$ [26]. It increases with decreasing ion density, from $\nu = 1$ to $\nu \sim m_e/m_i$. This is a reflection of the fact that the Alfvén speed rises as ν goes down. Because, for $\nu \gtrsim m_e/m_i$, $e\phi$ is of the

order of the ion kinetic energy measured in the wave frame, it increases with the Alfvén speed. In a pure electron-positron plasma ($\nu = 0$), however, $\phi = 0$.

The normalized amplitude of the magnetic field is given as

$$B_{\rm n} = 2(M_{\rm lf} - 1)\left(\frac{v_{\rm A}}{\tilde{v}_{\rm A}}\right)^2. \tag{2.159}$$

This is identical to Eq. (2.36) if $\tilde{v}_{\rm A} = v_{\rm A}$.

Nonlinear perpendicular high-frequency mode

Although the high-frequency mode has a finite cutoff frequency, the dispersion relation (2.151) in the wavenumber region $k_{\rm inf} \ll k \ll \omega_{pep}/c$ suggests that this mode is approximately governed by the KdV equation. Indeed, as in the case of the high-frequency mode in a two-ion-species plasma in Sec. 2.3.1, we can derive the KdV equation with the perturbation scheme focusing on this wavenumber region: Under the assumptions that

$$[\nu(r_{ei} + \nu)]^{1/2} \ll \epsilon \ll 1, \tag{2.160}$$

and that

$$r_{ei}^{1/2} \ll \epsilon, \tag{2.161}$$

we obtain a nonlinear evolution equation for this mode [26]: Eq. (2.52) with $v_{p0} = \tilde{v}_{\rm h}$, $\alpha = (3/2)(\tilde{v}_{\rm h}/v_{\rm h})^2$, and $\mu = -[\tilde{v}_{\rm h}^4/(2v_{\rm h}^4)](c^2/\omega_{pep}^2)$ [see Eq. (2.155)].

The soliton width, $D_{\rm hf} = 2(\tilde{v}_{\rm h}/v_{\rm h})(c/\omega_{pep})B_{\rm n}^{-1/2}$, is depicted in the middle panel of Fig. 2.16 as a function of ν. [The Mach number $M_{\rm hf}$ is related to the normalized pulse amplitude $B_{\rm n}$ through $M_{\rm hf} = 1 + (\tilde{v}_{\rm h}/v_{\rm h})^2 B_{\rm n}/2$.] The width $D_{\rm hf}$ is insensitive to ν, close to c/ω_{pe} for a wide range of ν.

The bottom panel of Fig. 2.16 shows the ratio of $\tilde{v}_{\rm A}$ to $\tilde{v}_{\rm h}$. The speed $\tilde{v}_{\rm A}$ is always smaller than $\tilde{v}_{\rm h}$; in particular, for $\nu > 0.1$, $\tilde{v}_{\rm A}/\tilde{v}_{\rm h}$ is less than 0.1 for these plasma parameters.

Another important feature of the high-frequency-mode soliton is that its potential is negligibly small compared with that of the low-frequency mode: In the

perturbation scheme for this mode, the longitudinal electric field is $E_x = 0$ in the lowest order.

Nonlinear coupling of high- and low-frequency modes in an EPI plasma

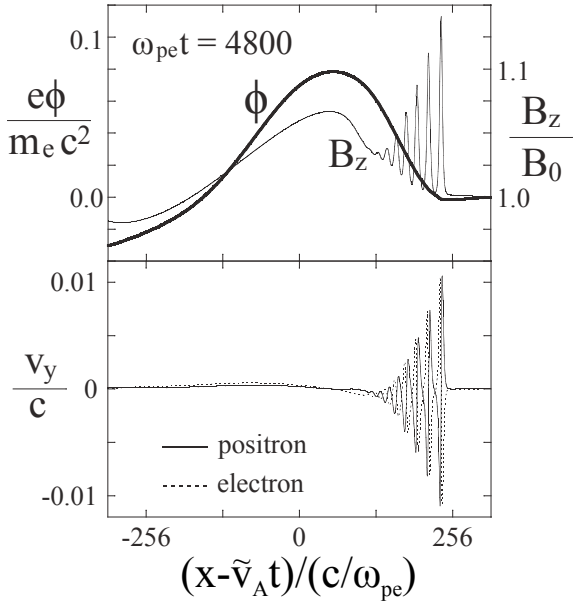

Figure 2.18: Snapshots of field profiles of high- and low-frequency-mode pulses. The upper panel shows B_z (thin line) and potential ϕ (thick line). The lower panel shows v_{py} (solid line) and v_{ey} (dotted line). Short-wavelength, high-frequency-mode pulses are emitted from a long-wavelength, low-frequency-mode pulse.

Similarly to the case of two-ion-species plasmas, high-frequency-mode pulses can be generated from a nonlinear, low-frequency-mode pulse. From the conditions $k \ll k_c$ and $\epsilon \sim \mu k^2$, we find the upper limit of the amplitude of low-frequency-mode pulses as $\epsilon_{\max} \sim \mu k_c^2$. As Fig. 2.15 shows, k_c and the difference $(\omega_{\rm hf0} - \omega_{\rm lfr})$ decrease with increasing positron density. It is thus expected that their nonlinear coupling becomes stronger as n_{p0} rises.

Three-fluid simulations for the investigation of nonlinear wave evolution in an EPI plasma have been performed, and a result quite similar to Fig. 2.8 has been reported [26]; i.e., many short-wavelength, high-frequency-mode pulses are generated from a large-amplitude, long-wavelength, low-frequency-mode pulse. This is

shown by Fig. 2.18. At the same time, however, this figure reveals properties of the high-frequency mode that are different from those in a two-ion-species plasma. The high-frequency-mode pulses here have virtually no electric potential ϕ, which we see by comparing the profiles of B_z and ϕ. In addition, these short-wavelength pulses have v_y perturbations with $v_{py} = -v_{ey}$. Here, the initial amplitude of the low-frequency-mode pulse is $\epsilon = B_{z1}/B_0 = 0.1$, which is greater than $\epsilon_{\max} = 0.024$; other parameters are $m_i/m_e = 100$, $n_{i0}/n_{e0} = 0.001$, and $|\Omega_e|/\omega_{pe} = 1$. In another simulation with the initial amplitude $\epsilon = 0.01$ ($< \epsilon_{\max}$), emission of high-frequency-mode pulses was not observed until the end of the run ($\omega_{pe}t = 14,400$). These features are in accord with the theoretical predictions.

2.4.3 Oblique waves in an EPI plasma

From the cold, three-fluid model with full Maxwell equations, one obtains the linear dispersion relation of oblique waves as [27]

$$\left(1 - \sum_j \frac{\omega_{pj}^2}{\omega^2 - \Omega_j^2} - \frac{c^2k^2}{\omega^2}\right)\left[\left(1 - \sum_j \frac{\omega_{pj}^2}{\omega^2}\right)\left(1 - \sum_j \frac{\omega_{pj}^2}{\omega^2 - \Omega_j^2} - \frac{c^2k^2}{\omega^2}\right) + \left(\sum_j \frac{\omega_{pj}^2}{(\omega^2 - \Omega_j^2)}\frac{\Omega_j^2}{\omega^2}\right)\frac{c^2k^2}{\omega^2}\sin^2\theta\right] - \left(\sum_j \frac{\omega_{pj}^2}{(\omega^2 - \Omega_j^2)}\frac{\Omega_j}{\omega}\right)^2\left(1 - \sum_j \frac{\omega_{pj}^2}{\omega^2} - \frac{c^2k^2}{\omega^2}\sin^2\theta\right) = 0. \tag{2.162}$$

Equation (2.162) gives six oblique waves as shown in Fig. 2.19 for $n_{p0}/n_{e0} = 0.02$ and Fig. 2.20 for $n_{p0}/n_{e0} = 0.9$, where the ion-to-electron mass ratio is taken to be $m_i/m_e = 1836$. These pictures indicate that in the low frequency regime such that $\omega \lesssim |\Omega_e|$, we have three modes: Line A represents the Alfvén wave, while lines H and L, respectively, show the high- and low-frequency modes of the magnetosonic wave.

In the limit of $k \to \infty$, these waves have resonance frequencies:

$$\omega_{\rm hfr} = |\Omega_e|, \tag{2.163}$$

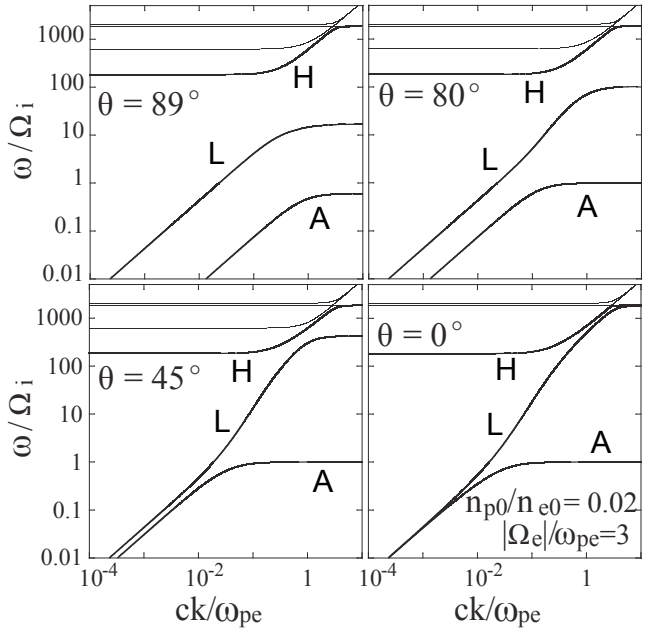

Figure 2.19: Dispersion curves of oblique magnetohydrodynamic waves for four different propagation angles in a cold EPI plasma with $n_{p0}/n_{e0} = 0.02$. In the frequency regime lower than $|\Omega_e|$, there are three modes: high-frequency mode (line H), low-frequency mode (line L), and Alfvén mode (line A). The high-frequency mode is in the region $\omega/\Omega_i \gtrsim 100$ for these parameters.

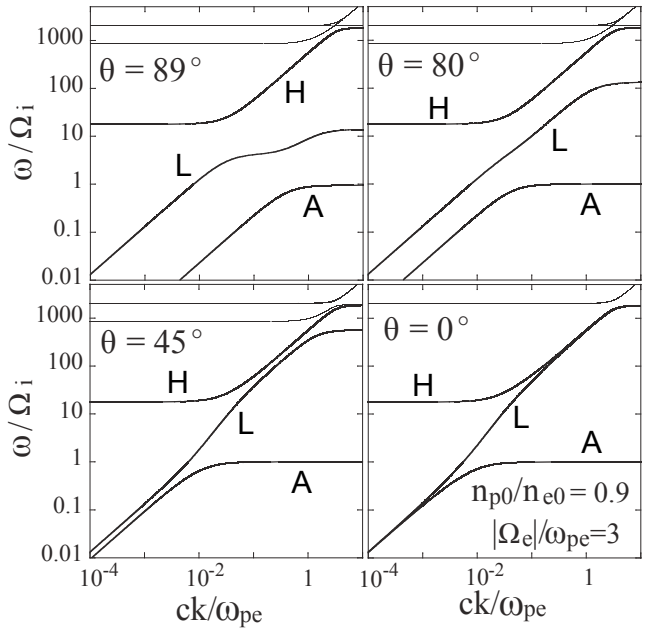

Figure 2.20: Dispersion curves for $n_{p0}/n_{e0} = 0.9$.

for the high-frequency mode,

$$\omega_{\rm lfr} \simeq |\Omega_e| \cos\theta, \tag{2.164}$$

for the low-frequency mode (except for the vicinity of $\theta = 90°$), and

$$\omega_{\rm Ar} \simeq \Omega_i, \tag{2.165}$$

for the Alfvén mode. At $\theta = 90°$, $\omega_{\rm lfr}$ is given by Eq. (2.130), and the Alfvén wave disappears. At $k = 0$, the high-frequency mode has a cutoff frequency $\omega_{\rm hf0}$ nearly equal to Eq. (2.133). Although $\omega_{\rm hf0}$ decreases with increasing positron density, it is much higher than the ion gyrofrequency even at $n_{p0}/n_{e0} = 0.9$. Furthermore, $\omega_{\rm lfr}$ is much higher than Ω_i at any angles and density ratios, so that the low-frequency mode is less affected, particularly in the situation that n_{p0}/n_{e0} is low, by the presence of high-frequency mode than in the case of two-ion-species plasmas.

In the long-wavelength region, the dispersion relation of the low-frequency mode is given as $\omega/k = \tilde{v}_{\rm A}(1 + \mu k^2)$ with the dispersion coefficient being

$$\mu = -\frac{\tilde{v}_{\rm A}^4}{2c^2}\left[\sum_j \frac{\omega_{pj}^2}{\Omega_j^4} - \frac{\tilde{v}_{\rm A}^2}{c^2 \sin^2\theta}\left(\sum_j \frac{\omega_{pj}^2}{\Omega_j^3}\right)^2\right], \tag{2.166}$$

which resembles $\mu_{\rm l}$ in a two-ion-species plasma, Eq. (2.101). This mode is governed by the KdV equation of the form (2.52) with $v_{p0} = \tilde{v}_{\rm A}$, $\alpha = (3/2)(\tilde{v}_{\rm A}/v_{\rm A})^2 \sin\theta$, and μ given by Eq. (2.166) [27]. The soliton width is $\sim c/\omega_{pi}$ except for the vicinity of $\theta = 90°$.

The critical angle θ_c, at which μ becomes zero, is given as

$$\sin\theta_c = \frac{(\tilde{v}_{\rm A}/c)\left(\sum_j \omega_{pj}^2/\Omega_j^3\right)}{\left(\sum_j \omega_{pj}^2/\Omega_j^4\right)^{1/2}}. \tag{2.167}$$

We see from Eqs. (2.166) and (2.167) that $\mu > 0$ for $0 < \theta < \theta_c$, and $\mu < 0$ for $\theta_c < \theta \leq 90°$. Figure 2.21 shows the dependence of θ_c on the positron-to-electron density ratio for the case with $m_i/m_e = 1836$ and $|\Omega_e|/\omega_{pe} = 1$. As n_{p0}/n_{e0} increases from zero to unity, θ_c goes down from 88.1° to 0°. The decrease is particularly rapid

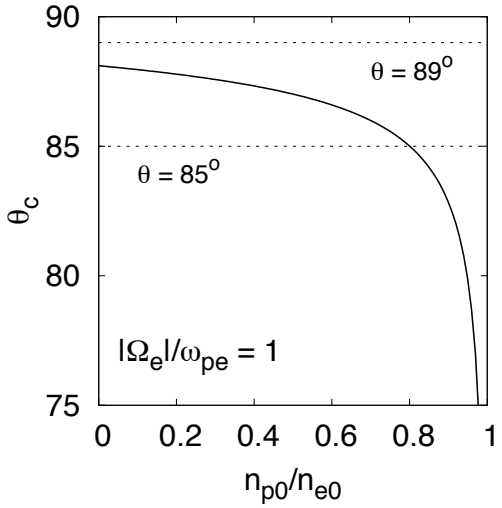

Figure 2.21: Critical angle θ_c as a function of n_{p0}/n_{e0}. The mass ratio is $m_i/m_e = 1836$. If the angle θ is taken to be 89°, for instance, it is greater than θ_c for any values of n_{p0}/n_{e0}. If the angle is 85°, it is smaller than θ_c for $n_{p0}/n_{e0} < 0.8007$.

for $n_{p0}/n_{e0} \gtrsim 0.8$. The propagation angle $\theta = 89°$, for instance, is greater than θ_c at any values of n_{p0}/n_{e0}; thus the solitary waves with this propagation angle are always compressive. On the other hand, the angle $\theta = 85°$ is lower than θ_c for $0 < n_{p0}/n_{e0} < 0.8$, for which we have rarefactive solitons, and is higher than θ_c for $0.8 < n_{p0}/n_{e0} < 1$, for which we have compressive solitons.

In an EPI plasma, in contrast to a pure electron-positron plasma, the magnetosonic wave can have a large electric potential, the magnitude of which in a low-frequency-mode solitary wave is given as [27]

$$e\phi = 2m_i\tilde{v}_{\rm A}^2 \frac{(1-r_{ei}^2)\nu}{(\nu + r_{ei})} \frac{(M_{\rm lf}-1)}{\sin^2\theta}. \tag{2.168}$$

For $n_{i0}/n_{e0} \sim 10^{-2}$, the potential is $\sim 10^2$ times as large as that in an ordinary electron-ion plasma, $\sim 2m_i v_{\rm A}^2(M-1)$.

To this point of this section, we have considered the cold plasma model. Finally, we summarize the result of finite-temperature theory for nonlinear magnetosonic waves in an EPI plasma [28, 29]. This theory will be used in the next section to investigate the electric field parallel to the magnetic field, $E_\parallel = (\boldsymbol{E}\cdot\boldsymbol{B})/B$.

From the set of three-fluid equations with finite temperatures coupled with full

Maxwell equations, we derive the linear dispersion relation, which, in the limit of $\omega \to 0$, becomes

$$\frac{c^2}{\tilde{v}_{\rm A}^2} - \frac{c^2}{v_{\rm p0}^2} - \frac{\sin^2\theta}{v_{\rm p0}^2} \sum_j \frac{\omega_{pj}^2 c_j^2/\Omega_j^2}{1 - c_j^2 \cos^2\theta / v_{\rm p0}^2}$$

$$+\tan^2\theta \left(\sum_j \frac{\omega_{pj}^2/\Omega_j^2}{1 - c_j^2\cos^2\theta/v_{\rm p0}^2} \right)^2 \Bigg/ \left(\sum_j \frac{\omega_{pj}^2}{1 - c_j^2\cos^2\theta/v_{\rm p0}^2} \right) = 0, \qquad (2.169)$$

where c_j is the speed related to the thermal speed,

$$c_j^2 = \Gamma_j {v_{Tj}}^2 = \Gamma_j \frac{p_{j0}}{n_{j0} m_j}, \qquad (2.170)$$

(for the details, see Ref. [29]). Assuming that the temperatures are low,

$$\frac{c_j^2}{v_{\rm p0}^2} \ll 1, \qquad (2.171)$$

and therefore ignoring higher order terms of $c_j^2/v_{\rm p0}^2$, we obtain

$$v_{\rm p0}^2 = \frac{v_{\rm A}^2 + c_s^2 \sin^2\theta}{1 + v_{\rm A}^2/c^2}, \qquad (2.172)$$

where c_s is the sound speed

$$c_{\rm s} = \left(\frac{n_{i0}\Gamma_i T_{i0} + n_{p0}\Gamma_p T_{p0} + n_{e0}\Gamma_e T_{e0}}{n_{i0} m_i + n_{p0} m_p + n_{e0} m_e} \right)^{1/2}. \qquad (2.173)$$

Calculating the phase velocity up to the terms of order k^2, $\omega/k = v_{\rm p0}(1 + \mu k^2)$, we find the dispersion coefficient μ as

$$\begin{aligned}
\mu = &- \frac{v_{\rm p0}^2 \tilde{v}_{\rm A}^2}{2c^2} \left[\left(\sum_j \frac{\omega_{pj}^2}{\Omega_j^4} \right) - \frac{\tilde{v}_{\rm A}^2}{c^2 \sin^2\theta} \left(\sum_j \frac{\omega_{pj}^2}{\Omega_j^3} \right)^2 \right] \\
&+ \frac{\tilde{v}_{\rm A}^2}{c^2} \sin^2\theta \left[\left(\sum_j \frac{\omega_{pj}^2}{\Omega_j^4} c_j^2 \right) - \frac{\tilde{v}_{\rm A}^2}{c^2 \sin^2\theta} \left(\sum_j \frac{\omega_{pj}^2}{\Omega_j^3} \right) \left(\sum_j \frac{\omega_{pj}^2}{\Omega_j^3} c_j^2 \right) \right] \\
&+ \frac{\tilde{v}_{\rm A}^2}{c^2 \omega_p^2} \cos^2\theta \left(\sum_j \frac{\omega_{pj}^2}{\Omega_j^3} \right) \left(\sum_j \frac{\omega_{pj}^2}{\Omega_j} c_j^2 \right) - \frac{\tilde{v}_{\rm A}^6 c_s^2}{2c^4 v_{\rm A}^2 \tan^2\theta} \left(\sum_j \frac{\omega_{pj}^2}{\Omega_j^3} \right)^2,
\end{aligned} \qquad (2.174)$$

which, in the limit of $T_j = 0$, reduces to Eq. (2.166). We have the KdV equation for this mode in a warm plasma of the form (2.52) with v_{p0} and μ given by Eqs. (2.172) and (2.174), respectively; α is

$$\alpha = \frac{\tilde{v}_{\rm A}^2 \sin\theta}{2 v_{\rm A}^2} \left[3 + \frac{c_s^2}{\tilde{v}_{\rm A}^2} (-5\sin^2\theta + 3) + \frac{v_{\rm A}^2 \sin^2\theta}{\tilde{v}_{\rm A}^2 c^2} \left(\sum_j \frac{\omega_{pj}^2}{\Omega_j^2} c_j^2 \Gamma_j \right) \right]. \qquad (2.175)$$

2.5 Parallel electric field

The electric field parallel to the magnetic field plays a crucial role in some particle acceleration mechanisms: Examples are found in electron acceleration in Chap. 3 and in positron acceleration in Chap. 6. This section examine the strength of the parallel electric field in nonlinear magnetosonic waves.

In the ideal MHD, perfect conductivity is assumed:

$$\boldsymbol{E} + \frac{\boldsymbol{v} \times \boldsymbol{B}}{c} = 0, \tag{2.176}$$

from which it follows that the electric field parallel to the magnetic field is zero,

$$E_\parallel = \frac{\boldsymbol{E} \cdot \boldsymbol{B}}{B} = 0. \tag{2.177}$$

The parallel electric field was generally thought to be quite weak in MHD phenomena in high-temperature plasmas. In fact, for instance, this is one of the main reasons for the difficulty in explaining the heating of the solar corona [39, 40].

Recently, however, it has been found that the parallel electric field can be strong in nonlinear magnetosonic waves in collisionless plasmas [28, 29].

2.5.1 Parallel pseudo potential

In the analysis of parallel electric field and particle acceleration in one-dimensional waves, the integral of the parallel electric field along the magnetic field,

$$F = -\int E_\parallel ds, \tag{2.178}$$

is a useful quantity [34, 41–43]. Since $E_\parallel$ can contain both longitudinal and transverse electric fields, F is not an ordinary electric potential; we call F the parallel pseudo potential. The bottom panel of Fig. 2.4 shows F in a shock wave. With use of the relation $ds/B = dx/B_{x0}$, Eq. (2.178) can be put into the following form:

$$F(x,t) = -\int^x \frac{\boldsymbol{E}(x,t) \cdot \boldsymbol{B}(x,t)}{B_{x0}} dx. \tag{2.179}$$

In many cases, the integral F is easier to measure than $E_\parallel$.

For a stationary wave, Eq. (2.179) becomes

$$F(x) = -\int \frac{E_x B_{x0} + E_{y0} B_y}{B_{x0}} dx, \tag{2.180}$$

in the wave frame, where, as shown by Eqs. (2.58) and (2.59), $E_y = E_{y0}$ and $E_z = 0$. (In the following, the subscript w for the wave frame is used only when necessary.) By virtue of the second relation of Eq. (2.58), Eq. (2.180) can be written as

$$F = -\int \left(E_x - \frac{v_{\rm sh} B_{z0} B_y}{c B_{x0}} \right) dx, \tag{2.181}$$

where $v_{\rm sh}$ is the wave speed. Using the electric potential ϕ and the z component of the vector potential $\boldsymbol{A}$ ($B_y = -\partial A_z/\partial x$), we can express F as

$$F = \phi - \frac{v_{\rm sh}}{c} \frac{B_{z0}}{B_{x0}} A_z. \tag{2.182}$$

As mentioned in Sec. 2.2.3, ϕ and B_z have similar profiles in magnetosonic waves, while B_y is proportional to $\partial B_z/\partial x$. Hence, F has a profile similar to ϕ and A_z, unless the two terms on the right-hand side of Eq. (2.182) nearly cancel.

Since $(\boldsymbol{E}\cdot\boldsymbol{B})$ is Lorentz invariant, we find from Eq. (2.179) the relation between the quantities in the wave and laboratory frames as

$$F_{\rm w} = \gamma_{\rm sh} F_{\rm l}. \tag{2.183}$$

2.5.2 Parallel electric field and parallel pseudo potential in nonlinear magnetosonic waves

Perturbation theory for $E_\parallel$ and F in an electron-ion plasma

As described in Sec. 2.2.2 and in Appendix B, the KdV equation is derived for nonlinear magnetosonic waves with the reductive perturbation method. In the finite beta theory [11], where beta is the ratio of the plasma to magnetic pressures, the perturbation of electric potential is related to magnetic perturbation B_{z1} as

$$\begin{aligned} e\phi_1 &= m_i \left(\frac{(\Omega_e + \Omega_i)(v_{p0}^2 - c_s^2) v_{p0}^2}{\Omega_e (v_{p0}^2 - v_{\rm A}^2 \cos^2\theta)} + \frac{\Gamma_e p_{e0}}{n_0 (m_i + m_e)} - \frac{m_e \Gamma_i p_{i0}}{m_i n_0 (m_i + m_e)} \right) \\ &\times \frac{v_{\rm A}^2 \sin\theta}{(v_{p0}^2 - c_s^2)} \frac{B_{z1}}{B_0}, \end{aligned} \tag{2.184}$$

[see Eq. (B.34) in Appendix B]. The first term on the right-hand side of Eq. (2.184) is mainly due to magnetic pressure, while the second and third terms are, respectively, due to electron and ion thermal pressures; the third term is $\sim m_e/m_i$ times as small as the second one. Equation (2.184) reduces to

$$e\phi_1 \simeq m_i \left(v_{\rm A}^2 + \frac{\Gamma_e p_{e0}}{n_0(m_i + m_e)} \right) \frac{B_{z1}}{B_0}, \tag{2.185}$$

in quasi-perpendicular waves with $\sin\theta \simeq 1$, which clearly shows the contributions of magnetic field and electron pressure.

In this perturbation scheme, the parallel electric field is proportional to the electron temperature T_e. As shown in Appendix B, the longitudinal electric field E_{x1} and the z component of the transverse electric field E_{z1} are given as

$$\frac{E_{x1}}{B_0} = -\frac{v_{\rm A}^2 \sin\theta}{\Omega_i \Omega_e c} \left[\frac{(\Omega_e + \Omega_i) v_{p0}^2}{(v_{p0}^2 - v_{\rm A}^2 \cos^2\theta)} + \frac{c_s^2 (\Omega_e \Gamma_e p_{e0} + \Omega_i \Gamma_i p_{i0})}{(v_{p0}^2 - c_s^2)(\Gamma_e p_{e0} + \Gamma_i p_{i0})} \right] \frac{\partial}{\partial \xi} \frac{B_{z1}}{B_0}, \tag{2.186}$$

$$\frac{E_{z1}}{B_0} = \frac{(\Omega_e + \Omega_i) v_{p0}^2 v_{\rm A}^2 \cos\theta}{\Omega_i \Omega_e c (v_{p0}^2 - v_{\rm A}^2 \cos^2\theta)} \frac{\partial}{\partial \xi} \frac{B_{z1}}{B_0}. \tag{2.187}$$

The first term on the right-hand side of Eq. (2.186) and the field E_{z1} are mainly due to magnetic pressure. These terms cancel in the lowest order calculation of $E_\parallel$,

$$E_{\parallel 1} = E_{x1} \cos\theta + E_{z1} \sin\theta. \tag{2.188}$$

With the aid of the relation between the magnetic perturbation B_{z1} and density perturbation n_1

$$\frac{B_{z1}}{B_0} = \frac{(v_{p0}^2 - c_s^2)}{v_{\rm A}^2 \sin\theta} \frac{n_1}{n_0}, \tag{2.189}$$

we can express the parallel electric field as

$$E_\parallel = -\frac{\Gamma_e T_e}{e} \frac{\partial}{\partial s} \left(\frac{n_1}{n_0} \right), \tag{2.190}$$

where s is the length along the magnetic field [28]. Integration of Eq. (2.190) along the magnetic field yields the parallel pseudo potential

$$eF = eF_T = \Gamma_e T_e \frac{n_1}{n_0}, \tag{2.191}$$

which resembles the electric potential in the ion-acoustic wave. We use the symbol F_T when emphasizing that F scales as T_e. The magnitude of F is determined by the electron temperature, $eF \lesssim T_e$. Comparison of Eqs. (2.184) and (2.191) shows that the parallel pseudo potential F is smaller than the electric potential ϕ; their difference is especially significant in low beta plasmas.

In some particle simulations [34, 42], however, the magnitude of eF far exceeds the electron temperature (Fig. 2.4), suggesting that, other than thermal pressure, there is a mechanism enhancing $E_\parallel$ and thus F. We therefore consider a cold plasma, $T_e = T_i = 0$, and carry out higher order calculations [28]. Since they are lengthy, we present only important results to show the outline of the calculation.

Let us look at the parallel electric field up to the second-order terms:

$$E_\parallel = \frac{\boldsymbol{E}\cdot\boldsymbol{B}}{B} = \frac{\boldsymbol{E}_1\cdot\boldsymbol{B}_0}{B_0}\left(1 - \frac{\boldsymbol{B}_1\cdot\boldsymbol{B}_0}{B_0^2}\right) + \frac{\boldsymbol{E}_1\cdot\boldsymbol{B}_1}{B_0} + \frac{\boldsymbol{E}_2\cdot\boldsymbol{B}_0}{B_0}. \tag{2.192}$$

The lowest order term $\boldsymbol{E}_1\cdot\boldsymbol{B}_0/B_0$ is finite (proportional to T_e) in warm plasmas and is zero in cold plasmas, as shown by Eq. (2.190). The term $\boldsymbol{E}_1\cdot\boldsymbol{B}_1 = E_{y1}B_{y1} + E_{z1}B_{z1}$ vanishes in both warm and cold plasmas: $\boldsymbol{E}_1$ and $\boldsymbol{B}_1$ are perpendicular. The term $\boldsymbol{E}_2\cdot\boldsymbol{B}_0/B_0$ is found to be expressed with lowest order quantities if $T_e = T_i = 0$. That is, $E_\parallel$ appears in the second order in a cold plasma.

We obtain $E_\parallel$ and F for quasi-perpendicular waves as

$$eE_\parallel = \frac{m_i v_{\mathrm{A}}^2}{\tan\theta}\left(\frac{c}{\omega_{pe}}\right)^2 \frac{\partial^3}{\partial\xi^3}\frac{B_{z1}}{B_0}, \tag{2.193}$$

$$eF = eF_B = -\frac{m_i v_{\mathrm{A}}^2}{\sin\theta}\left(\frac{c}{\omega_{pe}}\right)^2 \frac{\partial^2}{\partial\xi^2}\frac{B_{z1}}{B_0}, \tag{2.194}$$

which are proportional to B_0^2 for a fixed normalized amplitude B_{z1}/B_0; B_{z1} obeys the KdV equation as described in Sec. 2.2.2. The subscript B is used to stress that F is determined primarily by the magnetic field. The fact that F is proportional to $\partial^2 B_{z1}/\partial\xi^2$ indicates that F has a profile different from B_{z1} [In the conventional, lower order theory for a warm plasma, they have similar profiles, as shown by Eqs. (2.189) and (2.191)]. Furthermore, because $\partial^2/\partial\xi^2 \sim \epsilon$ in the perturbation scheme, F in Eq. (2.194) is of the order of ϵ^2: $eF \sim \epsilon^2 m_i v_{\mathrm{A}}^2$.

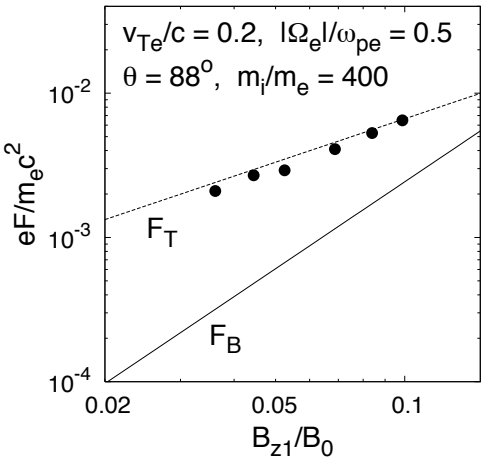

Figure 2.22: Magnitude of F as a function of pulse amplitude. The dots and the lines F_T and F_B show simulation results, warm-plasma theory, and higher-order cold-plasma theory, respectively. Here, the plasma beta value is of order unity, and the simulation results are explained by the warm-plasma theory F_T.

Simulations for F in an electron-ion plasma

These theoretical predictions have been verified with particle simulations, through the observation of magnetosonic solitary pulses [28]. In the simulations, initial profiles of fields, densities, and velocities are given according to the soliton theory. Because n_i and n_e are taken to be exactly the same at $t = 0$, the longitudinal electric field E_x is initially zero. In a self-consistent simulation, however, E_x is created in the evolution of the wave. The profiles of other physical quantities including $E_\parallel$ are also adjusted to their most stable forms. After the pulse propagation has become stationary, the field strengths are measured.

Figure 2.22 shows the magnitude of F obtained in this way as a function of the pulse amplitude B_{z1}/B_0 for a warm plasma, where the closed circles, dashed line, and solid line, respectively, represent the simulation result, warm-plasma theory (2.191) (denoted by F_T), and higher order cold-plasma theory (2.194) (denoted by F_B). Here, the propagation angle is $\theta = 88°$, the speed of light is $c/(\omega_{pe}\Delta_{\rm g}) = 10$, where $\Delta_{\rm g}$ is the grid spacing, the electron thermal velocity $v_{Te} = (T_e/m_e)^{1/2}$ is $v_{Te}/(\omega_{pe}\Delta_{\rm g}) = 2.0$, and the strength of the external magnetic field is $|\Omega_e|/\omega_{pe} = 0.5$,

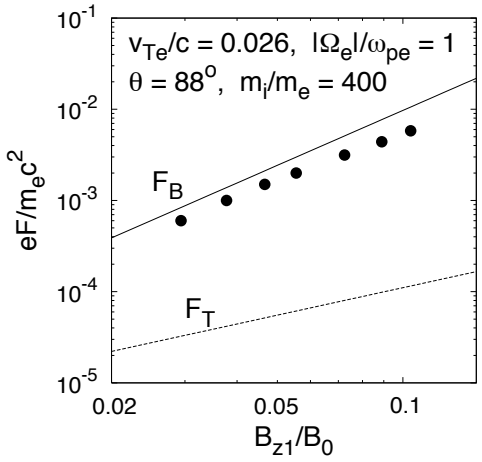

Figure 2.23: F versus pulse amplitude. Here, $|\Omega_e|/\omega_{pe}$ is higher, and v_{Te} is lower than those in Fig. 2.22. The simulation results (dots) are consistent with the higher order cold-plasma theory F_B.

which gives the Alfvén speed as $v_{\rm A}/(\omega_{pe}\Delta_{\rm g}) = 0.25$. For the present parameters, F_T is much greater than F_B, and the simulation results are close to F_T.

Figure 2.23 shows the parallel pseudo potential in a low beta plasma, with a lower T_e [$v_{Te}/(\omega_{pe}\Delta_{\rm g}) = 0.26$] and a higher B_0 ($|\Omega_e|/\omega_{pe} = 1.0$) [hence, $v_{\rm A}/(\omega_{pe}\Delta_{\rm g}) = 0.5$ and $m_ec^2 = m_iv_{\rm A}^2$], with other parameters kept unchanged. Here, F_B is much greater than F_T, and the simulation results agree with F_B much better than with F_T.

In both Figs. 2.22 and 2.23, the propagation angle θ ($= 88^\circ$) is greater than the critical angle θ_c, and thus the dispersion coefficient μ is negative; accordingly, pulses are compressive. Rarefactive pulses with $\theta < \theta_c$ were also investigated; the theory was confirmed to be consistent with simulation results [28].

F in shock waves

The above theories and simulations are for small-amplitude ($\epsilon \ll 1$) waves. We now examine F in large-amplitude ($\epsilon \gtrsim 1$) shock waves. Figure 2.24 shows the values of F (closed circles and triangles) and ϕ (open circles and triangles) formed in shock waves at $\theta = 60^\circ$ with the amplitudes $2 \lesssim B_{z1}/B_0 \lesssim 10$ in warm plasmas:

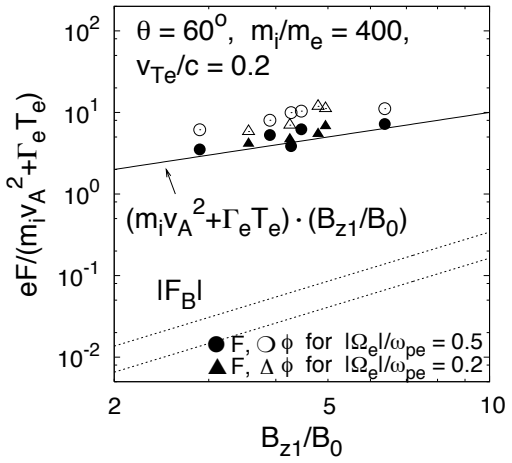

Figure 2.24: Magnitudes of F and ϕ in shock waves at $\theta = 60°$. The upper and lower dotted lines show extrapolated $|F_B|$ for $|\Omega_e|/\omega_{pe} = 0.5$ and 0.2, respectively. The solid line represents the relation (2.195), which is consistent with the simulation results.

$|\Omega_e|/\omega_{pe} = 0.5$ (circles) and 0.2 (triangles), and the electron temperature is the same as that in Fig. 2.22. The dotted lines represent $|F_B|$, which we have drawn by merely extrapolating F for small-amplitude pulses, Eq. (2.194), to a larger amplitude regime, while the solid line represents a phenomenological relation

$$eF \sim (m_i v_{\rm A}^2 + \Gamma_e T_e)\frac{B_{z1}}{B_0}, \tag{2.195}$$

to which the simulation values of F fit fairly well. Here, the dependence of eF on the external magnetic-field strength has changed from $eF \sim m_i v_{\rm A}^2 \epsilon^2$ in the small-amplitude regime to $eF \sim m_i v_{\rm A}^2 \epsilon$ in the large-amplitude regime. In addition to these studies, the low beta case has also been examined, and it has been found that Eq. (2.195) is also consistent with simulation results.

These investigations confirm that Eq. (2.195) is applicable to both low and high beta cases. Furthermore, as long as the shock wave has a steep profile near the shock front, simulation results fit to Eq. (2.195) even if $\theta < \theta_c$. Another important feature is that F is always smaller than ϕ, although their ratio F/ϕ is larger than those in small-amplitude waves.

The results of the theory and simulations for F may be summarized as follows:

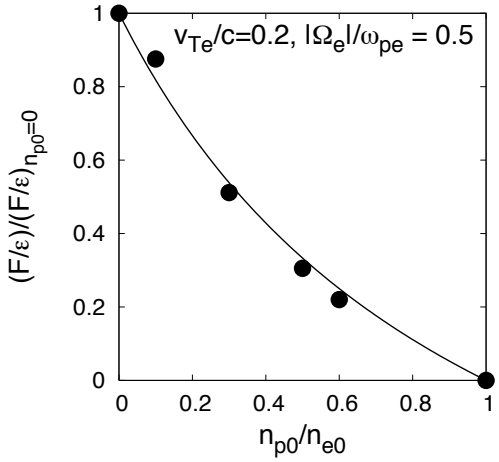

Figure 2.25: Magnitude of F/ϵ of small-amplitude pulse as a function of n_{p0}/n_{e0} for the case $F_T \gg F_B$. Here, F/ϵ is normalized to its value at $n_{p0}/n_{e0} = 0$, i.e, $(F/\epsilon)_{n_{p0}=0}$. The theory (solid line) and simulation result (dots) both show that F decreases with increasing n_{p0}/n_{e0}.

In small-amplitude pulses, the magnitude of F is

$$eF \sim \Gamma_e T_e \epsilon, \tag{2.196}$$

in warm plasmas and

$$eF \sim m_i v_{\rm A}^2 \epsilon^2, \tag{2.197}$$

in cold plasmas. In large-amplitude waves [$\epsilon \sim O(1)$], i.e., in shock waves, the relation

$$eF \sim (m_i v_{\rm A}^2 + \Gamma_e T_e)\epsilon, \tag{2.198}$$

explains the simulation results for both warm and cold plasmas. This indicates that strong parallel electric field can form in nonlinear magnetosonic waves.

Theory and simulations for $E_\parallel$ and F in an EPI plasma

Next, we consider the low-frequency mode of the magnetosonic wave in an EPI plasma. As proved in Chapter 6, a shock wave of this mode can accelerate positrons to ultrarelativistic energies with its parallel electric field; thus, to obtain $E_\parallel$ is crucial to understand this mechanism. Since even the linear theory requires a large

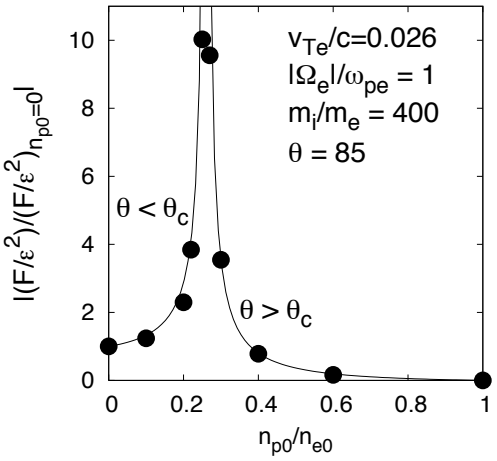

Figure 2.26: Dependence of F/ϵ^2 on n_{p0}/n_{e0} for the case $F_B \gg F_T$. Here, the propagation angle is 85° and becomes equal to θ_c at $n_{p0}/n_{e0} = 0.26$, around which F is quite large.

amount of calculations for oblique magnetosonic waves in finite beta plasmas, this section shows only results of calculations; the details are found in Ref. [29].

Positrons act to reduce the magnitude of F. For warm plasmas, $E_\parallel$ and F are given as

$$eE_\parallel = -\left(\frac{\omega_{pe}^2}{\omega_p^2}\Gamma_e T_e - \frac{\omega_{pp}^2}{\omega_p^2}\Gamma_p T_p - \frac{\omega_{pi}^2}{\omega_p^2}\frac{\Gamma_i T_i}{Z}\right)\sin\theta\cos\theta\frac{\partial}{\partial\xi}\left(\frac{B_{z1}}{B_0}\right), \tag{2.199}$$

$$eF_T = \left(\frac{\omega_{pe}^2}{\omega_p^2}\Gamma_e T_e - \frac{\omega_{pp}^2}{\omega_p^2}\Gamma_p T_p - \frac{\omega_{pi}^2}{\omega_p^2}\frac{\Gamma_i T_i}{Z}\right)\sin\theta\frac{B_{z1}}{B_0}, \tag{2.200}$$

where Z is the ionic charge state, $q_i = Ze$, and $\omega_p^2 = \sum_j \omega_{pj}^2$. Equations (2.199) and (2.200) indicate that the terms proportional to the ion temperature T_i are $\sim m_e/m_i$ times as small as the terms proportional to T_e and to T_p and that $E_\parallel$ and F decrease with increasing positron density n_{p0} and become zero in a pure electron-positron plasma ($n_{i0} = 0$). As shown in Fig. 2.25, simulations verify the theoretical prediction that F decreases with increasing n_{p0}. Here, a solitary wave was generated in each particle simulation, and its field values were measured.

The parallel pseudo potential F given by Eq. (2.200) goes to zero as $T_j \to 0$. As in the case of electron-ion plasmas, we need higher order calculations to obtain

$E_\parallel$ and F in a cold plasma ($T_j = 0$); they are given as

$$E_\parallel = \frac{4\pi\tilde{v}_{\rm A}^4}{B_0^2 \tan\theta} \left(\sum_j \frac{n_{j0} m_j^2}{q_j} \right) \left(\frac{c}{\omega_p} \right)^2 \frac{\partial^3}{\partial \xi^3} \left(\frac{B_{z1}}{B_0} \right), \tag{2.201}$$

$$F_B = -\frac{4\pi\tilde{v}_{\rm A}^4}{B_0^2 \sin\theta} \left(\sum_j \frac{n_{j0} m_j^2}{q_j} \right) \left(\frac{c}{\omega_p} \right)^2 \frac{\partial^2}{\partial \xi^2} \left(\frac{B_{z1}}{B_0} \right). \tag{2.202}$$

Here, Maxwell's equations with the displacement current have been used, and therefore the modified Alfvén speed $\tilde{v}_{\rm A}$, which was defined by Eq. (2.34), appears. In the cold plasma approximation, F is proportional to ϵ^2 and, if $v_{\rm A}^2 \ll c^2$, proportional to B_0^2. If $n_{i0} m_i \gg n_{e0} m_e$, Eqs. (2.201) and (2.202) can be approximated as

$$eE_\parallel = \frac{m_i \tilde{v}_{\rm A}^2}{\tan\theta \, (1 + v_{\rm A}^2/c^2)} \left(\frac{c}{\omega_p} \right)^2 \frac{\partial^3}{\partial \xi^3} \left(\frac{B_{z1}}{B_0} \right), \tag{2.203}$$

$$eF_B = -\frac{m_i \tilde{v}_{\rm A}^2}{\sin\theta \, (1 + v_{\rm A}^2/c^2)} \left(\frac{c}{\omega_p} \right)^2 \frac{\partial^2}{\partial \xi^2} \left(\frac{B_{z1}}{B_0} \right). \tag{2.204}$$

In the limit of $n_{p0} = 0$, for which $\omega_p \simeq \omega_{pe}$, Eq. (2.204) reduces to F in the cold, two-fluid model, Eq. (2.194). Figure 2.26 shows F for $\theta = 85^\circ$ in a low beta EPI plasma. In the vicinity of the n_{p0}/n_{e0} at which the critical angle θ_c is equal to θ, F becomes quite large. We recall that, as shown in Fig. 2.21, θ_c decreases with increasing n_{p0}/n_{e0}; thus, if n_{p0}/n_{e0} varies from zero to unity with θ fixed at a value not too close to 90°, θ_c becomes equal to θ at some value of n_{p0}/n_{e0}. Around this density ratio, F has large values. The critical angle θ_c is smaller in Fig. 2.26 than in Fig. 2.21 because the mass ratio of the former, $m_i/m_e = 400$, is smaller than that of the latter, $m_i/m_e = 1836$.

At $n_{p0}/n_{e0} = 1$, both $E_\parallel$ and F are zero, which we see from Eqs. (2.201) and (2.202). In pure electron-positron plasmas, the relation $E_\parallel = 0$ holds for both high and low beta cases.

With regard to large-amplitude waves (shock waves) with $\epsilon \sim O(1)$, the phenomenological equation for the parallel pseudo potential

$$n_{e0} eF \sim \left(\rho v_{\rm A}^2 + \Gamma_e p_{e0} \right) \frac{n_{i0}}{n_{e0}} \frac{B_{z1}}{B_0}, \tag{2.205}$$

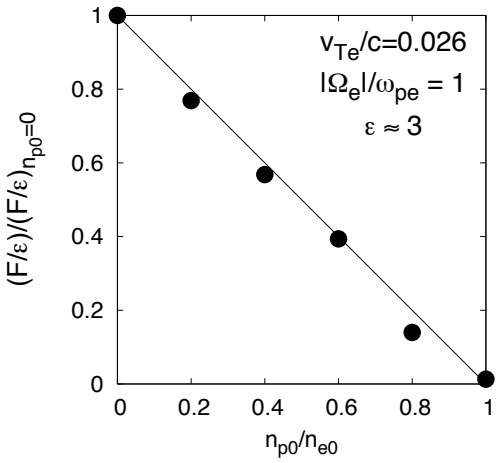

Figure 2.27: Parallel pseudo potential F versus positron density in shock waves. The propagation angle is $\theta = 60^\circ$ and the amplitudes are $B_{z1}/B_0 \sim 3$, with other parameters being the same as those in Fig. 2.23; a low beta case.

is consistent with the simulation results of both high and low beta cases. We plot in Fig. 2.27 the dependence of F on the density ratio n_{p0}/n_{e0} in the low beta case. The effect of the critical angle θ_c was not observed in shock waves with sharp field profiles in the shock transition region. As $n_{p0} \to 0$, Eq. (2.205) reduces to the equation for electron-ion plasmas, Eq. (2.195).

Bibliography

[1] H. Alfvén and C.-G. Fälthammer, *Cosmical Electrodynamics*, (Clarendon Press, Oxford, 1963).

[2] P. A. Sturrock, *Plasma Physics*, (Cambridge University Press, New York, 1994).

[3] D. Biskamp, *Nonlinear Magnetohydrodynamics*, (Cambridge University Press, Cambridge, 1993).

[4] A. Barnes, Phys. Fluids **9**, 1483 (1966).

[5] S. Irie and Y. Ohsawa, Phys. Plasmas **10**, 1253 (2003).

[6] Y. Takeyama, S. Nakayama, and Y. Ohsawa, Phys. Plasmas **18**, 092307 (2011).

[7] Yu. A. Berezin and V. I. Karpman, Sov. Phys. JETP **19**, 1265 (1964).

[8] T. Taniuti and C. C. Wei, J. Phys. Soc. Jpn. **24**, 941 (1968).

[9] T. Kakutani, H. Ono, T. Taniuti, and C. C. Wei, J. Phys. Soc. Jpn. **24**, 1159 (1968).

[10] T. Kakutani and H. Ono, J. Phys. Soc. Jpn. **26**, 1305 (1969).

[11] Y. Ohsawa, Phys. Fluids **29**, 1844 (1986).

[12] R. Z. Sagdeev, in *Reviews of Plasma Physics*, edited by M. A. Leontovich (Consultants Bureau, New York, 1966), Vol. 4, pp. 23-91.

[13] D. A. Tidman and N. A. Krall, *Shock Waves in Collisionless Plasmas*, (John Wiley & Sons, New York, 1971).

[14] R. C. Davidson, *Methods in Nonlinear Plasma Theory*, (Academic Press, New York, 1972).

[15] J. H. Adlam and J. E. Allen, Philos. Mag. **3**, 448 (1958).

[16] L. Davis, R. Lüst, and A. Schlüter, Z. Naturforsch. A **13**, 916 (1958).

[17] Y. Ohsawa, Phys. Fluids **29**, 2474 (1986).

[18] Y. Ohsawa, Phys. Fluids **28**, 2130 (1985).

[19] C. S. Gardner and G. K. Morikawa, Courant Institute of Mathematical Sciences, New York University, Report No. NYO 9082, 1960 (unpublished).

[20] C. S. Gardner and G. K. Morikawa, Commun. Pure Appl. Math. **18**, 35 (1965).

[21] S. J. Buchsbaum, Phys. Fluids **3**, 418 (1960).

[22] A. B. Mikhailovskii and A. I. Smolyakov, Sov. Phys. JETP **61**, 109 (1985).

[23] M. Toida, Y. Ohsawa, and T. Jyounouchi, Phys. Plasmas **2**, 3329 (1995).

[24] D. Dogen, M. Toida, and Y. Ohsawa, Phys. Plasmas **5**, 1298 (1998).

[25] M. Toida, H. Higashino, and Y. Ohsawa, J. Phys. Soc. Jpn. **76**, 104502 (2007).

[26] H. Hasegawa, S. Irie, S. Usami, and Y. Ohsawa, Phys. Plasmas **9**, 2549 (2002).

[27] H. Hasegawa and Y. Ohsawa, J. Phys. Soc. Jpn. **73**, 1764 (2004).

[28] S. Takahashi and Y. Ohsawa, Phys. Plasmas **14**, 112305 (2007).

[29] S. Takahashi, M. Sato, and Y. Ohsawa, Phys. Plasmas **15**, 082309 (2008).

[30] H. Washimi and T. Taniuti, Phys. Rev. Lett. **17**, 996 (1966).

[31] T. Taniuti and N. Yajima, J. Math. Phys. **10**, 1369 (1969).

[32] N. J. Zabusky and M. D. Kruskal, Phys. Rev. Lett. **15**, 240 (1965).

[33] C. Gardner, J. Greene, M. Kruskal and R. Miura, Phys. Rev. Lett. **19**, 1095 (1967).

[34] N. Bessho and Y. Ohsawa, Phys. Plasmas **9**, 979 (2002).

[35] S. Nakazawa and Y. Ohsawa, J. Phys. Soc. Jpn. **66**, 2044 (1997); *ibid.* **67**, 2965 (1998).

[36] S. Miyahara, T. Kawashima, and Y. Ohsawa, Phys. Plasmas **10**, 98 (2003).

[37] G. A. Stewart and E. W. Laing, J. Plasma Phys. **47**, 295 (1992).

[38] C. F. Kennel and R. Pellat, J. Plasma Phys. **15**, 335 (1976).

[39] J. V. Hollweg, Astrophys. J. **277**, 392 (1984).

[40] A. Hasegawa and L. Chen, Phys. Rev. Lett. **32**, 454 (1974); *ibid.* **35**, 370 (1975).

[41] N. Bessho and Y. Ohsawa, Phys. Plasmas **6**, 3076 (1999).

[42] H. Hasegawa, S. Usami, and Y. Ohsawa, Phys. Plasmas **10**, 3455 (2003).

[43] S. Takahashi, H. Kawai, Y. Ohsawa, S. Usami, C. Chiu, and W. Horton, Phys. Plasmas **16**, 112308 (2009); *ibid.* **16**, 129904-1 (2009).

Chapter 3

Trapping and ultrarelativistic acceleration of electrons

We now proceed to study particle acceleration. The first subject is electron energization triggered by reflection.

Shock waves can reflect electrons near the end of the main pulse. Here, the "main pulse" designates the first large pulse in a shock wave (Fig. 2.4): The front part of the main pulse is the shock transition region. As can be seen from Fig. 2.4, the parallel pseudo potential F takes small values near its end. Reflection occurs near the end of the main pulse when F becomes particularly small there in nonstationary shock evolution. The reflected electrons are rapidly accelerated and then trapped in the main pulse region [1–3]. Simulations have demonstrated electron acceleration to energies $\gamma > 100$ due to this mechanism. This indicates that the strong electric and magnetic fields formed in a shock wave can promptly accelerate electrons with a nonstochastic mechanism to energies higher than those of solar energetic electrons: Their highest energy is several tens of megaelectronvolts ($\gamma \sim 100$) [4,5]. Chapter 3 describes the theory and simulations of this mechanism: reflection, acceleration, and trapping.

This process takes place in a shock wave propagating obliquely to an external magnetic field. (Large-amplitude pulses such as quasi shock waves can also give rise to the same type of particle acceleration. The term "shock wave" includes these waves in this paper.) In an oblique shock wave, the electric and magnetic

fields both have three components, so that the analyses of their structures and of particle motions in them are rather complicated. To have a picture of the acceleration process, we first look at simulation results. We will then consider its physical mechanism and quantitative theory.

3.1 Particle simulation of shock waves

Collective and individual-particle motions are both important in plasma phenomena. This is particularly true for particle acceleration. The electromagnetic fields that energize some particles are created by collective plasma motions, and the accelerated particles can also affect the electromagnetic fields.

Particle simulations enable us to analyze these strongly nonlinear and highly relativistic phenomena in a self-consistent manner. Most of the simulation results that are shown here have been obtained by use of one-dimensional, fully kinetic, relativistic, electromagnetic codes. This section briefly describes this method [1,6] and then shows simulation results. More general and detailed descriptions on particle simulation methods are found in Refs. [7]- [13].

3.1.1 Simulation method

To simulate collisionless plasmas, we use finite-size particles. Their sizes are usually of the order of the Debye length $\lambda_{\rm D}$, which is taken to be comparable to the grid spacing $\Delta_{\rm g}$ (numerical instabilities can grow if $\lambda_{\rm D} < \Delta_{\rm g}$). In the one-dimensional code, spatial variations are allowed only in the x direction, with the y and z directions being ignorable coordinates. The simulation particles, however, have three velocity components (v_x, v_y, v_z). The trajectories of finite-size simulation particles are advanced by the following relativistic equation of motion:

$$\frac{d\boldsymbol{p}_j}{dt} = q_j \int dx S(x - x_j) \left(\boldsymbol{E}(x,t) + \frac{\boldsymbol{v}_j \times \boldsymbol{B}(x,t)}{c} \right), \tag{3.1}$$

$$\frac{dx_j}{dt} = v_{jx}, \tag{3.2}$$

where $\boldsymbol{p}_j$, $\boldsymbol{v}_j$, and x_j are, respectively, the relativistic momentum, velocity, and x position of the j-th simulation particle; $S(x - x_j)$ is the form factor showing the spatial distribution of the charge and mass of a finite-size particle with a Gaussian shape,

$$S(x - x_j) = \frac{1}{(2\pi)^{1/2} a} \exp\left(-\frac{(x - x_j)^2}{2a^2}\right), \tag{3.3}$$

with a ($\sim \lambda_{\rm D}$) giving a measure of the particle size. The plasma current and charge associated with each grid point are calculated from the positions and velocities of the simulated particles. These are then considered to be sources that generate the electric and magnetic fields. Fast Fourier transforms are used to calculate the field quantities from Maxwell's equations:

$$ikE_{\rm ln}(k,t) = 4\pi\rho(k,t), \tag{3.4}$$

$$\frac{\partial \boldsymbol{E}_{\rm t}}{\partial t} = ic\boldsymbol{k} \times \boldsymbol{B}_{\rm t}(k,t) - 4\pi \boldsymbol{J}_{\rm t}(k,t), \tag{3.5}$$

$$\frac{\partial \boldsymbol{B}_{\rm t}}{\partial t} = ic\boldsymbol{k} \times \boldsymbol{E}_{\rm t}(k,t). \tag{3.6}$$

Here, $\boldsymbol{k}$ is the wave vector in the x direction, $\rho(k,t)$ is the Fourier component of the charge density at time t, and the subscripts "ln" and "t" refer to the longitudinal and transverse components, respectively; the transverse current $\boldsymbol{J}_{\rm t}(k,t)$ is given by

$$\boldsymbol{J}_{\rm t} = \boldsymbol{J}(k,t) - [\boldsymbol{k} \cdot \boldsymbol{J}(k,t)]\boldsymbol{k}/k^2. \tag{3.7}$$

The time integration is performed with a centered finite-difference scheme, the leap-frog method.

As in the theory in Chap. 2, waves propagate in the x direction in an external magnetic field in the $(x,\ z)$ plane (Fig. 2.1): $\boldsymbol{B}_0 = B_0(\cos\theta, 0, \sin\theta) = (B_{x0}, 0, B_{z0})$. The transverse ($y$ and z) components of $\boldsymbol{B}$ can be created in electromagnetic waves; however, the x component is constant, $B_x = B_{x0}$, owing to the equation $\nabla \cdot \boldsymbol{B} = 0$.

Figure 3.1 shows a schematic diagram of the initial density profile. The high-density plasma (exploding plasma) has an initial velocity $\boldsymbol{v}_0$, while the low-density plasma (surrounding plasma) is at rest at $t = 0$. The exploding plasma pushes the surrounding plasma and creates a forward (right-going) shock wave. [In a large-size

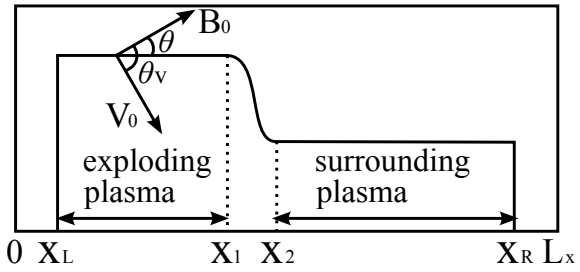

Figure 3.1: Schematic representation of initial density profile and velocity. The plasma in the high-density region (exploding plasma) has a velocity $\boldsymbol{v}_0$, while that in the low-density region (surrounding plasma) is at rest at $t = 0$. Both $\boldsymbol{B}_0$ and $\boldsymbol{v}_0$ are in the (x, z) plane.

simulation, a backward (left-going) shock wave is also observed, which is discussed in Chap. 7. We are concerned with the phenomena near the forward shock front in Chapters 3 through 6.] Both $\boldsymbol{B}_0$ and $\boldsymbol{v}_0$ are in the (x, z) plane. We usually take the angle between them to be $\theta_v = 90°$ to prevent fast particles with $v \sim |\boldsymbol{v}_0|$ from moving along the field lines.

The plasma is isolated with the vacuum outside: the bounded plasma model [11]. The simulation particles are confined in the region $x_{\rm L} < x < x_{\rm R}$, being specularly reflected at $x = x_{\rm L}$ and $x = x_{\rm R}$. The equation for the longitudinal electric fields is solved under the assumption that there is no charge in the regions $x < x_{\rm L}$ and $x > x_{\rm R}$. For the transverse fields, an absorbing boundary condition is used: Electromagnetic fields leaving the plasma region is absorbed in the vacuum regions [6].

The ion-to-electron mass ratio is taken to be $m_i/m_e = 100$ in this chapter. The speed of light is $c/(\omega_{pe}\Delta_{\rm g}) = 4$, where ω_{pe} is the electron plasma frequency calculated with use of the electron density averaged over the entire plasma region $x_{\rm L} < x < x_{\rm R}$. The electron thermal speed $v_{Te} = (T_e/m_e)^{1/2}$ is $v_{Te}/(\omega_{pe}\Delta_{\rm g}) = 0.4$ with $T_e = T_i$; $|\Omega_e|/\omega_{pe} = 3$; hence, the Alfvén speed becomes $v_{\rm A}/(\omega_{pe}\Delta_{\rm g}) = 1.2$. [Figure 3.4 has different simulation parameters, such as $m_i/m_e = 400$ and $c/(\omega_{pe}\Delta_{\rm g}) = 10$.]

3.1.2 Simulation results: Creation of ultrarelativistic electrons in the main pulse

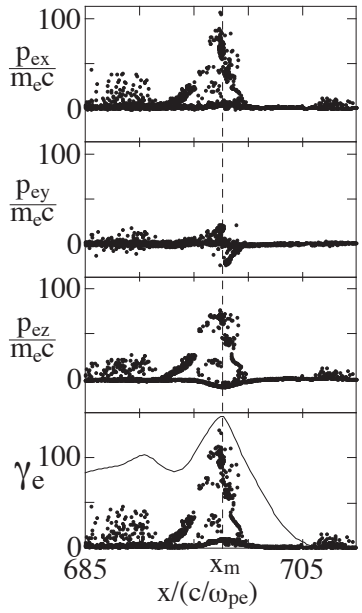

Figure 3.2: Electron phase space plots. The solid line in the bottom panel shows the profile of ϕ. We find ultrarelativistic electrons with $\gamma > 100$ in the main pulse region.

This section outlines the phenomenon of ultrarelativistic electron acceleration in an oblique shock wave, with use of simulation results.

Field profiles in an oblique shock wave observed in a particle simulation have been shown in Fig. 2.4. As mentioned there, the quantities B_z, E_y, ϕ, and plasma density have similar profiles, while B_y, E_x, and E_z are approximately proportional to $\partial B_z/\partial x$ near the shock front. The magnetic field B_z is particularly strong near the shock transition region, the width of which is $\sim c/\omega_{pi}$.

The electron acceleration discussed here takes place in the main pulse, which is in $695 \lesssim x/(c/\omega_{pe}) \lesssim 705$ in Fig. 2.4. Some electrons are reflected near the end of the main pulse region and then accelerated and trapped in the main pulse.

Figure 3.2 displays electron phase spaces $(x,\ p_x)$, $(x,\ p_y)$, $(x,\ p_z)$, and $(x,\ \gamma)$, where $\boldsymbol{p} = m_e \gamma \boldsymbol{v}$, and each point represents an electron in the phase space at the

same instant as that of Fig. 2.4 [2]. There are many ultrarelativistic electrons with $\gamma \gtrsim 100$ in the main pulse region. The highest energy electrons are found near the position of the strongest magnetic field, $x = x_m$, at which the electric potential ϕ also peaks.

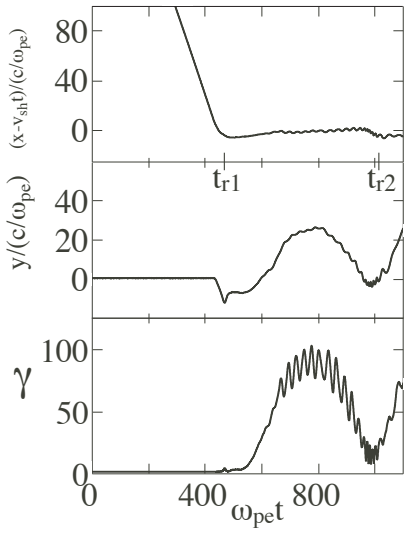

Figure 3.3: Time variations of positions $(x - v_{\rm sh}t)$ and y and energy γ of an accelerated electron. After entering the shock wave from the upstream region, this particle is reflected near the end of the main pulse region at time $t = t_{r1}$, accelerated to $\gamma \sim 100$ in the main pulse, and reflected again at $t = t_{r2}$. This particle is trapped by the shock wave and oscillates in the main pulse region.

Plotted in Fig. 3.3 are the time variations of the positions $(x - v_{\rm sh}t)$ and y and energy γ of an accelerated electron. The top panel indicates that this particle coming from the upstream region begins to move with the shock wave after the reflection at $t = t_{r1}$ near the end of the main pulse region. After moving forward for a short period, it returns to the end part of the main pulse and suffer the second reflection there at $t = t_{r2}$. That is, this particle is trapped by the shock wave in the main pulse region. The oscillation periods of y and γ, $\omega_{pe}t \sim 400$, are the same as that of $(x - v_{\rm sh}t)$. Simulations show that this oscillation period becomes longer as the particle energy rises. In addition to this long-period oscillation, we observe a short-period oscillation due to relativistic gyromotion, with a period $\omega_{pe}t \simeq 30$ around the time of the highest energy of this particle, $\omega_{pe}t \simeq 780$.

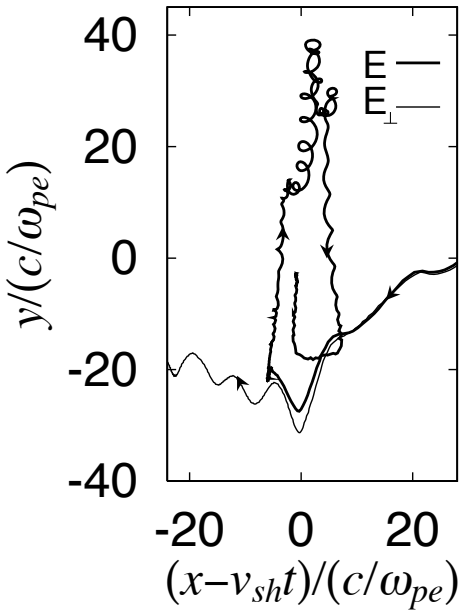

Figure 3.4: Trajectories of an accelerated electron (thick line) and a test electron (thin line) in the (x, y) plane. Although these two particles have the same initial positions and velocities, reflection does not occur in the test electron calculated without parallel electric field.

The parallel electric field, $\boldsymbol{E}_{\parallel} = (\boldsymbol{E} \cdot \boldsymbol{B})\boldsymbol{B}/B^2$, plays an essential role in this mechanism. The thick line in Fig. 3.4 represents the trajectory of an accelerated electron by a shock wave with $\theta = 60°$: This is a result of another simulation with $m_i/m_e = 400$ and $c/(\omega_{pe}\Delta_{\rm g}) = 10$ [14]. After reflected near the end of the main pulse, this particle oscillates, as the one in Fig. 3.3. Its energy becomes the highest near the maxima of y; around which, therefore, its gyromotion is appreciable. On the other hand, the thin line shows the trajectory of a test particle, which does not affect either other particles or fields. The test particle orbit has been obtained from the relativistic equation of motion with perpendicular electric field, $\boldsymbol{E}_{\perp} = \boldsymbol{E} - \boldsymbol{E}_{\parallel}$:

$$\frac{d\boldsymbol{p}}{dt} = -e\left(\boldsymbol{E}_{\perp} + \frac{\boldsymbol{v} \times \boldsymbol{B}}{c}\right), \tag{3.8}$$

where we use the electric and magnetic fields in the particle simulation. The test particle passes through the shock wave without suffering acceleration. Although the initial positions and velocities of the two particles are the same, neither reflection

nor acceleration occurs in the test particle calculated with no parallel electric field.

3.2 Theoretical analysis

3.2.1 Mechanism of electron acceleration

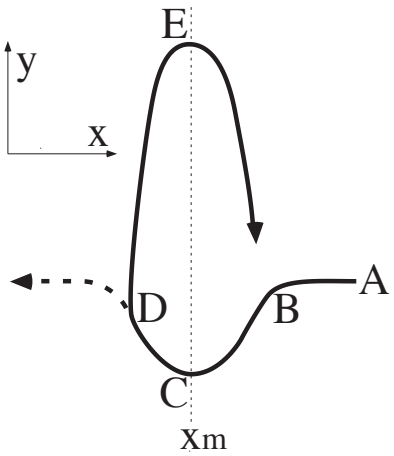

Figure 3.5: Schematic representation of guiding-center motions projected on the $(x,\ y)$ plane. Here, ϕ and B_z take their maximum values at $x = x_m$. Many of the electrons flowing from the upstream region pass through the shock wave (dotted line), while some are reflected near the end of the main pulse region (solid line: D→E). When electrons move from points A to D, their kinetic energies do not change much, whereas the electrons reflected at point D have great energies at point E.

We now consider the physical mechanism of the electron acceleration in the wave frame. Detailed calculations to derive the highest energy of these electrons, Eq. (3.24), are given in Appendix D.

Trajectories of passing and reflected electrons

Figure 3.5 shows schematic orbits of electron guiding centers projected on the (x, y) plane in the wave frame, where the line $x = x_m$ represents the ridge of B_z and ϕ, point A is a guiding-center position in the far upstream region, point B is the edge of the shock wave (the position at which B_z and ϕ begin to rise), points C and E

are the positions at $x = x_m$, and point D is the end of the main pulse region. In the upstream region (path A→B), the plasma moves with the velocity

$$v_x = -v_{\rm sh} = cE_{y0}/B_{z0} \quad (< 0). \tag{3.9}$$

After entering the shock wave, electrons drift in the negative y direction (B→C) owing to the rising electric potential (the $E_x \times B_z$ drift is in the negative y direction). After passing the potential peak, the guiding centers move in the positive y direction (C→D) because the sign of E_x becomes negative. Whereas many of the electrons continue to move to the downstream region (dotted line), some electrons are reflected near the end of the main pulse and then trapped by the shock wave (D→E); they oscillate around the line $x = x_m$.

Energy gain from potential ϕ and constant electric field E_{y0}

Electron kinetic energies do not change much as they drift along the trajectory A→D; after passing the main pulse region, their energies remain low. The electrons that are reflected at point D, however, have great energies at point E.

From the relativistic equation of motion for an electron in the wave frame,

$$m_e \frac{d(\gamma \boldsymbol{v})}{dt} = -e\left(\boldsymbol{E} + \frac{\boldsymbol{v} \times \boldsymbol{B}}{c}\right), \tag{3.10}$$

one obtains a differential equation for particle energy,

$$\frac{d}{dt}(m_e c^2 \gamma) = -e(E_x v_x + eE_{y0} v_y), \tag{3.11}$$

which can be integrated to give

$$m_e c^2(\gamma - \gamma_0) = e(\phi - \phi_0) - eE_{y0} \int v_y dt, \tag{3.12}$$

where the subscript 0 refers to the quantities in the far upstream region. As electrons drift from points A to C, they gain energy from the electric potential ϕ by an amount

$$\Delta E_1 = e\phi(x_C) - e\phi(x_A) \quad (> 0), \tag{3.13}$$

where x_C denotes the x position at point C. As stated in Chap. 2, $e\phi$ is of the order of $2m_i v_{\rm A}^2(M-1)$; hence, ΔE_1 can be much greater the electron rest mass energy $m_e c^2$. At the same time, however, they lose energy owing to the constant electric field E_{y0} (< 0),

$$\Delta E_2 = -eE_{y0}(y_C - y_A) \quad (< 0). \tag{3.14}$$

The net energy change along the path A→C is thus

$$\Delta E = \Delta E_1 + \Delta E_2. \tag{3.15}$$

Although the magnitudes of ΔE_1 and ΔE_2 are both great, they almost cancel [15], $\Delta E \simeq 0$. This is also the case with the trajectory C→D. The energies of passing electrons thus remain low.

If, however, electrons are reflected at point D and move to point E, then they would absorb energy from both ϕ and E_{y0}. The energy gain from E_{y0} is

$$\Delta E_3 = -eE_{y0}(y_E - y_D) \quad (> 0), \tag{3.16}$$

and that from the potential, $e\phi(x_E) - e\phi(x_D)$, is nearly equal to ΔE_1. Because ΔE_1 and ΔE_3 are both positive, the increment of kinetic energy at point E

$$\Delta E = \Delta E_1 + \Delta E_3, \tag{3.17}$$

is quite large.

Small relative velocity between reflected electrons and shock wave

There is another important effect that enhances the energization of reflected electrons: It takes long periods of time for reflected electrons to reach point E from point D, so that the distance $y_{\rm E} - y_{\rm D} = \int_{\rm D}^{\rm E} v_y dt$ becomes quite long.

This can be seen as follows. With use of the drift velocity $\boldsymbol{v}_d$ and the velocity component parallel to the magnetic field, $v_\parallel$, one may write the guiding-center velocity as

$$\boldsymbol{v}_g \simeq \boldsymbol{v}_d + v_\parallel \boldsymbol{B}/B. \tag{3.18}$$

In a shock wave, the drift velocity is approximately given by the $\boldsymbol{E} \times \boldsymbol{B}$ drift,

$$\boldsymbol{v}_d \simeq c\boldsymbol{E} \times \boldsymbol{B}/B^2, \tag{3.19}$$

unless the gyration speed is extremely high. The x, y, and z components of the guiding-center velocity can therefore be written as

$$v_{gx} = \frac{cE_{y0}B_z}{B^2} + v_\parallel \frac{B_{x0}}{B}, \tag{3.20}$$

$$v_{gy} = -\frac{cE_xB_z}{B^2} + v_\parallel \frac{B_y}{B}, \tag{3.21}$$

$$v_{gz} = c\frac{E_xB_y - E_{y0}B_{x0}}{B^2} + v_\parallel \frac{B_z}{B}. \tag{3.22}$$

The first term on the right-hand side of Eq. (3.20) is always negative because $E_{y0} < 0$, while the second term can be positive. Even though many of the incident particles have negative $v_\parallel$ in the upstream region, reflection makes $v_\parallel$ positive. The sign of v_{gx} is then reversed, and reflected electrons move from points D to E. The values of v_{gx} of these particles would be quite small if

$$\frac{cE_{y0}B_z}{B^2} \ + \ c\frac{B_{x0}}{B} \sim 0, \tag{3.23}$$

where the left-hand side is equivalent to the right-hand side of Eq. (3.20) if $v_\parallel \sim c$. Under these circumstances, it takes long periods of time for reflected particles to move from points D to E, during which they absorb a great amount of energy from E_{y0}. Indeed, in the time between $t_{\rm r1}$ and $t_{\rm r2}$ in the top panel of Fig. 3.3, the time period in which $(x - v_{\rm sh}t)$ rises is much longer than the period in which $(x - v_{\rm sh}t)$ goes down immediately before $t_{\rm r2}$: The former corresponds to the path D→E→B in Fig. 3.5, while the latter to B→C→D.

By integrating the term $-eE_{y0}\int v_y dt$ along the orbit from points B to E in Eq. (3.12), one finds the energy increment as

$$m_e c^2(\gamma - \gamma_0) = \frac{e\phi_{\rm E}}{1 - (v_{\rm sh}/c)(B_{z0}/B_{x0})}, \tag{3.24}$$

in terms of the quantities in the wave frame [2] (for the details, see Appendix D). Since the magnitude of the potential is $e\phi \sim 2m_i v_{\rm A}^2(M-1)$, the Lorentz factor

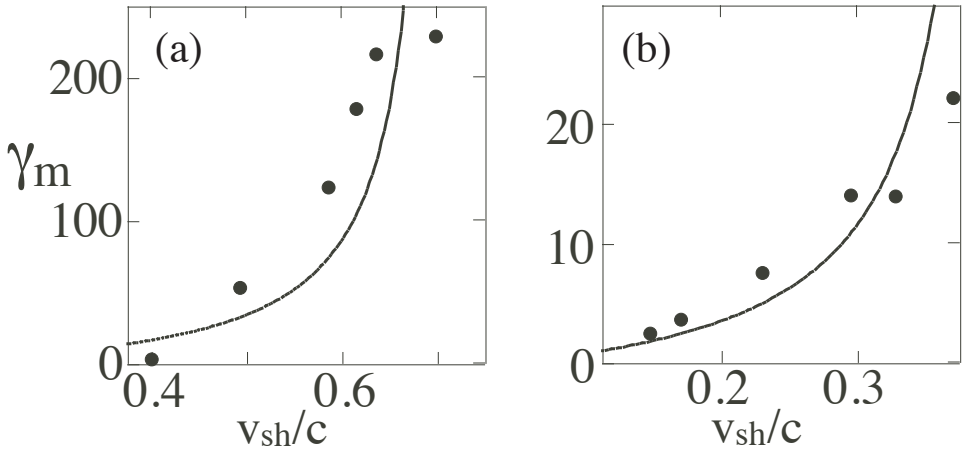

Figure 3.6: Highest electron energy versus shock propagation speed $v_{\rm sh}$. The strength of the external magnetic field and the propagation angle are $|\Omega_e|/\omega_{pe} = 3$ and $\theta = 45^\circ$ in the left panel and are $|\Omega_e|/\omega_{pe} = 1$ and $\theta = 66^\circ$ in the right panel. The relation $v_{\rm sh} \sim c\cos\theta$ holds at $v_{\rm sh}/c = 0.71$ in the left panel and at $v_{\rm sh}/c = 0.41$ in the right panel, around which γ is high in both theory (solid lines) and simulation (dots) results.

can be quite large and increases with the magnetic-field strength. Furthermore, Eq. (3.24) indicates that γ is particularly large if its denominator is close to zero, $(v_{\rm sh}/c)(B_{z0}/B_{x0}) \sim 1$, which, with the aid of Eqs. (2.58) and (2.61), can be put into the following form:

$$v_{\rm sh} \sim c\cos\theta, \tag{3.25}$$

where θ is the angle in the laboratory frame. It is interesting to note that $c\cos\theta$ is the relativistic ($v_\parallel \sim c$) particle velocity $\langle v_x \rangle$ averaged over a gyroperiod in an external magnetic field.

Because the Alfvén speed and thus the shock speed $v_{\rm sh}$ decrease with increasing ion mass, the angle θ that satisfies Eq. (3.25) becomes closer to 90° as m_i goes up. In low beta plasmas, where the shock speed is approximately given by $v_{\rm sh} = Mv_{\rm A}$, Eq. (3.25) can be rewritten as

$$M\left(\frac{m_e}{m_i}\right)^{1/2}\frac{|\Omega_e|}{\omega_{pe}} \sim \cos\theta. \tag{3.26}$$

Hence, the angle is $\theta = 45^\circ$ for the parameters $M = 10$, $m_i/m_e = 100$, and

$|\Omega_e|/\omega_{pe} = 1$, while for the real mass ratio $m_i/m_e = 1836$, θ is 77°.

Figure 3.6 shows the highest energy of electrons as a function of the shock propagation speed $v_{\rm sh}$ for the cases with $|\Omega_e|/\omega_{pe} = 3$ and $\theta = 45°$ (left panel) and with $|\Omega_e|/\omega_{pe} = 1$ and $\theta = 66°$ (right panel). In both panels, the simulation results (dots) are consistent with the theoretical values (lines). The Lorentz factor becomes particularly large near the shock speed given by Eq. (3.25). Furthermore, as predicted by the theory, the stronger the magnetic field is, the higher the electron energy is.

Since the length along the field line from the end of the main pulse to the location of $x = x_m$ is $\sim (c/\omega_{pi})(B_z/B_{x0})$, the acceleration time is estimated to be $\sim N(1/\omega_{pi})(B_z/B_{x0})$, where N is a numerical factor much greater than unity. If this ultrarelativistic acceleration takes place in large-amplitude magnetosonic waves created by a solar flare, electron γ's would reach 100 in time periods much shorter than one second, even if N is as great as 10 or 100.

3.2.2 Reflection and parallel pseudo potential

We have seen that reflected electrons gain a great amount of energy. This section describes the mechanism of electron reflection. Since the shock wave has a positive electric potential, it is understandable that positively charged ions can be reflected from the shock front, which will be discussed in Chap. 4. On the other hand, electrons coming from the upstream region usually tend to be pulled into the shock wave. The electron reflection takes place in the end part of the main pulse when the parallel pseudo potential F becomes small there; nonstationarity of wave propagation is related to this phenomenon.

Nonrelativistic description

First, we make a nonrelativistic analysis for physical processes involved in the reflection [3]. In the drift approximation,

$$\boldsymbol{v} = v_\parallel \frac{\boldsymbol{B}}{B} + c\frac{\boldsymbol{E}\times\boldsymbol{B}}{B^2} + \tilde{\boldsymbol{v}}, \tag{3.27}$$

where $\tilde{\boldsymbol{v}}$ is the gyration velocity, we have

$$\boldsymbol{E}\cdot\boldsymbol{v} = \frac{\boldsymbol{E}\cdot\boldsymbol{B}}{B}v_{\parallel} + \boldsymbol{E}\cdot\tilde{\boldsymbol{v}}. \tag{3.28}$$

The treatment here can be either in the wave frame or in the laboratory frame.

In association with gyromotion, the kinetic energy $m_e\tilde{\boldsymbol{v}}^2/2$ can vary with time owing to the rotational electric field [16]:

$$-e\langle\boldsymbol{E}\cdot\tilde{\boldsymbol{v}}\rangle = \frac{d}{dt}(\mu_{\rm m}B), \tag{3.29}$$

where the brackets denote the time average over the gyroperiod and $\mu_{\rm m}$ is the magnetic moment,

$$\mu_{\rm m} = \frac{m_e\tilde{v}^2}{2B}. \tag{3.30}$$

Equation (3.28) thus gives a time-averaged energy equation as

$$\frac{d}{dt}\left(\frac{1}{2}m_ev^2 - \mu_{\rm m}B\right) = -e\frac{\boldsymbol{E}\cdot\boldsymbol{B}}{B}v_{\parallel}. \tag{3.31}$$

We may write the kinetic energy as

$$m_ev^2/2 = m_e(v_{\parallel}^2 + v_{\rm d}^2)/2 + \mu_{\rm m}B. \tag{3.32}$$

Since $m_ev_{\rm d}^2$ is usually smaller than $m_ev_{\parallel}^2$, the quantity in the parentheses on the left-hand side of Eq. (3.31) is approximately the kinetic energy of the parallel velocity,

$$m_ev^2/2 - \mu_{\rm m}B \simeq m_ev_{\parallel}^2/2. \tag{3.33}$$

Integration of Eq. (3.31) from time t_0 to time t_1 yields the increment of the energy $(m_ev^2/2 - \mu_{\rm m}B)$ as

$$\left(\frac{1}{2}m_ev(t_1)^2 - \mu_{\rm m}B(t_1)\right) - \left(\frac{1}{2}m_ev(t_0)^2 - \mu_{\rm m}B(t_0)\right) = -e\int_{t_0}^{t_1} E_{\parallel}(t)v_{\parallel}(t)dt, \tag{3.34}$$

where $B(t)$ is the magnetic-field strength at the position of the particle.

Eliminating $\tilde{\boldsymbol{v}}$ in Eq. (3.27) through time averaging, we obtain the x component of the guiding-center velocity,

$$\frac{dx}{dt} = \frac{B_{x0}}{B}v_{\parallel} + v_{{\rm d}x}. \tag{3.35}$$

In the wave frame, this equation is identical to Eq. (3.20).

Substituting $v_\parallel$ given by Eq. (3.35) in Eq. (3.31), and using the relations

$$\frac{\partial F(x,t)}{\partial x} = -\frac{\boldsymbol{E}(x,t)\cdot\boldsymbol{B}(x,t)}{B_{x0}}, \tag{3.36}$$

$$\frac{dF(x,t)}{dt} = \frac{\partial F(x,t)}{\partial t} + \frac{dx}{dt}\frac{\partial F(x,t)}{\partial x}, \tag{3.37}$$

one finds that

$$\frac{d\varepsilon_\parallel}{dt} = -e\frac{\partial F}{\partial t} - e\frac{\partial F}{\partial x}v_{\mathrm{d}x}, \tag{3.38}$$

where the quantity

$$\varepsilon_\parallel = m_e v^2/2 - \mu_{\mathrm{m}}B - eF, \tag{3.39}$$

is approximately the sum of the parallel kinetic energy ($m_e v_\parallel^2/2$) and the parallel pseudo potential ($-eF$).

It is noted that in the time integration of Eq. (3.38) along the path B→C→D in Fig. 3.5 in the wave frame, the contribution of the right-hand side is negligibly small, because its time period is short: Electrons drift from points B to D before F significantly changes. (We also note that $v_{\mathrm{d}x}$ and $\partial F/\partial x$ are roughly even and odd, respectively, around the line $x = x_m$.) On the other hand, in the integration along the long-time path D→E→B, the effect of the change in F should be included.

Thus, integrating Eq. (3.38) along the path A→D in the wave frame, we obtain an equation that resembles the energy conservation form of a particle in a "potential" F:

$$m_e v_\parallel^2/2 - eF \simeq m_e v_{\parallel 0}^2/2 - eF_0, \tag{3.40}$$

where the terms on the right-hand side are the quantities in the far upstream region. Electrons would move to the downstream region if $eF + m_e v_{\parallel 0}^2/2 - eF_0 > 0$ when they arrive at point D, end of the main pulse. If, however, F happens to be particularly small, $eF + m_e v_{\parallel 0}^2/2 - eF_0 < 0$, when they arrive there, they would be reflected, taking the path D→E→B. Because the wave propagation is not perfectly stationary, this can occur.

Relativistic description

Next, we consider relativistic motions in a stationary wave in the wave frame [1], for which we have the energy equation: the differential form (3.11) and the integrated form (3.12). Substituting v_y obtained from the z component of the relativistic equation of motion,

$$v_y = \frac{c}{eB_{x0}}\frac{dp_z}{dt} + v_x\frac{B_y}{B_{x0}}, \tag{3.41}$$

in Eq. (3.11), one finds that

$$\frac{d}{dt}(m_e c^2\gamma) = -e\left(\frac{\boldsymbol{E}\cdot\boldsymbol{B}}{B_{x0}}\right)\frac{dx}{dt} - \frac{cE_{y0}}{B_{x0}}\frac{dp_z}{dt}. \tag{3.42}$$

Then, introducing the quantity

$$\varepsilon = m_e c^2\gamma - eF + \frac{cE_{y0}}{B_{x0}}p_z, \tag{3.43}$$

and using Eqs. (3.36) and (3.37) with $\partial/\partial t = 0$, one can put Eq. (3.42) into the following form:

$$\frac{d\varepsilon}{dt} = 0. \tag{3.44}$$

The quantity ε is constant along the particle orbit. Because of the presence of the third term on the right-hand side of Eq. (3.43), the particle energy $m_e c^2\gamma$ is not limited by the magnitude of eF: γ and p_z can both rise.

Integrating Eq. (3.44) yields

$$m_e c^2(\gamma - \gamma_0) = e(F - F_0) - \frac{m_e cE_{y0}}{B_{x0}}(\gamma v_z - \gamma_0 v_{z0}), \tag{3.45}$$

which, with use of the quantity defined as

$$h = m_e c^2\left(1 - \frac{B_{z0}}{B_{x0}}\frac{v_{\rm sh}v_z}{c^2}\right), \tag{3.46}$$

can be written as

$$\gamma = [e(F - F_0) + h_0\gamma_0]/h. \tag{3.47}$$

Equation (3.46) indicates that h is positive unless B_{z0}/B_{x0} is much greater than unity:

$$\frac{B_{z0}}{B_{x0}} > \frac{c^2}{v_{\rm sh}v_z}. \tag{3.48}$$

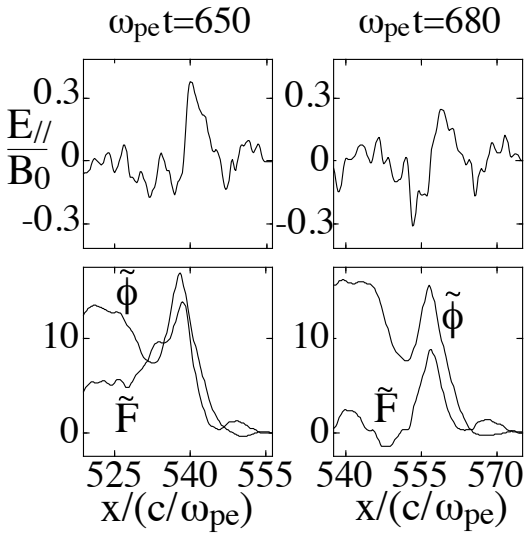

Figure 3.7: Profiles of $E_\parallel$, F, and ϕ in a shock wave at two different times in a simulation. Here, $\tilde{F} = eF/(m_e c^2)$ and $\tilde{\phi} = e\phi/(m_e c^2)$. Near the end of the main pulse region, F and ϕ become small; in particular, F has a negative dip in the right panel.

If $h > 0$, then Eq. (3.47) suggests again that electrons cannot penetrate regions where F is small, $eF < eF_0 - h_0\gamma_0$. Furthermore, it shows that γ becomes particularly large if $h \sim 0$; it can occur in the situation that

$$v_{\rm sh} \sim c^2 B_{x0}/v_z B_{z0}. \tag{3.49}$$

Under the circumstances such that $B_z/B \sim 1$ and $v_\parallel \sim c$ (and thus $v_z \sim cB_z/B$), Eq. (3.49) becomes identical to Eq. (3.23).

One may write the nonrelativistic form of Eq. (3.44) as

$$\frac{d}{dt}\left(\frac{1}{2}m_e v^2 - eF + m_e \frac{cE_{y0}}{B_{x0}} v_z\right) = 0. \tag{3.50}$$

Appendix E proves that Eq. (3.50) is identical to Eq. (3.38) for the stationary case, $\partial F/\partial t = 0$ [3].

Nonstationarity and deep trapping

Figure 3.7 shows $E_\parallel$ (upper panels) and F and ϕ (lower panels) in a shock wave at two different times observed in a simulation [1]. In the main pulse region

[$530 \lesssim x/(c/\omega_{pe}) \lesssim 550$ in the left panels], F and ϕ are large, and $E_\parallel$ is positive in the front part of F (shock transition region) and negative in the region of the back slope of F. Near the end of the main pulse region, F is small and sometimes becomes negative, when electron reflection can occur there. In this example, at $\omega_{pe}t = 680$ (right panels) F has a negative dip around $x/(c/\omega_{pe}) = 550$ and $E_\parallel$ has large negative values.

The reflected electrons are then deeply trapped in the main pulse region with large F. After the reflection they move forward to the front part of the shock wave, where they are reflected backward again. Even if the values of F have been restored to the normal (time-averaged) ones by the time they return to the end of the main pulse, they are reflected forward again.

In fact, simulations show that the relativistic energy level (3.43) of a particle in the wave frame slightly decreases after the reflection [3]. This indicates that the energy level ε of the particle falls by a small amount in the "potential well" given by the time-averaged F; thus, the trapping becomes stronger.

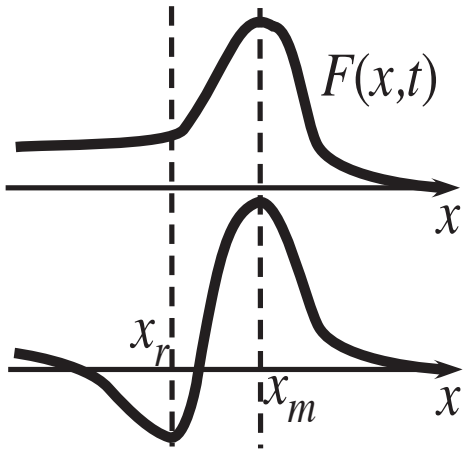

Figure 3.8: Model profiles of F. The upper figure shows the time-averaged profile, while the lower one shows the profile with a negative dip near the end of the main pulse. Electrons can be reflected near $x = x_r$, after which F will quickly recover there from negative to positive values as in the upper figure.

The slight decline in the energy level ε can be interpreted as follows [3]. As mentioned earlier, it takes a long time for a reflected electron to move along the

path D→E→B in Fig. 3.5. During this drift, F can significantly change, which can affect the particle motion. Let $\langle F(x)\rangle$ be the stationary (time-averaged) profile of F in the wave frame and F_1 be the perturbation near the end of the main pulse ($x = x_r$ in Fig. 3.8). In the case $F_1 = 0$, the reflection does not occur. If $F = \langle F(x)\rangle + F_1$ is sufficiently small at some time, then some electrons are reflected there. If F recovers after this, i.e., if $\partial F_1/\partial t > 0$, the parallel kinetic energy $m_e v_\parallel^2/2$ would decrease in time, which we see by integrating Eq. (3.38) along the particle orbit over time [since Eq. (3.43) is for a stationary wave, we use Eq. (3.38) even though it is nonrelativistic]: Provided that an electron is reflected at $t = t_\mathrm{r}$ and F_1 vanishes at time t ($> t_\mathrm{r}$), then from Eq. (3.38), one obtains

$$\frac{1}{2}m_e v^2(t) - \mu_\mathrm{m} B(t) - e\langle F\rangle = -e\int_{t_\mathrm{r}}^{t} \frac{\partial F_1}{\partial t} dt, \tag{3.51}$$

where we have used the relation

$$\frac{1}{2}m_e v^2(t_\mathrm{r}) - \mu_\mathrm{m} B(t_\mathrm{r}) - e\langle F(t_\mathrm{r})\rangle \sim 0, \tag{3.52}$$

and have ignored the second term on the right-hand side of Eq. (3.38), assuming that the time scale of the perturbations of F is much shorter than the ion gyroperiod with their scale length of the order of the shock width ($\sim c/\omega_{pi}$). Equation (3.51) indicates that the energy level of $\varepsilon_\parallel$ slightly falls in the well of the pseudo potential $\langle F\rangle$, resulting in deeper trapping. [Furthermore, the reflection of electrons with a negative charge would act to make the values of F near the reflection point larger (make $\partial F_1/\partial t$ positive).]

It is noted, however, that the present discussion should be valid in the case that $v_\mathrm{sh} \lesssim c\cos\theta$. If the shock speed is so fast that $v_\mathrm{sh} > c\cos\theta$, then particles will not be able to move with the shock wave for long periods of time; they will eventually go to the downstream region.

The number of trapped, high-energy electrons continually grows in the main pulse region unless $v_\mathrm{sh} > c\cos\theta$. It is because electrons are newly trapped at times when a dip of F is created, and those electrons are hardly detrapped. Shock fronts can therefore be source regions of radio waves due to synchrotron radiation and of x and γ rays due to bremsstrahlung and inverse Compton scattering.

Bibliography

[1] N. Bessho and Y. Ohsawa, Phys. Plasmas **6**, 3076 (1999).

[2] N. Bessho and Y. Ohsawa, Phys. Plasmas **9**, 979 (2002).

[3] A. Zindo, Y. Ohsawa, N. Bessho, and R. Sydora, Phys. Plasmas **12**, 052321 (2005).

[4] S. R. Kane, K. Kai, T. Kosugi, S. Enome, P. B. Landecker, and D. L. McKenzie, Astrophys. J. **271**, 376 (1983).

[5] S. R. Kane, E. L. Chupp, D. J. Forrest, G. H. Share, and E. Rieger, Astrophys. J. **300**, L95 (1986).

[6] Y. Ohsawa, Phys. Fluids **28**, 2130 (1985).

[7] A. B. Langdon and C. K. Birdsall, Phys. Fluids **13**, 2115 (1970).

[8] A. B. Langdon, J. Comput. Phys. **6**, 247 (1970).

[9] H. Okuda, Phys. Fluids **15**, 1268 (1972).

[10] H. Okuda, J. Comput. Phys. **10**, 475 (1972).

[11] V. K. Decyk and J. M. Dawson, J. Comput. Phys. **30**, 407 (1979).

[12] P. C. Liewer, A. T. Lin, J. M. Dawson, and M. Z. Caponi, Phys. Fluids **24**, 1364 (1981).

[13] J. M. Dawson, Rev. Mod. Phys. **55**, 403 (1983).

[14] S. Takahashi, H. Kawai, Y. Ohsawa, S. Usami, C. Chiu, and W. Horton, Phys. Plasmas **16**, 112308 (2009); *ibid.* **16**, 129904-1 (2009).

[15] Y. Ohsawa, J. Phys. Soc. Jpn. **58**, 4445 (1989).

[16] G. Schmidt, *Physics of High Temperature Plasmas*, (Academic Press, New York, 1979), Chap. 2.

Chapter 4

Ion acceleration

The electric potential and magnetic-field strength sharply rise in the shock transition region. This leads to ion reflection from the shock front; because of the magnetic field in the upstream region, however, most of the reflected ions return to the shock front and finally move to the downstream region. This process has been discussed by many authors [1]- [14].

Morawetz showed in 1961 that ion reflection can create a steady-state shock structure even in a collisionless plasma [1,2]. In 1970's and 80's, particle simulations demonstrated ion reflection due to a shock wave and resulting plasma heating [3]- [9]. Furthermore, it was pointed out that reflected ions can reach relativistic energies if the magnetic field is rather strong such that $|\Omega_e| \gtrsim \omega_{pe}$ [8, 10]. This result was applied [13, 14] to the ion acceleration in solar flares [15, 16], in which the highest ion energy, 1$\sim$10 GeV, is weakly relativistic, $\gamma \lesssim 10$.

Sagdeev and Shapiro analyzed in 1973 the ion orbit moving across the magnetic field along the wave front in a perpendicular shock wave and showed that these ions gain great energies [17]- [20]. These particles suffer multiple reflections in the shock transition region and eventually pass through the shock front to the downstream region. Extending their work, Katsouleas and Dawson calculated in 1983 particle orbits in a perpendicular, electrostatic, monochromatic wave and argued that particles could continue to move along the wave front and undergo unlimited acceleration if the wave electric field is stronger than the external magnetic field, $E/B > 1$. They proposed an accelerator based on this model [21]. The particle

acceleration due to multiple reflections has attracted a great deal of attention and is now called the surfatron.

Multiple reflections can take place in the case that the particle speed v is close to the shock speed $v_{\rm sh}$, while if v is much lower than $v_{\rm sh}$, particles can be reflected only once [8]. In a low beta plasma, in which the ion thermal speed is lower than the Alfvén speed and thus much lower than $v_{\rm sh}$, multiple reflections will rarely occur.

If nonthermal, energetic particles with $v > v_{\rm sh}$ encounter a shock wave, they can experience another distinct energization process [22]- [29]. Since such energetic ions have gyroradii ρ much greater than the width of the shock transition region, they can move back and forth between the shock and upstream regions in association with their gyromotions. They absorb energy from the transverse electric field when they are in the shock wave, with their perpendicular velocities $v_\perp$ going up, while their energies are nearly constant when they are in the upstream region; consequently, their kinetic energies increase stepwise [24]- [28].

In the oblique case, particles with $v_\parallel \cos\theta \sim v_{\rm sh}$ can move with the shock wave, because the time-averaged particle velocity in the x direction, $\langle v_x \rangle$, is nearly equal to $v_\parallel \cos\theta$. Its interaction time is, however, limited. Because of the steep profile of the magnetic field in the transition region, $v_\perp$ that has grown in the shock wave is converted to $v_\parallel$ in each cycle of gyromotion. Since $v_\parallel$ and thus $\langle v_x \rangle$ rise, particles can stay near the shock transition region for only a few gyroperiods. They escape from the shock wave to the upstream region, and their energization ceases [25].

If, however, the shock speed is close to $c\cos\theta$,

$$v_{\rm sh} \sim c\cos\theta, \tag{4.1}$$

then the particle speed $\langle v_x \rangle = v_\parallel \cos\theta$ cannot easily exceed $v_{\rm sh}$: Particle velocity $v_\parallel$ is limited by the speed of light, whereas particle momentum $p_\parallel$ can increase indefinitely. Particles with $v_\parallel \sim c$ can therefore move with the shock wave for long periods of time, and they can be incessantly accelerated. By means of simulations that combine particle simulations and test particle calculations, ion acceleration

from $\gamma \sim O(1)$ to $\gamma \sim 160$ has been demonstrated [27].

These three energization processes of ions are the subject of this chapter: one reflection, multiple reflections (surfatron), and incessant acceleration of relativistic particles.

4.1 Physical considerations and numerical calculations on one and multiple reflections

4.1.1 Conditions for reflection

Large electric potential forms in a shock wave; as shown in Eq. (2.39), its magnitude is $e\phi \sim 2m_i v_{\rm A}^2(M-1)$ in a perpendicular pulse in a low beta plasma. It was also mentioned there that the potential is smaller than the kinetic energy of an ion with the fluid speed in the wave frame, $m_i(Mv_{\rm A})^2/2$, and thus the ions with the average velocity (fluid velocity) are not reflected by the potential.

Reflection can occur, however, because each particle has a thermal, random velocity $\boldsymbol{v}'$ in addition to the average velocity, $\boldsymbol{v} = -v_{\rm sh}\boldsymbol{e}_x + \boldsymbol{v}'$, and therefore can have a kinetic energy smaller than the potential. If the inequality

$$\frac{m_i}{2}(v_x' - v_{\rm sh})^2 < e\phi, \tag{4.2}$$

holds when a particle enters the shock wave, then this particle would be reflected from the shock front. (In the narrow shock transition region with its width $\sim c/\omega_{pe}$ of a perpendicular shock wave, the electric force on the ions is stronger than the magnetic force, and thus the condition for the reflection is determined primarily by the electric force. Appendix F gives a more detailed discussion on the condition for ion reflection including the effect of magnetic force.)

In the laboratory frame, ions with $v_{\rm ref} < v_x < v_{\rm sh}$ at the time of encounter with a shock wave will be reflected. Here, $v_{\rm ref} \simeq v_{\rm sh} - (2e\phi/m_i)^{1/2}$ is the minimum velocity for reflection, Eq. (F.27) in Appendix F. The velocity distribution function $f(v_x)$ will be quite small at $v_x = v_{\rm sh}$ in a low beta plasma, while $f(v_{\rm ref})$ increases with ϕ; large-amplitude pulses can reflect many ions.

Immediately after the reflection, the x component of the particle velocity is $(v_{\rm sh} - v_x')$ in the wave frame and is $(2v_{\rm sh} - v_x')$ in the laboratory frame. The kinetic energy of a reflected ion increases with increasing relative velocity $(v_{\rm sh} - v_x')$ at the time of encounter. As Eq. (4.2) shows, however, if the relative velocity is too large (i.e., $v_x < v_{\rm ref}$ in the laboratory frame), reflection does not occur. Ion ring velocity distribution can thus be created in a low beta plasma [9]. On the other hand, particles with $v_x' \simeq v_{\rm sh}$ could experience multiple reflections; the energy gain in each reflection is rather small though.

The multiple reflections would rarely occur in a low beta plasma. If the ion thermal speed is much lower than the Alfvén speed, few particles would satisfy the relation $v_x' \simeq v_{\rm sh}$. Since the relative speed is greater at the second collision with the shock wave than at the first one, the second reflection is less likely than the first one. The velocity range that allows multiple reflections is narrow: A quantitative analysis for this is also given in Appendix F.

4.1.2 One reflection

Figure 4.1 displays the trajectories of an ion reflected by a pulse once [8]. This is a result of numerical calculations for particle orbits in a given stationary, perpendicular solitary pulse, in which the maximum and equilibrium field strengths have been taken to be $B_m/B_0 = 2.8$ and $|\Omega_e|/\omega_{pe} = 0.1$, respectively. The upper panel plotted in the wave frame indicates that the particle approaches the pulse in a curtate-cycloid orbit (because its gyration speed is lower than the pulse speed) from the far upstream region and is reflected by the pulse gaining a large amount of energy, after which it exhibits a prolate-cycloid orbit with a large radius. When reentering the pulse, it is not reflected, passing through the pulse to the downstream region. In the momentum space (lower panel), it moves in a circle with a small radius when it is in the upstream region. When it is reflected, however, p_x rapidly goes up. The particle then makes a circular motion with a large radius.

Particles reflected by a shock wave with a speed $v_{\rm sh}$ have speeds $v \sim 2v_{\rm sh}$ in

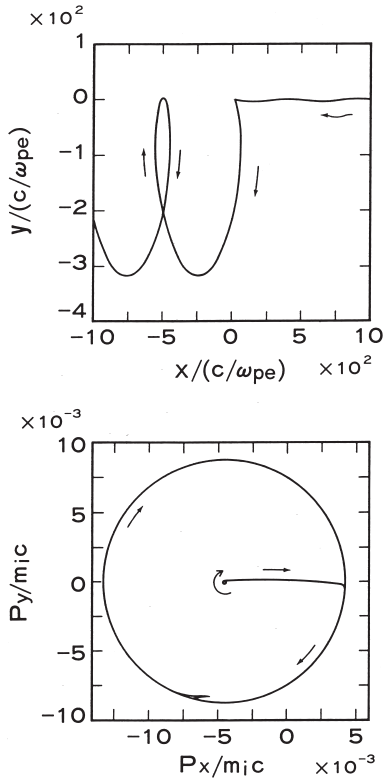

Figure 4.1: Orbits in the (x, y) and (p_x, p_y) planes of an ion reflected once. These orbits are depicted in the wave frame. The magnitude of the initial momentum is $p/(m_i c) = 1.0 \times 10^{-4}$ in the laboratory system. This particle is reflected by a solitary wave near $x = 0$ and gains a great amount of energy.

the laboratory frame; calculations for particle reflection are given in Appendix F, which is based on Refs. [8, 9]. This is a significant energy multiplication if $v_{\rm sh}$ is much higher than the ion thermal velocity v_{Ti}. Indeed, from the relation

$$\frac{2v_{\rm sh}}{c} = 2\left(\frac{m_e}{m_i}\right)^{1/2}\frac{|\Omega_e|}{\omega_{pe}}M, \tag{4.3}$$

for a shock wave with $v_{\rm sh} = Mv_{\rm A}$, one sees that particle energy becomes relativistic with one reflection if $m_i/m_e = 1836$, $M = 10$, and $|\Omega_e|/\omega_{pe} = 3$. Equation (4.3) also implies that shock waves (large-amplitude magnetosonic waves) create protons with much higher energies in coronal magnetic tubes than in the interplanetary space where the magnetic field is much weaker, $|\Omega_e| \ll \omega_{pe}$.

4.1.3 Multiple reflections

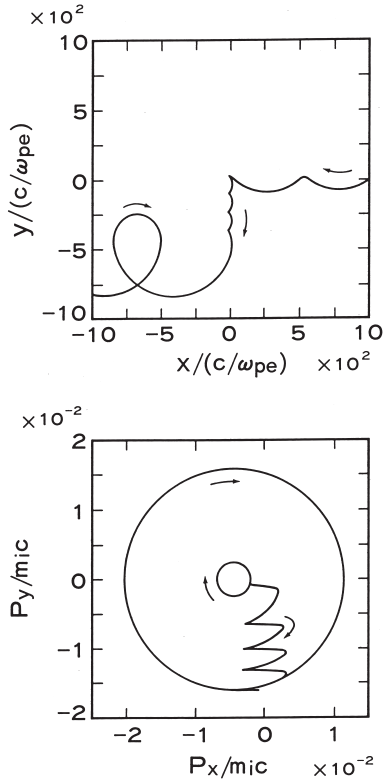

Figure 4.2: Orbits of an ion reflected several times. The initial momentum is $p/(m_i c) = 2.5 \times 10^{-3}$ in the laboratory system.

Figure 4.2 presents the orbits of a particle that has suffered multiple reflections. After the encounter with the pulse, this particle moves along the wave front repeating small reflections, during which its p_y grows. The initial speed of this particle is much greater than that of the particle in Fig. 4.1, and therefore the multiple reflections are possible.

This type of motion was studied in detail by Sagdeev and Shapiro in 1973 [17–20]. Here, however, following Katsouleas and Dawson [21], we analyze the motion in a heuristic manner. We consider a monochromatic, electrostatic wave $E_x = E_0 \cos k(x - v_{\rm sh}t)$ propagating perpendicular to an external magnetic field $\boldsymbol{B} = (0, 0, B_{z0})$. The equation of motion for an ion then reads as

$$m_i \frac{d(\gamma v_x)}{dt} = q_i E_x + \frac{q_i v_y B_{z0}}{c}, \tag{4.4}$$

$$m_i \frac{d(\gamma v_y)}{dt} = - \frac{q_i v_x B_{z0}}{c}. \tag{4.5}$$

If, owing to the strong E_x, the ion moves with the wave,

$$v_x = v_{\rm sh}, \tag{4.6}$$

then Eq. (4.5) gives

$$v_y = - \frac{\Omega_i v_{\rm sh} t}{\gamma_{\rm sh}(1 + \Omega_i^2 t^2 v_{\rm sh}^2/c^2)^{1/2}}. \tag{4.7}$$

The velocity v_y increases with time, with the particle speed v approaching c.

Equation (4.6), however, will not hold for a long time because of the presence of the magnetic field. If we suppose that the trapping ends when the magnetic force surpasses the electric force in Eq. (4.4), then we obtain the upper limit of the speed as $v \sim cE_0/B_{z0}$.

Katsouleas and Dawson [21] have suggested that if the electric field is so strong that $E_0 > \gamma_{\rm sh} B_{z0}$ (this condition can be seen more easily if we write Eq. (4.4) in the wave frame), then the assumption (4.6) does not break down; thus, unlimited acceleration could occur. Developing this idea, they proposed a new plasma-based accelerator.

Nevertheless, as can be seen from Eq. (2.44), the wave theory indicates that $E_x < B_z$ in stationary, nonlinear, magnetosonic waves [30]. Consequently, the unlimited surfatron acceleration will not be realized in magnetosonic waves.

4.1.4 Demonstration with particle simulations

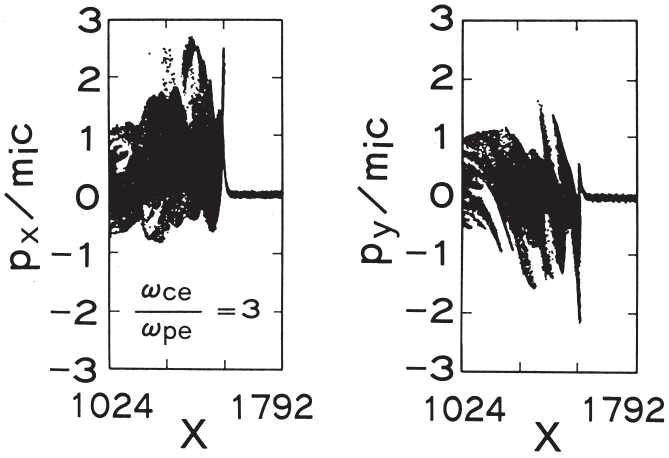

Figure 4.3: Ion phase spaces (x, p_x) and (x, p_y) near a perpendicular shock wave. Ions are rapidly accelerated to relativistic energies in the shock transition region.

Figure 4.3 is a result of a particle simulation, showing relativistic ion acceleration caused by a perpendicular shock wave [14], where the equilibrium magnetic field strength is taken to be $|\Omega_e|/\omega_{pe} = 3$, and the observed shock speed is $v_{\rm sh} = 2.7v_{\rm A}$. Here, ions are rapidly accelerated to relativistic energies in the shock transition region. [The vertical axis of the left panel is $p_x/(m_ic) = \gamma v_x/c$; the particles with $p_x/(m_ic) \gtrsim 1$ are relativistic.] In this simulation, the Alfvén speed $v_{\rm A}$ is 15 times as fast as the ion thermal velocity v_{Ti}; thus, the energization is due to one reflection.

Figure 4.4 shows the differential energy spectra $f(\gamma)$ of the ions at $t = 0$ and at $\omega_{pe}t = 480$. The shock wave produces a large number of relativistic particles; the energy spectrum at $\omega_{pe}t = 480$ is well approximated by the power-law with a spectral index $s = 1.2$: $f = (\gamma - 1)^{-1.2}$. Furthermore, it has a sharp cutoff near the highest energy $\gamma \sim 3$. These features are consistent with the observations of solar

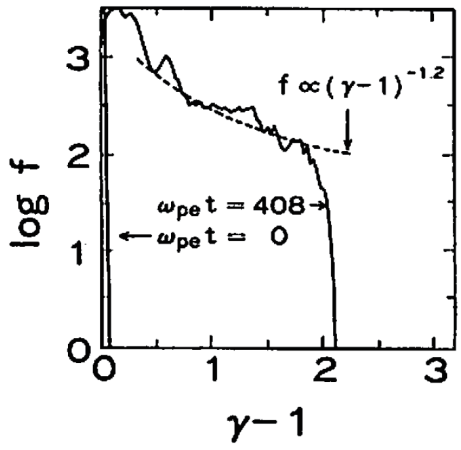

Figure 4.4: Power spectra $f(\gamma)$ of ions at $t = 0$ and at $\omega_{pe}t = 480$. The dashed line represents a power-law form scaling as $(\gamma - 1)^{-1.2}$, which fits fairly well to the spectrum at $\omega_{pe}t = 480$. The observed spectrum has a sharp cutoff near $\gamma = 3$.

energetic particles reported in Refs. [15, 16].

It is noted, however, shock waves can create various types of energy spectra. In fact, as mentioned earlier, a shock wave can also generate a ring velocity distribution [9]. The energy spectra depend on several physical parameters, such as time, wave amplitude, magnetic-field strength, propagation angle, and plasma temperature. Furthermore, if many large-amplitude magnetosonic pulses are generated in a plasma owing to strong disturbances, the distribution of their amplitudes would play an important role in determining the energy spectrum for high-energy ions.

4.2 Incessant acceleration of fast ions

We have seen the ion acceleration for the cases with $v < v_{\rm sh}$ and with $v \sim v_{\rm sh}$. We now proceed to consider fast ions with

$$v > v_{\rm sh}. \tag{4.8}$$

Their gyroradii are much greater than the width of the shock transition region, which is $\sim c/\omega_{pi}$ in oblique shock waves,

$$\rho > c/\omega_{pi}. \tag{4.9}$$

4.2.1 Energy absorption from a perpendicular shock wave

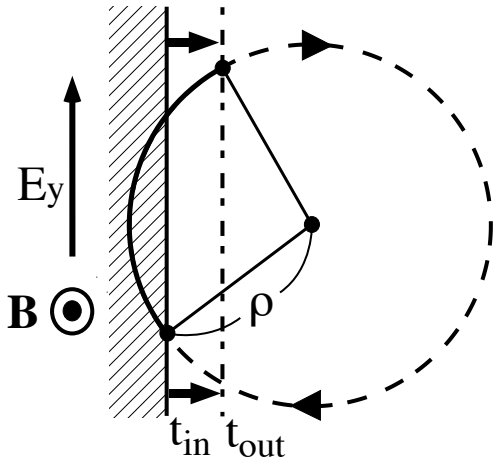

Figure 4.5: Schematic representation of the orbit of a fast ion and the front of a shock wave. When the particle is in the shock wave (shaded area), it absorbs energy from the transverse electric field. When it is in the upstream region, its energy is constant. This figure shows the case of a perpendicular shock wave. In the case of oblique shock waves, B_{x0} is added to the external magnetic field, and particles have gyro-averaged velocities $\langle v_x \rangle \simeq v_{\parallel} \cos\theta$ in the x direction.

Figure 4.5 shows a schematic diagram of the interaction of a fast ion and a perpendicular shock wave. This particle enters the shock wave at $t = t_{\rm in}$ and goes out to the upstream region at $t = t_{\rm out}$. Such gyromotion is possible because of the relations (4.8) and (4.9). Since the energy of the particle is high, it nearly follows the unperturbed orbit. When in the shock wave, the particle gains energy from the electric field E_y, while the work done by E_x is small: The field E_x is strong only in the transition region, and the work done by E_x when the particle goes in the shock wave and that when it goes out almost cancel. Integrating the electric force along the unperturbed gyro-orbit from time $t_{\rm in}$ to $t_{\rm out}$, one obtains the increment of γ as [24, 26]

$$\delta\gamma = \frac{2q_i p_{1\perp} E_{y1}}{m_i^2 c^2 \Omega_{i1}} \sin\left(\frac{\Omega_{i1}(t_{\rm out} - t_{\rm in})}{2\gamma}\right), \tag{4.10}$$

where $p_{1\perp}$ is the magnitude of perpendicular momentum in the shock wave (the subscript 1 refers to quantities in the shock wave). Equation (4.10), which is also

applicable to oblique shock waves, is derived in Appendix G. Since the gryoradius ρ is large, the contribution from the thin transition region has been ignored in the above calculation, which is consistent with the treatment of E_x; the profiles of B_z, E_y, and ϕ are approximated with step functions near the shock front in the theoretical model for the incessant acceleration in Sec. 4.2. The increment $\delta\gamma$ increases with $p_{1\perp}$, which is a reflection of the fact that the arc length of a particle orbit in the shock wave becomes longer as the particle energy goes up.

This type of motion has been observed in particle simulations. After gyrations of a few times [$\sim \rho\Omega_i/(2\pi v_{\rm sh})$], fast ions eventually move to the downstream region, and some of them undergo energy multiplication by a factor of two or three [24].

4.2.2 Energy absorption from an oblique shock wave

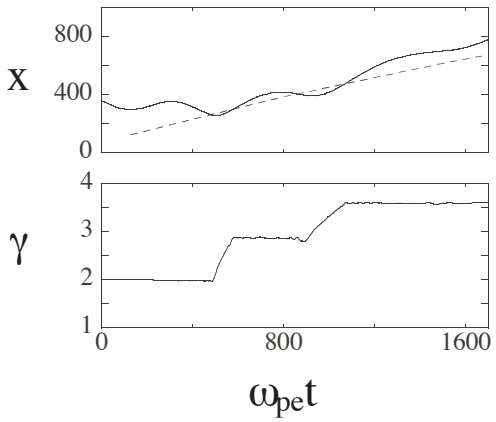

Figure 4.6: Interaction between a fast ion and an oblique shock wave. The shock speed is $v_{\rm sh} = 1.74 v_{\rm A}$ with $\theta = 45°$. In the upper panel, the solid and dashed lines, respectively, represent the time variations of the positions of the ion and the wave front. The lower panel shows the time variation of γ of the ion. This particle enters the shock wave twice and eventually goes away from the front to the upstream region. Its energy goes up when it is in the shock wave.

In a magnetic field forming an angle θ with the x axis, the x component of the gyro-averaged particle velocity is given by

$$\langle v_x \rangle \simeq v_{\parallel} \cos\theta. \tag{4.11}$$

Particles can therefore move with an oblique shock wave propagating in the x direction if

$$v_{\rm sh} \simeq v_{\parallel} \cos\theta. \tag{4.12}$$

Figure 4.6 shows an example of the interaction between a fast ion and an oblique shock wave [26], where the solid and dashed lines in the upper panel represent the x positions of the particle and shock wave, respectively, while the lower panel displays the time variation of γ. This particle barely enters the shock wave twice, and its energy rises when it is in the shock wave; the rise in γ is due to the increase in the perpendicular momentum $p_{\perp}$ caused by E_y.

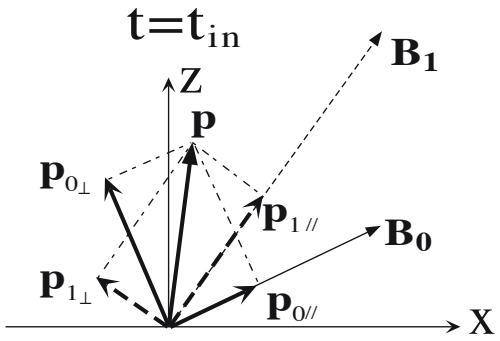

Figure 4.7: Schematic representation of magnetic field and momentum at $t = t_{\rm in}$ projected on the (x, z) plane. The subscripts 0 and 1 refer to quantities in the upstream and shock wave regions, respectively. Although $\boldsymbol{p}$ is continuous, $\boldsymbol{p}_0 = \boldsymbol{p}_1$, the perpendicular and parallel components change from $(\boldsymbol{p}_{0\perp}, \boldsymbol{p}_{0\parallel})$ to $(\boldsymbol{p}_{1\perp}, \boldsymbol{p}_{1\parallel})$. Note that $p_{1\parallel} > p_{0\parallel}$. The abrupt change in the momentum components also occurs at $t = t_{\rm out}$.

Unlike the case of perpendicular shock waves, this particle finally outruns the shock wave, although $v_{\parallel} \cos\theta$ is initially smaller than $v_{\rm sh}$. This arises because part of the perpendicular momentum $\boldsymbol{p}_{\perp}$ is converted to the parallel momentum $\boldsymbol{p}_{\parallel}$ when the particle crosses the shock transition region with a steep magnetic-field profile: At this moment, the perpendicular and parallel components of $\boldsymbol{p}$ rapidly change because of the change in the direction of $\boldsymbol{B}$, whereas the total momentum $\boldsymbol{p}$ is continuous. That is, $\boldsymbol{p}_0 = \boldsymbol{p}_1$ and $\boldsymbol{p}_{0\perp} \neq \boldsymbol{p}_{1\perp}$, where $\boldsymbol{p}_0$ is the momentum when the particle is in the upstream region and $\boldsymbol{p}_1$ is the one in the shock wave (Fig. 4.7).

If a fast ion enters a shock wave at time $t = t_{\rm in}$ and goes out of it to the upstream region at $t = t_{\rm out}$, then the increase in the parallel momentum of this particle is given by

$$\delta p_{\parallel} \equiv [\boldsymbol{p}_0(t_{\rm out}) - \boldsymbol{p}_0(t_{\rm in})] \cdot \boldsymbol{B}_0/B_0 = [\boldsymbol{p}_{1\perp}(t_{\rm out}) - \boldsymbol{p}_{1\perp}(t_{\rm in})] \cdot \boldsymbol{B}_0/B_0, \tag{4.13}$$

where because of the above definition of $\boldsymbol{p}_0$, $\boldsymbol{p}_0(t_{\rm out})$ and $\boldsymbol{p}_0(t_{\rm in})$ are the momenta right after $t = t_{\rm out}$ and before $t_{\rm in}$, respectively. The increment $\delta p_{\parallel}$ is always positive [25]- [28], as proved in Appendix G. Since the increase in $p_{\parallel}$ is caused by the magnetic-field structure, the particle energy is unchanged in this process; $p_{\perp}$ falls when $p_{\parallel}$ rises.

The parallel velocity $v_{\parallel}$ and thus $\langle v_x \rangle$ grow in this process, so that the condition (4.12) breaks down after a few cycles of gyromotion across the thin transition region. The fast ion outruns the shock wave, and the acceleration process ceases. This is a kind of particle reflection due to a shock wave, even though its mechanism is different from that described in Sec. 4.1.

4.2.3 Relativistic incessant acceleration

Whereas $p_{\parallel}$ can increase indefinitely, $v_{\parallel}$ is limited by the speed of light c. Equation (4.11) therefore suggests that relativistic particles with $v_{\parallel} \sim c$ cannot easily outrun the shock wave if

$$v_{\rm sh} \simeq c \cos\theta. \tag{4.14}$$

No matter how large $p_{\parallel}$ becomes, $\langle v_x \rangle$ ($\simeq v_{\parallel} \cos\theta$) does not exceed $c \cos\theta$. Some particles will move with the shock wave for long periods of time and undergo energy jumps many times.

Fast particles that barely enter the shock wave spend most of the time in the upstream region in each cycle of their gyromotion. Their gyroperiods are therefore approximately given by $2\pi\gamma/\Omega_{i0}$, where Ω_{i0} is the nonrelativistic ion gyrofrequency in the upstream region and is related to the gyrofrequency Ω_{i1} in the shock wave through $\Omega_{i1} = (B_1/B_0)\Omega_{i0}$. Thus, dividing Eq. (4.10) by $2\pi\gamma/\Omega_{i0}$, we obtain a

gyro-averaged differential equation for the time rate of change of γ of a relativistic particle accelerated many times by one shock wave as

$$\frac{d\gamma}{dt} \sim \frac{q_i v_{1\perp} E_y}{\pi m_i c^2 (B_1/B_0)} \sin\left(\frac{\Omega_{i1}(t_{\rm out} - t_{\rm in})}{2\gamma}\right). \tag{4.15}$$

For a stationary wave with a propagation speed $v_{\rm sh}$, the z component of Faraday's law gives the relation $E_y = (v_{\rm sh}/c)(B_{z1} - B_{z0})$. Equation (4.15) can then be written as [27]

$$\frac{d\gamma}{dt} \sim \frac{g}{\pi}\frac{v_{\rm sh}}{c}\Omega_{i0}, \tag{4.16}$$

where g is a numerical factor smaller than unity,

$$g = \frac{v_{1\perp}}{c}\left(1 - \frac{B_{z0}}{B_{z1}}\right)\left(1 - \frac{B_{x0}^2}{2B_{z1}^2}\right)\sin\left(\frac{\Omega_{i1}(t_{\rm out} - t_{\rm in})}{2\gamma}\right). \tag{4.17}$$

Here, we have expanded the term $(B_{z1}^2 + B_{x0}^2)^{-1/2}$ assuming that $B_{z1} \gg B_{x0}$. If the time dependence of $v_{1\perp}$ and $(t_{\rm out} - t_{\rm in})$ is weak, roughly speaking, γ linearly increases with time as $\gamma \sim (g/\pi)(v_{\rm sh}/c)\Omega_{i0}t + \gamma_0$, where γ_0 is the initial value of γ.

With particle simulations containing fast ions, it was found that, under the condition $v_{\rm sh} \sim c\cos\theta$, some fast particles continue to interact with the shock wave until the end of the simulation run, with their γ rising stepwise; the particle in Fig. 9 in Ref. [26] exhibits nine energy jumps.

To observe the acceleration process from $\gamma \sim 1$ to $\gamma \gg 1$, we need a simulation time much longer than the relativistic ion gyroperiod.

To numerically study long-time behavior of incessantly accelerated relativistic ions, we have adopted a test particle method. We obtain the field data and propagation speed of an oblique shock wave from a one-dimensional, fully kinetic, relativistic, electromagnetic, particle simulation. Then, assuming that the shock propagation is stationary, we follow test particle orbits based on the field data in this shock wave. In so doing, we are supposing that the abundance of nonthermal, relativistic particles is much smaller than that of bulk particles; thus, the effect of fast particles on wave evolution should be negligibly small.

The plasma parameters in the test particle calculations are taken to be the same as those in the corresponding particle simulation [27]. The ion-to-electron

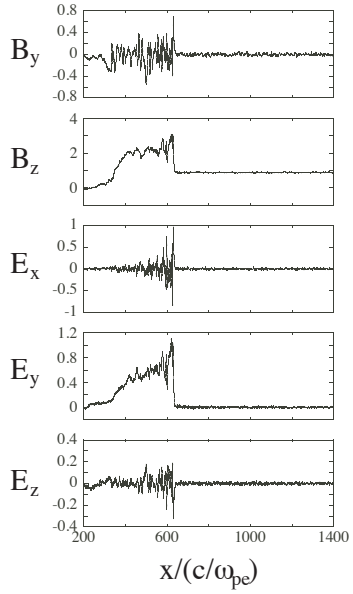

Figure 4.8: Field profiles obtained from a particle simulation. These fields have been used for test particle calculations.

mass ratio is $m_{\rm H}/m_e = 50$ (since the particle simulation contained He ions with $m_{\rm He}/m_{\rm H} = 4$ and $n_{\rm He}/n_{\rm H} = 0.1$, rather a small value of $m_{\rm H}/m_e = 50$ was chosen); the electron skin depth is $c/(\omega_{pe}\Delta_{\rm g}) = 4$; and the frequency ratio $|\Omega_{e0}|/\omega_{pe}$ is 1.5 in the upstream region. For these parameters, the Alfvén speed is $v_{\rm A}/c = 0.20$. The propagation angle is taken to be $\theta = 61°$. The numerical integration of the relativistic equation of motion of test particles was performed with Adams-Bashforth-Moulton method [31].

Figure 4.8 shows the field profiles of a shock wave with a propagation speed $v_{\rm sh} = 2.4v_{\rm A}$, which is close to $c\cos 61°$. These fields obtained from a particle simulation were used for test particle calculations.

Plotted in Fig. 4.9 is the time variation of γ of an accelerated test particle. An expanded view of the early stage is also presented in the small panel. The Lorentz factor γ increases stepwise 42 times from $\gamma = 4.2$ to $\gamma \simeq 160$. At $\Omega_{\rm H0}t = 1.1 \times 10^4$, where $\Omega_{\rm H0}$ is the nonrelativistic hydrogen gyrofrequency in the upstream region, the particle escaped from the shock wave to the upstream region. The time intervals

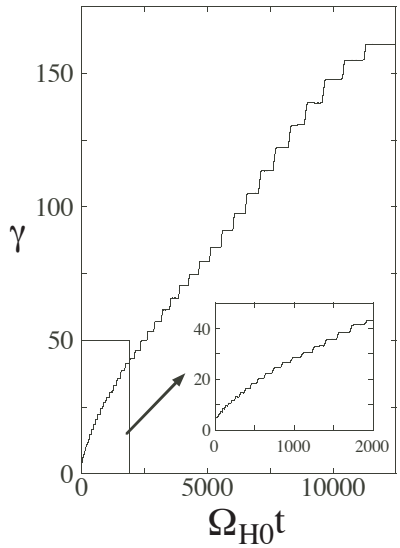

Figure 4.9: Time variation of γ of a relativistic ion incessantly accelerated by a shock wave. The fields shown in Fig. 4.8 have been used in the test particle calculation. The energy of this particle rises stepwise from $\gamma \simeq 4$ to $\gamma \simeq 160$. This particle finally outruns the shock wave owing to the increase in $p_\parallel$.

and the magnitudes of energy jumps both grow with time, because the gyroperiod and gyroradius become longer as γ goes up. The gyro-averaged γ rises almost linearly with time, as suggested by Eq. (4.16).

The top panel of Fig. 4.10 presents the time variation of the x position of this particle relative to the shock front, $X = (x - v_{\rm sh}t)/(c/\omega_{pe})$. Here, $X = 0$ is the position of the shock front; hence, X is negative when the particle is in the shock wave. Although $X > 0$ for most of the time, the minima of X are negative until $\Omega_{\rm H0}t = 1.1 \times 10^4$, indicating that the particle has interacted with the wave for a very long time. After this time, the particle goes away ahead of the shock wave. As shown in the second to fourth panels, the parallel momentum $p_\parallel$ grows steadily and $v_\parallel$ approaches the speed of light c, while $p_\perp$ and $v_\perp$ rapidly change exhibiting fish-bone profiles. The rise in $p_\perp$ and $v_\perp$ is caused by the transverse electric field in the shock wave, and their fall is due to the conversion to the parallel component. The velocity v_x oscillates around the shock speed $v_{\rm sh}$, which is indicated by the dashed line. With use of the observed average values of $v_{1\perp}/c$

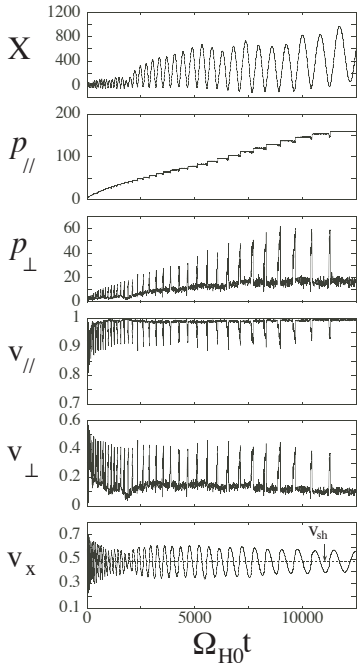

Figure 4.10: Time variations of the position, momentum, and velocity of an incessantly accelerated ion. Here, $X = x - v_{\rm sh}t$, with $X = 0$ being the position of the shock front. The particle is in the upstream region ($X > 0$) most of the time. The parallel momentum $p_\parallel$ goes up stepwise, while $p_\perp$ exhibits a fish-bone oscillation. The parallel velocity $v_\parallel$ approaches the speed of light c, and v_x oscillates around $v_{\rm sh}$.

$(= 0.2 \sim 0.3)$, B_{z0}/B_{z1} $(= 0.3 \sim 0.5)$, and $\sin[\Omega_{i1}(t_{\rm out} - t_{\rm in})]/(2\gamma)]$ (~ 0.7), we find from Eq. (4.17) that $g = 0.07 \sim 0.13$, which gives an estimate for the energy increase rate as $\Omega_{i0}^{-1} d\gamma/dt = 0.01 \sim 0.02$, while the gyro-averaged slope of γ in Fig. 4.9 for $1.4 \times 10^3 < \Omega_{\rm H0} t < 1.1 \times 10^4$ is observed to be $\Omega_{i0}^{-1} d\gamma/dt = 0.014$. The simulation results are consistent with the theoretical predictions.

Highly relativistic positrons and electrons, as well as ions, can have gyroradii greater than the width of the shock transition region and therefore satisfy the conditions for the incessant acceleration, Eqs. (4.8) and (4.9). They can thus also suffer this energization process, after becoming relativistic with some mechanisms. Such an example will be shown in Chap. 6.

Bibliography

[1] C. S. Morawetz, Phys. Fluids **4**, 988 (1961).

[2] C. S. Morawetz, Phys. Fluids **5**, 1447 (1962).

[3] D. Biskamp and H. Welter, Nuclear Fusion **12**, 663 (1972).

[4] D. W. Forslund, K. B. Quest, J. U. Brackbill, and K. Lee, J. Geophys. Res., **89**, 2142 (1984).

[5] Y. Ohsawa, Phys. Fluids **28**, 2130 (1985).

[6] B. Lembege and J. M. Dawson, Phys. Fluids **B1**, 1001 (1989).

[7] R. L. Tokar, S. P. Gary, and K. B. Quest, Phys. Fluids **30**, 2569 (1987).

[8] Y. Ohsawa, J. Phys. Soc. Jpn. **59**, 2782 (1990).

[9] M. Toida, T. X. Zhang, and Y. Ohsawa, J. Phys. Soc. Jpn. **61**, 3038 (1992).

[10] S. Nakazawa and Y. Ohsawa, J. Phys. Soc. Jpn. **67**, 176 (1998).

[11] C. F. Kennel and R. Pellat, J. Plasma Phys. **15**, 335 (1976).

[12] T. Kawashima, S. Miyahara, and Y. Ohsawa, J. Phys. Soc. Jpn. **72**, 1664 (2003).

[13] Y. Ohsawa and J-I. Sakai, Astrophys. J. **332**, 439 (1988).

[14] Y. Ohsawa and Y. Terashima, Publ. Astron. Soc. Jpn. **42**, 551 (1990).

[15] D. B. McDonald and M. A. I. Van Hollelbeke, Astrophys. J. Lett. **290**, L67 (1985).

[16] E. L. Chupp, H. Debrunner, E. Flückiger *et al.*, Astrophys. J. **318**, 913 (1987).

[17] R. Z. Sagdeev, in *Reviews of Plasma Physics*, edited by M. A. Leontovich (Consultants Bureau, New York, 1966), Vol. 4, pp. 23-91.

[18] R. Z. Sagdeev and V. D. Shapiro, JETP Lett. **17**, 279 (1973).

[19] M. A. Lee, V. D. Shapiro, and R. Z. Sagdeev, J. Geophys. Res. **101**, 4777 (1996).

[20] V. D. Shapiro and D. Üçer, Planetary and Space Science **51**, 665 (2003).

[21] T. Katsouleas and J. M. Dawson, Phys. Rev. Lett. **51**, 392 (1983).

[22] T. P. Armstrong, G. Chen, E. T. Sarris, and S. M. Krimigis, in *Study of Traveling Interplanetary Phenomena*, edited by M. A. Shea and D. F. Smart (Reidel, Dordrecht, 1977), p. 367.

[23] R. B. Decker, Space Science Reviews **48**, 195 (1988).

[24] K. Maruyama, N. Bessho, and Y. Ohsawa, Phys. Plasmas **5**, 3257 (1998).

[25] T. Masaki, H. Hasegawa, and Y. Ohsawa, Phys. Plasmas **7**, 529 (2000).

[26] S. Usami, H. Hasegawa, and Y. Ohsawa, Phys. Plasmas **8**, 2666 (2001).

[27] S. Usami and Y. Ohsawa, Phys. Plasmas **9**, 1069 (2002).

[28] S. Usami and Y. Ohsawa, Phys. Plasmas **11**, 918 (2004).

[29] S. Usami, R. Horiuchi, and Y. Ohsawa, Phys. Plasmas **16**, 122104 (2009).

[30] Y. Ohsawa, Phys. Fluids **29**, 2474 (1986).

[31] W. H. Press, S. A. Teukolsky, W. T. Vetterling, and B. P. Flannery, *Numerical Recipes in Fortran* (Cambridge Univ. Press, New York, 1992), Chap. 16.

Chapter 5

Heavy-ion acceleration

The elemental compositions of solar energetic heavy ions are on average similar to that of the solar corona [1, 2]: The ratio of the number density of high-energy heavy ions, $n_j(h)$, to that of the background heavy ions, $n_j(0)$, is independent of particle species j,

$$\frac{n_j(h)}{n_j(0)} \sim \text{const.} \tag{5.1}$$

This is also the case with galactic cosmic rays.

The motivation of the work in the present chapter stems from this fact, which places a stringent constraint on the theory of cosmic-ray acceleration. If the acceleration model were based on Landau resonance [3], for instance, it would be excluded out because of this fact. The number of resonance particles, n_{jr}, whose velocities are near the wave phase velocity ω/k approximately scales as

$$\frac{n_{jr}}{n_{j0}} \sim \exp\left(-\frac{m_j(\omega/k)^2}{2T}\right), \tag{5.2}$$

where T is the plasma temperature. In a multi-ion-species plasma, this ratio exponentially decreases with increasing m_j, which contradicts Eq. (5.1). The acceleration model based on the reflection caused by the electric potential would also be excluded out: The number of reflected ions is given by an equation similar to Eq. (5.2) [4], which can be seen from the expression for the minimum velocity for reflection, $v_{\rm ref} \simeq v_{\rm sh} - (2e\phi/m_j)^{1/2}$, discussed in Sec. 4.1.1. The value of the velocity distribution function at this speed, $f_j(v_{\rm ref})$, will decrease rapidly with increasing ion mass m_j. In fact, one can confirm with particle simulations that few thermal

heavy ions are reflected by a shock wave in a multi-ion-species plasma with protons being the major ion component.

Simulations for a multi-ion-species plasma show, however, that there is a mechanism that energizes heavy ions in such a way that their compositions are consistent with Eq. (5.1) [5]. Furthermore, the energization of heavy ions takes place even in a small-amplitude, soliton-like pulse; thus, unlike the solitary pulses in a single-ion-species plasma [6], it is damped even in the propagation perpendicular to a magnetic field [7, 8]. (Periodic perpendicular waves are undamped in both single- and two-ion-species plasmas [7–10].) The presence of multiple ion species tends to enhance the dissipation of wave energy, which has also been studied for Bernstein waves in a thermal equilibrium state [11, 12].

In this chapter, we first show a simulation of heavy-ion acceleration caused by a shock wave in a multi-ion-species plasma. Next, we present the theory of heavy-ion acceleration due to a shock wave and that due to a small-amplitude pulse. We then theoretically and numerically study the damping of small-amplitude pulses arising from the heavy-ion acceleration.

5.1 Simulation of heavy-ion acceleration

Simulations have revealed simple and remarkable properties of heavy-ion acceleration: A shock wave accelerates all the heavy ions that pass through the shock front, and these particles reach nearly the same speed [5]. The heavy-ion speeds and density ratios $n_j(h)/n_j(0)$ thus become independent of particle species.

To show this, we use a particle simulation code containing four ion species, in which, as in space plasmas, protons (H) are the major constituent, and He is 10 percent of H in number. The other two ion species are O and Fe with smaller abundances: Their mass densities are $n_{\rm O}m_{\rm O}/(n_{\rm H}m_{\rm H}) = 4 \times 10^{-3}$ and $n_{\rm Fe}m_{\rm Fe}/(n_{\rm H}m_{\rm H}) = 2 \times 10^{-3}$. Assuming the plasma temperature to be of the order of the temperature of the solar corona, $T \simeq 2 \times 10^6$ K, we take the gyrofrequencies to be $\Omega_{\rm He}/\Omega_{\rm H} = 1/2$, $\Omega_{\rm O}/\Omega_{\rm H} = 7/16$, and $\Omega_{\rm Fe}/\Omega_{\rm H} = 1/4$. In short, the abundances

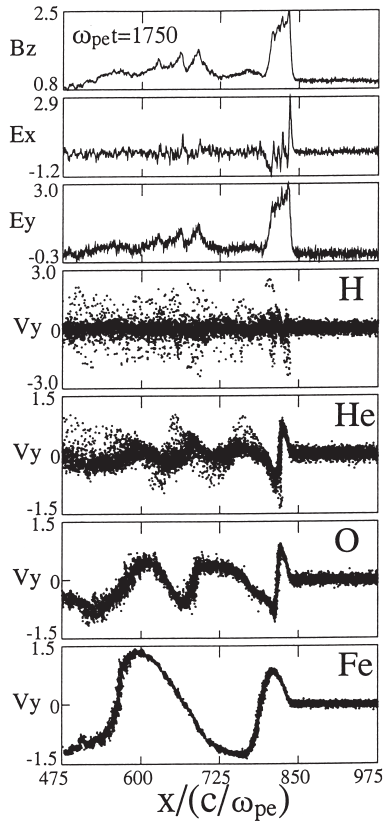

Figure 5.1: Snapshots of field profiles of a shock wave and phase spaces (x, v_y) of protons and heavy ions. Some protons (H) are reflected near the shock front and gain energies. All the heavy ions entering the shock wave are accelerated by the transverse electric field and reach nearly the same speed.

of heavy ions are small, and their gyrofrequencies are equal to or lower than $\Omega_{\rm H}/2$.

Figure 5.1 displays snapshots of the field profiles and phase spaces $(x,\ v_y)$ of the four ion species in a perpendicular shock wave with $v_{\rm sh} = 2.0v_{\rm h}$ $(= 2.1v_{\rm A})$ [5]. This wave is the high-frequency mode: As described in Sec. 2.3, the magnetosonic wave is split into several modes in a multi-ion-species plasma, and large-amplitude pulses evolve into high-frequency-mode pulses or shock waves.

The orbits of all the ion species are strongly distorted near the shock transition region $[x/(c/\omega_{pe}) \simeq 840]$. Some protons are reflected there and gain energies, with the mechanism discussed in Chap. 4. The heavy ions, on the other hand, exhibit distinct behavior. All of them are accelerated in the shock wave with similar trajectories, and their resultant speeds are nearly the same. These properties of heavy-ion acceleration have also been confirmed for an oblique shock wave with $\theta = 50^\circ$ [5].

5.2 Theory of heavy-ion acceleration

5.2.1 Acceleration due to a shock wave

This section discusses the physical mechanism and obtains the maximum speed of accelerated heavy ions in a heuristic way.

In the wave frame, each particle species flows in the negative x direction with velocity v_{jx}. The y component of the equation of motion in a perpendicular shock wave reads as

$$m_j \frac{dv_{jy}}{dt} = q_j \left(E_{y0} - \frac{v_{jx} B_z}{c} \right), \tag{5.3}$$

which can be viewed as either a fluid equation for particle species j or an equation for a particle j with no thermal motion; in the former, d/dt stands for $\partial/\partial t + \boldsymbol{v}_j \cdot \nabla$.

In the upstream region, the relatin $v_{jx} = -v_{\rm sh}$ holds, and $v_{\rm sh}$ is related to E_{y0} as $E_{y0} = -v_{\rm sh} B_{z0}/c$; hence, the right-hand side of Eq. (5.3) is zero.

In the shock wave, however, the magnetic field B_z becomes much stronger. Let us see how each particle species reacts to this change.

For the electrons, the right-hand side of Eq. (5.3) remains to be nearly zero,

$$E_{y0} - v_{jx}B_z/c \simeq 0, \tag{5.4}$$

because the drift approximation is sufficiently accurate for them. Furthermore, H ions that are the major and lightest ion component move with the velocity $v_{\mathrm{H}x}$ nearly equal to v_{ex} to keep charge neutrality. Consequently, although the hydrogen motion is not described by the drift approximation, the H ions also satisfy Eq. (5.4); the term $m_{\mathrm{H}}dv_{\mathrm{H}y}/dt$ is kept small.

Heavy ions with large inertia, on the other hand, cannot be quickly decelerated when they enter the shock wave; thus, they penetrate deep into it keeping the speed $v_{jx} \simeq -v_{\mathrm{sh}}$. Substituting Eq. (2.58) in Eq. (5.3) yields

$$m_j \frac{dv_{jy}}{dt} \simeq \frac{q_j v_{\mathrm{sh}}}{c}(B_z - B_{z0}). \tag{5.5}$$

Since B_z in the shock wave is much greater than B_{z0}, the right-hand side of Eq. (5.5) has large values, leading to the rapid increase in v_{jy} of heavy ions.

Denoting the acceleration time by Δt, we can estimate the maximum value of v_{jy} as

$$v_{jym} \simeq \frac{q_j v_{\mathrm{sh}}}{m_j c}\langle B_z - B_{z0}\rangle \Delta t, \tag{5.6}$$

where $\langle B_z - B_{z0}\rangle$ is the average value of $(B_z - B_{z0})$ that the particle feels during Δt. The approximation $v_{jx} \simeq -v_{\mathrm{sh}}$ used here will break down in a time $\sim 1/\Omega_j$, in which v_{jx} is substantially converted to v_{jy}. Taking the acceleration time to be $\Delta t \sim m_j c/(q_j\langle B_z\rangle) \sim m_j c/[q_j(B_{zm} + B_{z0})/2]$, where B_{zm} is the maximum value of B_z, and using the relation $v_{\mathrm{sh}} = Mv_{\mathrm{h}}$, we find the maximum v_{jy} as

$$v_{jym} \sim Mv_{\mathrm{h}}\frac{B_{zm} - B_{z0}}{B_{zm} + B_{z0}}. \tag{5.7}$$

All the quantities on the right-hand side are determined by the wave properties; hence, v_{jy} is independent of particle species j. That is, all the heavy ions are accelerated, and their final speeds are nearly the same.

Reference [5] discusses the mechanism seen in the laboratory frame, in which heavy ions absorb energy from the transverse electric field formed in the shock wave. Their final speeds are also given by Eq. (5.7).

If large-amplitude magnetosonic waves (shock waves) are generated in solar flares, they will accelerate all the heavy ions that pass through the wave front with the present mechanism. As a result, if one observes these high-energy heavy ions that have flown to the earth, their elemental compositions would be similar to that of the solar corona. Since the magnetic fields are strong in coronal magnetic tubes, their energies can be quite high.

5.2.2 Acceleration due to a small-amplitude pulse

The analysis in the previous section shows that the heavy ions of the same particle species follow nearly the same orbit. This indicates that the acceleration of heavy ions can be described with a multi-fluid model, in which each particle species is treated as one fluid.

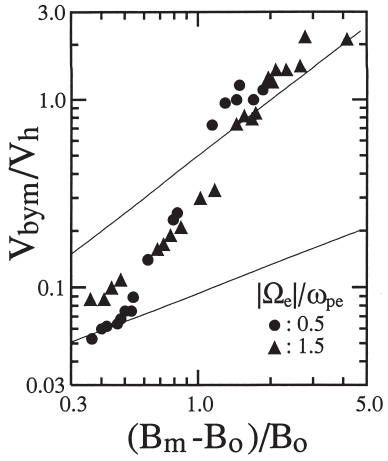

Figure 5.2: Maximum speed of accelerated heavy ions in a H-He plasma as a function of the wave amplitude. Here, He is the heavy ion "*b*." The upper and lower lines, respectively, show the theoretical prediction for the acceleration due to shock waves, Eq. (5.7), and that due to small-amplitude solitary pulses, Eq. (5.9). The closed circles and triangles present simulation results, which are consistent with the shock theory (5.7) in the large-amplitude region such that $(B_m - B_0)/B_0 \gtrsim 1$ and consistent with the soliton theory (5.9) in the small amplitude region $(B_m - B_0)/B_0 \ll 1$.

Another important feature of this mechanism is that the heavy-ion acceleration takes place even in small-amplitude pulses. This is in contrast to the proton

acceleration due to reflection, which virtually disappears as the amplitude of the magnetosonic pulse decreases. Since we know the field profiles of a small-amplitude pulse, we can calculate the speed of a heavy ion after the passage of the pulse:

$$v_{jy} = \frac{q_j}{m_j} \int_{-\infty}^{\infty} \left(E_y - \frac{v_{jx} B_z}{c} \right) dt. \tag{5.8}$$

For a small-amplitude, perpendicular solitary pulse of the high-frequency mode in a two-ion-species plasma with light ions "a" and heavy ions "b" ($\Omega_b < \Omega_a$) with $\omega_{\mathrm{p}b} \ll \omega_{\mathrm{p}a}$, one obtains, with the help of Eqs. (C.28) and (C.29) in Appendix C, the speed of the "b" ions that have passed through the pulse as

$$v_{by\mathrm{m}} = g_{vB} B_{\mathrm{n}}^{1/2}, \tag{5.9}$$

where B_{n} is the normalized amplitude, $B_{\mathrm{n}} = (B_{zm} - B_{z0})/B_{z0}$, and the coefficient g_{vB} is defined as

$$g_{vB} = \frac{2\sqrt{6}}{\alpha^{1/2}\eta^3} \frac{\Omega_b \omega_{\mathrm{p}a}^2}{|\Omega_{\mathrm{e}}| \omega_{\mathrm{pe}}^2} \left(1 - \frac{\Omega_b}{\Omega_a} \right) v_{\mathrm{h}}, \tag{5.10}$$

with η [$\sim (m_e/m_i)^{1/2}$] given by Eq. (2.107) and α by Eq. (2.97); g_{vB} depends on the heavy-ion mass.

This has been quantitatively confirmed with particle simulations. In Fig. 5.2 [13], the heavy-ion speed is plotted as a function of the wave amplitude; the simulation results (closed circles and triangles) are close to the theoretical prediction (5.7) for shock waves (the upper line) in the large-amplitude regime $B_{\mathrm{n}} \gtrsim 1$, while they are close to the prediction (5.9) for solitary pulses (the lower line) in the small-amplitude regime $B_{\mathrm{n}} \ll 1$.

The speed (5.9) due to a small-amplitude pulse is considerably lower than the speed (5.7) due to a shock wave. The difference between them stems from the fact that perturbed fields B_z and E_y remain strong in the large region behind the shock front, while for a small-amplitude, soliton-like pulse with a short pulse width, perturbed fields exist only inside it; heavy ions thus move to the downstream region before they are sufficiently accelerated. With use of the assumption $\omega_{\mathrm{p}b} \ll \omega_{\mathrm{p}a}$, the heavy-ion speed (5.9) can be approximated as

$$v_{by\mathrm{m}} \sim \frac{\Omega_b \omega_{\mathrm{pe}}}{|\Omega_{\mathrm{e}}| \omega_{\mathrm{p}a}} v_{\mathrm{h}} B_{\mathrm{n}}^{1/2}. \tag{5.11}$$

5.3 Damping of small-amplitude pulses in a multi-ion-species plasma

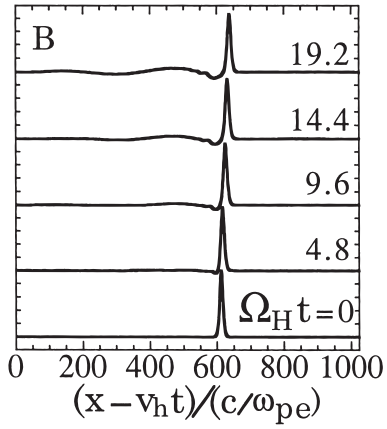

Figure 5.3: Profiles of B_z of a perpendicular solitary wave in a H-He plasma at various times. The initial amplitude is $B_n(0) = 0.1$. The solitary pulse propagates almost steadily. However, it is gradually damped. Furthermore, a long-wavelength perturbation is generated behind the original pulse.

The heavy-ion acceleration causes the damping of a pulse even if its propagation is perpendicular to a magnetic field [7,8]. This is a phenomenon that is not found in a single-ion-species plasma, in which perpendicular magnetosonic solitary waves [6] as well as periodic waves [9,10] are undamped. This section analyzes this damping with theory and three-fluid simulations.

The code contains H and He with $n_{He}/n_H = 0.1$ (light ion a is H and heavy ion b is He). The hydrogen-to-electron mass ratio is taken to be $m_H/m_e = 1000$; the magnetic field strength is $|\Omega_e|/\omega_{pe} = 0.5$, so that $c/v_A = 68.3$ and $v_A/v_h = 0.967$.

Figure 5.3 shows the propagation of a perpendicular solitary pulse [7]. As the initial field and density profiles in this simulation, we have used a solitary wave solution obtained from the KdV equation for the high-frequency mode derived in Appendix C. The profile of B_z moves almost steadily. Unlike the magnetosonic solitary wave in a single-ion-species plasma, however, its amplitude gradually decreases.

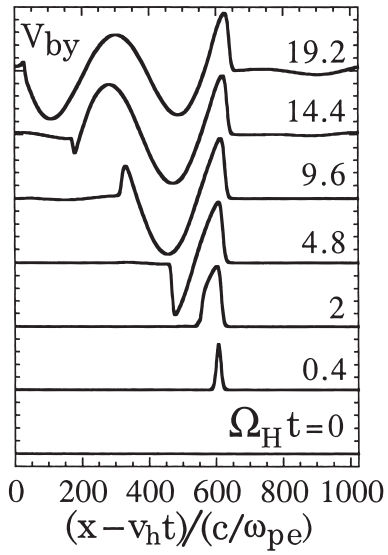

Figure 5.4: Profiles of heavy-ion velocity parallel to the wave front, v_{by}, at various times. A solitary pulse is near $(x - v_{\rm h}t)/(c/\omega_{pe}) = 650$, where v_{by} grows with time. After having sufficiently grown there, v_{by} exhibits a long-wavelength oscillation behind the pulse.

Figure 5.4 shows the profiles of heavy-ion velocity v_{by} near this pulse at various times. Since v_{by} is zero in the nonlinear wave theory [see Eq. (C.32) in Appendix C], the initial v_{by} was taken to be zero everywhere. Near the pulse region [$(x - v_{\rm h}t)/(c/\omega_{pe}) \simeq 650$], however, v_{by} grows with time, reaching its steady state value, $v_{by} \simeq 0.01 v_{\rm h}$, at $\Omega_{\rm H}t \simeq 0.75$. Then v_{by} begins to oscillate behind the pulse. This behavior of v_{by}, which is related to wave damping, is a higher order effect that is not included in the KdV equation. The observed frequency and wavelength of this oscillation are $\omega = 1.053\omega_{\rm hf0}$ and $\lambda = 1.2(2\pi/k_{\rm c})$, respectively, for this case (for $\omega_{\rm hf0}$ and $k_{\rm c}$, see Fig. 2.7). Other quantities also oscillate with the same frequency and wavelength (one also finds this oscillation of B_z behind the original pulse from an expanded view of Fig. 5.3). That is, the cross-field motion of heavy ions (v_{by}) induces a perturbation of the high-frequency mode with $k \sim k_{\rm c}$ (hence, $\omega \sim \omega_{\rm hf0}$). The wave energy of the original pulse is thereby gradually transferred to long-wavelength perturbations through the weak acceleration of heavy ions.

One can make a rough estimate of the damping rate of the original pulse by

calculating the kinetic energy that the heavy ions gain in this process per unit time, $n_{b0}(m_b v_{bym}^2/2)Mv_{\rm h}$. Comparison between this energy and that of the original pulse leads to a fairly good estimate for the damping rate, the same order of magnitude as the observed one.

Calculations taking into account the collective motion induced by v_{by} give a more accurate damping rate. By expressing the field and velocity components of the long-wavelength perturbation of the high-frequency mode in terms of v_{by}, one can write its wave energy density as $w(\omega)v_{bym}^2$, where

$$w(\omega) = \frac{1}{2}\frac{m_b n_{b0}}{m_a n_{a0}}(m_a n_{a0} + m_b n_{b0})\left(\frac{\omega_{\rm lfr}^2}{\omega^2} + \frac{(\omega^2 - \omega_{\rm lfr}^2)^2}{\omega^2(\omega_{\rm hf0}^2 - \omega_{\rm lfr}^2)}\right). \tag{5.12}$$

(For the details of the calculation, see Appendix H.) The amount of energy that the perturbation gains per unit time is $w(\omega)v_{bym}^2 Mv_{\rm h}$, which is equal to the time rate of change of the total wave energy $E_{\rm w}$ of the original pulse:

$$\frac{dE_{\rm w}}{dt} = -w(\omega)v_{bym}^2 Mv_{\rm h}. \tag{5.13}$$

Equation (5.13) can be put into the differential equation for $B_{\rm n}$. The Mach number M of a solitary wave is related to $B_{\rm n}$ through $M = 1 + B_{\rm n}/2$. Furthermore, as shown in Eq. (5.9), the amplitude of the long-wavelength perturbation, v_{bym}, is proportional to $B_{\rm n}^{1/2}$. We can also express the total energy of the original pulse as a function of $B_{\rm n}$, by integrating the wave energy density over the pulse region:

$$E_{\rm w} = \int\left(\frac{(B - B_0)^2 + E^2}{8\pi} + \sum_j \frac{m_j n_j v_j^2}{2}\right){\rm d}x. \tag{5.14}$$

(Because perpendicular waves are considered here, $\boldsymbol{B}$ has only the z component.) Substituting the soliton solution in Eq. (5.14) yields the dependence of $E_{\rm w}$ on $B_{\rm n}$. For instance, since the magnetic-field profile is expressed by Eqs. (2.54) and (2.55) with $v_{p0} = v_{\rm h}$, $\mu = -c^2/(2\omega_{pe}^2)$, and α given by Eq. (2.97), the magnetic field energy of the soliton is found to be

$$\int_{-\infty}^{\infty}\frac{(B - B_0)^2}{8\pi}dx = \frac{4}{3}\left(\frac{B_0^2}{8\pi}\right)B_{\rm n}^2 D. \tag{5.15}$$

Calculating the other components in the same manner, we find that the total ion kinetic energy is equal to the magnetic field energy and that the electric-field and electron kinetic energies are much smaller than them. Hence, the total energy of the soliton is

$$E_{\rm w} = \frac{8}{3}\sqrt{\frac{6}{\alpha}}\frac{c}{\omega_{\rm pe}}\left(\frac{B_0^2}{8\pi}\right)B_{\rm n}^{3/2}. \tag{5.16}$$

The energy $E_{\rm w}$ scales as $B_{\rm n}^{3/2}$. This dependence arises from the fact that the wave energy density and the soliton width are proportional to $B_{\rm n}^2$ and to $B_{\rm n}^{-1/2}$, respectively. Equation (5.13) thus becomes the differential equation for the amplitude $B_{\rm n}$ of the original pulse,

$$\frac{dB_{\rm n}^{3/2}}{dt} = -\frac{3}{2}\gamma_{\rm d}B_{\rm n}(0)^{1/2}B_{\rm n}\left(1+\frac{B_{\rm n}}{2}\right), \tag{5.17}$$

where $\gamma_{\rm d}$ is defined as

$$\gamma_{\rm d} = \frac{\alpha^{1/2}\omega_{\rm pe}v_{\rm h}}{4\sqrt{6}cB_{\rm n}(0)^{1/2}}\left(\frac{w(\omega)g_{vB}^2}{B_0^2/(8\pi)}\right). \tag{5.18}$$

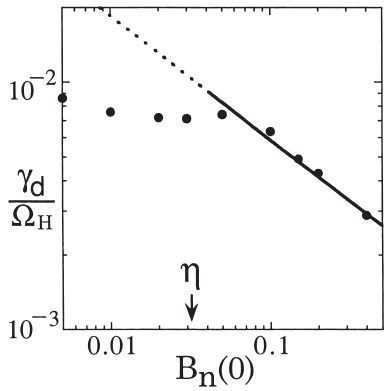

Figure 5.5: Damping rate $\gamma_{\rm d}$ as a function of the initial normalized amplitude $B_{\rm n}(0)$. The solid line and dots show, respectively, the theoretical prediction and simulation results. In the region where the theoretical treatment is valid [$B_{\rm n}(0) \gtrsim \eta$], the theory and simulation results are consistent.

If we ignore the second term on the right-hand side of Eq. (5.17), we have

$$B_{\rm n}(t)^{1/2} = B_{\rm n}(0)^{1/2}(1-\gamma_{\rm d}t/2). \tag{5.19}$$

Because the amplitude must be positive, this solution is valid in the time range $0 \leq t < 2/\gamma_{\rm d}$. For small t, $\gamma_{\rm d} t << 1$, $B_{\rm n}(t)$ can be approximated as

$$B_{\rm n}(t) = B_{\rm n}(0)(1 - \gamma_{\rm d} t), \tag{5.20}$$

indicating that $\gamma_{\rm d}$ is the initial damping rate. As can be seen from Eq. (5.18), the damping rate $\gamma_{\rm d}$ is proportional to $B_{\rm n}(0)^{-1/2}$.

Figure 5.5 compares the theoretical prediction and simulation results on $\gamma_{\rm d}$. In the region $B_{\rm n}(0) \gtrsim \eta$, they are consistent. It is because the soliton theory for the high-frequency mode, which the above theory is based on, is valid for amplitudes greater than η, as shown by the condition (2.96).

For a fully-ionized, H-He plasma with the density ratio $n_{\rm He}/n_{\rm H} = 0.1$, the amplitude of a solitary pulse with $B_{\rm n}(0) = 0.1$ becomes 0.9 times as small as the initial one after the pulse has traversed a length $l \simeq 6 \times 10^4$ cm in a plasma with $n_{\rm e} = 10^8$ cm^{-3}. For a density $n_{\rm e} = 10^{14}$ cm^{-3}, it is $l \simeq 60$ cm.

It is noted that, unlike solitary pulses, small-amplitude periodic waves are undamped even in a two-ion-species plasma [7]. In a periodic wave profile, the direction of the heavy-ion acceleration also periodically changes. Thus, the net increase in v_{by} is zero in one wavelength.

Bibliography

[1] J. P. Meyer, Astrophys. J. Suppl. **57**, 151 (1985).

[2] J. P. Meyer, Astrophys. J. Suppl. **57**, 173 (1985).

[3] L. D. Landau, J. Phys. (USSR) **10**, 25 (1946).

[4] M. Toida, T. X. Zhang, and Y. Ohsawa, J. Phys. Soc. Jpn. **61**, 3587 (1992).

[5] M. Toida and Y. Ohsawa, Solar Physics **171**, 161 (1997).

[6] C. S. Gardner and G. K. Morikawa, Commun. Pure Appl. Math. **18**, 35 (1965).

[7] D. Dogen, M. Toida, and Y. Ohsawa, Phys. Plasmas **5**, 1298 (1998).

[8] S. Irie and Y. Ohsawa, Phys. Plasmas **10**, 1253 (2003).

[9] I. B. Bernstein, Phys. Rev. **109**, 293 (1958).

[10] D. E. Baldwin and G. Rowlands, Phys. Fluids **9**, 2444 (1966).

[11] M. Toida, T. Suzuki, and Y. Ohsawa, Phys. Plasmas **11**, 3028 (2004).

[12] M. Toida, T. Yoshiya, and Y. Ohsawa, Phys. Plasmas **12**, 102306 (2005).

[13] M. Toida and Y. Ohsawa, J. Phys. Soc. Jpn. **64**, 2036 (1995).

Chapter 6

Positron acceleration

Plasmas containing positrons have been studied in various fields, such as astrophysics and plasma-based accelerators [1]- [12]; the wave theory in Sec. 2.4 is one example of the studies in basic plasma physics. The presence of positrons around pulsars was suggested by Sturrock in 1971 [1], and relativistic pulsar winds of electron-positron plasmas were predicted by Kennel and Coroniti [2]. In addition, some observations claim that major components of relativistic jets from active galactic nuclei are electrons and positrons [3, 4]. Furthermore, intense lasers now enable us to produce plasmas containing positrons in laboratory experiments [5]. Positron acceleration is studied in some experiments of plasma-based accelerators [11, 12].

The subject of the present chapter is positron acceleration in a shock wave in a magnetized plasma consisting of electrons, positrons, and ions [13]- [18]. In this mechanism, some positrons are accelerated in the shock transition region for long periods of time with an energy increase rate proportional to the parallel electric field $E_{\parallel}$ [13, 14]. Particle simulations have demonstrated energization to $\gamma \sim 10^4$ [17]. Since the acceleration was not saturated until the end of those simulation runs, $\omega_{pe}t \sim 7000$, longer time simulations would give higher energies.

In the surfatron acceleration mentioned in Sec. 4.1.3, particles move along the wave front across the magnetic field [19, 20], while in this mechanism, positrons move in the transition region nearly parallel to the magnetic field; thus, the latter can operate in a weaker electric field than the former. Furthermore, simulations

show that this mechanism is quite stable; that is, even if the shock profile is temporarily distorted and the acceleration stops, energy multiplication processes can start again after the wave profile has been recovered. Besides the nearly parallel motion, curtate and prolate cycloid orbits along the shock front appear in these processes after such perturbations.

6.1 Theory of ultrarelativistic positron acceleration

The theory in Sec. 2.4 tells us that the magnetosonic wave is split into two modes in an EPI plasma. As was shown in Figs. 2.19 and 2.20, except for the vicinity of the density ratio $n_{p0}/n_{e0} = 1$, the cutoff frequency of the high-frequency mode of the magnetosonic wave is much higher than the ion gyrofrequency in EPI plasmas; thus, the nonlinear coupling of the high- and low-frequency modes is rather weak. This differs from the case of two-ion-species plasmas, in which the cutoff frequency of the high-frequency mode is of the order of Ω_i and thus the nonlinear coupling of the two modes is strong. The shock wave in an EPI plasma analyzed below can therefore be viewed as the low-frequency mode, affected little by the presence of the high-frequency mode particularly when n_{p0}/n_{e0} is small.

Although both positrons and ions can be reflected by a shock wave, their orbits are distinct from each other because of their large mass ratio m_i/m_p. As discussed in Chap. 4, the ion reflection, which is caused by the sharp rise of the magnetic field and electric potential, mainly occurs across the magnetic field. On the other hand, the reflection of thermal positrons is primarily along the magnetic field and is caused by the parallel pseudo potential F that rapidly rises in the shock transition region. The parallel kinetic energy of a thermal positron in the upstream region would be $m_p v_\parallel^2/2 \sim m_p v_{Tp}^2/2$ in the wave frame; if the thermal speed v_{Tp} is lower than the Alfvén speed, then we would have $m_p v_\parallel^2/2 \sim m_p v_{\rm A}^2/2$. Comparing these values with the magnitude of eF given by Eq. (2.205), one sees that a substantial fraction of thermal positrons can be reflected by a shock wave.

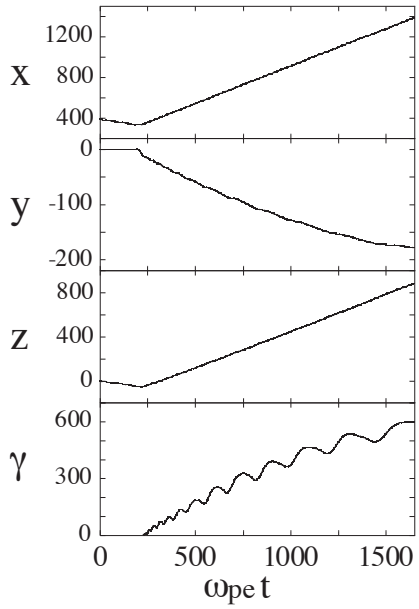

Figure 6.1: Time variations of x, y, z, and γ of an accelerated positron.

Figure 6.1 is a simulation result [13] showing a typical motion of a positron accelerated by this mechanism. After the encounter with a shock wave, this particle stays in the shock transition region, moving in the direction nearly parallel to $\boldsymbol{B}_0$, which we see from the time variations of x and z; we also note that the change in y is much smaller than those of x and z (they are normalized to c/ω_{pe}). The Lorentz factor γ rises with time. More quantitative analysis of simulation results will be given in Sec. 6.2, after we have described the theory in the next section.

6.1.1 Acceleration nearly parallel to the magnetic field

In the theory of ultrarelativistic acceleration of positrons along the magnetic field in a shock wave [13]- [17], the shock speed $v_{\rm sh}$ is assumed to be close to $c\cos\theta$, Eq. (3.25). Since the gyro-averaged particle velocity in the x direction is given by $\langle v_x\rangle \simeq v_\parallel \cos\theta$, if $v_{\rm sh} \sim c\cos\theta$, then reflected positrons with $v \sim c$ can move with the shock wave for long periods of time, with the x component of the positron velocity being

$$v_x \simeq v_{\rm sh}. \tag{6.1}$$

Furthermore, for ultrarelativistic positrons moving nearly parallel to the magnetic field, the following relation should hold:

$$v\frac{d\gamma}{dt} \gg \gamma \left| \frac{d\boldsymbol{v}}{dt} \right|. \tag{6.2}$$

That is, for particles with $v \simeq c$, a slight change in the speed results in a huge change in γ. Indeed, because

$$\frac{d\gamma}{dt} = \frac{\gamma^3}{2}\frac{d}{dt}\left(\frac{v^2}{c^2}\right), \tag{6.3}$$

$d\gamma/dt$ is $\gamma^3/2$ times as large as $d(v^2/c^2)/dt$. In the relativistic equation of motion,

$$m_p \frac{d(\gamma \boldsymbol{v})}{dt} = e\left(\boldsymbol{E} + \frac{\boldsymbol{v}}{c} \times \boldsymbol{B}\right), \tag{6.4}$$

we therefore ignore the term $\gamma d\boldsymbol{v}/dt$ in comparison with $\boldsymbol{v}d\gamma/dt$. Another assumption is that the y component of the velocity is smaller than the other components, $|v_y| \ll |v_x|,\ |v_z|$, which differs from the surfatron acceleration [19, 20], in which v_y is the dominant velocity component.

Under these assumptions, we adopt the following ordering:

$$\frac{v_{\rm sh}}{c} \sim \frac{v_z}{c} \sim \frac{B_{x0}}{B_0} \sim \frac{B_z}{B_0} \sim \frac{E_y}{B_0} \sim O(1), \tag{6.5}$$

$$\frac{1}{\Omega_p}\frac{d\gamma}{dt} \sim \frac{v_y}{c} \sim \frac{B_y}{B_0} \sim \frac{E_x}{B_0} \sim \frac{E_z}{B_0} \ll 1. \tag{6.6}$$

We then obtain the lowest order equations as

$$m_p v_{\rm sh}\frac{d\gamma}{dt} = eE_x + e\frac{v_y}{c}B_z - e\frac{v_z}{c}B_y, \tag{6.7}$$

$$0 = e\frac{v_z}{c}B_{x0} - e\frac{v_{\rm sh}}{c}B_{z0}, \tag{6.8}$$

$$m_p v_z \frac{d\gamma}{dt} = -e\frac{v_y}{c}B_{x0}. \tag{6.9}$$

Here, we have eliminated E_y and E_z using the following equations:

$$E_y = (v_{\rm sh}/c)(B_z - B_{z0}), \tag{6.10}$$

$$E_z = -(v_{\rm sh}/c)B_y, \tag{6.11}$$

which result from Faraday's law for one-dimensional, stationary waves, in which the fields depend only on $\xi = x - v_{\rm sh}t$. Equation (6.8) shows that the positron motion is nearly parallel to the external magnetic field $\boldsymbol{B}_0$:

$$\frac{v_z}{v_{\rm sh}} = \frac{B_{z0}}{B_{x0}}. \tag{6.12}$$

With the help of Eqs. (6.9) and (6.12), we eliminate v_y and v_z in Eq. (6.7) and find the time rate of change of γ as

$$\frac{1}{\Omega_p}\frac{d\gamma}{dt} = \frac{c\cos\theta}{v_{\rm sh}}\frac{(\boldsymbol{E}\cdot\boldsymbol{B})}{(\boldsymbol{B}\cdot\boldsymbol{B}_0)}. \tag{6.13}$$

It is noted that from Eqs. (6.10) and (6.11), it follows that $(\boldsymbol{E}\cdot\boldsymbol{B}) = (\boldsymbol{E}\cdot\boldsymbol{B}_0)$ for stationary waves. Substitution of Eq. (6.13) in Eq. (6.9) yields v_y as

$$\frac{v_y}{c} = \frac{v_{\rm sh}B_yB_{z0}^2/(cB_{x0}) - E_xB_{z0}}{B_{z0}B_z + B_{x0}^2}. \tag{6.14}$$

The energy increase rate $d\gamma/dt$ is constant. Because of the assumption (6.1), the particle position ξ and thus the vectors $\boldsymbol{E}(\xi)$ and $\boldsymbol{B}(\xi)$ in Eq. (6.13) are constant.

The theory has been extended in Ref. [14] to a more general case, in which no assumptions are made on the magnitudes of velocity components and wave fields: Equation (6.8) is replaced by

$$m_pv_y\frac{d\gamma}{dt} = e\frac{v_z}{c}B_{x0} - e\frac{v_{\rm sh}}{c}B_{z0}, \tag{6.15}$$

and the ordering of wave fields, Eqs. (6.5) and (6.6), are not used. This calculation gives the energy increase rate as

$$\frac{1}{\Omega_p}\frac{d\gamma}{dt} = \frac{E_xB_{z0}v_{\rm sh}/c \;-\; B_{x0}B_y(\gamma_{\rm sh}^{-2} - \gamma^{-2})}{B_zB_0(\gamma_{\rm sh}^{-2} - \gamma^{-2}) + B_{z0}B_0v_{\rm sh}^2/c^2}. \tag{6.16}$$

In this generalized theory, the only assumption on the wave is that it is stationary and one-dimensional. Other than magnetosonic waves, therefore, there might be waves that can accelerate positrons with this mechanism.

6.1.2 Surfatron and generalized theory

We here discuss the relation between the surfatron acceleration and the generalized theory. In the limit of $\theta \to 90^\circ$, B_{x0} vanishes, and it follows from Eq. (6.9) that

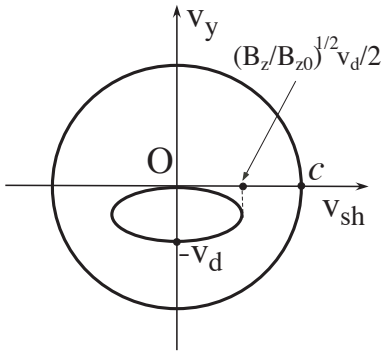

Figure 6.2: Speed-of-light circle (6.17) and ellipse (6.20) of zeroth-order velocities for perpendicular waves in the $(v_{\rm sh}, v_y)$ plane. If these lines cross, we have solutions.

$v_z = 0$; hence,

$$v_x^2 + v_y^2 = v_{\rm sh}^2 + v_y^2 \simeq c^2, \tag{6.17}$$

which gives

$$v_y^2/c^2 \simeq \gamma_{\rm sh}^{-2}. \tag{6.18}$$

From Eqs. (6.15) and (6.18), one finds that

$$\gamma = (v_{\rm sh}/c)\gamma_{\rm sh}\Omega_p t, \tag{6.19}$$

which is identical to the particle speed in the limit of $\gamma \gg 1$ in the unlimited surfatron acceleration [20]: On using Eqs. (4.6) and (4.7), we obtain the same form as Eq. (6.19), with Ω_p replaced by Ω_i, for $\gamma \gg 1$ [$\Omega_i^2 t^2 v_{\rm sh}^2/c^2 \gg 1$ in Eq. (4.7)].

If the propagation angle is $\theta = 90°$, strong longitudinal electric fields are required even in the present model. From Eqs. (6.7) and (6.15), we have an elliptic equation in the $(v_{\rm sh}, v_y)$ plane:

$$\frac{v_{\rm sh}^2}{(B_z/B_{z0})(v_{\rm d}/2)^2} + \frac{(v_y + v_{\rm d}/2)^2}{(v_{\rm d}/2)^2} = 1, \tag{6.20}$$

where $v_{\rm d} = cE_x/B_z$. Figure 6.2 displays the speed-of-light circle (6.17) and the ellipse (6.20) in the $(v_{\rm sh}, v_y)$ plane [14]. In the case that these two lines cross, we have solutions; they exist if $E_x/B_z \gtrsim 1$ or $(B_z/B_{z0})[E_x/(2B_z)]^2 \gtrsim 1$. This indicates that the longitudinal electric field E_x must be strong for the perpendicular case.

Since E_x/B_z is always smaller than unity in stationary perpendicular magnetosonic waves [21] [see Eq. (A.12)], they will not have these solutions. For this reason, the perpendicular case would be practically unimportant in positron acceleration in the present mechanism.

6.1.3 Perturbed motions

Careful observations of simulations reveal that γ and other physical quantities of an accelerated positron exhibit small-amplitude oscillations, such as the one in the bottom panel of Fig. 6.1, in addition to the increase in γ predicted by Eq. (6.13). To realize this phenomenon, perturbations to the zeroth-order motion described in Sec. 6.1.1 have been analyzed in Ref. [14]. We here summarize its result, giving the detailed calculations in Appendix I.

The perturbation is an elliptic motion in the plane perpendicular to the vector

$$\boldsymbol{U} = \gamma_0^2 \left(\frac{\boldsymbol{v}_0 \cdot \boldsymbol{B}}{cB_0} \right) \frac{\boldsymbol{v}_0}{c} + \frac{\boldsymbol{B}}{B_0}, \tag{6.21}$$

where γ_0 and $\boldsymbol{v}_0$ are the Lorentz factor and velocity in the zeroth-order theory, respectively. The vector $\boldsymbol{U}$ is nearly parallel to the zeroth-order velocity $\boldsymbol{v}_0$ because $\gamma_0 \gg 1$. The frequency of this perturbation is

$$\left(\frac{\omega}{\Omega_p} \right)^2 = \gamma_0^{-4} \left[\gamma_0^2 \left(\frac{\boldsymbol{v}_0 \cdot \boldsymbol{B}}{cB_0} \right)^2 + \frac{B^2}{B_0^2} \right], \tag{6.22}$$

with the velocity components v_{y1} and v_{z1} being related to v_{x1} as

$$v_{y1} = \frac{[(\omega/\Omega_p)^2 \gamma_0^4 (v_{y0} v_{z0}/c^2) + B_y B_z/B_0^2] - i(\omega/\Omega_p)\gamma_0 U_x}{[(\omega/\Omega_p)^2 \gamma_0^4 (v_{x0} v_{z0}/c^2) + B_x B_z/B_0^2] + i(\omega/\Omega_p)\gamma_0 U_y} v_{x1}, \tag{6.23}$$

$$v_{z1} = \frac{[(\omega/\Omega_p)^2 \gamma_0^4 (v_{y0} v_{z0}/c^2) + B_y B_z/B_0^2] + i(\omega/\Omega_p)\gamma_0 U_x}{[(\omega/\Omega_p)^2 \gamma_0^4 (v_{x0} v_{y0}/c^2) + B_x B_y/B_0^2] - i(\omega/\Omega_p)\gamma_0 U_z} v_{x1}. \tag{6.24}$$

Appendix I gives the velocity components in the plane perpendicular to $\boldsymbol{U}$, from which one would see more directly that the motion is elliptic.

The zeroth-order theory in Sec. 6.1.1 is also applicable to the ions if we replace m_p by m_i. However, one needs a slightly different perturbation scheme for the ions, which is also given in Appendix I. The ion perturbation motion is one-dimensional and can be unstable [14, 22].

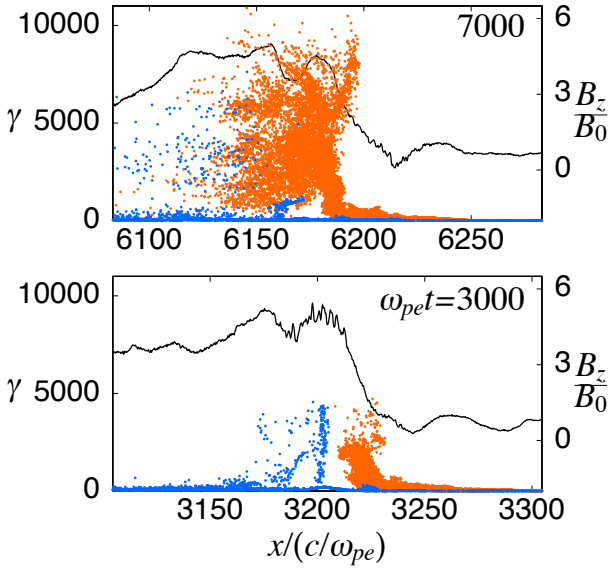

Figure 6.3: Phase spaces (x, γ) of positrons (orange dots) and electrons (blue dots) and the profiles of B_z at two different times. Some positrons have been accelerated to $\gamma \sim 10^4$ by the end of the simulation run, $\omega_{pe}t = 7000$.

6.2 Simulations of ultrarelativistic acceleration of positrons

6.2.1 Demonstration and analysis of acceleration

Figure 6.3 shows phase spaces (x, γ) of positrons (orange dots) and electrons (blue dots) near a shock front at two different times, $\omega_{pe}t = 3000$ and 7000 [17]. By the end of the simulation run, $\omega_{pe}t = 7000$, some positrons reach energy $\gamma \sim 10^4$. Since the acceleration has not been saturated, positron energies would further rise if we carry out a longer time simulation with a larger system size. We also find high-energy electrons with $\gamma \sim 7000$, which is due to the mechanism described in Chap. 3 and is not further mentioned here. This is a result of a shock simulation with $m_i/m_e = 1836$, $n_{p0}/n_{e0} = 0.02$, $\theta = 43°$, $|\Omega_e|/\omega_{pe} = 12$, $c/\omega_{pe} = 10\Delta_g$, and the system length $L = 65536\Delta_g$. The shock speed is $v_{sh} = 2.64v_A$ with $v_A/c = 0.28$; thus, v_{sh} is close to $c\cos\theta$.

We show below three types of motions of accelerated positrons reported in

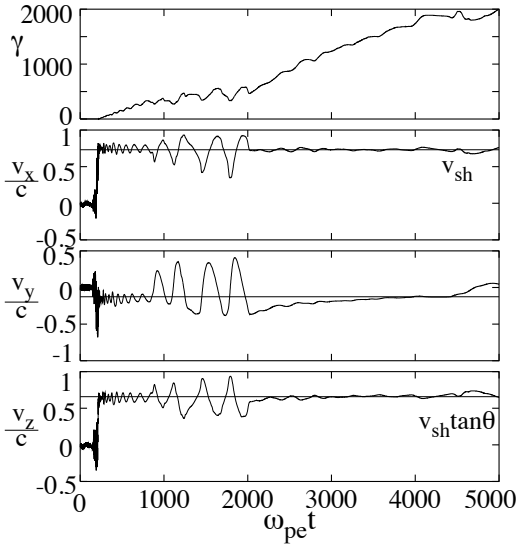

Figure 6.4: Time variations of γ and $\boldsymbol{v}$ of a positron accelerated along the magnetic field. Except for the time period $\omega_{pe}t \simeq 1000$ to 2000, the velocity is nearly parallel to $\boldsymbol{B}_0$, and γ goes up with time.

Ref. [16], in which the system size is 1/4 of that in Fig. 6.3; other simulation parameters are $m_i/m_e = 100$, $n_{p0}/n_{e0} = 0.02$, $\theta = 42°$, $|\Omega_e|/\omega_{pe} = 3.0$, and $c/\omega_{pe} = 4\Delta_{\rm g}$ (thus, $v_{\rm A}/c = 0.301$); the shock speed, $v_{\rm sh} = 2.42 v_{\rm A}$, is close to $c\cos\theta$. The highest energy in this case is $\gamma \sim 2000$.

Figure 6.4 displays the time variations of energy and velocity components of an accelerated positron. The horizontal line in the panel for v_x represents the theoretical relation $v_x = v_{\rm sh}$, Eq. (6.1), and that for v_z is $v_z = v_{\rm sh}\tan\theta$, Eq. (6.12). The simulation results for v_x and v_z are close to these theoretical predictions. The velocity component v_y is small and is explained by the theory (6.14), which is also shown by the horizontal line. This particle moves nearly parallel to $\boldsymbol{B}_0$, with its γ going up with time.

For the time period $1000 \lesssim \omega_{pe}t \lesssim 2000$, however, the increase in γ is rather slow, and all the velocity components exhibit large-amplitude oscillations. As can be seen from Fig. 6.5, the shock profile in this period significantly deviates from the normal one: The shock transition region broadens and the electric field E_x

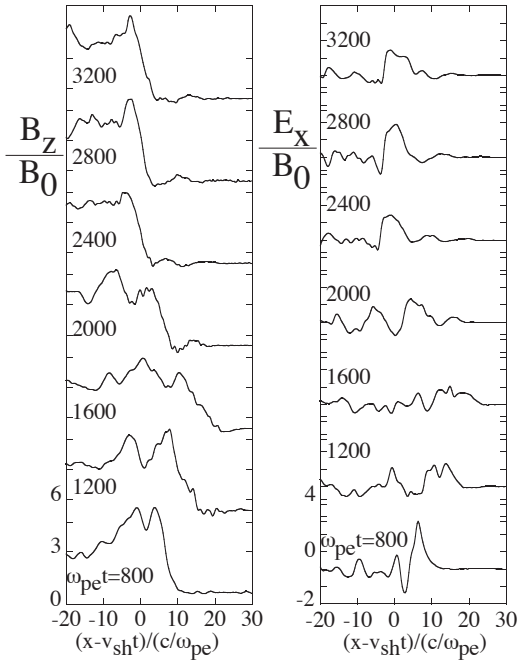

Figure 6.5: Profiles of B_z and E_x at various times. At $\omega_{pe}t = 1200$ and 1600, the fields have diffusive profiles: The gradient of B_z is small and E_x is weak even in the shock transition region, compared with those at other times.

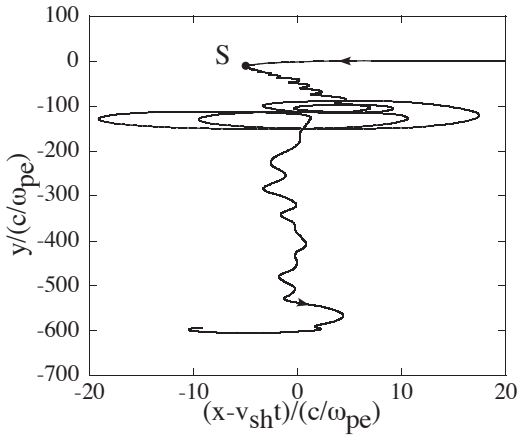

Figure 6.6: Orbit in the $(x - v_{\rm sh}t, y)$ plane of the positron analyzed in Fig. 6.4. After the encounter with the shock wave at point S, this particle moves primarily in the negative y direction along the shock front. However, owing to the deviation of the wave profile, the orbit turns to a circular one at $\omega_{pe} \simeq 1000$, which continues until $\omega_{pe} \simeq 2000$, during which γ does not increase much.

becomes weak.

Figure 6.6 shows the orbit of this particle in the $(x - v_{\rm sh}t, y)$ plane. It (1) encounters the shock wave at point S, (2) moves along the shock front (note the difference in the scales of the horizontal and vertical axes), (3) exhibits a circular orbit, and then (4) moves along the front again. For the phases (2) and (4), γ increases with time, while for the phase (3), which is $1000 \lesssim \omega_{pe}t \lesssim 2000$, the shock profile is diffusive and γ does not grow much. From Figs. 6.4–6.6, we see that this acceleration is quite stable: Although the acceleration is temporarily stopped by the deviation of wave profile, it can start again when the shock is restored to the normal, sharp profile.

Figure 6.7 compares the time variations of observed γ and theoretical prediction $\gamma_{\rm HUO}$, which is the integral of Eq. (6.13) derived by Hasegawa, Usami, and Ohsawa [13]:

$$\gamma_{\rm HUO} = \Omega_p \int \frac{c\cos\theta}{v_{\rm sh}} \frac{(\boldsymbol{E}\cdot\boldsymbol{B})}{(\boldsymbol{B}\cdot\boldsymbol{B}_0)} dt. \tag{6.25}$$

In the numerical calculation of $\gamma_{\rm HUO}$, the simulation values of $\boldsymbol{E}$ and $\boldsymbol{B}$ along the particle orbit were used. The observed γ and the theory $\gamma_{\rm HUO}$ are quite close. The

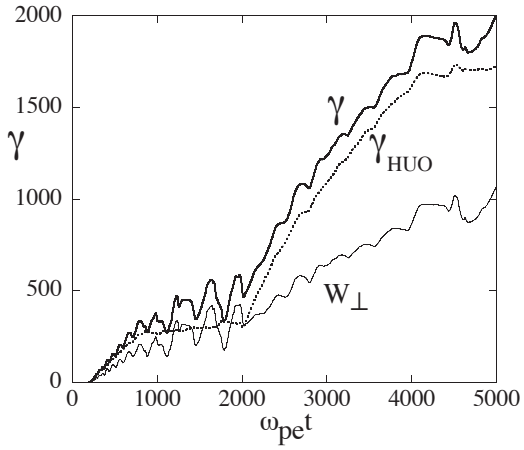

Figure 6.7: Time variation of γ of a positron accelerated along the magnetic field. Here, $W_\perp$ is the work done by the perpendicular electric field defined by Eq. (6.26), and $\gamma_{\rm HUO}$ represents the theory (6.25). The observed energy γ is significantly higher than $W_\perp$ and close to $\gamma_{\rm HUO}$.

work done by the electric field $\boldsymbol{E}_\perp$ perpendicular to $\boldsymbol{B}$,

$$W_\perp = \frac{e}{m_p c^2} \int \boldsymbol{E}_\perp \cdot \boldsymbol{v} dt, \tag{6.26}$$

is considerably smaller than them.

The perturbation motion theoretically predicted in Sec. 6.1.3 has also been quantitatively examined with simulations. Figure 6.8 shows the frequencies of the perturbation oscillations in γ and velocity components [14]. The theoretical line representing Eq. (6.22) fits well to the simulation result (dots).

Rapid variations of field structures can change or modify the mechanism of particle acceleration. Figure 6.9 shows one such example. This particle encounters the shock wave at point S and moves along the shock front and nearly along the magnetic field. Due to the deformation of the shock profile, however, significant part of $v_\parallel$ is converted to $v_\perp$, with the particle orbit turning to a prolate cycloid in the $(x - v_{\rm sh}t, y)$ plane. As Fig. 6.10 shows, the contribution of $\boldsymbol{E}_\perp$ becomes important in the energy multiplication; both $W_\perp$ and γ go up stepwise, with their values fairly close and much greater than $\gamma_{\rm HUO}$ for $\omega_{pe}t \gtrsim 1000$. Because of the increase in $v_\perp$, the gyroradius ($\sim \gamma c/\Omega_p$) exceeds the shock width, and the incessant

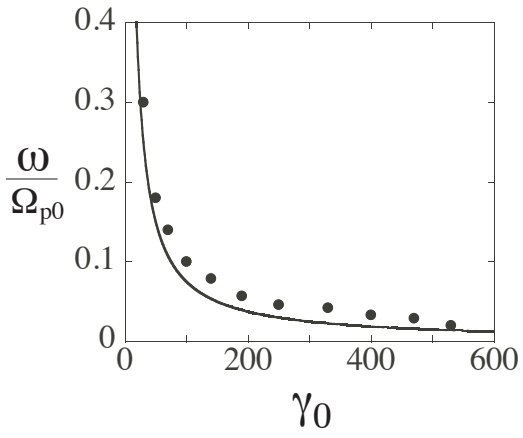

Figure 6.8: Perturbation frequency vs γ_0. Here, γ_0 is the Lorentz factor averaged over each oscillation period. The dots and solid line show simulation results and theoretical curve, respectively.

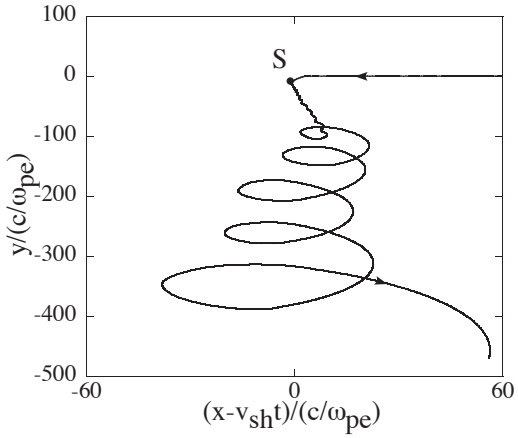

Figure 6.9: Orbit of an accelerated positron in the $(x - v_{\rm sh}t, y)$ plane. The particle enters the shock region at point S and is accelerated nearly along the magnetic field in the shock transition region. Then, after the deviation of the shock profile, its orbit changes to that of the incessant acceleration.

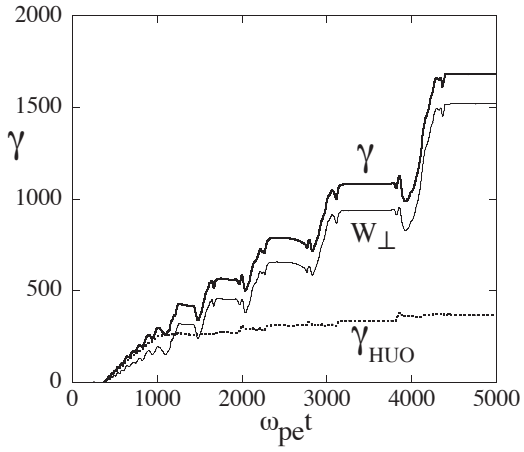

Figure 6.10: Time variation of γ of the positron in Fig. 6.9. Here, $\gamma_{\rm HUO}$ is small, while γ and $W_\perp$ exhibit similar time dependence. The change to the incessant acceleration occurs at $\omega_{pe}t \simeq 1000$, at which the deviation of the shock profile begins.

acceleration discussed in Sec. 4.2 begins.

Figure 6.11 shows the third, intermediate type. As in the previous two examples, the acceleration in Fig. 6.11 is nearly parallel to the magnetic field in the early phase. This particle, however, exhibits a curtate cycloid motion after the deformation of the shock profile. The magnitude of $v_\perp$ of this particle is between those of Figs. 6.6 and 6.9. Figure 6.12 shows that $W_\perp$ and $\gamma_{\rm HUO}$ noticeably increase, indicating that both $\boldsymbol{E}_\parallel$ and $\boldsymbol{E}_\perp$ significantly contribute to the energization.

We see from these results that positron acceleration is persistent. It can last for a long time in non-stationary wave propagation.

6.2.2 Dependence on plasma parameters

At the end of this chapter, we briefly mention how the acceleration depends on the propagation angle θ, and density ratio n_{p0}/n_{e0} [15].

Figure 6.13 shows the highest γ observed in simulations as a function of θ, where the shock speeds are taken to be $v_{\rm sh}/c \simeq 0.73$. Other parameters are the same as those for Figs. 6.4–6.12, whereas the simulation times, $\omega_{pe}t = 2400$, were nearly a half of theirs. We find the peak of γ near the dotted vertical line that shows the

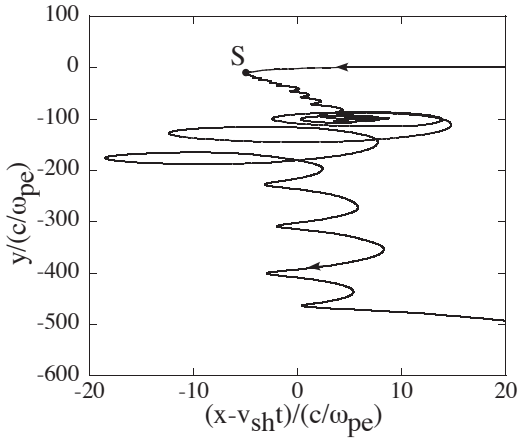

Figure 6.11: Orbit of an accelerated positron in the $(x - v_{\rm sh}t, y)$ plane. After the acceleration nearly along the magnetic field in the shock transition region, the orbit changes to a circular one owing to the deformation of the shock profile. The orbit then turns to a curtate cycloid.

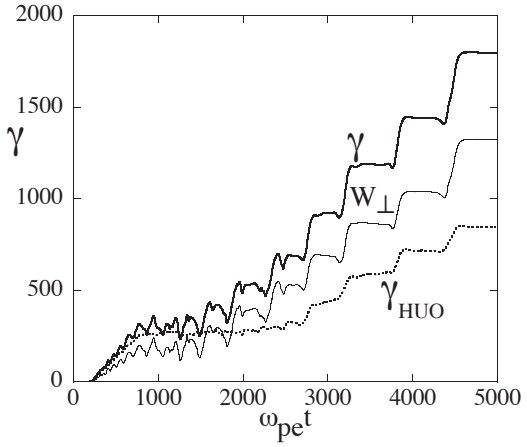

Figure 6.12: Time variation of γ of the positron in Fig. 6.11. Both perpendicular and parallel electric fields contribute to the energization.

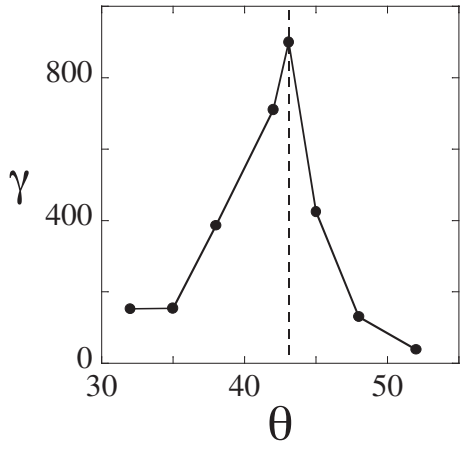

Figure 6.13: Dependence of γ on θ. The shock speed is fixed at $v_{\rm sh}/c \simeq 0.73$ for all the simulation runs. There is a peak near the dotted line at $v_{\rm sh} = c\cos\theta$.

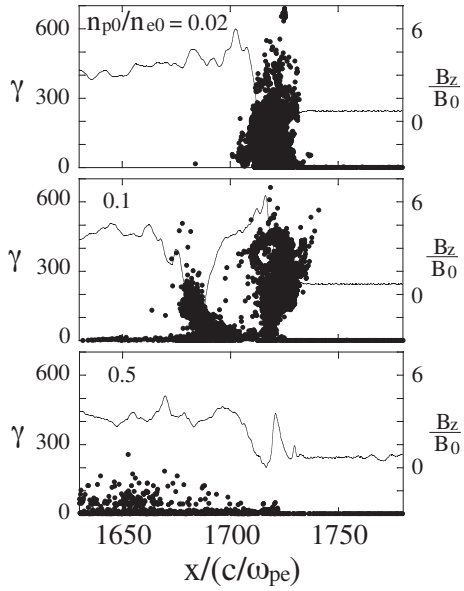

Figure 6.14: Positron phase spaces (x, γ) for $n_{p0}/n_{e0} = 0.02$, 0.1, and 0.5. Here, $v_{\rm A}/c = 0.301$, $v_{\rm sh}/c \simeq 0.73$, and $\theta = 42°$. As n_{p0}/n_{e0} increases, the acceleration becomes weaker.

angle with $v_{\rm sh} = c\cos\theta$; γ exceeds 100 in the range $30^\circ \lesssim \theta \lesssim 50^\circ$. Similarly, if we fix θ and $\boldsymbol{B}_0$ and observe the highest energy γ as a function of the shock speed $v_{\rm sh}$, which is altered by the shock amplitude, γ has a peak near the shock speed $v_{\rm sh} = c\cos\theta$.

This acceleration is strong in a plasma with a low positron-to-electron density ratio, as shown in Fig. 6.14, where the positron phase spaces (x, γ) near the shock front are depicted for three different density ratios: $n_{p0}/n_{e0} = 0.02$, 0.1, and 0.5. As the ratio n_{p0}/n_{e0} rises, the number of high-energy positrons and their highest energy both go down. This result was first found with simulations [15] and then explained by the theory for the parallel electric field in an EPI plasma [18, 23] described in Sec. 2.5: The parallel pseudo potential F becomes small and more nonstationary as n_{p0}/n_{e0} rises.

Bibliography

[1] P. A. Sturrock, Astrophys. J. **164**, 529 (1971).

[2] C. F. Kennel and F. V. Coroniti, Astrophys. J. **283**, 694 (1984).

[3] C. S. Reynolds, A. C. Fabian, A. Celotti, and M. J. Rees, Mon. Not. R. Astron. Soc. **283**, 873 (1996).

[4] K. Hirotani, S. Iguchi, M. Kimura, and K. Wajima, Publ. Astron. Soc. Japan **51**, 263 (1999).

[5] T. E. Cowan, M. D. Perry, M. H. Key *et al.*, Laser Particle Beams **17**, 773 (1999).

[6] C. F. Kennel and R. Pellat, J. Plasma Phys. **15**, 335 (1976).

[7] J.-I. Sakai and T. Kawata, J. Phys. Soc. Jpn. **49**, 753 (1980).

[8] M. Ashour-Abdalla, J. N. Leboeuf, T. Tajima, J. M. Dawson, and C. F. Kennel, Phys. Rev. A **23**, 1906 (1981).

[9] G. A. Stewart and E. W. Laing, J. Plasma Phys. **47**, 295 (1992).

[10] G. S. Lakhina and F. Verheest, Astrophys. Space Sci. **253**, 97 (1997).

[11] C. Joshi, B. Blue, E. Clayton, E. Dodd, C. Huang, *et al.*, Phys. Plasmas **9**, 1845 (2002).

[12] W. B. Mori, P. Muggli, R. Siemann, and D. Waltz, Phys. Rev. Lett. **90**, 214801 (2003).

[13] H. Hasegawa, S. Usami, and Y. Ohsawa, Phys. Plasmas **10**, 3455 (2003).

[14] S. Usami and Y. Ohsawa, Phys. Plasmas **11**, 3203 (2004).

[15] H. Hasegawa and Y. Ohsawa, Phys. Plasmas **12**, 012312 (2005).

[16] H. Hasegawa, K. Kato, and Y. Ohsawa, Phys. Plasmas **12**, 082306 (2005).

[17] T. Iwata, S. Takahashi, and Y. Ohsawa, Phys. Plasmas **19**, 022302 (2012).

[18] S. Takahashi, M. Sato, and Y. Ohsawa, Phys. Plasmas **15**, 082309 (2008).

[19] R. Z. Sagdeev and V. D. Shapiro, JETP Lett. **17**, 279 (1973).

[20] T. Katsouleas and J. M. Dawson, Phys. Rev. Lett. **51**, 392 (1983).

[21] Y. Ohsawa, Phys. Fluids **29**, 2474 (1986).

[22] S. Usami, R. Horiuchi, and Y. Ohsawa, Phys. Plasmas **16**, 122104 (2009).

[23] S. Takahashi and Y. Ohsawa, J. Plasma Fusion Res. Series **8**, 238 (2009).

Chapter 7

Wave evolution and particle acceleration behind a shock front

The previous chapters were concerned with the phenomena near a shock front. This final chapter studies wave evolution and particle acceleration in a much larger region.

Strong disturbances create shock waves and generate large-amplitude Alfvén waves behind them [1,2]. The plasma behind a shock front has a velocity $\boldsymbol{v}$ across the magnetic field and thus has nearly a constant electric field $\boldsymbol{E} = -\boldsymbol{v} \times \boldsymbol{B}/c$, in addition to $\boldsymbol{B}_0$ and wave fields. Furthermore, this region would have an alternating magnetic field if the amplitude of a generated Alfvén wave is greater than the magnitude of $\boldsymbol{B}_0$.

These circumstances can give rise to particle acceleration in the Alfvén wave region with mechanisms different from those near a shock front [2]. Three types of such acceleration have been found: type 1 in which particles move along a pulse with an intense magnetic field [3], type 2 in which particles meander along a moving magnetic neutral sheet [4,5], and type 3 in which particles traverse the Alfvén wave region with an alternating magnetic field [1,2]. Ultrarelativistic electron acceleration caused by these mechanisms has been demonstrated with particle simulations. These mechanisms differ from that of trapped electrons described in Chap. 3 in that

1) they do not require the condition $v_{\rm sh} \sim c\cos\theta$, and

2) they can work in weak magnetic fields such that $|\Omega_e| < \omega_{pe}$ as well as in strong ones.

In addition, unlike the mechanisms described in Chapters 3 to 6, many of the electrons that gain energy in the Alfvén wave are supplied from the downstream region.

7.1 Electron acceleration due to a compressive pulse

Type 1 acceleration was first found near a small compressive pulse generated in a shock wave [3]. Here, the term "compressive pulse" means fluctuations in which the magnetic field and plasma density are higher than outside. Such pulses can be occasionally generated by, for instance, a strong deformation of shock profile [6] due to the ion reflection discussed in Sec. 4.1. A few years later, simulations with a larger system size revealed that type 1 can also take place in the Alfvén wave region behind a shock front [1, 2]. It has been thus recognized that type 1 operates in more general circumstances than had initially been thought. Before studying the acceleration in Alfvén waves, which accompanies several complicated processes, we investigate in this section the mechanism of electron acceleration caused by a compressive pulse. Since types 2 and 3 are related to this mechanism, we describe this process in some detail.

7.1.1 Theoretical considerations

Before making a theoretical analysis, we present a simulation result showing electron acceleration due to a compressive pulse behind a shock front: Figure 7.1 displays field profiles and electron phase space (x, γ) near the pulse [3]. Here, the center of the pulse is at $(x - v_{\rm cp}t)/(c/\omega_{pe}) = 0$, where $v_{\rm cp}$ is the speed of the compressive pulse. There are many high-energy electrons on the left side of the pulse; clearly, they were not produced near the shock front at $(x - v_{\rm cp}t)/(c/\omega_{pe}) \simeq 34$ at this moment ($\omega_{pe}t = 800$); this position is out of this figure. It is also noteworthy

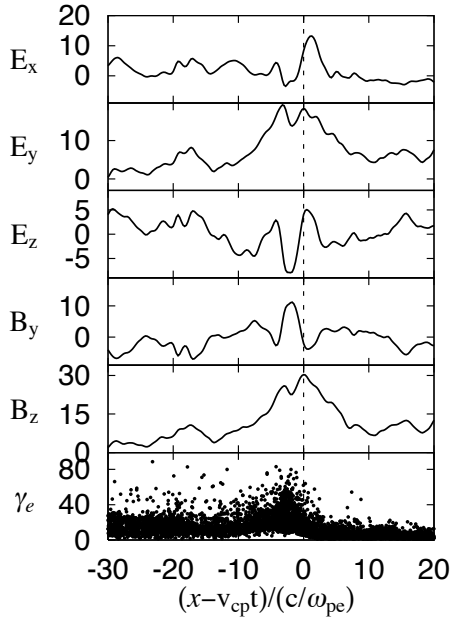

Figure 7.1: Snapshots of field profiles and electron phase space (x, γ) near a small compressive pulse behind a shock front. The field values are normalized to B_{z0}. The shock propagation angle is $\theta = 60^\circ$ and the field strength is $|\Omega_e|/\omega_{pe} = 0.4$.

that the transverse electric field E_y is present outside the compressive pulse as well as inside it, which is because the pulse is behind the shock front. Particle motions in this simulation are shown in Sec. 7.1.2, after the theoretical discussion below.

In the light of the above simulation result, we analyze particle motions near a compressive pulse behind a shock front in the perpendicular case, $\boldsymbol{B}_0 = (0, 0, B_{z0})$; extension to the oblique case is straightforward [1]. The shock wave and compressive pulse are both supposed to propagate in the x direction.

The x component of the $\boldsymbol{E} \times \boldsymbol{B}$ drift velocity is then

$$v_{dx}(x) = c\frac{E_y(x)}{B_z(x)}. \tag{7.1}$$

Since E_y and B_z are both positive, v_{dx} is also positive. With use of the relation

$$E_y(x) = \frac{v_{\rm sh}}{c}[B_z(x) - B_{z0}], \tag{7.2}$$

which is obtained from Faraday's law for a stationary wave, Eq. (7.1) can be written

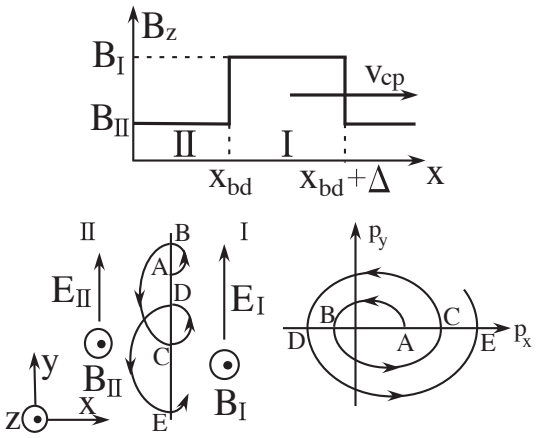

Figure 7.2: Schematic diagram of a compressive pulse behind a shock front and electron orbits in the (x, y) and (p_x, p_y) planes. In the configuration space, the particle moves along the rear boundary of the pulse; points A to E are on the rear boundary. In the (p_x, p_y) plane, its orbit is an outward elliptic spiral.

as

$$v_{dx}(x) = v_{\rm sh}\left(1 - \frac{B_{z0}}{B_z(x)}\right). \tag{7.3}$$

[Strictly speaking, this system is not perfectly stationary, because the shock wave and compressive pulse have different propagation speeds. Equation (7.2) should be viewed as an approximate relation near the small compressive pulse.] Since B_z behind the shock front is greater than B_{z0}, v_{dx} is in the range $0 < v_{dx} < v_{\rm sh}$; electrons move to the downstream region of the shock wave.

If there is a compressive pulse with its speed lower than $v_{dx}(x)$, then electrons would enter the pulse from its rear (left) edge. They would stay near the rear edge for some periods of time because the high magnetic field in the pulse prevents them from quickly passing through the pulse region.

We consider these particle motions assuming that their gyroradii are greater than the pulse width. For simplicity, we take the shape of the compressive pulse to be rectangular with a width Δ (Fig. 7.2); the x position of its left boundary is denoted by $x_{\rm bd}$. Accordingly, the electric and magnetic fields are constant and may be written as $\boldsymbol{E}_{\rm I} = (0, E_{\rm I}, 0)$ and $\boldsymbol{B}_{\rm I} = (0, 0, B_{\rm I})$ in the pulse region, $x_{\rm bd} < x < x_{\rm bd} + \Delta$, and $\boldsymbol{E}_{\rm II} = (0, E_{\rm II}, 0)$ and $\boldsymbol{B}_{\rm II} = (0, 0, B_{\rm II})$ behind the pulse, $x < x_{\rm bd}$.

The fields are stronger inside the pulse than outside: $E_{\rm I} > E_{\rm II}$ and $B_{\rm I} > B_{\rm II}$. Although E_x will also be present near the boundaries of the pulse, it does not play an important role here and is ignored.

When an electron is inside the pulse, $x_{\rm bd} < x < x_{\rm bd} + \Delta$, it moves in an ellipse in the momentum space (see Appendix J). Its orbit may be expressed as

$$\frac{(p_x - P_{\rm I})^2}{a_{\rm I}^2} + \frac{p_y^2}{(a_{\rm I}/\gamma_{\rm dI})^2} = 1, \tag{7.4}$$

where $\gamma_{\rm dI} = (1 - v_{\rm dI}^2/c^2)^{-1/2}$ with

$$v_{\rm dI} = c\frac{E_{\rm I}}{B_{\rm I}}. \tag{7.5}$$

The quantities $P_{\rm I}$ and $a_{\rm I}$ are functions of $v_{\rm dI}$ and gyration speed and are given by Eqs. (J.7) and (J.8), respectively, in Appendix J, where it is proved that $P_{\rm I}$ and $a_{\rm I}^2$ are both positive. We take $a_{\rm I}$ to be positive. Because of the drift $v_{\rm dI}$ in the x direction, the center of p_x is shifted by $P_{\rm I}$ from the origin.

Behind the compressive pulse, $x < x_{\rm bd}$, electrons also make elliptic motions in the momentum space,

$$\frac{(p_x - P_{\rm II})^2}{a_{\rm II}^2} + \frac{p_y^2}{(a_{\rm II}/\gamma_{\rm dII})^2} = 1, \tag{7.6}$$

where $P_{\rm II}$ and $a_{\rm II}^2$ are given by Eqs. (J.9) and (J.10), and with use of the drift speed

$$v_{\rm dII} = c\frac{E_{\rm II}}{B_{\rm II}}, \tag{7.7}$$

$\gamma_{\rm dII}$ is defined as $\gamma_{\rm dII} = (1 - v_{\rm dII}^2/c^2)^{-1/2}$.

As an electron moves from the inside to the outside, crossing the rear boundary of the pulse, the elliptic motion in the momentum space changes from the one represented by Eq. (7.4) to the one by Eq. (7.6). When the electron returns to the pulse region, the ellipse center and radius change again.

The electron shown in the lower left picture in Fig. 7.2 goes out from the pulse crossing the rear boundary $x = x_{\rm bd}$ at point B, and, after a half gyroperiod, goes into the pulse at point C: The vertical line on which points A–F are located

represents the rear boundary. Because $E_y > 0$, the electron gains energy during the motion B→C. It absorbs the greatest amount of energy, i.e., the shift in the y direction $|y(\mathrm{C}) - y(\mathrm{B})|$ becomes the largest, in the situation that the orbit crosses the rear boundary $x = x_{\mathrm{bd}}$ at right angles, for which $p_y(\mathrm{B})$ and $p_y(\mathrm{C})$ are both zero.

At point B, the center of the ellipse is shifted along the p_x axis by

$$\Delta P(t_0) = P_{\mathrm{II}}(t_0) - P_{\mathrm{I}}(t_0), \tag{7.8}$$

where t_0 is the time at point B. As proved in Appendix J, the shift is positive,

$$\Delta P(t_0) > 0, \tag{7.9}$$

if $v_{\mathrm{dI}} - v_{\mathrm{dII}} < 0$. One can also calculate the shift of the ellipse center occurring at point C at $t = t_1$: $\Delta P(t_1) = P_{\mathrm{I}}(t_1) - P_{\mathrm{II}}(t_1)$, which is negative if $v_{\mathrm{dI}} - v_{\mathrm{dII}} < 0$.

Since we know the equations for the ellipses, we can find the momenta and thus energies at points B, C, D, $\cdots$, if the momentum at point A is given. Because P_{II} is the center of p_x and a_{II} is the radius along the p_x axis, the momentum at point C is given as a function of $p_x(t_0)$ as

$$p_x(t_1) = P_{\mathrm{II}}[p_x(t_0)] + a_{\mathrm{II}}[p_x(t_0)]. \tag{7.10}$$

Similarly, the momentum at point D at $t = t_2$ is given as a function of $p_x(t_1)$,

$$p_x(t_2) = P_{\mathrm{I}}[p_x(t_1)] - a_{\mathrm{I}}[p_x(t_1)]. \tag{7.11}$$

In this way, we can successively obtain the momentum at the l-th crossing ($l = 1, 2, 3, \cdots$) from $p_x(t_0)$.

For $\gamma \gg 1$ with

$$\gamma(t_0) \sim -p_x(t_0)/(m_e c), \tag{7.12}$$

i.e., $p_x(t_0)$ is much greater than p_y and p_z in magnitude, we can put Eq. (7.10) into the following form:

$$\gamma(t_1) \sim \frac{1 + E_{\mathrm{II}}/B_{\mathrm{II}}}{1 - E_{\mathrm{II}}/B_{\mathrm{II}}}\gamma(t_0). \tag{7.13}$$

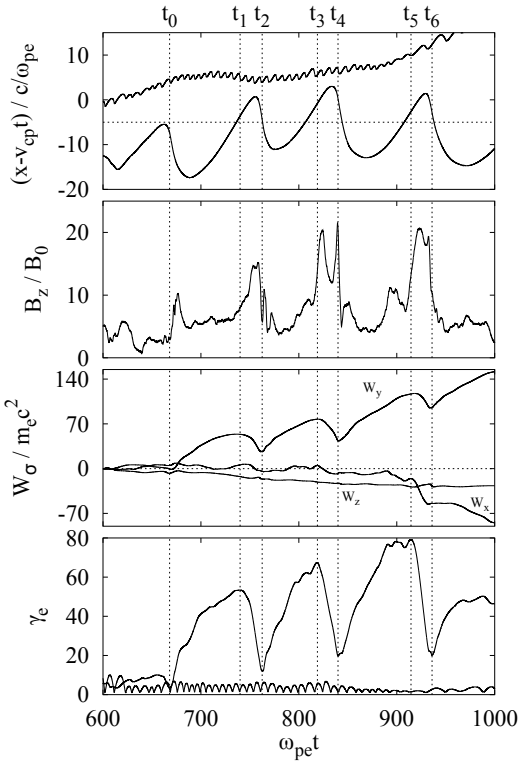

Figure 7.3: Time variations of x, B_z, W_σ, and γ of an accelerated electron. Here, $B_z[x(t)]$ is the magnetic field at the position of the electron, and W_σ is the work done by the electric field E_σ ($\sigma = x,\ y,$ or z). For comparison, the time variations of x and γ of a non-accelerated electron with a much shorter gyroperiod are also plotted.

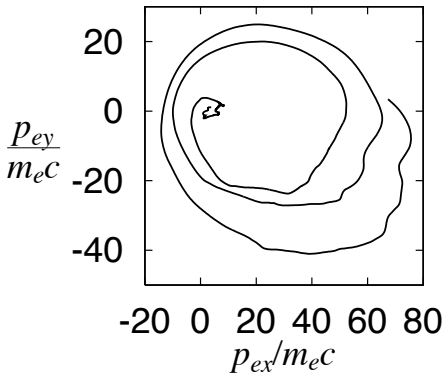

Figure 7.4: Trajectory of the accelerated electron in the (p_x, p_y) plane. The orbit is an outward elliptic spiral.

If $E_{\rm II}/B_{\rm II}$ is close to unity behind the pulse, $\gamma(t_1)$ should become significantly greater than $\gamma(t_0)$. In addition, because $\gamma(t_1)$ is proportional to $\gamma(t_0)$, we see that the energy increment can be huge for high-energy particles in this mechanism. For $\gamma(t_2)$, we find that

$$\gamma(t_2) \sim \frac{1 - E_{\rm I}/B_{\rm I}}{1 + E_{\rm I}/B_{\rm I}}\gamma(t_1). \tag{7.14}$$

Equations (7.13) and (7.14) also hold in the oblique case if the magnitude of p_z remains small; in which $E_{\rm I}$ and $E_{\rm II}$ are the y components and $B_{\rm I}$ and $B_{\rm II}$ are the strengths of $\boldsymbol{B}$ [3]. Particles with their v_x [$\simeq c(\boldsymbol{E} \times \boldsymbol{B}/B^2)_x + v_\parallel B_{x0}/B$] close to the pulse speed can undergo this process. Another interesting and important point is that, also in the oblique case, the high magnetic field in the compressive pulse prevents the particles that have caught up with the pulse from passing through it. It is because the parallel momentum $p_\parallel = (\boldsymbol{p} \cdot \boldsymbol{B})/B$ of the particle gyrating near the rear edge of the pulse decreases, owing to the mechanism described in Sec. 4.2.1. The high magnetic field acts to make these particles stay near the pulse for long periods of time.

7.1.2 Observed particle motions

We now examine simulation results. Plotted in the top panel of Fig. 7.3 is the time variation of $(x - v_{\rm cp}t)$ of an electron energized by a compressive pulse with a propagation speed $v_{\rm cp}$: Field profiles and phase space (x, γ) near this pulse were shown in Fig. 7.1. Here, the center of the pulse is at $(x - v_{\rm cp}t)/(c/\omega_{pe}) = 0$ and the dotted horizontal line indicates the rear edge of the pulse, $(x - v_{\rm cp}t)/(c/\omega_{pe}) = -5$. After catching up with the pulse, this particle stays near the back slope of the pulse for some period because of the high magnetic field in the compressive pulse. The second, third, and fourth panels display, respectively, the time variation of B_z as seen by this particle; the work done by the electric field,

$$W_\sigma = -e \int E_\sigma v_\sigma dt, \tag{7.15}$$

with $\sigma = x, y$, or z; and the Lorentz factor γ of this particle. When the particle is in the pulse, $B_z[x(t)]$ is high and γ goes down. On the other hand, when the

particle is outside the pulse, B_z is low and γ rises. The variations of W_y and γ are quite similar, indicating that the particle absorbs energy mainly from E_y. The lines with a short-period oscillation in the top and bottom panels represent an electron that did not suffer energization.

Figure 7.4 shows the orbit of this particle projected on the (p_x, p_y) plane. The orbit is an elliptic spiral, with its radius growing with time.

Even though the theory described in Sec. 7.1.1 is based on the simplified model (for instance, we have used rectangular field profiles in the calculation of particle motion), its predictions are consistent with these simulation results.

7.2 Acceleration around a moving neutral sheet

Type 2 acceleration was first found with a simulation for a collision of a shock wave and a magnetic neutral sheet [4,5]. If a shock wave propagates crossing a magnetic neutral sheet, at which the magnetic polarity changes, the sheet begins to move following the shock front. Unlike the ordinary, static, field-reversed configuration [7], the moving neutral sheet has transverse electric fields on both sides of the sheet because $\partial \boldsymbol{B}/\partial t \neq 0$. These fields can energize particles meandering along the sheet. Figure 7.5 illustrates the magnetic-field profile of a moving magnetic neutral sheet and orbits of an accelerated particle in it; this model was used in the theory in Ref. [4] and will be compared with simulation results. The sign of the magnetic field changes ($B_{\rm I}B_{\rm II} < 0$) at the neutral sheet $x = x_{\rm bd}$, which is propagating with a speed $v_{\rm np}$ behind a shock front. The particle is moving in the negative y direction along the sheet, absorbing energy from the transverse electric field. When the particle crosses the neutral sheet, the direction of the orbit sharply changes at $p_y \simeq 0$ in the momentum space; as a result, the momentum trajectory is in the lower-half plane. Despite the fact that the field structure and particle motion in the field-reversed pulse are completely different from those in the compressive pulse, the increment of kinetic energy in this process is given by the same equations as those in the compressive pulse [4,5]: Eqs. (7.13) and (7.14). A few years after

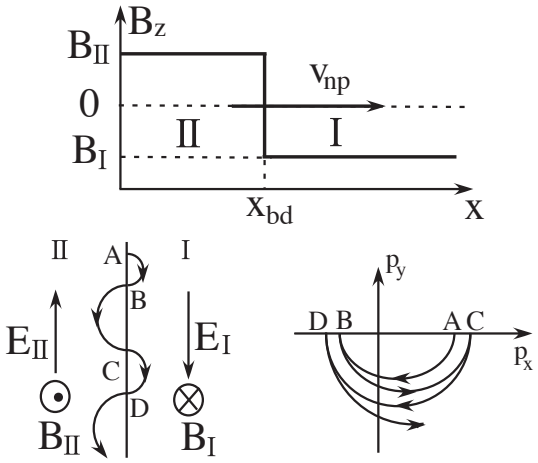

Figure 7.5: Schematic diagram of moving magnetic neutral sheet behind a shock front and electron orbits in the (x, y) and (p_x, p_y) planes. Here, $v_{\rm np}$ is the speed of the pulse containing the neutral sheet. In the configuration space, the particle goes in the negative y direction, meandering along the moving neutral sheet. The direction of the momentum abruptly changes at $p_y \simeq 0$ in the momentum space; therefore, the orbit is in the lower-half plane.

these studies, type 2 acceleration was also found in large-amplitude Alfvén waves behind a shock front [1, 2].

We now show some results of a simulation [4] in which a shock wave collides with an initially static, magnetic neutral sheet: Plotted in Fig. 7.6 are the time variations of W_σ, which is the work done by E_σ, $B_z[x(t)]$, and γ of an electron energized near a moving neutral sheet. The energy γ increases when $B_z[x(t)]$ is positive, i.e., when the particle is in region II in Fig. 7.5. This particle gains energy mainly from E_y, which we see from the fact that W_y and γ have similar time profiles. Figure 7.7 displays the orbits of this particle. In the (x, y) plane, this particle exhibits a meandering orbit, moving along the neutral sheet. The trajectory in the momentum space lies in the lower-half plane, with its direction rapidly changing near $p_y = 0$. Figures 7.6 and 7.7 are consistent with Fig. 7.5.

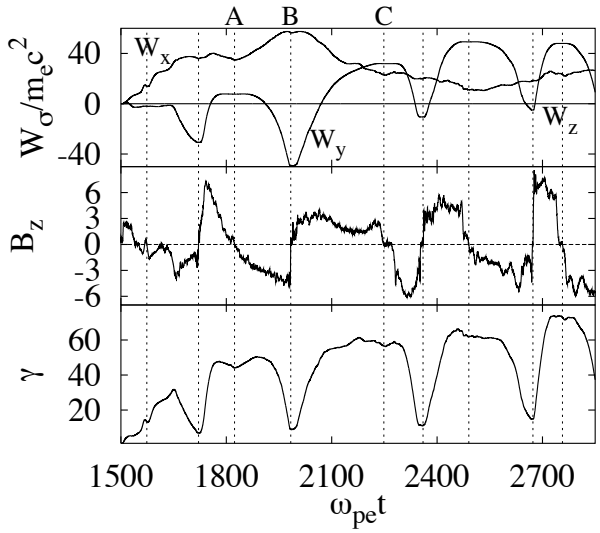

Figure 7.6: Time variations of W_σ, B_z, and γ of an electron accelerated near a moving neutral sheet. The energy increases when the particle is in the region with $B_z > 0$. The quantities W_y and γ have similar time profiles.

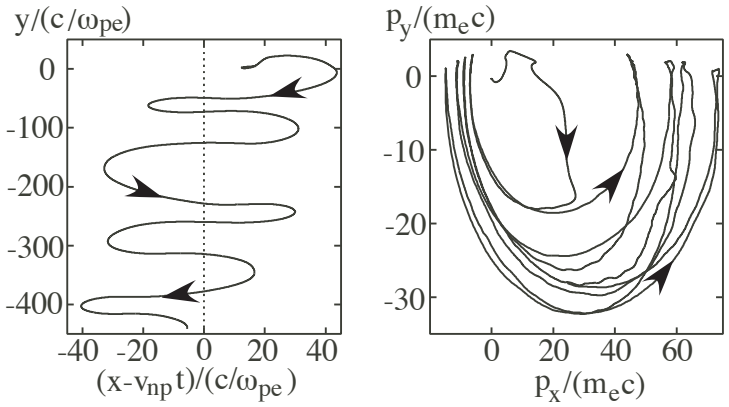

Figure 7.7: Orbits of the accelerated electron in the $(x - v_{\rm np}t, y)$ and (p_x, p_y) planes. The dotted vertical line in the left panel indicates the magnetic neutral sheet. These orbits resemble the ones in Fig. 7.5.

7.3 Alfvén waves and particle acceleration behind a shock front

Strong disturbances can generate Alfvén waves behind magnetosonic shock fronts. In this section, we investigate wave evolution and particle acceleration in such circumstances. Before doing that, however, we make a short mention of the motion of bulk particles arising from a plasma disturbance.

7.3.1 Motions of bulk particles

Figure 7.8 presents a result of a simulation [8] in which a high-density plasma (exploding plasma) collides with a low-density plasma (surrounding plasma) in an external magnetic field in the z direction (Fig. 3.1); the initial macroscopic velocity $\boldsymbol{v}_0$ of the exploding plasma is in the positive x direction whereas that of the surrounding plasma is zero. The speed of the exploding plasma, $v_0/(\omega_{pe}\Delta_g) = 2.05$, is much higher than the Alfvén speed, $v_{\rm A}/(\omega_{pe}\Delta_g) = 0.04$, and the linear magnetosonic speed, $v_{p0}/(\omega_{pe}\Delta_g) = 0.18$. Other parameters are as follows: The total system length is $L = 16,384\Delta_g$; $m_i/m_e = 100$, $c/(\omega_{pe}\Delta_g) = 4$, and $|\Omega_e|/\omega_{pe} = 0.1$. The top and middle panels of Fig. 7.8 display the (x, t) diagrams of exploding and surrounding ions, respectively, and the bottom panel shows electron trajectories. Here, x_{iSb} (thick dotted lines) and x_{iEb} (thick solid lines) are, respectively, the trajectories of the surrounding and exploding ions that were initially at the boundary of the two plasmas, $x = b$; for comparison, they are plotted in all the panels. From the top and middle panels we see that the surrounding ions begin to move upon the passage of the exploding ions. Although x_{iEb} goes faster than x_{iSb} in the early phase, x_{iSb} is quickly accelerated; moreover, x_{iEb} moves backward around the time $\Omega_{i0}t = 2$, where Ω_{i0} is the nonrelativistic ion gyrofrequency calculated with use of the external magnetic field strength. Thus, x_{iSb} passes $x_{iEb}(t)$ at $\Omega_{i0}t = 2.1$. The exploding electrons (solid lines) in the bottom panel do not pass the surrounding electrons (dotted lines), indicating that the two groups of electrons are not mixed: The width of the boundary layer is of the order of the electron gyroradius. Their

boundary x_{eb}, which is represented by the thick dashed-and-dotted line, is between x_{iSb} and x_{iEb} for $\Omega_{i0}t \lesssim 2$. After $\Omega_{i0}t \simeq 1$, on both sides of the boundary x_{eb}, we find regions where electron and ion trajectories are concentrated. These two regions gradually move away from each other. These are shock waves; one propagating forward in the surrounding plasma away from x_{eb} and the other backward relative to its background (exploding) plasma.

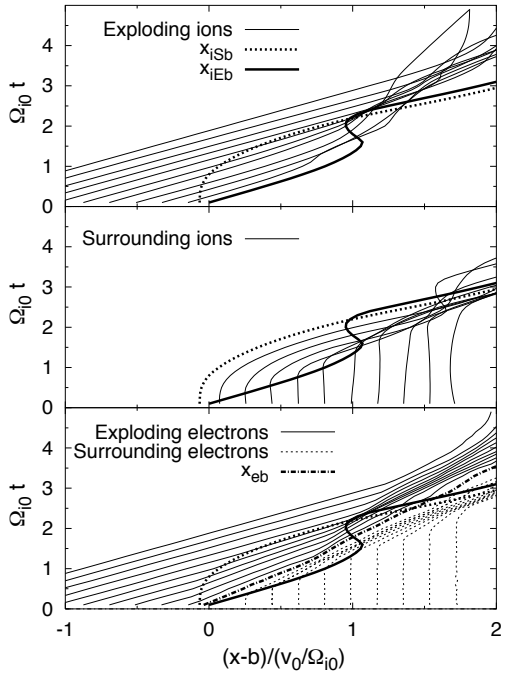

Figure 7.8: Ion and electron trajectories in a collision of exploding and surrounding plasmas. The top, middle, and bottom panels show, respectively, exploding ions, surrounding ions, and electrons. The thick solid and dotted lines indicate $x_{iEb}(t)$ and $x_{iSb}(t)$, respectively. The dash-dotted line $x_{eb}(t)$ in the bottom panel represents the boundary of the two groups of electrons.

The physical processes of these phenomena may be summarized as follows. The cross-field motion of the exploding plasma induces strong E_y, with its velocity v_x being nearly equal to the $E_y \times B_z$ drift speed: We can view the ions as unmagnetized and the electrons as magnetized in the early phase. This E_y accelerates the

surrounding ions behind x_{iEb} in the y direction in the very early phase, $\Omega_{i0}t \ll 1$. This velocity is gradually converted to v_x owing to the magnetic force; these surrounding ions thus begin to move in the x direction with their final speed close to that of the exploding ions. The magnetic field causes the oscillation of x_{iEb}; when x_{iEb} is significantly slowed down for the first time, $\Omega_{i0}t = 1 \sim 2$, the compression of magnetic-field lines near the front of the exploding ions is particularly enhanced. The compression of field lines results in the formation of shock waves, which will also be discussed in the next section.

As the angle θ decreases, the velocity component parallel to $\boldsymbol{B}$ becomes important [9]. Because of the parallel velocity $v_{\parallel}$, the two groups of electrons are more easily mixed. The amplitude of the oscillation of x_{iEb} and the acceleration of x_{iSb} both decrease with decreasing θ; Ref. [9] shows that x_{iSb} does not catch up with x_{iEb} for $\theta < 65°$. The region where the exploding and surrounding ions are overlapping, $x_{iSb} \lesssim x \lesssim x_{iEb}$, expands with time.

Alfvén waves have been observed in the ion overlapping region in oblique shock simulations. Furthermore, rapid acceleration of electrons caused by these Alfvén waves has also been reported [1, 2]; these mechanisms can be understood by extending the theory for the compressive pulses and moving neutral sheets discussed in Sections 7.1 and 7.2. In the next section, we examine these simulation results.

7.3.2 Evolution of waves and phase spaces

To observe the evolution of several kinds of waves with different propagation speeds in a simulation, we take the total system length to be long, $L = 32,768\Delta_{\rm g}$ [2]. Initially, the plasma in the region $800\Delta_{\rm g} < x < 10,400\Delta_{\rm g}$ (exploding plasma) has a density twice as high as that in the region $10,440\Delta_{\rm g} < x < 31,968\Delta_{\rm g}$ (surrounding plasma). The angle between $\boldsymbol{B}_0$ and the x axis is $\theta = 30°$. The exploding plasma has an initial velocity $\boldsymbol{v}_0$ perpendicular to $\boldsymbol{B}_0$ ($\theta_v = 90°$) with $v_0/c = 0.98$ while the surrounding plasma is at rest (Fig. 2.1). Some other important parameters are $m_i/m_e = 400$, $v_{Ti}/(\omega_{pe}\Delta_{\rm g}) = 2.9\times10^{-2}$, $v_{Te}/(\omega_{pe}\Delta_{\rm g}) = 5.8\times10^{-1}$, $c/(\omega_{pe}\Delta_{\rm g}) = 10$,

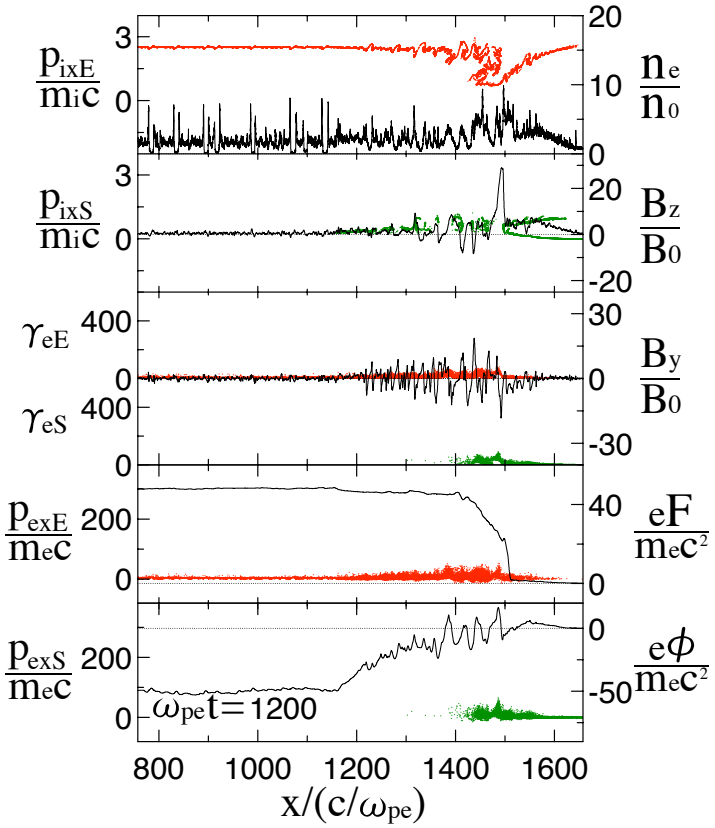

Figure 7.9: Snapshots of phase spaces and field profiles in the early phase. Here, p_{ixE} is the x component of the momentum of the exploding ions, while p_{ixS} is the momentum of the surrounding ions. The SMF pulse is developing near $x/(c/\omega_{pe}) = 1500$, reflecting exploding ions to the left and surrounding ions to the right. Around there, we find growing magnetic perturbations and turbulent structure in the ion phase spaces [2].

$|\Omega_e|/\omega_{pe} = 0.4$; hence, the Alfvén speed is $v_{\rm A}/(\omega_{pe}\Delta_{\rm g}) = 0.200$. The speed of the linear magnetosonic wave is $v_{p0}/(\omega_{pe}\Delta_{\rm g}) = 0.202$ for $\theta = 30°$. We can produce strong shock waves if we make the density of the exploding plasma high, its volume large, or its initial speed v_0 high.

A collision of two plasmas generates large-amplitude density and field perturbations, which evolve into shock waves and Alfvén waves. We first sketch the overall picture of plasma behavior in such circumstances. The field structures are much more complicated in the oblique case than in the perpendicular case ($\theta = 90°$) in

which Alfvén waves do not appear.

Phase spaces and field profiles

Figure 7.9 displays ion and electron phase spaces and field profiles in the early phase ($\omega_{pe}t = 1200$) of a simulation run. (To depict phase spaces, we have used 1/20 of the particles.) The fields F (fourth panel) and ϕ (bottom panel) are the parallel pseudo potential, Eq. (2.178), and electric potential, respectively. The subscripts E and S denote exploding and surrounding plasmas, respectively. Near $x/(c/\omega_{pe}) = 1500$ in the second panel, there is a strong-magnetic-field (SMF) pulse, which is created near the boundary of the colliding two plasmas through the compression of magnetic field lines. Some surrounding ions are reflected there to the right (second panel) and exploding ions to the left (top panel). These ion motions lead to the formation of forward and backward shock waves [8, 9]. Near the SMF pulse, magnetic perturbations are growing and the ion phase spaces are turbulent. As shown in the third panel, electron energies are still much lower than $\gamma = 100$ at this moment.

Because v_0 is large and $\boldsymbol{B}_0$ is rather weak, exploding ions penetrate deep into the surrounding plasma, creating a region where exploding and surrounding ions coexist. Counter-streaming instabilities become unstable in this region: We find small-amplitude, short-wavelength perturbations in the density profile in Fig. 7.9. However, the instabilities grow only in the early phase ($\omega_{pe}t \lesssim 700$), quickly saturated with small amplitudes. The details of the instabilities are described in Refs. [8, 9].

Shock waves have formed and ultrarelativistic electrons have been created in the Alfvén wave region in Fig. 7.10 ($\omega_{pe}t = 2600$). The forward and backward shock fronts are at $x/(c/\omega_{pe}) = 2180$ and at $x/(c/\omega_{pe}) = 1900$, respectively. Because the initial density of the exploding plasma is higher than that of the surrounding one, the forward shock wave is stronger than the backward one. In the region $1650 \lesssim x/(c/\omega_{pe}) \lesssim 2100$ behind the forward shock front, there are Alfvén waves (including the SMF pulse); their amplitudes are still growing, and their wave-

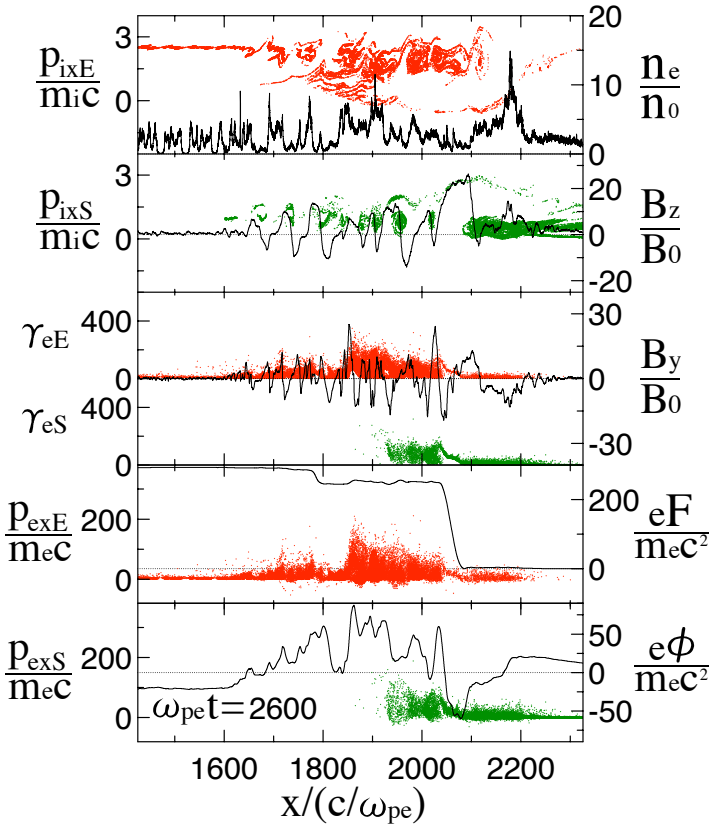

Figure 7.10: Snapshots of phase spaces and field profiles. The forward and backward shock fronts are at $x/(c/\omega_{pe}) = 2180$ and at $x/(c/\omega_{pe}) = 1900$, respectively. In the region where Alfvén waves are forming, $1650 \lesssim x/(c/\omega_{pe}) \lesssim 2100$, ultrarelativistic electrons are present. The parallel pseudo potential F sharply rises near the SMF pulse, indicating that a strong $E_\parallel$ is created there at this moment [2].

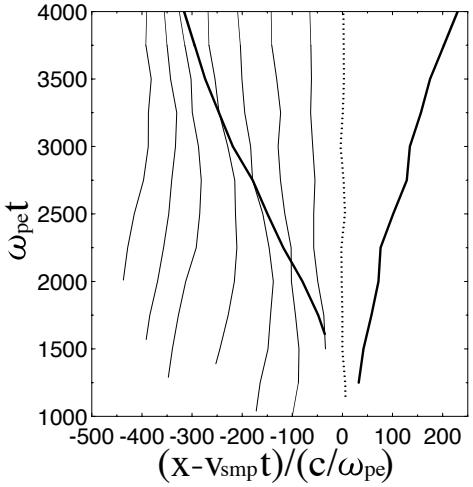

Figure 7.11: Trajectories of shock fronts and Alfvén waves. The quantity $v_{\rm smp}$ in the horizontal axis is the speed of the SMF pulse. The right and left thick lines represent forward and backward shock fronts, respectively. The dotted and thin solid lines denote the SMF pulse and Alfvén waves, respectively [2].

lengths are increasing. Furthermore, many reflected exploding ions are present there; accordingly, the momentum distribution of the exploding ions has greatly broadened. In addition, we find vortices in the phase space of the surrounding ions. These imply that the ion kinetic motions affect the evolution of the Alfvén waves. Electron energies in this region have reached $\gamma = 300$ by this time. The plasma density is rather low in the SMF pulse, $2020 \lesssim x/(c/\omega_{pe}) \lesssim 2100$. The magnitude of the parallel pseudo potential, which is highly nonstationary, is quite large, $eF/(m_e c^2) \sim 200$, in the SMF pulse at this moment, indicating that a strong parallel electric field $E_\parallel$ is created there.

Wave trajectories

Shock waves propagate much faster than other low-frequency waves, as shown in Fig. 7.11. Here, the trajectories of the forward and backward shock fronts are plotted by the thick solid lines; the speed of the former is $v_{\rm sh} \sim 24 v_{p0}$ and that of the latter is $v'_{\rm sh} \sim 14 v_{p0}$ in the laboratory frame. On the other hand, the speed of the backward shock wave relative to the flow speed $\langle v'_{\rm fl} \rangle$ of its upstream

plasma is $v'_{\rm sh} - \langle v'_{\rm fl}\rangle = -4.2v_{p0}$; here, $\langle v'_{\rm fl}\rangle$ is the average fluid speed in the region $x'_{\rm sh}/(c/\omega_{pe}) - 20 < x/(c/\omega_{pe}) < x'_{\rm sh}/(c/\omega_{pe})$, where $x'_{\rm sh}$ is the x position at which n_e of the backward shock wave begins to sharply rise. (The upstream region of the backward shock wave is $x < x'_{\rm sh}$.)

The SMF pulse (dotted line) is between the two shock fronts. Its speed is of the order of the Alfvén speed, $v_{\rm smp} - \langle v_{\rm fl}\rangle = (0.6 \pm 2.7)v_{\rm A}\cos\theta$, where $v_{\rm smp} - \langle v_{\rm fl}\rangle$ is the average plasma flow velocity near the pulse and $\sigma = 2.7v_{\rm A}\cos\theta$ represents the standard deviation of the observed values of $v_{\rm fl}(x,t)$. Electromagnetic pulses behind the SMF pulse are shown by the thin solid lines. Their propagation speeds are approximately equal to that of the SMF pulse.

From the simulation results that the speeds are close to $v_{\rm A}\cos\theta$ and that the density perturbations are rather small, these electromagnetic perturbations (including the SMF pulse) are identified as the Alfvén wave [10]- [17].

7.3.3 Electron acceleration due to Alfvén waves

Figure 7.12 illustrates three types of ultrarelativistic electron acceleration observed in the Alfvén wave region behind a shock front. Type 1 shown in the top panel is the same as the mechanism caused by the compressive pulse discussed in Sec. 7.1. This process is found near the back slope of the SMF pulse. Both the SMF and compressive pulses have a magnetic-field bump, which is an essential pulse character for this mechanism; the density profile is unimportant. Type 2 in the middle panel is the same as the mechanism caused by the moving magnetic neutral sheet discussed in Sec. 7.2. As shown in Fig. 7.10, the signs of B_z and B_y change with x in the large-amplitude Alfvén wave, indicating the presence of moving magnetic neutral sheets. Particles meandering along these sheets can suffer Type 2 acceleration. Type 3 acceleration occurs in particles traversing the region with an alternating magnetic field. An important point here is that the plasma behind a shock front is moving across a magnetic field and thus has an electric field $E_y \simeq -(\boldsymbol{v}\times\boldsymbol{B}/c)_y$, as well as wave fields. Particles can absorb energy from this field.

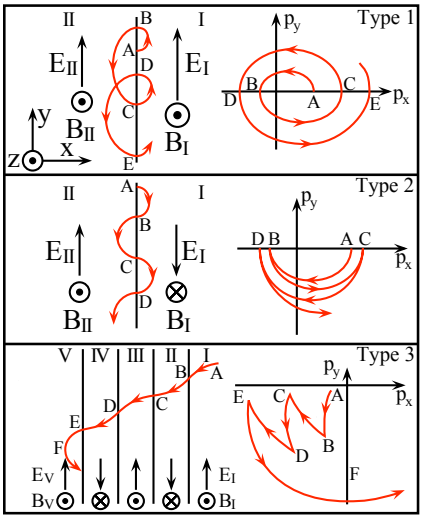

Figure 7.12: Schematic diagram of three types of acceleration occurring in the Alfvén wave region behind a shock front. The left and right pictures show the orbits in the configuration and momentum spaces, respectively. Type 1 (top panel) takes place in the back slope of an SMF pulse. Type 2 (middle panel) is found around a moving magnetic neutral sheet. Particles traversing the region of an alternating magnetic field can exhibit the orbit of type 3 (bottom panel) [2].

Particles can experience multiple energization processes. The motion of a particle that suffers the three types of acceleration is reported in Ref. [1].

We now look at particle motions observed in the simulation of Figs. 7.9–7.11.

The red line in the upper left panel in Fig. 7.13 shows the time variation of the x position of an accelerated electron relative to the SMF pulse, $x - v_{\rm smp}t$. The other lines are the wave trajectories same as those in Fig. 7.11 although the vertical and horizontal axes have been exchanged; i.e., the two thick lines represent shock fronts, and the dotted and thin solid lines are the SMF pulse and Alfvén waves, respectively. This particle enters the shock wave from the upstream region and, at point B ($\omega_{pe}t = 1610$), begins to move in the negative y direction along the SMF pulse. This motion leads to the rapid growth of γ, as shown by the lower left panel. The orbits B→E in the $(x - v_{\rm smp}t, y)$ and (p_x, p_y) planes resemble those in type 1 in Fig. 7.12.

The particle in Fig. 7.14 is initially behind the Alfvén wave region. It catches

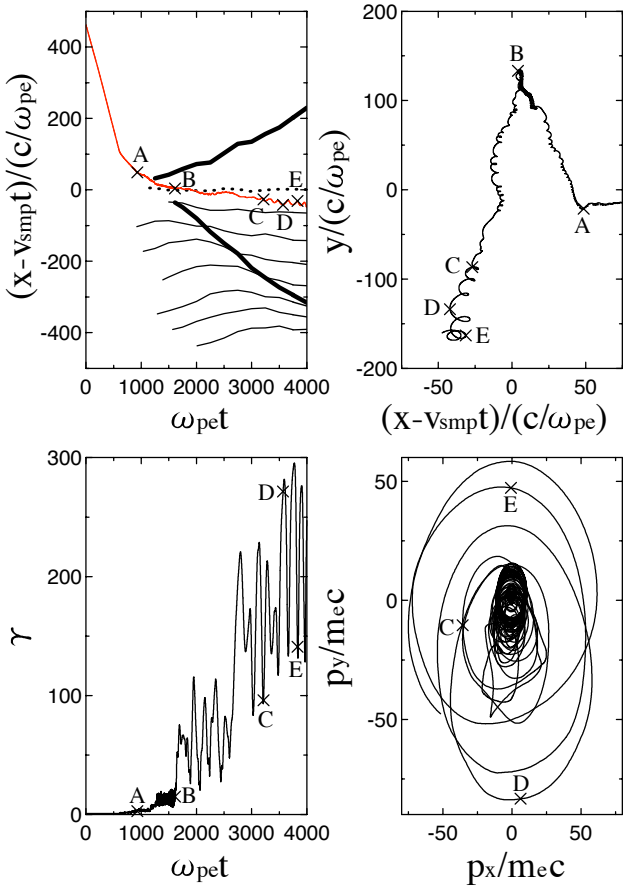

Figure 7.13: Trajectories of an electron with type 1 acceleration. The upper left panel shows the time variation of $(x - v_{\rm smp}t)$ of this particle (red line) and the wave trajectories same as those in Fig. 7.11. The times at points A in the four panels are the same; this is also the case with points B–E. This particle absorbs energy moving along the SMF pulse [2].

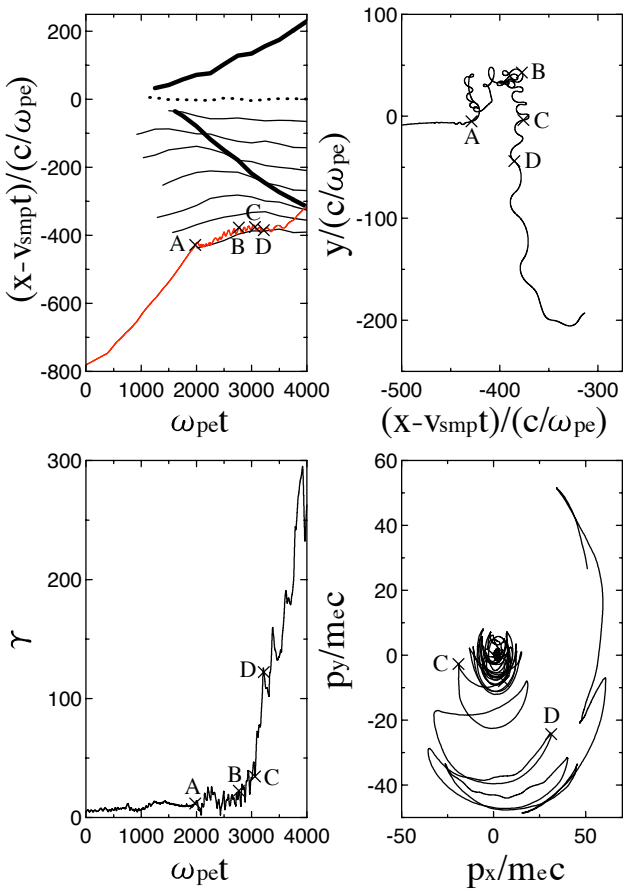

Figure 7.14: Trajectories of an electron with type 2 acceleration. This particle gains energy in a meandering orbit along a moving neutral sheet. The p_x in the lower right panel is the momentum in the frame moving with the Alfvén wave; i.e., $p_x = \gamma_{\rm smp}(p_{lx} - m_e\gamma v_{\rm smp})$, where p_{lx} is the momentum in the laboratory frame and $\gamma_{\rm smp} = (1 - v_{\rm smp}^2/c^2)^{-1/2}$ [2].

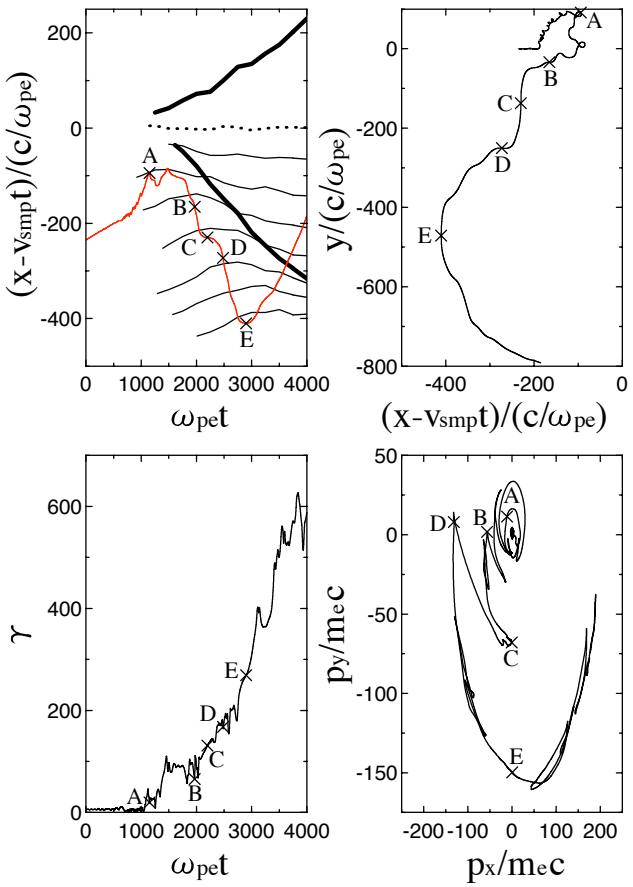

Figure 7.15: Trajectories of an electron with type 3 acceleration. This particle traverses the Alfvén wave region with an alternating magnetic field [2].

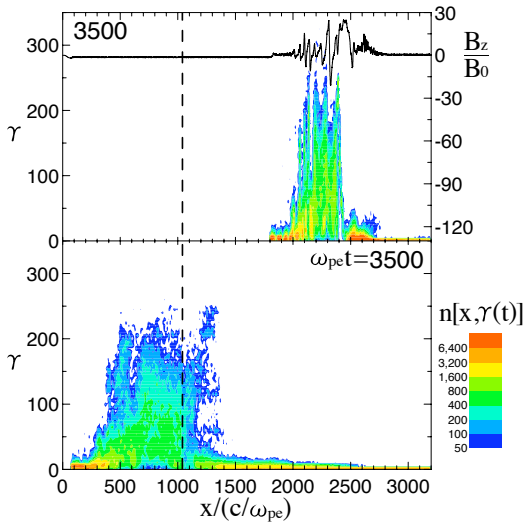

Figure 7.16: Electron density distributions in the (x, γ) plane. The upper panel shows $n(x, \gamma)$ at time $\omega_{pe}t = 3500$. The solid line indicates the profile of B_z at this time. Ultrarelativistic electrons are in the Alfvén wave region. The horizontal and vertical axes in the lower panel show initial particle positions $x(0)$ and energies $\gamma(t)$ at $\omega_{pe}t = 3500$, respectively. The vertical dashed line represents the initial boundary between the exploding and surrounding plasmas. Comparison of the two panels shows that many of the electrons that eventually become high energy are initially in the downstream region [2].

up with the left end of this region at point A. From point B ($\omega_{pe}t = 2770$), it gains a large amount of energy, going in the negative y direction in a meandering orbit along a moving magnetic neutral sheet. The orbits in the configuration and momentum spaces indicate that this acceleration is type 2 in Fig. 7.12.

The particle in Fig. 7.15 is in the Alfvén wave region from the beginning; i.e., when the Alfvén waves were being generated, it was in that region. Between points A and E, it traverses the Alfvén wave region with an alternating magnetic field. Its y position considerably decreases with its γ rapidly growing. The right panels show that this acceleration is type 3 in Fig. 7.12.

Many of the particles that become high energy in the Alfvén wave are supplied from the downstream region. The upper panel of Fig. 7.16 shows the electron density distribution in the $[x(t), \gamma(t)]$ plane at time $\omega_{pe}t = 3500$; the vertical

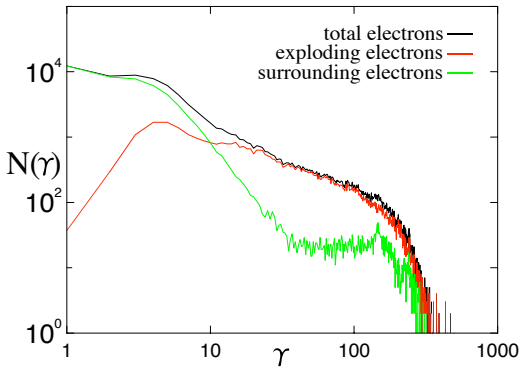

Figure 7.17: Energy spectra of total, exploding, and surrounding electrons at time $\omega_{pe}t = 3800$. The vertical axis $N(\gamma)$ shows the number of electrons in the interval $\gamma - 0.5 < \gamma < \gamma + 0.5$. The energy spectrum of the total electrons is approximately given by $N(\gamma) \sim \gamma^{-0.93}$ in the range $10 < \gamma < 150$ [2].

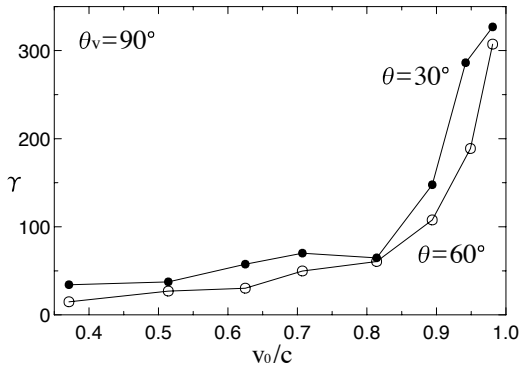

Figure 7.18: Electron energy versus collision speed v_0. The electron energy observed in the simulations rises with v_0 in both $\theta = 30°$ and $\theta = 60°$ cases.

dashed line denotes the boundary between the exploding and surrounding plasmas at $t = 0$. Most of the ultrarelativistic electrons are in the Alfvén wave region $2000 \lesssim x/(c/\omega_{pe}) \lesssim 2500$ at this moment. As shown in the lower panel for the density distribution $n_e[x(0), \gamma(t)]$, however, the initial positions of these high-energy particles are mostly in the downstream region: The vertical axis of the lower panel represents γ of particles at $\omega_{pe}t = 3500$, while the horizontal axis shows their initial x positions. (The initial density $n_e[x(0), \gamma(0)]$, which is not shown here, is in the low-energy region, $\gamma \lesssim 5$, in the entire plasma region.) Comparison of the upper and lower panels indicates that high-energy electrons that are in the Alfvén wave region at $\omega_{pe}t = 3500$ are mostly exploding electrons; i.e., they were in the downstream region at $t = 0$.

Figure 7.17 shows energy spectra of electrons at $\omega_{pe}t = 3800$, where $N(\gamma)$ indicates the number of electrons in the bin $\gamma - 0.5 < \gamma < \gamma + 0.5$. The spectrum of the total electrons denoted by the black line can be approximated by a power law with $N(\gamma) \sim \gamma^{-0.93}$ in the range $10 < \gamma < 150$. (As in Figs. 7.9 and 7.10, we have used 1/20 of the electrons here.)

The electron energy in the Alfvén wave region becomes high in a strong collision of two plasmas. Figure 7.18 shows the dependence of the highest electron energy on the collision speed v_0. In both $\theta = 30°$ and $\theta = 60°$ cases, γ rises rapidly with v_0, particularly in the region with large v_0.

Bibliography

[1] M. Sato and Y. Ohsawa, J. Phys. Soc. Jpn. **77**, 084502 (2008).

[2] Y. Takeyama, S. Nakayama, and Y. Ohsawa, Phys. Plasmas **18**, 092307 (2011).

[3] M. Sato, S. Miyahara, and Y. Ohsawa, Phys. Plasmas **12**, 052308 (2005).

[4] M. Sato and Y. Ohsawa, Phys. Plasmas **13**, 063110 (2006).

[5] M. Sato and Y. Ohsawa, J. Phys. Soc. Jpn. **76**, 104501 (2007).

[6] T. Kawashima, S. Miyahara, and Y. Ohsawa, J. Phys. Soc. Jpn. **72**, 1664 (2003).

[7] E. G. Harris, Nuovo Cimento **23**, 115 (1962).

[8] K. Yamauchi and Y. Ohsawa, Phys. Plasmas **14**, 053110 (2007).

[9] K. Yamauchi and Y. Ohsawa, J. Phys. Soc. Jpn. **77**, 054501 (2008).

[10] H. Alfvén and C.-G. Fälthammer, *Cosmical Electrodynamics*, (Clarendon Press, Oxford, 1963).

[11] T. Taniuti and N. Yajima, J. Math. Phys. **10**, 1369 (1969).

[12] A. Hasegawa, Phys. Fluids **15**, 870 (1972).

[13] K. Mio, T. Ogino, K. Minami, and S. Takeda, J. Phys. Soc. Jpn. **41**, 265 (1976).

[14] E. Mjølhus, J. Plasma Physics **19**, 798 (1978).

[15] E. Mjølhus and J. Wyller, Physica Scripta **33**, 442 (1986).

[16] N. Ya. Kotsarenko, Yu. G. Rapoport, A. A. Shvidkij, and Yu. V. Khotyaintsev, Physica Scripta **58**, 499 (1998).

[17] M. S. Ruderman, J. Plasma Physics **67**, 271 (2002).

Appendix A

Finite-amplitude, stationary, relativistic, perpendicular wave

We obtain stationary perpendicular waves from a relativistic, cold, two-fluid model; i.e., $p_j = 0$ and $\theta = 90°$. Because we consider low-frequency phenomena, we assume charge neutrality, $n_i \simeq n_e = n$. The continuity equations for the ions and electrons then give $v_{ix} \simeq v_{ex} = v_x$ for one-dimensional propagation ($\partial/\partial y = \partial/\partial z = 0$). Since the time derivatives are zero, $\partial/\partial t = 0$, in the wave frame, we have the following basic equations:

$$m_j v_x \frac{d}{dx}(\gamma_j v_x) = q_j E_x + \frac{q_j}{c} v_{jy} B, \tag{A.1}$$

$$m_j v_x \frac{d}{dx}(\gamma_j v_{jy}) = q_j E_y - \frac{q_j}{c} v_x B, \tag{A.2}$$

$$\nabla \times \boldsymbol{E} = 0. \tag{A.3}$$

$$\frac{dB}{dx} = -\frac{4\pi n e}{c}\left(v_{iy} - v_{ey}\right), \tag{A.4}$$

where γ_j is the Lorentz factor for the fluid speed v_j, $\gamma_j = (1 - v_j^2/c^2)^{-1/2}$, and $B = B_z$.

Equation (A.3) indicates that E_y and E_z are constant in space and time:

$$E_y = E_{y1} = \text{const.}, \tag{A.5}$$

$$E_z = E_{z1} = \text{const.}, \tag{A.6}$$

where the subscript 1 refers to quantities at a position $x = x_1$ in the far upstream

region. From the continuity equation with $\partial/\partial t = 0$, one finds that

$$nv_x = n_1 v_1 = \text{const.} \tag{A.7}$$

Adding the ion and electron components of Eq. (A.2) leads to

$$\frac{d}{dx}(m_i \gamma_i v_{iy} + m_e \gamma_e v_{ey}) = 0, \tag{A.8}$$

from which it follows that

$$v_{iy} \simeq -\frac{m_e}{m_i}\frac{\gamma_e}{\gamma_i} v_{ey}. \tag{A.9}$$

Hence, if

$$\gamma_e \ll m_i/m_e, \tag{A.10}$$

and $v_x \lesssim M v_{\rm A} \ll c$, where M is the Alfvén Mach number, the ion speed is nonrelativistic,

$$\gamma_i \simeq 1. \tag{A.11}$$

Furthermore, because of the assumption (A.10), the left-hand side of Eq. (A.1) for the electrons can be ignored, resulting in

$$E_x = -\frac{v_{ey}}{c} B. \tag{A.12}$$

This indicates that the magnitude of E_x/B is always smaller than unity.

Summing Eq. (A.1) over particle species, ignoring the term $m_e v_x d(\gamma_e v_x)/dx$, and using Eq. (A.11), we have

$$m_i v_x \frac{dv_x}{dx} = \frac{eB}{c}(v_{iy} - v_{ey}). \tag{A.13}$$

With the aid of Eqs. (A.4) and (A.7), we eliminate $(v_{iy} - v_{ey})$ and nv_x to obtain

$$m_i n_1 v_1 \gamma_i \frac{dv_x}{dx} = -\frac{1}{8\pi}\frac{dB^2}{dx}, \tag{A.14}$$

which can be integrated from x_1 to x to give

$$v_x = v_1 s, \tag{A.15}$$

where s is defined as

$$s = 1 - \frac{B^2 - B_1^2}{8\pi m_i n_1 v_1^2}. \tag{A.16}$$

From Eqs. (A.7) and (A.15), it follows that

$$n = \frac{n_1}{s}. \tag{A.17}$$

Substituting Eq. (A.17) in Eq. (A.4) yields

$$v_{ey} = \frac{cs}{4\pi e n_1}\frac{dB}{dx}, \tag{A.18}$$

where v_{iy} has been ignored.

With use of Eqs. (A.15) and (A.18), the Lorentz factor of the electrons can be written as

$$\gamma_e = \left\{1 - s^2\left[\left(\frac{v_1}{c}\right)^2 + \frac{1}{(4\pi n_1 e)^2}\left(\frac{dB}{dx}\right)^2\right]\right\}^{-1/2},$$

which can be approximated as

$$\gamma_e = \left[1 - \left(\frac{s}{4\pi n_1 e}\right)^2\left(\frac{dB}{dx}\right)^2\right]^{-1/2}, \tag{A.19}$$

because $v_1 \lesssim M v_{\rm A} \ll c$ in the entire region.

Combining Eq. (A.2) for the electrons and Ampère's law (A.4), and eliminating γ_e, we find that

$$\frac{d}{dx}\left[v_{ey}\left(1 - \frac{v_{ey}^2}{c^2}\right)^{-1/2}\right] = -\frac{e}{m_e v_1 s}E_{y1} + \frac{e}{cm_e}B. \tag{A.20}$$

We multiply Eq. (A.20) by v_{ey}. Then using Eqs. (A.16) and (A.18), we obtain

$$\begin{aligned}&(4\pi n_1 e)^2\frac{v_{ey}}{c}\frac{d}{dx}\left[\frac{v_{ey}}{c}\left(1 - \frac{v_{ey}^2}{c^2}\right)^{-1/2}\right]\\ &= \frac{\omega_{pe}^2}{2c^2}\frac{d}{dx}\left[\left(B - \frac{c}{v_1}E_{y1}\right)^2 - \frac{(B^2 - B_1^2)^2}{16\pi m_i n_1 v_1^2}\right].\end{aligned} \tag{A.21}$$

Here, ω_{pe} is the plasma frequency at $x = x_1$. With the help of the identity

$$f(x)\frac{d}{dx}\frac{f(x)}{[1 - f^2(x)]^{1/2}} = \frac{d}{dx}\frac{1}{[1 - f^2(x)]^{1/2}}, \tag{A.22}$$

we integrate Eq. (A.21) from $x = x_1$ to x to have

$$(4\pi n_1 e)^2 \left[\left(1 - \frac{v_{ey}^2}{c^2}\right)^{-1/2} - \left(1 - \frac{v_{ey1}^2}{c^2}\right)^{-1/2} \right] = \frac{\omega_{pe}^2}{2c^2} \left[(B - B_1) \left(B + B_1 - \frac{2cE_{y1}}{v_1} \right) - \frac{(B^2 - B_1^2)^2}{16\pi m_i n_1 v_1^2} \right]. \tag{A.23}$$

One can put this equation into a form analogous to the equation for a particle in a potential:

$$\frac{1}{2} \left(\frac{d\tilde{B}}{d\tilde{x}} \right)^2 + \Phi(\tilde{B}) = 0, \tag{A.24}$$

where $\tilde{B}$ and $\tilde{x}$ are non-dimensional quantities defined as

$$\tilde{B} = B/B_1, \tag{A.25}$$

$$\tilde{x} = x/(c/\omega_{pe}), \tag{A.26}$$

and the "potential" $\Phi(\tilde{B})$ is

$$\Phi(\tilde{B}) = \frac{\omega_{pe}^2}{2\Omega_e^2 s^2} \left(-1 + \left\{ \frac{\Omega_e^2}{2\omega_{pe}^2} \left[\left(\tilde{B} - 1 \right) \left(\tilde{B} + 1 - \frac{2cE_{y1}}{v_1 \tilde{B}} \right) - \frac{v_A^2 (\tilde{B}^2 - 1)^2}{4v_1^2} \right] + \left[1 - \left(\frac{\Omega_e s_1}{\omega_{pe}} \frac{d\tilde{B}}{d\tilde{x}_1} \right)^2 \right]^{-1/2} \right\}^{-2} \right), \tag{A.27}$$

where Ω_e and $v_{\rm A}$, as well as ω_{pe}, are the values at $x = x_1$, and $d\tilde{B}/d\tilde{x}_1$ stands for the $\tilde{x}$ derivative of $\tilde{B}$ at $\tilde{x} = \tilde{x}_1$. Figure A.1 gives an example of $\Phi(\tilde{B})$. The value of $\tilde{B}$ oscillates in this "potential well," a periodic solution corresponding to a nonlinear wavetrain.

If $d\tilde{B}/d\tilde{x} \to 0$ as $|\tilde{x}|$ goes to infinity (hence, $d\tilde{B}/d\tilde{x}_1 = 0$), we have a solitary wave solution. Let $\tilde{B}_m$ designate the maximum value of $\tilde{B}$. Then it follows from Eq. (A.24) that $\Phi(\tilde{B}_m) = 0$ because $d\tilde{B}/d\tilde{x} = 0$ there. Besides, we can take E_{y1} as $E_{y1} = v_1 B_1/c$. Thus, the Alfvén Mach number is given by

$$M = (\tilde{B}_m + 1)/2, \tag{A.28}$$

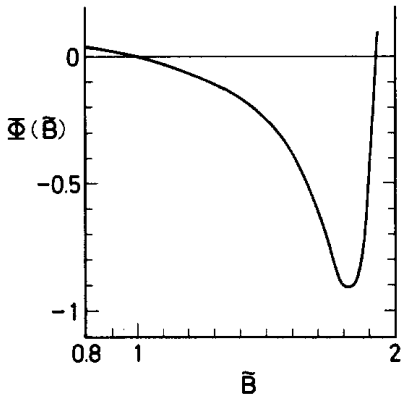

Figure A.1: Profile of $\Phi(\tilde{B})$ for $d\tilde{B}/d\tilde{x_1} = 0.1$, $|\Omega_e|/\omega_{pe} = 1$, $v_1/v_{\rm A} = 1.2$, and $cE_{y1}/(v_1 B_1) = 0.8$.

in the solitary wave. The "potential" Φ can be expressed as

$$\Phi(\tilde{B}) = \frac{\omega_{pe}^2}{2\Omega_e^2 s^2}(-1 + Q^{-2}), \tag{A.29}$$

with

$$s = 1 - 2(\tilde{B}^2 - 1)/(\tilde{B}_m + 1)^2, \tag{A.30}$$

$$Q = 1 + \frac{\Omega_e^2}{2\omega_{pe}^2}(\tilde{B} - 1)^2 \left(1 - \frac{(\tilde{B} + 1)^2}{(\tilde{B}_m + 1)^2}\right). \tag{A.31}$$

Since $\Phi(\tilde{B})$ and hence s are finite (s does not become zero), inspection of Eq. (A.30) indicates that $(\tilde{B}_m + 1)^2 > 2(\tilde{B}_m^2 - 1)$; i.e.,

$$1 < \tilde{B}_m < 3. \tag{A.32}$$

Equations (A.28) and (A.32) are the same as those in the nonrelativistic case.

The characteristic soliton width D is given by

$$\frac{D}{(c/\omega_{pe})} \sim (\tilde{B}_m - 1)^{-1/2}, \tag{A.33}$$

for $\tilde{B} \simeq 1$ and by

$$\frac{D}{(c/\omega_{pe})} \sim \frac{|\Omega_e|}{\omega_{pe}}(\tilde{B}_m - 1), \tag{A.34}$$

for $(|\Omega_e|/\omega_{pe})(\tilde{B}_m - 1) > 1$. In the case that the amplitude is small, $\tilde{B} \simeq 1$, we can expand Eq. (A.29) as

$$\Phi(\tilde{B}) = -\frac{1}{2}\left(1 - \frac{(\tilde{B}+1)^2}{(\tilde{B}_m+1)^2}\right)(\tilde{B}-1)^2, \tag{A.35}$$

which is estimated to be of the order $\sim (\tilde{B}_m - 1)^3$. Equation (A.24) then gives Eq. (A.33). On the other hand, if $\tilde{B}_m$ and $|\Omega_e|/\omega_{pe}$ are both large, it follows from Eq. (A.29) that $\Phi(\tilde{B}) \sim \omega_{pe}^2/|\Omega_e|^2$. From this order estimate and Eq. (A.24), we find Eq. (A.34). A physical picture for this is given in Sec. 2.2.1 [see Eq. (2.45)].

One can calculate the magnitude of the electric potential in a solitary wave with the help of Eqs. (A.12), (A.16), and (A.18):

$$\phi = -\int_{x_1}^{x} E_x dx = \int_{B_1}^{B} \frac{B}{4\pi n_1 e}\left(1 - \frac{2(\tilde{B}^2-1)}{(\tilde{B}_m+1)^2}\right) dB. \tag{A.36}$$

Integrating this and using the relation (A.28), one finds Eq. (2.39).

The above results reduce to nonrelativistic ones under the following conditions:

$$\left(\frac{\Omega_e^2}{2\omega_{pe}^2}\right)\left(\tilde{B}-1\right)^2 \ll 1, \tag{A.37}$$

$$\left(\frac{\Omega_e}{\omega_{pe}}\frac{d\tilde{B}}{d\tilde{x}}\right)^2 \ll 1. \tag{A.38}$$

That is, relativistic treatment is required for large-amplitude waves in a strong magnetic field. The nonrelativistic Φ is derived from Eq. (A.27) as

$$\Phi(\tilde{B}) = -\frac{1}{2s^2}\left[\left(\tilde{B}-1\right)\left(\tilde{B}+1-\frac{2cE_{y1}}{v_1\tilde{B}}\right) - \frac{v_A^2(\tilde{B}^2-1)^2}{4v_1^2} + \left(\frac{d\tilde{B}}{d\tilde{x_1}}\right)^2\right]. \tag{A.39}$$

Appendix B

KdV Equation in a warm, single-ion-species plasma

This appendix derives the KdV equation for magnetosonic waves in an electron-ion plasma with finite thermal pressures from the two-fluid model (2.7)–(2.13). Since we consider low frequency phenomena, we ignore the displacement current in Ampère's law (2.11) and assume charge neutrality,

$$n_e \simeq n_i = n. \tag{B.1}$$

Then, from the continuity equation, it follows that

$$v_{ex} \simeq v_{ix} = v_x. \tag{B.2}$$

In the following calculations, the ion and electron masses are treated as being the same order of magnitude; we therefore define the sound and Alfvén speed as

$$c_s^2 = \frac{\Gamma_i p_{i0} + \Gamma_e p_{e0}}{n_0 \left(m_i + m_e\right)}, \tag{B.3}$$

$$v_{\mathrm{A}}^2 = \frac{B_0^2}{4\pi n_0 \left(m_i + m_e\right)}. \tag{B.4}$$

With use of these quantities, the phase velocities $v_{p0} = \omega/k$ of the fast and slow magnetosonic waves are given by Eq. (2.6) in the long-wavelength limit.

We introduce stretched coordinates, Eqs. (2.46) and (2.47), and expand physical quantities as

$$n = n_0 + \epsilon n_1 + \epsilon^2 n_2 + \cdots, \tag{B.5}$$

$$v_x = \epsilon v_{x1} + \epsilon^2 v_{x2} + \cdots , \tag{B.6}$$

$$v_{jz} = \epsilon v_{jz1} + \epsilon^2 v_{jz2} + \cdots , \tag{B.7}$$

$$p_j = p_{j0} + \epsilon p_{j1} + \epsilon^2 p_{j2} + \cdots , \tag{B.8}$$

$$E_y = \epsilon E_{y1} + \epsilon^2 E_{y2} + \cdots , \tag{B.9}$$

$$B_z = B_{z0} + \epsilon B_{z1} + \epsilon^2 B_{z2} + \cdots , \tag{B.10}$$

$$v_{jy} = \epsilon^{3/2} v_{jy1} + \epsilon^{5/2} v_{jy2} + \cdots , \tag{B.11}$$

$$E_x = \epsilon^{3/2} E_{x1} + \epsilon^{5/2} E_{x2} + \cdots , \tag{B.12}$$

$$E_z = \epsilon^{3/2} E_{z1} + \epsilon^{5/2} E_{z2} + \cdots , \tag{B.13}$$

$$B_y = \epsilon^{3/2} B_{y1} + \epsilon^{5/2} B_{y2} + \cdots . \tag{B.14}$$

Then the continuity equation (2.7) gives

$$\begin{aligned} &\epsilon^{3/2} \left(n_0 \frac{\partial v_{x1}}{\partial \xi} - v_{p0} \frac{\partial n_1}{\partial \xi} \right) \\ &+\epsilon^{5/2} \left(\frac{\partial n_1}{\partial \tau} - v_{p0} \frac{\partial n_2}{\partial \xi} + n_0 \frac{\partial v_{x2}}{\partial \xi} + \frac{\partial (n_1 v_{x1})}{\partial \xi} \right) + \cdots = 0. \end{aligned} \tag{B.15}$$

The x, y, and z components of the equation of motion (2.8) are, respectively,

$$\begin{aligned} &\epsilon^{3/2} \left[v_{p0} \frac{\partial v_{x1}}{\partial \xi} + \Omega_j \left(c \frac{E_{z1}}{B_0} + v_{jy1} \sin\theta \right) - \frac{1}{m_j n_0} \frac{\partial p_{j1}}{\partial \xi} \right] \\ &+\epsilon^{5/2} \left[v_{p0} \frac{\partial v_{x2}}{\partial \xi} - \frac{\partial v_{x1}}{\partial \tau} - v_{x1} \frac{\partial v_{x1}}{\partial \xi} - \frac{1}{m_j n_0} \frac{\partial p_{j2}}{\partial \xi} + \frac{n_1}{m_j n_0^2} \frac{\partial p_{j1}}{\partial \xi} \right. \\ &\left. +\Omega_j \left(c \frac{E_{x2}}{B_0} + v_{jy1} \frac{B_{z1}}{B_0} - v_{jz1} \frac{B_{z1}}{B_0} + v_{jy2} \sin\theta \right) \right] + \cdots = 0, \end{aligned} \tag{B.16}$$

$$\begin{aligned} &\epsilon \Omega_j \left(c \frac{E_{y1}}{B_0} + v_{jz1} \cos\theta - v_{x1} \sin\theta \right) \\ &+\epsilon^2 \left[v_{p0} \frac{\partial v_{jy1}}{\partial \xi} + \Omega_j \left(c \frac{E_{y2}}{B_0} - v_{x1} \frac{B_{z1}}{B_0} + v_{jz2} \cos\theta - v_{x2} \sin\theta \right) \right] + \cdots = 0, \end{aligned} \tag{B.17}$$

and

$$\begin{aligned} &\epsilon^{3/2} \left[v_{p0} \frac{\partial v_{jz1}}{\partial \xi} + \Omega_j \left(c \frac{E_{z1}}{B_0} - v_{jy1} \cos\theta \right) \right] + \epsilon^{5/2} \left[v_{p0} \frac{\partial v_{jz2}}{\partial \xi} - \frac{\partial v_{jz1}}{\partial \tau} \right. \\ &\left. -v_{x1} \frac{\partial v_{jz1}}{\partial \xi} + \Omega_j \left(c \frac{E_{z2}}{B_0} + v_{x1} \frac{B_{y1}}{B_0} - v_{jy2} \cos\theta \right) \right] + \cdots = 0. \end{aligned} \tag{B.18}$$

The equation for the pressure (2.9) becomes

$$\epsilon^{3/2}\left(v_{p0}\frac{\partial p_{j1}}{\partial \xi}-p_{j0}\frac{\partial \Gamma_j v_{jx1}}{\partial \xi}\right)+\epsilon^{5/2}\left(v_{p0}\frac{\partial p_{j2}}{\partial \xi}-\frac{\partial p_{j1}}{\partial \tau}-v_{x1}\frac{\partial p_{j1}}{\partial \xi}\right.$$
$$\left.-p_{j0}\Gamma_j\frac{\partial v_{x2}}{\partial \xi}-p_{j1}\Gamma_j\frac{\partial v_{x1}}{\partial \xi}\right)+\cdots=0. \tag{B.19}$$

From the y and z components of Faraday's law (2.10), we have

$$\epsilon^2\left(\frac{v_{p0}}{c}\frac{\partial B_{y1}}{\partial \xi}+\frac{\partial E_{z1}}{\partial \xi}\right)+\epsilon^3\left(\frac{v_{p0}}{c}\frac{\partial B_{y2}}{\partial \xi}+\frac{\partial E_{z2}}{\partial \xi}-\frac{1}{c}\frac{\partial B_{y1}}{\partial \tau}\right)+\cdots=0, \tag{B.20}$$

$$\epsilon^{3/2}\left(\frac{v_{p0}}{c}\frac{\partial B_{z1}}{\partial \xi}-\frac{\partial E_{y1}}{\partial \xi}\right)+\epsilon^{5/2}\left(\frac{v_{p0}}{c}\frac{\partial B_{z2}}{\partial \xi}-\frac{\partial E_{y2}}{\partial \xi}-\frac{1}{c}\frac{\partial B_{z1}}{\partial \tau}\right)+\cdots=0. \tag{B.21}$$

Ampère's law (2.11) takes the following forms:

$$\epsilon\left(\sum_j n_0 q_j v_{jx1}\right)+\epsilon^2\left(\sum_j q_j(n_0 v_{jx2}+n_{j1}v_{jx1})\right)+\cdots=0, \tag{B.22}$$

$$\epsilon^{3/2}\left(\frac{\partial B_{z1}}{\partial \xi}+\frac{4\pi}{c}\sum_j n_0 q_j v_{jy1}\right)$$
$$+\epsilon^{5/2}\left(\frac{4\pi}{c}\sum_j q_j\left(n_0 v_{jy2}+n_{j1}v_{jy1}\right)+\frac{\partial B_{z2}}{\partial \xi}\right)+\cdots=0, \tag{B.23}$$

and

$$\epsilon\left(\frac{4\pi}{c}\sum_j n_0 q_j v_{jz1}\right)+\epsilon^2\left(\frac{4\pi}{c}\sum_j q_j(n_0 v_{jz2}+n_{j1}v_{jz1})-\frac{\partial B_{y1}}{\partial \xi}\right)+\cdots=0. \tag{B.24}$$

Gauss's law (2.12) is

$$\epsilon\left(4\pi\sum_j n_{j1}q_j\right)+\epsilon^2\left((4\pi\sum_j n_{j2}q_j)-\frac{\partial E_{x1}}{\partial \xi}\right)+\cdots=0. \tag{B.25}$$

From the equations of order ϵ, for instance, we have

$$c\frac{E_{y1}}{B_0}+v_{jz1}\cos\theta-v_{x1}\sin\theta=0, \tag{B.26}$$

$$v_{iz1}=v_{ez1}=v_{z1}. \tag{B.27}$$

In this way, from the lowest order equations in Eqs. (B.15)–(B.25), we find the lowest order perturbations in terms of B_{z1} as

$$\frac{n_1}{n_0} = \frac{v_{\rm A}^2 \sin\theta}{\left(v_{p0}^2 - c_s^2\right)} \frac{B_{z1}}{B_0}, \tag{B.28}$$

$$\frac{v_{x1}}{v_{p0}} = \frac{v_{\rm A}^2 \sin\theta}{\left(v_{p0}^2 - c_s^2\right)} \frac{B_{z1}}{B_0}, \tag{B.29}$$

$$\frac{v_{iy1}}{v_{p0}} = \frac{v_{\rm A}^2}{v_{p0}^2 - v_{\rm A}^2\cos^2\theta} \left(\frac{v_{p0}}{\Omega_e} + \frac{v_{\rm A}^2\cos^2\theta}{\Omega_i v_{p0}} \right) \frac{\partial}{\partial\xi} \frac{B_{z1}}{B_0}, \tag{B.30}$$

$$\frac{v_{ey1}}{v_{p0}} = \frac{v_{\rm A}^2}{v_{p0}^2 - v_{\rm A}^2\cos^2\theta} \left(\frac{v_{p0}}{\Omega_i} + \frac{v_{\rm A}^2\cos^2\theta}{\Omega_e v_{p0}} \right) \frac{\partial}{\partial\xi} \frac{B_{z1}}{B_0}, \tag{B.31}$$

$$\frac{v_{z1}}{v_{p0}} = -\frac{\cos\theta v_{\rm A}^2}{v_{p0}^2} \frac{B_{z1}}{B_0}, \tag{B.32}$$

$$\frac{p_{j1}}{p_{j0}} = \Gamma_j \frac{n_1}{n_0} = \Gamma_j \frac{v_{\rm A}^2 \sin\theta}{\left(v_{p0}^2 - c_s^2\right)} \frac{B_{z1}}{B_0}, \tag{B.33}$$

$$\frac{E_{x1}}{B_0} = \frac{v_{\rm A}^2 \sin\theta}{\Omega_i \Omega_e c} \left(\frac{(\Omega_i + \Omega_e) v_{p0}}{(v_{p0}^2 - v_{\rm A}^2\cos^2\theta)} - \frac{(\Omega_e \Gamma_e p_{e0} + \Omega_i \Gamma_i p_{i0})}{n_0 (m_i + m_e)(v_{p0}^2 - c_s^2)} \right) \frac{\partial}{\partial\xi} \frac{B_{z1}}{B_0}, \tag{B.34}$$

$$\frac{E_{y1}}{B_0} = \frac{v_{p0}}{c} \frac{B_{z1}}{B_0}, \tag{B.35}$$

$$\frac{E_{z1}}{B_0} = \frac{(\Omega_i + \Omega_e)\, v_{\rm A}^2 v_{p0}^2 \cos\theta}{\Omega_i \Omega_e c \left(v_{p0}^2 - v_{\rm A}^2\cos^2\theta\right)} \frac{\partial}{\partial\xi} \frac{B_{z1}}{B_0}, \tag{B.36}$$

$$\frac{B_{y1}}{B_0} = -\frac{(\Omega_i + \Omega_e)\, v_{\rm A}^2 v_{p0} \cos\theta}{\Omega_i \Omega_e \left(v_{p0}^2 - v_{\rm A}^2\cos^2\theta\right)} \frac{\partial}{\partial\xi} \frac{B_{z1}}{B_0}. \tag{B.37}$$

Integration of Eq. (B.34) yields the electric potential ϕ_1, Eq. (2.184).

From the momentum equation in the order ϵ^2, we obtain

$$\begin{aligned} -v_{p0} \frac{\partial}{\partial\xi} \left(v_{iy1} - v_{ey1}\right) = (\Omega_i - \Omega_e) \left(c\frac{E_{y2}}{B_0} - v_{x1}\frac{B_{z1}}{B_0} - v_{x2}\sin\theta \right) \\ + \left(\Omega_i v_{iz2} - \Omega_e v_{ez2}\right)\cos\theta, \end{aligned} \tag{B.38}$$

$$-v_{p0}\frac{\partial}{\partial\xi}\left(\frac{v_{iy1}}{\Omega_i}-\frac{v_{ey1}}{\Omega_e}\right)=(v_{iz2}-v_{ez2})\cos\theta. \tag{B.39}$$

The z component of Ampère's law in the order ϵ^2 becomes

$$\frac{\partial B_{y1}}{\partial\xi}=\frac{4\pi}{c}n_0\sum_j q_j v_{jz2}. \tag{B.40}$$

The momentum equation in the order $\epsilon^{5/2}$ gives

$$\begin{aligned}&\left(\frac{1}{\Omega_i}-\frac{1}{\Omega_e}\right)\left(\frac{\partial}{\partial\tau}+v_{x1}\frac{\partial}{\partial\xi}\right)v_{x1}-v_{p0}\left(\frac{1}{\Omega_i}-\frac{1}{\Omega_e}\right)\frac{\partial v_{x2}}{\partial\xi}\\&=(v_{iy2}-v_{ey2})\sin\theta+\frac{B_{z1}}{B_0}(v_{iy1}-v_{ey1})\\&+\frac{c}{eB_0n_0}\left(\frac{n_1}{n_0}\frac{\partial}{\partial\xi}(p_{i1}+p_{e1})-\frac{\partial}{\partial\xi}(p_{i2}+p_{e2})\right),\end{aligned} \tag{B.41}$$

$$\begin{aligned}&\left(\frac{1}{\Omega_i}-\frac{1}{\Omega_e}\right)\left(\frac{\partial}{\partial\tau}+v_{x1}\frac{\partial}{\partial\xi}\right)v_{z1}-v_{p0}\frac{\partial}{\partial\xi}\left(\frac{v_{iz2}}{\Omega_i}-\frac{v_{ez2}}{\Omega_e}\right)\\&\qquad=-(v_{iy2}-v_{ey2})\cos\theta.\end{aligned} \tag{B.42}$$

The equation for the pressure in the order $\epsilon^{5/2}$ is

$$\begin{aligned}v_{p0}\frac{\partial}{\partial\xi}(p_{i2}+p_{e2})&=\left(\frac{\partial}{\partial\tau}+v_{x1}\frac{\partial}{\partial\xi}\right)(p_{i1}+p_{e1})\\&+(\Gamma_i p_{i0}+\Gamma_e p_{e0})\frac{\partial v_{x2}}{\partial\xi}+(\Gamma_i p_{i1}+\Gamma_e p_{e1})\frac{\partial v_{x1}}{\partial\xi}.\end{aligned} \tag{B.43}$$

From Eqs. (B.21) and (B.23) in the order $\epsilon^{5/2}$, we find

$$\frac{\partial B_{z1}}{\partial\tau}=-c\frac{\partial E_{y2}}{\partial\xi}-\frac{4\pi e n_0 v_{p0}}{c}\left((v_{iy2}-v_{ey2})+\frac{n_1}{n_0}(v_{iy1}-v_{ey1})\right). \tag{B.44}$$

We now eliminate the second-order quantities with the subscript 2 from the above equations to derive an equation that contains only the equilibrium and first-order quantities. Combining Eqs. (B.38), (B.40), (B.42), and (B.44), we eliminate the quantities $(v_{iz2}/\Omega_i - v_{ez2}/\Omega_e)$, $(v_{iy2}-v_{ey2})$, and $(v_{iz2}-v_{ez2})$ to have the following

equation:

$$\frac{4\pi e n_0 v_{p0}^2}{c B_0 \Omega_i \Omega_e} \frac{\partial^2}{\partial \xi^2} \left(v_{iy1} - v_{ey1} \right) = \frac{4\pi e n_0 v_{p0}}{B_0^2} \left(\frac{1}{\Omega_i} - \frac{1}{\Omega_e} \right) \frac{\partial E_{y2}}{\partial \xi}$$
$$- \frac{c \cos^2 \theta}{v_{p0} B_0} \frac{\partial E_{y2}}{\partial \xi} + \frac{4\pi e n_0 v_{p0}^2}{c B_0} \cos \theta \left(\frac{1}{\Omega_i} - \frac{1}{\Omega_e} \right) \left(\frac{\partial}{\partial \tau} + v_{x1} \frac{\partial}{\partial \xi} \right) v_{z1}$$
$$- \frac{4\pi e n_1 \cos^2 \theta}{c B_0} \left(v_{iy1} - v_{ey1} \right) - \frac{\cos^2 \theta}{v_{p0} B_0} \frac{\partial B_{z1}}{\partial \tau} - \frac{v_{p0} \cos \theta}{B_0} \left(\frac{1}{\Omega_i} + \frac{1}{\Omega_e} \right) \frac{\partial^2 B_{y1}}{\partial \xi^2}$$
$$- \frac{4\pi e n_0 v_{p0}}{c B_0^2} \left(\frac{1}{\Omega_i} - \frac{1}{\Omega_e} \right) \frac{\partial}{\partial \xi} \left(v_{x1} B_{z1} \right) - \frac{4\pi e n_0 v_{p0}}{c B_0 \sin \theta} \left(\frac{1}{\Omega_i} - \frac{1}{\Omega_e} \right) \frac{\partial v_{x2}}{\partial \xi}. \quad \text{(B.45)}$$

From Eqs. (B.41), (B.43), and (B.44), it follows that

$$\frac{\partial E_{y2}}{\partial \xi} = - \frac{1}{c} \frac{\partial B_{z1}}{\partial \tau} - \frac{B_0 v_{p0}}{c v_A^2 \sin \theta} \left(\frac{\partial}{\partial \tau} + v_{x1} \frac{\partial}{\partial \xi} \right) v_{x1} - \frac{4\pi e n_1 v_{p0}}{c^2} \left(v_{iy1} - v_{ey1} \right)$$
$$+ \frac{4\pi e n_0 v_{p0}}{c^2 \sin \theta} \frac{B_{z1}}{B_0} \left(v_{iy1} - v_{ey1} \right) + \frac{4\pi v_{p0}}{c B_0 \sin \theta} \frac{n_1}{n_0} \frac{\partial}{\partial \xi} \left(p_{i1} + p_{e1} \right)$$
$$- \frac{B_0}{n_0 (m_i + m_e) c v_{\mathrm{A}}^2 \sin \theta} \left(\frac{\partial}{\partial \tau} + v_{x1} \frac{\partial}{\partial \xi} \right) \left(p_{i1} + p_{e1} \right)$$
$$+ \frac{B_0 (v_{p0}^2 - c_s^2)}{c v_{\mathrm{A}}^2 \sin \theta} \frac{\partial v_{x2}}{\partial \xi} - \frac{B_0 \left(\Gamma_i p_{i1} + \Gamma_e p_{e1} \right)}{n_0 (m_i + m_e) c v_{\mathrm{A}}^2 \sin \theta} \frac{\partial v_{x1}}{\partial \xi}. \quad \text{(B.46)}$$

By substituting Eq. (B.46) in Eq. (B.45), we can eliminate both v_{x2} and E_{y2}. Then expressing the first-order quantities with B_{z1}, we obtain the KdV equation (2.52) in the main text.

Appendix C

Derivation of KdV Equation for the high-frequency mode

This appendix considers nonlinear evolution of the high-frequency mode in a plasma consisting of electrons, light ions (a), and heavy ions ($b, c, \cdots$). The gyrofrequencies of the heavy ions are supposed to be lower than that of the light ions, Ω_a, and the heavy-ion densities are lower than the light-ion density n_{a0}. We can write the relation between ω and k of the high-frequency mode in the form of "weak dispersion," Eq. (2.115), in large part of the frequency domain above its cutoff frequency of the order of the ion gyrofrequency.

We derive the KdV equation for quasi-perpendicular waves from the cold, fluid model for a multi-ion-species plasma:

$$\frac{\partial n_j}{\partial t} + \nabla \cdot (n_j \boldsymbol{v}_j) = 0, \tag{C.1}$$

$$\left(\frac{\partial}{\partial t} + (\boldsymbol{v}_j \cdot \nabla) \right) \boldsymbol{v}_j = \frac{\Omega_j}{|\Omega_e|} \frac{1}{\eta} (\boldsymbol{E} + \boldsymbol{v}_j \times \boldsymbol{B}), \tag{C.2}$$

$$\frac{\partial \boldsymbol{B}}{\partial t} = -\nabla \times \boldsymbol{E}, \tag{C.3}$$

$$\nabla \times \boldsymbol{B} = \eta \sum_j n_j q_j \boldsymbol{v}_j, \tag{C.4}$$

where η is defined by Eq. (2.107), a small quantity of order $(m_e/m_i)^{1/2}$. We have normalized the length, velocity, and time, respectively, to c/ω_{pe}, $v_{\rm h}$, and $(c/\omega_{pe})/v_{\rm h}$. Furthermore, we have normalized the number density, charge, magnetic field, and

electric field to n_{e0}, e, B_0, and $v_{\rm h}B_0/c$, respectively. The coefficient on the right-hand side of Eq. (C.2), $\Omega_j/(|\Omega_e|\eta)$, is of order η for the ions ($j = a, b, c, \cdots$) and of order η^{-1} for the electrons ($j = e$). Ampère's law, Eq. (C.4), also contains η.

We introduce stretched coordinates,

$$\xi = \epsilon^{1/2}(x - t), \tag{C.5}$$

$$\tau = \epsilon^{3/2}t, \tag{C.6}$$

and expand the plasma variables as

$$B_z = \sin\theta + \epsilon B_{z1} + \epsilon^2 B_{z2} + \cdots, \tag{C.7}$$

$$E_y = \epsilon E_{y1} + \epsilon^2 E_{y2} + \cdots, \tag{C.8}$$

$$v_{jx} = \epsilon v_{jx1} + \epsilon^2 v_{jx2} + \cdots, \tag{C.9}$$

$$v_{jz} = \eta^{-1}(\epsilon^2 v_{jz1} + \epsilon^3 v_{jz2} + \cdots), \tag{C.10}$$

$$n_j = n_{j0} + \epsilon n_{j1} + \epsilon^2 n_{j2} + \cdots, \tag{C.11}$$

and

$$B_y = \epsilon^{3/2} B_{y1} + \epsilon^{5/2} B_{y2} + \cdots, \tag{C.12}$$

$$E_x = \eta^{-1}(\epsilon^{3/2} E_{x1} + \epsilon^{5/2} E_{x2} + \cdots), \tag{C.13}$$

$$E_z = \epsilon^{3/2} E_{z1} + \epsilon^{5/2} E_{z2} + \cdots, \tag{C.14}$$

$$v_{jy} = \eta^{-1}(\epsilon^{3/2} v_{jy1} + \epsilon^{5/2} v_{jy2} + \cdots). \tag{C.15}$$

To avoid the frequency regime $\omega \lesssim \Omega_a$, we assume that $\eta \ll \epsilon \ll 1$, inequality (2.96). In addition, the propagation angle is supposed to be nearly perpendicular, so that $\sin\theta \sim O(1)$ and $\cos\theta \sim O(\eta)$; hence, $B_{x0} = \cos\theta \sim O(\eta)$. This expansion differs from the conventional reductive perturbation scheme [Eqs. (B.5)–(B.14) in Appendix B] in that the quantities E_x, v_{jy}, and v_{jz} are proportional to η^{-1}.

Applying the above scheme, Eqs. (C.5)–(C.15), to Eqs. (C.1)–(C.4), we have the following equations. The continuity equation is

$$\epsilon^{3/2}\left(-\frac{\partial n_{j1}}{\partial \xi}+n_{j0}\frac{\partial v_{jx1}}{\partial \xi}\right)+\epsilon^{5/2}\left(-\frac{\partial n_{j2}}{\partial \xi}+\frac{\partial n_{j1}}{\partial \tau}+n_{j0}\frac{\partial v_{jx2}}{\partial \xi}+\frac{\partial n_{j1}v_{jx1}}{\partial \xi}\right)+\cdots=0. \tag{C.16}$$

The x component of the equation of motion for the ions becomes

$$\epsilon^{3/2}\left(\frac{\partial v_{ix1}}{\partial \xi}+\frac{\Omega_i}{|\Omega_e|\eta^2}(E_{x1}+v_{iy1})\right)+\epsilon^{5/2}\left(\frac{\partial v_{ix2}}{\partial \xi}-\frac{\partial v_{ix1}}{\partial \tau}-v_{ix1}\frac{\partial v_{ix1}}{\partial \xi}\right.$$
$$\left.+\frac{\Omega_i}{|\Omega_e|\eta^2}(E_{x2}+v_{iy2}+v_{iy1}B_{z1})\right)+\cdots=0, \tag{C.17}$$

where the subscript i refers to ion species, $i=a,b,c,\cdots$. The quantity $\Omega_i/(|\Omega_e|\eta^2)$ is of order unity. The y and z components of the equation of motion for the ions read as

$$\eta^{-1}\epsilon^2\frac{\partial v_{iy1}}{\partial \xi}+\eta^{-1}\epsilon^3\left(\frac{\partial v_{iy2}}{\partial \xi}-\frac{\partial v_{iy1}}{\partial \tau}-v_{ix1}\frac{\partial v_{iy1}}{\partial \xi}\right)+\cdots$$
$$+\eta\epsilon\left(\frac{\Omega_i}{|\Omega_e|\eta^2}(E_{y1}-v_{ix1})\right)$$
$$+\eta\epsilon^2\left[\frac{\Omega_i}{|\Omega_e|\eta^2}\left(E_{y2}+\frac{\cos\theta}{\eta}v_{iz1}-v_{ix2}-v_{ix1}B_{z1}\right)\right]+\cdots=0, \tag{C.18}$$

$$\eta^{-1}\epsilon^{5/2}\frac{\partial v_{iz1}}{\partial \xi}+\eta^{-1}\epsilon^{7/2}\left(\frac{\partial v_{iz2}}{\partial \xi}-\frac{\partial v_{iz1}}{\partial \tau}-v_{ix1}\frac{\partial v_{iz1}}{\partial \xi}\right)+\cdots$$
$$+\eta\epsilon^{3/2}\left[\frac{\Omega_i}{|\Omega_e|\eta^2}\left(E_{z1}-\frac{\cos\theta}{\eta}v_{iy1}\right)\right]$$
$$+\eta\epsilon^{5/2}\left[\frac{\Omega_i}{|\Omega_e|\eta^2}\left(E_{z2}+v_{ix1}B_{y1}-\frac{\cos\theta}{\eta}v_{iy2}\right)\right]+\cdots=0. \tag{C.19}$$

For the x, y, and z components of the electron equation of motion, we have

$$\eta^{-2}\epsilon^{3/2}(E_{x1}+v_{ey1})+\eta^{-2}\epsilon^{5/2}(E_{x2}+v_{ey2}+v_{ey1}B_{z1})+\cdots=0, \tag{C.20}$$

$$\eta^{-1}\epsilon(E_{y1}-v_{ex1})+\eta^{-1}\epsilon^2\left(-\frac{\partial v_{ey1}}{\partial \xi}+E_{y2}+\frac{\cos\theta}{\eta}v_{ez1}-v_{ex2}-v_{ex1}B_{z1}\right)+\cdots=0, \tag{C.21}$$

$$\eta^{-1}\epsilon^{3/2}\left(E_{z1}-\frac{\cos\theta}{\eta}v_{ey1}\right)+\eta^{-1}\epsilon^{5/2}\left(-\frac{\partial v_{ez1}}{\partial \xi}+E_{z2}+v_{ex1}B_{y1}-\frac{\cos\theta}{\eta}v_{ey2}\right)+\cdots=0. \tag{C.22}$$

The y and z components of Faraday's law are

$$\epsilon^2\left(-\frac{\partial B_{y1}}{\partial\xi}-\frac{\partial E_{z1}}{\partial\xi}\right)+\epsilon^3\left(-\frac{\partial B_{y2}}{\partial\xi}+\frac{\partial B_{y1}}{\partial\tau}-\frac{\partial E_{z2}}{\partial\xi}\right)+\cdots=0, \tag{C.23}$$

$$\epsilon^{3/2}\left(-\frac{\partial B_{z1}}{\partial\xi}+\frac{\partial E_{y1}}{\partial\xi}\right)+\epsilon^{5/2}\left(-\frac{\partial B_{z2}}{\partial\xi}+\frac{\partial B_{z1}}{\partial\tau}+\frac{\partial E_{y2}}{\partial\xi}\right)+\cdots=0. \tag{C.24}$$

The x, y, and z components of Ampère's law become

$$\epsilon\sum_j n_{j0}q_j v_{jx1}+\epsilon^2\left(\sum_j n_{j0}q_j v_{jx2}+\sum_j n_{j1}q_j v_{jx1}\right)+\cdots=0, \tag{C.25}$$

$$\epsilon^{3/2}\left(\frac{\partial B_{z1}}{\partial\xi}+\sum_j n_{j0}q_j v_{jy1}\right)+\epsilon^{5/2}\left(\frac{\partial B_{z2}}{\partial\xi}+\sum_j n_{j0}q_j v_{jy2}+\sum_j n_{j1}q_j v_{jy1}\right)+\cdots=0, \tag{C.26}$$

$$\epsilon^2\left(\frac{\partial B_{y1}}{\partial\xi}-\sum_j n_{j0}q_j v_{jz1}\right)+\epsilon^3\left(\frac{\partial B_{y2}}{\partial\xi}-\sum_j n_{j0}q_j v_{jz2}-\sum_j n_{j1}q_j v_{jz1}\right)+\cdots=0, \tag{C.27}$$

where $\sum_j$ denotes summation over all the particle species including electrons.

With the aid of the assumption $\eta\ll\epsilon\ll 1$, we obtain, from the lowest order terms in Eqs. (C.16)–(C.27), the following relations among the quantities with the subscript 1:

$$n_{e1}=v_{ex1}=E_{y1}=B_{z1}, \tag{C.28}$$

$$n_{i1}=\frac{n_{i0}\Omega_i}{|\Omega_e|\eta^2}B_{z1},\quad v_{ix1}=\frac{\Omega_i}{|\Omega_e|\eta^2}B_{z1}, \tag{C.29}$$

$$v_{ey1}=-E_{x1}=\partial B_{z1}/\partial\xi, \tag{C.30}$$

$$v_{ez1}=\frac{\cos\theta}{\eta}\frac{\partial^2 B_{z1}}{\partial\xi^2},\quad E_{z1}=-B_{y1}=\frac{\cos\theta}{\eta}\frac{\partial B_{z1}}{\partial\xi}, \tag{C.31}$$

$$v_{iy1}=v_{iz1}=0. \tag{C.32}$$

Unlike the case of single-ion-species plasmas, v_{jx1} depends on particle species, although their currents in the x direction cancel as shown below by Eq. (C.34).

By virtue of the $O(\eta^{-1}\epsilon^3)$ terms in Eq. (C.18) and the $O(\eta^{-1}\epsilon^{7/2})$ terms in Eq. (C.19), we find

$$v_{iy2}=v_{iz2}=0. \tag{C.33}$$

[The $O(\eta^{-1}\epsilon^3)$ terms are greater than the $O(\eta\epsilon)$ terms because $\eta \ll \epsilon \ll 1$.] From the terms of order ϵ and ϵ^2 in Eq. (C.25), we have

$$\sum_i n_{i0} q_i v_{ix1} = v_{ex1}, \tag{C.34}$$

$$\sum_i n_{i0} q_i v_{ix2} = v_{ex2} - \sum_j n_{j1} q_j v_{jx1}, \tag{C.35}$$

where $\sum_i$ denotes summation over ion species. We multiply the $O(\epsilon^{5/2})$ terms in Eq. (C.17) by $n_{i0}q_i$ and take summation over ion species i; in which we substitute Eq. (C.35) for $\sum_i n_{i0} q_i v_{ix2}$:

$$\frac{\partial v_{ex1}}{\partial \tau} - \frac{\partial}{\partial \xi}\left(v_{ex2} - \sum_j n_{j1} q_j v_{jx1} \right) + \frac{1}{2}\frac{\partial}{\partial \xi}\left(\sum_i n_{i0} q_i {v_{ix1}}^2 \right) - \left(\sum_i \frac{n_{i0} q_i \Omega_i}{|\Omega_e| \eta^2} \right) E_{x2} = 0. \tag{C.36}$$

Here, we have used Eqs. (C.33) and (C.34). We can eliminate the quantities with the subscript 2 such as v_{ex2} and E_{x2} from Eq. (C.36) and from the second order equations in Eqs. (C.20), (C.21), (C.24), and (C.26) by similar calculations. We then obtain the KdV equation for the high-frequency mode in the normalized form,

$$\frac{\partial B_{z1}}{\partial \tau} + \alpha B_{z1} \frac{\partial B_{z1}}{\partial \xi} + \frac{1}{2}\left(1 - \frac{\cos^2\theta}{\eta^2} \right) \frac{\partial^3 B_{z1}}{\partial \xi^3} = 0. \tag{C.37}$$

The coefficient α is given by Eq. (2.119) in the main text.

Appendix D

Highest energy of trapped electrons

We here derive Eq. (3.24), the highest energy of electrons that are reflected and then trapped by an oblique shock wave.

Electron velocities in the upstream region

We consider the electron motion in the wave frame, where the electric field is $\boldsymbol{E} = (E_x,\ E_{y0},\ 0)$; E_{y0} is negative and is related to the shock speed $v_{\rm sh}$ through Eq. (2.58). The guiding-center velocity of an electron, $\boldsymbol{v}_g$, is given by Eqs. (3.18)–(3.22).

In the far upstream region, the z component of the guiding-center velocity averaged over the electrons in a small volume element is zero, $\langle v_{gz0}\rangle = 0$, where the subscript 0 refers to the quantities in the far upstream region. Then, because $\langle v_{gx0}\rangle = -v_{\rm sh} = cE_{y0}/B_{z0}$, the average parallel velocity is given by

$$\langle v_{\parallel 0}\rangle = -v_{\rm sh}B_{x0}/B_0 < 0. \tag{D.1}$$

Incoming electrons have negative v_{gx0}; thus, from Eq. (3.20) it follows that

$$v_{\parallel 0} < v_{\rm sh}\frac{B_{z0}^2}{B_{x0}B_0}, \tag{D.2}$$

which, combined with Eq. (3.22), gives

$$v_{gz0} < v_{\rm sh}\frac{B_{z0}^2}{B_0^2}\left(\frac{B_{x0}}{B_{z0}} + \frac{B_0}{B_{x0}}\right). \tag{D.3}$$

Electrons with these velocity components will encounter the shock wave.

Estimate of the highest electron energy

From the relativistic equation of motion for an electron, Eq. (3.10), we have an energy equation (3.12). Figure 3.5 in Sec. 3.2.1 shows a schematic diagram of the guiding-center orbit of a trapped electron projected on the (x, y) plane; the electron is reflected at point D. Points C and E are at the peak position of the potential ϕ; hence, $x_C = x_E = x_m$. The electric field E_x is positive in the region $x > x_m$ and is negative in $x < x_m$.

Substituting the guiding-center velocity, Eqs. (3.20) and (3.21), in Eq. (3.12), we find the increase in the kinetic energy when the guiding-center moves from point B to point C as

$$K_{BC} = e(\phi_C - \phi_B) + eE_{y0}\int_B^C I dx - eE_{y0}\int_B^C \frac{v_\parallel B_y}{B} dt, \tag{D.4}$$

where

$$I = \frac{E_x}{E_{y0} + (v_\parallel/c)(BB_{x0}/B_z)}. \tag{D.5}$$

Its denominator is proportional to the guiding-center velocity v_{gx}. The first term on the right-hand side of Eq. (D.4) shows the energy increase due to the potential difference. The second and third terms represent the work done by the electric field E_{y0}. If an electron moves with a velocity nearly equal to the fluid velocity, then $v_\parallel$ would be negative, as suggested by Eq. (D.1). Thus, the denominator of Eq. (D.5) cannot be close to zero because E_{y0} is also negative, which implies that the electron moves quickly from points B to C.

We have a similar equation for the change in energy K_{CD}; the energy increase along the orbit B→C→D→E can be written as

$$K_{BE} = K_{BC} + K_{CD} + e(\phi_E - \phi_D) + eE_{y0}\int_D^E I dx - eE_{y0}\int_D^E \frac{v_\parallel B_y}{B} dt. \tag{D.6}$$

When the electron guiding center moves from points D to E, $v_\parallel$ has rather large positive values; otherwise v_{gx} cannot be positive. If the parallel velocity is

$$v_\parallel \sim -\frac{cE_{y0}B_z}{B_{x0}B}, \tag{D.7}$$

then $v_{gx} \sim 0$, and the denominator of I in the fourth term on the right-hand side of Eq. (D.6) becomes quite small; the fourth term can therefore take a large value. In other words, if v_{gx} is small, it takes a long time for the electron to reach x_E from x_D, during which it traverses a long distance in the y direction. As a result, this particle gains a great amount of energy from E_{y0}, with its $v_\parallel$ approaching c. Accordingly, it follows that

$$\left| \int_D^E I dx \right| \gg \left| \int_B^C I dx \right|, \ \left| \int_C^D I dx \right|. \tag{D.8}$$

This is also the case with the integral $\int v_\parallel (B_y/B) dt$. We thus have

$$K_{BE} = e(\phi_E - \phi_B) + eE_{y0} \int_D^E I dx - eE_{y0} \int_D^E dt \frac{v_\parallel B_y}{B}. \tag{D.9}$$

In view of the facts that the second and third terms on the right-hand side of Eq. (D.9) arise from the integral $\int v_{gy} dt$ in Eq. (3.12) and that $v_\parallel$ is approximately given by Eq. (D.7), we find that the ratio of the magnitude of the third term to that of the second one is $\sim B_y/B_{x0}$. Since $B_y \sim 0$ near x_m $(= x_E)$ (see Fig. 2.4), the third term can be ignored compared with the second term:

$$K_{BE} = e\phi_E + eE_{y0} \int_D^E I dx, \tag{D.10}$$

where ϕ_B has been taken to be zero.

The expression for I in Eq. (D.10) can be further simplified. Because B_z has large values in the shock wave, especially around the point $x = x_m$, we can assume that

$$B/B_z \sim 1. \tag{D.11}$$

Furthermore, since $v_\parallel$ is large along the path D $\rightarrow$ E, we take the magnitude of $v_\parallel$ to be

$$v_\parallel \sim c. \tag{D.12}$$

The denominator of I in Eq. (D.10) can then be approximated as

$$E_{y0} + (v_\parallel/c)(BB_{x0}/B_z) \sim E_{y0} + B_{x0}. \tag{D.13}$$

Electron reflection occurs when the potential ϕ and thus the parallel pseudo potential F become small at point D; for this reason, ϕ_D is ignored compared with ϕ_E. Under these circumstances, we obtain from Eq. (D.10) a simple expression for K_{BE} in the wave frame, Eq. (3.24).

Appendix E

Equivalence of Eqs. (3.38) and (3.50)

We prove here that Eqs. (3.38) and (3.50) are identical for a stationary wave ($\partial F/\partial t = 0$). To do this, we first note that in the drift approximation, Eq. (3.50) can be written as

$$\frac{d}{dt}\left(\frac{m_e}{2}(v_\parallel^2 + v_{\rm d}^2) + \mu_{\rm m}B - eF + m_e c\frac{E_{y0}}{B_{x0}}v_{gz}\right) = 0, \tag{E.1}$$

where v_{gz} is the z component of the guiding-center velocity.

The time derivative of v_{gz} can be expressed in terms of $\partial F/\partial x$ and $d(\mu_{\rm m}B)/dt$. Since $E_z = 0$ in the wave frame, the following equation holds:

$$m_e c\frac{E_{y0}}{B_{x0}}\frac{dv_z}{dt} = \frac{m_e c}{B_{x0}}\left(E_{y0}\frac{dv_z}{dt} - E_z\frac{dv_y}{dt}\right), \tag{E.2}$$

the right-hand side of which is proportional to the x component of $\boldsymbol{E} \times d\boldsymbol{v}/dt$. Substituting the equation of motion for $d\boldsymbol{v}/dt$, we find that

$$\boldsymbol{E} \times \frac{d\boldsymbol{v}}{dt} = -\frac{e}{m_e c}\boldsymbol{E} \times (\boldsymbol{v} \times \boldsymbol{B}), \tag{E.3}$$

which, with the aid of Eq. (3.27), becomes

$$\boldsymbol{E} \times \frac{d\boldsymbol{v}}{dt} = -\frac{e}{m_e c}[(\boldsymbol{E}\cdot\boldsymbol{B})\boldsymbol{v}_d + (\boldsymbol{E}\cdot\boldsymbol{B})\tilde{\boldsymbol{v}} - (\boldsymbol{E}\cdot\tilde{\boldsymbol{v}})\boldsymbol{B}], \tag{E.4}$$

where the relation $\boldsymbol{E}\cdot\boldsymbol{v}_d = 0$ has been used. On account of Eqs. (2.174) and (3.36), the x component of Eq. (E.4) time-averaged over a gyroperiod can be written as

$$\left\langle \boldsymbol{E} \times \frac{d\boldsymbol{v}}{dt} \right\rangle_x = \frac{eB_{x0}}{m_e c}\frac{\partial F}{\partial x}v_{dx} - \frac{B_{x0}}{m_e c}\frac{d}{dt}(\mu_{\rm m}B), \tag{E.5}$$

where we have dropped the term $(\boldsymbol{E}\cdot\boldsymbol{B})\tilde{v}_x$ through the averaging. We can thus put Eq. (E.2) into the following form:

$$\left\langle m_e c\frac{E_{y0}}{B_{x0}}\frac{dv_z}{dt}\right\rangle = e\frac{\partial F}{\partial x}v_{dx} - \frac{d}{dt}(\mu_{\rm m}B). \tag{E.6}$$

Since $\langle v_z\rangle = v_{gz}$, we find that Eq. (3.38) is equivalent to Eq. (E.1) and hence to Eq. (3.50).

Appendix F

Conditions for ion reflection

We calculate in the wave frame the motion of ions reflected by a perpendicular shock wave and derive the conditions for ion reflection. It is shown that many ions can experience one reflection at the shock front. However, only ions with their speeds close to $v_{\rm sh}$ can experience multiple reflections.

F.1 Motions in the upstream and transition regions

Since we are in the wave frame, E_y is constant, $E_y = E_{y0}$ (< 0), in the upstream region ($x > x_1$ in Fig. F.1). The electric potential is assumed to rise in the shock transition region with a constant gradient from zero at $x = x_1$ to a finite value at $x = x_1 - \Delta$, where Δ is the width of the shock transition region (shaded area in Fig. F.1). The longitudinal electric field E_x (> 0) is then constant in this region; outside of which, it is zero. The sharp rise of the magnetic field also acts to reflect particles. For simplicity, however, we assume a uniform magnetic field, focusing on the effect of the electric field on reflection.

Under these circumstances, the ion motion in the upstream region can be described as

$$v_x = V_0 \cos\Psi + V_{Ey}, \tag{F.1}$$

$$v_y = V_0 \sin\Psi, \tag{F.2}$$

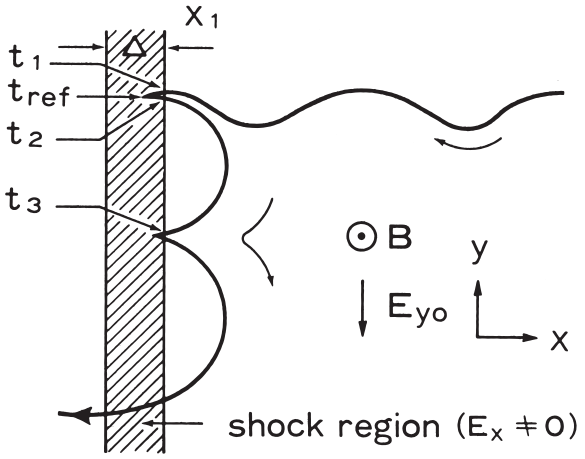

Figure F.1: Schematic diagram of ion orbit in a perpendicular shock wave in the wave frame. The electric potential is assumed to rise in the shock transition region (shaded area) with a constant gradient. In the upstream region ($x > x_1$), ions with their gyration speeds lower than $v_{\rm sh}$ move in a curtate cycloid. Some ions are reflected in the shock transition region by E_x.

where

$$V_{Ey} = cE_{y0}/B, \tag{F.3}$$

$$\Psi = -\Omega_i t + \delta, \tag{F.4}$$

with δ a constant. We suppose that a particle reaches the line $x = x_1$ at time $t = t_1$ with $y = y_1$ and with the phase

$$\Psi_1 = -\Omega_i t_1 + \delta. \tag{F.5}$$

We may write the velocity in the shock transition region as

$$v_x = V_1 \cos[-\Omega_i(t - t_1) + \delta_1] + V_{Ey}, \tag{F.6}$$

$$v_y = V_1 \sin[-\Omega_i(t - t_1) + \delta_1] - V_{Ex}, \tag{F.7}$$

where

$$V_{Ex} = cE_x/B, \tag{F.8}$$

and the position as

$$x - x_1 = -(V_1/\Omega_i)\{\sin[-\Omega_i(t - t_1) + \delta_1] - \sin\delta_1\} + V_{Ey}(t - t_1), \tag{F.9}$$

$$y - y_1 = (V_1/\Omega_i)\{\cos[-\Omega_i(t-t_1)+\delta_1] - \cos\delta_1\} - V_{Ex}(t-t_1). \tag{F.10}$$

Because the velocity given by Eqs. (F.1) and (F.2) and that given by Eqs. (F.6) and (F.7) are equal at $t = t_1$, the constants V_1 and δ_1 are related to V_0 and Ψ_1 through

$$V_1 = [V_0^2 + V_{Ex}^2 + 2V_0 V_{Ex}\sin\Psi_1]^{1/2}, \tag{F.11}$$

$$\cos\delta_1 = (V_0/V_1)\cos\Psi_1, \tag{F.12}$$

$$\sin\delta_1 = (V_0\sin\Psi_1 + V_{Ex})/V_1. \tag{F.13}$$

In a perpendicular magnetosonic wave, in which Δ is small ($\sim c/\omega_{pe}$), the longitudinal electric field is so strong that V_{Ex} should be large:

$$V_{Ex} \gg |V_{Ey}|, \quad V_0. \tag{F.14}$$

In this case, we see from Eqs. (F.11)-(F.13) that

$$V_1 \simeq V_{Ex}\left[1 + \frac{1}{2}\left(\frac{V_0}{V_{Ex}}\right)^2 + \left(\frac{V_0}{V_{Ex}}\right)\sin\Psi_1\right], \tag{F.15}$$

$$\delta_1 \simeq \pi/2. \tag{F.16}$$

F.2 First reflection in the transition region

This section computes the position and time of the first reflection, and then shows the velocity range for reflection to occur.

At the reflection point, v_x becomes zero,

$$\cos[-\Omega_i(t-t_1)+\delta_1] = -V_{Ey}/V_1. \tag{F.17}$$

The right-hand side of Eq. (F.17) is positive and is much smaller than unity, as can be seen from Eqs. (F.14) and (F.15). In addition, since the velocity v_x is negative at $t = t_1$, it follows that

$$\cos\delta_1 < -V_{Ey}/V_0. \tag{F.18}$$

On account of Eqs. (F.14) and (F.16), the left-hand side of Eq. (F.17) can be approximated as

$$\cos[-\Omega_i(t-t_1)+\delta_1] = \Omega_i(t-t_1)-\delta_1+\pi/2 = \Omega_i(t-t_1)+(V_0/V_1)\cos\Psi_1, \quad \text{(F.19)}$$

where the following relation has been used:

$$\delta_1 - \pi/2 = -(V_0/V_1)\cos\Psi_1, \quad \text{(F.20)}$$

which is found from Eqs. (F.12) and (F.16). From Eqs. (F.17) and (F.19), we have the reflection time as

$$t_{\rm ref} - t_1 = -\frac{V_{Ey}+V_0\cos\Psi_1}{\Omega_i V_1}. \quad \text{(F.21)}$$

Substituting Eq. (F.19) in Eq. (F.6) and integrating it over time, we find the reflection point as

$$x_{\rm ref} - x_1 = -\frac{(V_{Ey}+V_0\cos\Psi_1)^2}{2\Omega_i V_{Ex}}. \quad \text{(F.22)}$$

If the length $|x_{\rm ref}-x_1|$ is smaller than the shock width,

$$x_1 - x_{\rm ref} < \Delta, \quad \text{(F.23)}$$

then the incoming particles ($V_0\cos\Psi_1 + V_{Ey} < 0$) satisfying the following condition are reflected by the electric field E_x at least once:

$$-V_{Ey} > V_0\cos\Psi_1 > v_{\rm ref}, \quad \text{(F.24)}$$

where $v_{\rm ref}$ is the minimum velocity for reflection,

$$v_{\rm ref} = -V_{Ey} - \left(2\Delta\Omega_i V_{Ex}\right)^{1/2}. \quad \text{(F.25)}$$

For a stationary solitary wave with $e\phi = 2m_i v_{\rm A}^2(M-1)$, we can estimate the magnitude of $E_x\Delta$ as

$$eE_x\Delta \simeq 2m_i v_{\rm A}^2(M-1). \quad \text{(F.26)}$$

Or, with use of the relation $eE_x\Delta \simeq e\phi$, $v_{\rm ref}$ may be written as

$$v_{\rm ref} \simeq v_{\rm sh} - (2e\phi/m_i)^{1/2}. \quad \text{(F.27)}$$

F.3 Second reflection

Here, we examine the velocity after the first reflection and then give the velocity range for the second reflection.

Similarly to the previous section, one obtains from Eq. (F.9) the time t_2 at which the particle crosses the line $x = x_1$ as

$$\Omega_i(t_2 - t_1) = -2(V_{Ey} + V_0 \cos\Psi_1)/V_1. \tag{F.28}$$

The velocity at time t_2 is expressed as

$$\begin{aligned} v_{x2} &\simeq -(V_{Ey} + V_0 \cos\Psi_1) \\ &+ \left(\frac{2V_{Ey}}{V_{Ex}}\right)^2 \frac{(V_{Ey} + V_0 \cos\Psi_1)}{(2V_{Ey} + V_0 \cos\Psi_1)} \left(V_{Ey} + V_0 \cos\Psi_1 + \frac{V_0^2 \cos^2\Psi_1}{2V_{Ey}}\right), \end{aligned} \tag{F.29}$$

$$v_{y2} = V_{Ey}\Omega_i(t_2 - t_1) + V_0 \sin\Psi_1. \tag{F.30}$$

Under the condition (F.14), the following approximations are possible:

$$v_{x2} \sim -(V_{Ey} + V_0 \cos\Psi_1), \tag{F.31}$$

$$\Psi_2 \simeq -\pi/2, \tag{F.32}$$

where Ψ_2 is the phase at $t = t_2$ in the shock region,

$$\Psi_2 = -\Omega_i(t_2 - t_1) + \delta_1. \tag{F.33}$$

The motion of the particle that has returned to the upstream region again ($x > x_1$, $t > t_2$) may be written as

$$v_x = V_2 \cos[-\Omega_i(t - t_2) + \delta_2] + V_{Ey}, \tag{F.34}$$

$$v_y = V_2 \sin[-\Omega_i(t - t_2) + \delta_2]. \tag{F.35}$$

From the continuity of the velocity at $t = t_2$, the constants V_2 and δ_2 are given by

$$V_2 = [(v_{x2} - V_{Ey})^2 + v_{y2}^2]^{1/2}, \tag{F.36}$$

$$\cos\delta_2 = (V_1/V_2)\cos\Psi_2 \ [= (v_{x2} - V_{Ey})/V_2], \tag{F.37}$$

$$\sin\delta_2 = (V_1 \sin\Psi_2 - V_{Ex})/V_2 \ (= v_{y2}/V_2). \tag{F.38}$$

Substituting Eqs. (F.29) and (F.30) in Eq. (F.36) and using Eq. (F.28), we obtain V_2 in terms of V_0 and Ψ_1:

$$\begin{aligned} V_2^2 &= V_0^2 + 4(V_{Ey} + V_0\cos\Psi_1)\left[V_{Ey} - \frac{V_{Ey}V_0}{V_{Ex}}\sin\Psi_1\right. \\ &+ \left.\left(\frac{V_{Ey}}{V_{Ex}}\right)^2 \frac{V_0^2}{V_{Ey}}\frac{(3\sin^2\Psi_1 - 1)}{2}\right]. \end{aligned} \tag{F.39}$$

If $V_0 \ll |V_{Ey}|$, then V_0 and δ_2 can be approximated as

$$V_2 \simeq -2V_{Ey}, \tag{F.40}$$

$$\delta_2 \simeq 0. \tag{F.41}$$

The direction of the velocity of the reflected particle changes again in the upstream region owing to the magnetic force. The time t_3 at which the particle reenters the shock wave (reaches the line $x = x_1$) is found from Eq. (F.9):

$$\sin\Psi_3 - \sin\delta_2 = (V_{Ey}/V_2)\Omega_i(t_3 - t_2), \tag{F.42}$$

where Ψ_3 is the phase at $t = t_3$ in the upstream region,

$$\Psi_3 = -\Omega_i(t_3 - t_2) + \delta_2. \tag{F.43}$$

Then, similarly to Eq. (F.24), one obtains the condition for particles to be reflected again in the shock region as

$$-V_{Ey} > V_2\cos\Psi_3 > v_{\rm ref}. \tag{F.44}$$

Particles with small initial gyration speeds ($V_0 \ll |V_{Ey}|$) are not reflected twice by the shock wave. Indeed, with use of Eqs. (F.40) and (F.41), which is valid for $V_0 \ll |V_{Ey}|$, Eq. (F.42) can be written as

$$\sin\Psi_3 = \Psi_3/2. \tag{F.45}$$

Hence, Ψ_3 is in the region $\pi/2 < \Psi_3 < \pi$ or in $-\pi/2 > \Psi_3 > -\pi$; thus, $\cos\Psi_3 < 0$. Since $v_{\rm ref} > 0$, the relation (F.44) is not satisfied.

F.4 Multiple reflections with small relative velocity

This section analytically shows that the second reflection is possible if the relative speed is small.

We consider the following circumstances:

$$v_x = V_0 \cos\Psi_1 + V_{Ey} = -\epsilon v, \tag{F.46}$$

$$0 < \epsilon v \ll V_0,\ |V_{Ey}|,\ V_{Ex}, \tag{F.47}$$

$$v_y = V_0 \sin\Psi_1 \simeq V_0 \Psi_1 = \epsilon u,\ |\epsilon u| \ll V_0, \tag{F.48}$$

where ϵ is the smallness parameter. Then Eqs. (F.21) and (F.22) become

$$t_{\rm ref} - t_1 = \frac{\epsilon v}{\Omega_i V_1}, \tag{F.49}$$

$$x_{\rm ref} - x_1 = -\frac{(\epsilon v)^2}{2\Omega_i V_{Ex}}. \tag{F.50}$$

That is, the reflection time is quite short, and the reflection point is in the vicinity of the line $x = x_1$.

This suggests that these ions can be reflected many times. Indeed, we can show that Eq. (F.44) is satisfied. Similarly to Eqs. (F.36)–(F.38), we obtain

$$V_2 = -V_{Ey} + \epsilon v, \tag{F.51}$$

$$\delta_2 = -\epsilon u / V_{Ey}. \tag{F.52}$$

Equation (F.42) then gives

$$\Omega_i (t_3 - t_2) \simeq (6\epsilon v / |V_{Ey}|)^{1/2}. \tag{F.53}$$

Using Eqs. (F.43) and (F.51)–(F.53), one finds that

$$V_2 \cos\Psi_3 \simeq -V_{Ey} - 2\epsilon v. \tag{F.54}$$

Since ϵv is small, $V_2 \cos\Psi_3$ is greater than $v_{\rm ref}$: The condition for the second reflection, Eq. (F.44), is met.

Appendix G

Jumps in energy and parallel momentum

We consider fast particles moving with an oblique shock wave and making gyromotions across its transition region (Fig. 4.5); i.e., fast particles satisfying the relation $v_\parallel \cos\theta \sim v_{\rm sh}$. If they barely enter the shock wave, they will quickly go out again to the upstream region. They can repeat this process several times near the shock transition region, during which they suffer jumps in their energies and parallel momenta. By the latter effect, these particles can eventually outrun the shock wave. We treat these processes here.

G.1 Magnitude of an energy jump

Since the gyroradii of fast ions are much greater than the width of the shock transition region, the magnetic-field profile is approximated by a step function in the following analysis of particle orbit; i.e., the magnetic field in the upstream region is $\boldsymbol{B}_0 = B_0(\cos\theta, 0, \sin\theta)$, and that in the shock wave is $\boldsymbol{B}_1 = B_1(\cos\theta_1, 0, \sin\theta_1)$. The magnetic force on fast particles is stronger than the electric force, and their orbits are well approximated by the unperturbed orbits. In the shock wave, their orbits may be written as

$$x(t) = v_\parallel t\cos\theta_1 + \rho\sin\theta_1\cos(-\Omega_{i1}t/\gamma + \eta) + a_x, \tag{G.1}$$

$$y(t) = \rho\sin(-\Omega_{i1}t/\gamma + \eta) + a_y, \tag{G.2}$$

$$z(t) = v_{\parallel} t \sin\theta_1 - \rho \cos\theta_1 \cos(-\Omega_{i1} t/\gamma + \eta) + a_z, \tag{G.3}$$

where Ω_{i1} is the nonrelativistic ion gyrofrequency in the shock wave, and θ_1, η, a_x, a_y, and a_z are constant. The momentum is then given as

$$p_x(t) = p_{1\parallel} \cos\theta_1 + p_{1\perp} \sin\theta_1 \sin(-\Omega_{i1} t/\gamma + \eta), \tag{G.4}$$

$$p_y(t) = -p_{1\perp} \cos(-\Omega_{i1} t/\gamma + \eta), \tag{G.5}$$

$$p_z(t) = p_{1\parallel} \sin\theta_1 - p_{1\perp} \cos\theta_1 \sin(-\Omega_{i1} t/\gamma + \eta). \tag{G.6}$$

Taking the scalar product of the relativistic equation of motion with momentum $\boldsymbol{p}$, one has

$$\frac{d}{dt}\left(\frac{p^2}{2}\right) = q_i \boldsymbol{p} \cdot \boldsymbol{E}. \tag{G.7}$$

Substituting the unperturbed orbit (G.1)–(G.6) in Eq. (G.7) and integrating it over time from $t = t_{\rm in}$ to $t = t_{\rm out}$, one obtains the increase in p^2 as

$$\begin{aligned}
\delta\left(\frac{p^2}{2}\right) &= q_i p_{1\parallel} E_{\parallel} (t_{\rm out} - t_{\rm in}) \\
&- \frac{2 q_i \gamma p_{1\perp}}{\Omega_i} (E_x \sin\theta_1 - E_z \cos\theta_1) \sin\left(-\frac{\Omega_i (t_{\rm out} + t_{\rm in})}{2\gamma} + \eta\right) \sin\left(-\frac{\Omega_i (t_{\rm out} - t_{\rm in})}{2\gamma}\right) \\
&+ \frac{2 q_i \gamma p_{1\perp}}{\Omega_i} E_y \cos\left(-\frac{\Omega_i (t_{\rm out} + t_{\rm in})}{2\gamma} + \eta\right) \sin\left(-\frac{\Omega_i (t_{\rm out} - t_{\rm in})}{2\gamma}\right),
\end{aligned} \tag{G.8}$$

where $E_{\parallel} = E_x \cos\theta_1 + E_z \sin\theta_1$. The first term on the right-hand side of Eq. (G.8) is ignored, because $E_{\parallel}$ is small compared with E_y in shock waves and is appreciable only in the thin shock transition region. (In these calculations, the contribution from the transition region is not included.) Furthermore, since the gyro-averaged particle velocity $\langle v_x \rangle$ is supposed to be close to $v_{\rm sh}$, we can assume that

$$\cos\left(-\frac{\Omega_i (t_{\rm out} + t_{\rm in})}{2\gamma} + \eta\right) \simeq -1. \tag{G.9}$$

Equation (G.8) is then reduced to

$$\delta\left(\frac{p^2}{2}\right) = -\frac{2 q_i \gamma p_{1\perp}}{\Omega_i} E_y \sin\left(-\frac{\Omega_i (t_{\rm out} - t_{\rm in})}{2\gamma}\right), \tag{G.10}$$

which gives the amount of energy that a fast particle gains per gyroperiod. A fast particle moving with a shock wave can undergo energy jumps, each given by Eq. (G.10), while it is gyrating across the shock transition region.

It is interesting to note that the right-hand side of Eq. (G.10) increases with the particle energy. Substituting Eq. (G.11) in the equation for the increment of energy

$$\delta\gamma = \frac{1}{m_i^2 c^2 \gamma}\delta\left(\frac{p^2}{2}\right), \tag{G.11}$$

which is obtained from the relation $\gamma = [1 + p^2/(m_i^2 c^2)]^{1/2}$, we have Eq. (4.10) in the main text. Since $p_{1\perp}$ is proportional to γ, we find that

$$\delta\gamma \sim C v_\perp \gamma, \tag{G.12}$$

where C is a constant. Because $v_\perp$ is supposed to be of the order of c, this relation between γ and $\delta\gamma$ nearly coincides with the one assumed in the Fermi acceleration model, even though the two mechanisms are distinct.

G.2 Increase in parallel momentum

During the process discussed in Sec. G.1, the parallel momentum and thus $\langle v_x \rangle$ increase. Fast particles with initial velocities $v_\parallel \cos\theta \simeq v_{\rm sh}$ thus tend to finally outrun the shock wave. The increase in $p_\parallel$ is caused by the rapid change in the magnetic field in the shock transition region, as shown below.

Since the gyroradius of a fast ion is much greater than the width of the shock transition region, the time rate of change of the magnetic field that an energetic ion feels along its orbit can be expressed as

$$\frac{d\boldsymbol{B}}{dt} = (\boldsymbol{B}_1 - \boldsymbol{B}_0)[\delta(t - t_{\rm in}) - \delta(t - t_{\rm out})]. \tag{G.13}$$

Furthermore, it follows from the relativistic equation of motion,

$$\frac{d\boldsymbol{p}}{dt} = q\left(\boldsymbol{E} + \frac{\boldsymbol{v}}{c} \times \boldsymbol{B}\right), \tag{G.14}$$

that

$$\frac{d\boldsymbol{p}}{dt} \cdot \boldsymbol{B} = q\boldsymbol{E} \cdot \boldsymbol{B}, \tag{G.15}$$

and thus

$$\frac{d(\boldsymbol{p} \cdot \boldsymbol{B})}{dt} = \boldsymbol{p} \cdot \frac{d\boldsymbol{B}}{dt} + q\boldsymbol{E} \cdot \boldsymbol{B}. \tag{G.16}$$

The second term on the right-hand side of Eq. (G.16) can be ignored, because $E_\parallel$ is weak and mainly present near the shock transition region. Substituting Eq. (G.13) in Eq. (G.16) and integrating it over time from $t = t_a$ (time right before $t = t_{\rm in}$) to $t = t_b$ (time right after $t = t_{\rm out}$), we find

$$\boldsymbol{p}(t_b) \cdot \boldsymbol{B}(t_b) - \boldsymbol{p}(t_a) \cdot \boldsymbol{B}(t_a) = [\boldsymbol{p}(t_{\rm in}) - \boldsymbol{p}(t_{\rm out})] \cdot (\boldsymbol{B}_1 - \boldsymbol{B}_0). \tag{G.17}$$

At $t = t_a$ and $t = t_b$, the particle is in front of the shock wave; thus, $\boldsymbol{B}(t_a) = \boldsymbol{B}(t_b) = \boldsymbol{B}_0$. Hence, the left-hand side of Eq. (G.17) is equal to $[\boldsymbol{p}_0(t_b) - \boldsymbol{p}_0(t_a)] \cdot \boldsymbol{B}_0$, to which only the parallel component of $\boldsymbol{p}_0$ contributes, where the subscript 0 refers to quantities in the upstream region. Let $\delta p_\parallel$ designate the increase in the momentum parallel to $\boldsymbol{B}_0$,

$$\delta p_\parallel = [\boldsymbol{p}_0(t_b) - \boldsymbol{p}_0(t_a)] \cdot \boldsymbol{B}_0 / B_0, \tag{G.18}$$

then the left-hand side of Eq. (G.17) is equal to $\delta p_\parallel B_0$.

Because of the change in the direction of the magnetic field ($\boldsymbol{B}_1$ is not parallel to $\boldsymbol{B}_0$), the magnitudes of the parallel and perpendicular components of the momentum change when the energetic particle enters the shock wave. The values of the momentum components also change when the particle goes out to the upstream region. That is, even though the momentum is continuous, $\boldsymbol{p}(t_{\rm in}) = \boldsymbol{p}_0(t_{\rm in}) = \boldsymbol{p}_1(t_{\rm in})$, $p_{1\parallel}(t_{\rm in})$ is not equal to $p_{0\parallel}(t_{\rm in})$. Furthermore, because $E_\parallel$ is ignored here, $p_{1\parallel}(t)$ is constant during the time from $t = t_{\rm in}$ to $t = t_{\rm out}$, which leads to the relation

$$\boldsymbol{p}(t_{\rm in}) - \boldsymbol{p}(t_{\rm out}) = \boldsymbol{p}_{1\perp}(t_{\rm in}) - \boldsymbol{p}_{1\perp}(t_{\rm out}). \tag{G.19}$$

Then, noting that $\boldsymbol{p}_{1\perp} \cdot \boldsymbol{B}_1 = 0$, we find that

$$[\boldsymbol{p}(t_{\rm in}) - \boldsymbol{p}(t_{\rm out})] \cdot (\boldsymbol{B}_1 - \boldsymbol{B}_0) = [\boldsymbol{p}_{1\perp}(t_{\rm out}) - \boldsymbol{p}_{1\perp}(t_{\rm in})] \cdot \boldsymbol{B}_0. \tag{G.20}$$

Equation (G.17) thus gives the increase in the parallel momentum as

$$\delta p_\parallel = [\boldsymbol{p}_{1\perp}(t_{\rm out}) - \boldsymbol{p}_{1\perp}(t_{\rm in})] \cdot \boldsymbol{B}_0 / B_0. \tag{G.21}$$

We prove that $\delta p_\parallel$ is always positive. Let $\boldsymbol{e}_{x\prime}$ be the unit vector in the direction perpendicular to $\boldsymbol{B}_1$ and to $\boldsymbol{e}_y$, the unit vector in the y direction; i.e., $\boldsymbol{e}_{x\prime} = \boldsymbol{e}_y \times \boldsymbol{B}_1/B_1$. We then introduce the quantity

$$p_{1\perp x\prime} = \boldsymbol{p}_{1\perp} \cdot \boldsymbol{e}_{x\prime}, \tag{G.22}$$

to put Eq. (G.21) into the form

$$\delta p_\parallel = [p_{1\perp x\prime}(t_{\rm out}) - p_{1\perp x\prime}(t_{\rm in})] \sin(\theta_1 - \theta_0). \tag{G.23}$$

At the moment that the particle enters the shock region from the upstream region, the x component of the particle velocity must be smaller than the shock speed $v_{\rm sh}$:

$$v_{1\parallel}(t_{\rm in}) \cos\theta_1 + v_{1\perp x\prime}(t_{\rm in}) \sin\theta_1 < v_{\rm sh}, \tag{G.24}$$

where $v_{1\perp x\prime} = \boldsymbol{v}_{1\perp} \cdot \boldsymbol{e}_{x\prime}$. When the particle goes out to the upstream region, v_x must be greater than $v_{\rm sh}$:

$$v_{1\parallel}(t_{\rm out}) \cos\theta_1 + v_{1\perp x\prime}(t_{\rm out}) \sin\theta_1 > v_{\rm sh}. \tag{G.25}$$

In terms of momentum, Eqs. (G.24) and (G.25) can be expressed as

$$p_{1\parallel}(t_{\rm in}) \cos\theta_1 + p_{1\perp x\prime}(t_{\rm in}) \sin\theta_1 < m_i \gamma(t_{\rm in}) v_{\rm sh}, \tag{G.26}$$

$$p_{1\parallel}(t_{\rm out}) \cos\theta_1 + p_{1\perp x\prime}(t_{\rm out}) \sin\theta_1 > m_i \gamma(t_{\rm out}) v_{\rm sh}. \tag{G.27}$$

The inequalities (G.26) and (G.27) indicate that

$$p_{1\perp x\prime}(t_{\rm out}) > p_{1\perp x\prime}(t_{\rm in}), \tag{G.28}$$

because $p_{1\parallel}(t_{\rm in}) = p_{1\parallel}(t_{\rm out})$ and $\gamma(t_{\rm out}) > \gamma(t_{\rm in})$. [As shown in Sec. G.1, the electric field E_y makes $\gamma(t_{\rm out})$ greater than $\gamma(t_{\rm in})$. Obviously, however, even in the case that $\gamma(t_{\rm out}) = \gamma(t_{\rm in})$, the relation (G.28) holds.] Because $\theta_1 > \theta_0$, it follows from Eqs. (G.23) and (G.28) that $p_\parallel$ always increases,

$$\delta p_\parallel = p_{0\parallel}(t_{\rm out}) - p_{0\parallel}(t_{\rm in}) > 0. \tag{G.29}$$

Simulations show that $p_\parallel$ increases at both $t = t_{\rm in}$ and $t = t_{\rm out}$ in the case that $v_{\rm sh} < c\cos\theta_0$, whereas it tends to decrease at $t = t_{\rm in}$ if $v_{\rm sh} \sim c\cos\theta_0$ although the total $\delta p_\parallel$ is positive (Fig. 4.10). This was explained in Ref. [28] in Chap. 4.

Finally, we note that among the quantities $\delta p_\parallel$, $\delta\gamma = \gamma(t_{\rm out}) - \gamma(t_{\rm in})$, and $\delta v_\parallel = m_i^{-1}[p_{0\parallel}(t_{\rm out})/\gamma(t_{\rm out}) - p_{0\parallel}(t_{\rm in})/\gamma(t_{\rm in})]$, the following relation holds

$$\frac{\delta p_\parallel}{p_{0\parallel}(t_{\rm in})} = \frac{\delta v_\parallel}{v_{0\parallel}(t_{\rm in})} + \frac{\delta\gamma}{\gamma(t_{\rm in})}, \tag{G.30}$$

if $\delta p_\parallel/p_{0\parallel}(t_{\rm in}) \ll 1$ and $\delta\gamma/\gamma(t_{\rm in}) \ll 1$. Equation (G.30) indicates that $\delta p_\parallel$ is positive if $\delta\gamma > 0$, even in the case that $\delta v_\parallel \sim 0$. This can occur when, as a result of the acceleration, $v_{0\parallel}$ has become close to c, while γ increases because of the transverse electric field.

Appendix H

Wave energy density of the high-frequency mode

This appendix calculates the wave energy density of the high-frequency mode with $\theta = 90°$, Eq. (5.12). For small-amplitude perturbations such as Eq. (2.2), we linearize the cold, three-fluid equations. Then using the quantity σ defined as

$$\sigma(\omega) = \frac{\omega[-|\Omega_{\rm e}|\omega^2 + (\omega_{{\rm p}a}^2\Omega_b^2/\Omega_a + \omega_{{\rm p}b}^2\Omega_a^2/\Omega_b)\Omega_{\rm e}^2/\omega_{pe}^2]}{\omega^4 - \omega_{\rm hfr}^2\omega^2 + \omega_{\rm hfr}^2\omega_{\rm lfr}^2}, \tag{H.1}$$

we can express the perturbations in terms of v_{by1} as

$$v_{ax1} = -i\,\frac{\Omega_a}{\Omega_b}\frac{(\Omega_a - \sigma\omega)(\omega^2 - \Omega_b^2)}{(\Omega_a^2 - \omega^2)(\omega - \sigma\Omega_b)}v_{by1}, \tag{H.2}$$

$$v_{ay1} = -\,\frac{\Omega_a}{\Omega_b}\frac{(\omega - \sigma\Omega_a)(\omega^2 - \Omega_b^2)}{(\Omega_a^2 - \omega^2)(\omega - \sigma\Omega_b)}v_{by1}, \tag{H.3}$$

$$v_{bx1} = i\,\frac{(\Omega_b - \sigma\omega)}{(\omega - \sigma\Omega_b)}v_{by1}, \tag{H.4}$$

$$v_{ex1} = -i\,\frac{|\Omega_{\rm e}|}{\Omega_b}\frac{(\omega^2 - \Omega_b^2)(\sigma\omega + |\Omega_{\rm e}|)}{(\Omega_{\rm e}^2 - \omega^2)(\omega - \sigma\Omega_b)}v_{by1}, \tag{H.5}$$

$$v_{ey1} = \frac{|\Omega_{\rm e}|}{\Omega_b}\frac{(\omega^2 - \Omega_b^2)(\omega + \sigma|\Omega_{\rm e}|)}{(\Omega_{\rm e}^2 - \omega^2)(\omega - \sigma\Omega_b)}v_{by1}, \tag{H.6}$$

$$B_1 = -i\,\frac{B_0}{(\omega/k)}\frac{(\omega^2 - \Omega_b^2)}{\Omega_b(\omega - \sigma\Omega_b)}v_{by1}, \tag{H.7}$$

$$E_{x1} = -\,\frac{B_0}{c}\sigma\frac{\omega^2 - \Omega_b^2}{\Omega_b(\omega - \sigma\Omega_b)}v_{by1}, \tag{H.8}$$

$$E_{y1} = -i\,\frac{B_0}{c}\frac{\omega^2 - \Omega_b^2}{\Omega_b(\omega - \sigma\Omega_b)}v_{by1}. \tag{H.9}$$

The energy density of the perturbation averaged over the wavelength λ is obtained if we substitute the real part of each component in the following equation:

$$E_{\rm per} = \frac{1}{\lambda}\int_0^\lambda \left(\frac{(\boldsymbol{B}-\boldsymbol{B}_0)^2+\boldsymbol{E}^2}{8\pi} + \sum_j \frac{m_j n_j \boldsymbol{v}_j^2}{2} \right) dx. \tag{H.10}$$

The energy density of the magnetic perturbation is found to be

$$\left\langle \frac{B_1^2}{8\pi} \right\rangle = \frac{\omega_{pe}^2(\omega^2-\omega_{\rm hf0}^2)}{2(\omega_{\rm hfr}^2\omega^2-\omega_{\rm hfr}^2\omega_{\rm lfr}^2-\omega^4)} \left(\frac{\omega^2-\Omega_b^2}{\Omega_b(\omega-\sigma\Omega_b)} \right)^2 \left(\frac{B_0^2}{8\pi} \right) \frac{v_{by1}^2}{c^2}. \tag{H.11}$$

Here, we have eliminated the wavenumber k in Eq. (H.7) using the dispersion relation (2.80), and v_{by1} was assumed to be real. The ion-kinetic-energy densities are

$$\left\langle \frac{m_a n_a v_a^2}{2} \right\rangle = \frac{\omega_{\rm pa}^2}{2\Omega_b^2} \left(\frac{\omega^2-\Omega_b^2}{\omega^2-\Omega_a^2} \right)^2 \frac{[(1+\sigma^2)(\omega^2+\Omega_a^2)-4\sigma\Omega_a\omega]}{(\omega-\sigma\Omega_b)^2} \left(\frac{B_0^2}{8\pi} \right) \frac{v_{by1}^2}{c^2}, \tag{H.12}$$

$$\left\langle \frac{m_b n_b v_b^2}{2} \right\rangle = \frac{\omega_{\rm pb}^2}{2\Omega_b^2} \frac{[(1+\sigma^2)(\omega^2+\Omega_b^2)-2\sigma\Omega_b\omega]}{(\omega-\sigma\Omega_b)^2} \left(\frac{B_0^2}{8\pi} \right) \frac{v_{by1}^2}{c^2}. \tag{H.13}$$

In this way we obtain the energy densities of all the components. The ratio of the electron to total ion kinetic energies is $\sim m_e/m_i$, and the ratio of the electric to magnetic energies is $\sim v_{\rm h}^2/c^2$. We can therefore ignore the electron kinetic energy and electric field energy. Adding the magnetic and ion kinetic energies, and noting that the relation $\omega_{\rm hfr} \gg \omega \geq \omega_{\rm hf0}$ holds for the high-frequency mode with $k \lesssim k_{\rm c}$, we find, after some manipulations, Eq. (5.12).

Appendix I

Perturbed motions of positrons and ions

This appendix investigates the perturbations of the position $\boldsymbol{x}$ and velocity $\boldsymbol{v}$ of an accelerated positron around the zeroth-order solution obtained in Sec. 6.1. We also examine the perturbations of an ion accelerated by the same mechanism.

I.1 Perturbations of positron motion

We normalize the time, velocity, and length using the nonrelativistic positron gyrofrequency Ω_p as $\hat{t} = \Omega_p t$, $\hat{\boldsymbol{v}} = \boldsymbol{v}/c$, and $\hat{x} = x/(c/\Omega_p)$; however, the hat is omitted below in this appendix. We expand the particle position and velocity as

$$\boldsymbol{x} = \boldsymbol{x}(0) + \boldsymbol{v}_0 t + \epsilon \boldsymbol{x}_1(t) + \epsilon^2 \boldsymbol{x}_2(t) + \cdots , \tag{I.1}$$

$$\boldsymbol{v} = \boldsymbol{v}_0 + \epsilon' \boldsymbol{v}_1(t) + (\epsilon')^2 \boldsymbol{v}_2(t) + \cdots , \tag{I.2}$$

where $\boldsymbol{x}(0)$ is the initial position, $\boldsymbol{v}_0$ is the zeroth-order solution, and ϵ and ϵ' are smallness parameters. We introduce a parameter Γ showing large values,

$$\Gamma \sim \gamma \gg 1, \tag{I.3}$$

and assume that

$$dv_0/dt \sim \Gamma^{-3}. \tag{I.4}$$

The equation for γ, (6.3), then gives

$$d\gamma_0/dt \sim O(1), \tag{I.5}$$

where $\gamma_0 = (1 - v_0^2)^{-1/2}$. The ordering for the perturbed velocity is

$$d\boldsymbol{v}_1/dt \sim \Gamma^{-1}\boldsymbol{v}_1, \tag{I.6}$$

i.e., the characteristic frequency ω is of the order of the relativistic gyrofrequency. Accordingly, from the relation $\boldsymbol{v} = d\boldsymbol{x}/dt$ and Eqs. (I.1) and (I.2), it follows that

$$\epsilon' \sim \Gamma^{-1}\epsilon. \tag{I.7}$$

The perturbed velocity $\boldsymbol{v}_1$ is taken to be almost perpendicular to the zeroth-order velocity $\boldsymbol{v}_0$:

$$\boldsymbol{v}_0 \cdot \boldsymbol{v}_1 \sim \Gamma^{-2} v_0 v_1, \tag{I.8}$$

which leads to

$$\epsilon' \boldsymbol{v}_0 \cdot \frac{d\boldsymbol{v}_1}{dt} \sim \epsilon' \Gamma^{-3} v_0 v_1 \sim \epsilon \Gamma^{-4}. \tag{I.9}$$

Furthermore, using the variable $\xi = x - v_{\rm sh}t$, we expand the field quantities around ξ_0 $[= x(0)]$ as

$$E_x(\xi) = E_x(\xi_0) + \frac{dE_x}{d\xi_0}(\xi - \xi_0) + \cdots, \tag{I.10}$$

where $dE_x/d\xi_0$ designates the value of $dE_x(\xi)/d\xi$ at $\xi = \xi_0$.

We apply this expansion scheme to the exact relativistic equation of motion, (6.4).

First, we discuss the expansion of γ. With the aid of Eq. (I.2) and the relation $\gamma = (1 - \boldsymbol{v}^2)^{-1/2}$, we expand γ as

$$\gamma = \gamma_0 + \delta\gamma_0 + \epsilon' \gamma_0^3 (\boldsymbol{v}_0 \cdot \boldsymbol{v}_1) + \cdots, \tag{I.11}$$

where $\delta\gamma_0$ represents a small correction to γ_0, which we have obtained ignoring $d\boldsymbol{v}_0/dt$. Indeed, it follows from the exact relativistic equation of motion (6.4) that

$$\frac{d\gamma}{dt} = \boldsymbol{E} \cdot \boldsymbol{v}, \tag{I.12}$$

while the equation of motion that ignores $\gamma_0 d\boldsymbol{v}_0/dt$ compared with $\boldsymbol{v}_0 d\gamma_0/dt$ gives

$$v_0^2 \frac{d\gamma_0}{dt} = \boldsymbol{E} \cdot \boldsymbol{v}_0. \tag{I.13}$$

From Eqs. (I.2), (I.12), and (I.13), we see that $d\gamma_0/dt$ differs from the true $d\gamma/dt$ by an amount $d(\gamma-\gamma_0)/dt \sim -\boldsymbol{E}\cdot\boldsymbol{v}_0/(v_0^2\gamma_0^2) \sim \Gamma^{-2}$, even if $\boldsymbol{v}_0$ is very close to the true velocity $\boldsymbol{v}$. This small difference $\delta\gamma_0$ exists even in the absence of the perturbation $\boldsymbol{v}_1$ which is considered below. The time derivative of γ is then given as

$$\frac{d\gamma}{dt} = \frac{d\gamma_0}{dt} + \frac{d\delta\gamma_0}{dt} + \epsilon'\gamma_0^3\left(\boldsymbol{v}_0\cdot\frac{d\boldsymbol{v}_1}{dt}\right) + \epsilon'\gamma_0^3\left(\frac{d\boldsymbol{v}_0}{dt}\cdot\boldsymbol{v}_1\right) + \epsilon' 3\gamma_0^2\frac{d\gamma_0}{dt}(\boldsymbol{v}_0\cdot\boldsymbol{v}_1) + \cdots . \tag{I.14}$$

It is supposed that $\delta\gamma_0$ varies with the same time scale as γ_0.

We find the zeroth-order equation of motion as

$$\frac{d\gamma_0}{dt}\boldsymbol{v}_0 = \boldsymbol{E}(\xi_0) + \boldsymbol{v}_0\times\boldsymbol{B}(\xi_0). \tag{I.15}$$

The relation between $\delta\gamma_0$ and $\boldsymbol{v}_0$ becomes

$$\frac{d\delta\gamma_0}{dt}\boldsymbol{v}_0 + \gamma_0\frac{d\boldsymbol{v}_0}{dt} + \delta\gamma_0\frac{d\boldsymbol{v}_0}{dt} = 0, \tag{I.16}$$

which can be integrated to give

$$\boldsymbol{v}_0(t) = \boldsymbol{v}_0(0)\exp\left(-\int\frac{d\delta\gamma_0/dt}{\gamma_0+\delta\gamma_0}dt\right). \tag{I.17}$$

In the first order of ϵ' (and ϵ), we obtain

$$\begin{aligned}
&\epsilon'\gamma_0^3\left(\frac{d\boldsymbol{v}_0}{dt}\cdot\boldsymbol{v}_1\right)\boldsymbol{v}_0 + \epsilon' 3\gamma_0^2\frac{d\gamma_0}{dt}(\boldsymbol{v}_0\cdot\boldsymbol{v}_1)\boldsymbol{v}_0 + \epsilon'\gamma_0^3\left(\boldsymbol{v}_0\cdot\frac{d\boldsymbol{v}_1}{dt}\right)\boldsymbol{v}_0 \\
&+ \epsilon'\frac{d\gamma_0}{dt}\boldsymbol{v}_1 + \epsilon'\frac{d\delta\gamma_0}{dt}\boldsymbol{v}_1 + \epsilon'\gamma_0\frac{d\boldsymbol{v}_1}{dt} + \epsilon'\delta\gamma_0\frac{d\boldsymbol{v}_1}{dt} + \epsilon'\gamma_0^3(\boldsymbol{v}_0\cdot\boldsymbol{v}_1)\frac{d\boldsymbol{v}_0}{dt} \\
&= \epsilon\frac{d\boldsymbol{E}}{d\xi_0}x_1 + \epsilon\boldsymbol{v}_0\times\frac{d\boldsymbol{B}}{d\xi_0}x_1 + \epsilon'\boldsymbol{v}_1\times\boldsymbol{B}(\xi_0).
\end{aligned} \tag{I.18}$$

Here, some of the terms are negligibly small. The magnitudes of $x_1 d\boldsymbol{E}/d\xi_0$ and $x_1 d\boldsymbol{B}/d\xi_0$ are small if the wavelength is greater than the magnitude of x_1 ($\sim c/\Omega_p$). For the magnetosonic wave, for instance, we have

$$x_1\frac{dB}{d\xi_0} \sim \frac{B(c/\Omega_p)}{(c/\omega_{pi})}, \tag{I.19}$$

because the characteristic width of nonlinear oblique magnetosonic waves is $\sim c/\omega_{pi}$. From Eqs. (I.4)–(I.6), we see that

$$\left|\boldsymbol{v}_1 \cdot \frac{d\boldsymbol{v}_0}{dt}\right| \ll \left|\boldsymbol{v}_0 \cdot \frac{d\boldsymbol{v}_1}{dt}\right|, \tag{I.20}$$

$$\left|\boldsymbol{v}_1 \frac{d\gamma_0}{dt}\right| \ll \left|\gamma_0 \frac{d\boldsymbol{v}_1}{dt}\right|. \tag{I.21}$$

We thus obtain the equation to solve:

$$\gamma_0^3 \left(\boldsymbol{v}_0 \cdot \frac{d\boldsymbol{v}_1}{dt}\right) \boldsymbol{v}_0 + \gamma_0 \frac{d\boldsymbol{v}_1}{dt} = \boldsymbol{v}_1 \times \boldsymbol{B}. \tag{I.22}$$

Taking the scalar product of Eq. (I.22) with $\boldsymbol{B}$, we find that

$$\boldsymbol{U} \cdot \frac{d\boldsymbol{v}_1}{dt} = 0, \tag{I.23}$$

where $\boldsymbol{U}$ is a vector defined by

$$\boldsymbol{U} = \gamma_0^2 (\boldsymbol{v}_0 \cdot \boldsymbol{B}) \boldsymbol{v}_0 + \boldsymbol{B}. \tag{I.24}$$

Equation (6.21) in the main text presents its unnormalized form. Since $\gamma_0 \gg 1$, $\boldsymbol{U}$ is nearly parallel to $\boldsymbol{v}_0$. Equation (I.23) indicates that the component of $\boldsymbol{v}_1$ parallel to the vector $\boldsymbol{U}$ is constant. If it is initially zero, the perturbed velocity $\boldsymbol{v}_1$ is always in the plane perpendicular to $\boldsymbol{U}$.

Assuming that $\boldsymbol{v}_1$ varies with time as $\exp(-i\omega t)$, we put Eq. (I.22) into the following form:

$$\begin{aligned}
\left(-i\omega\gamma_0^3 v_{x0}^2 - i\omega\gamma_0\right) v_{x1} + \left(-i\omega\gamma_0^3 v_{x0} v_{y0} - B_z\right) v_{y1} \\
+ \left(-i\omega\gamma_0^3 v_{x0} v_{z0} + B_y\right) v_{z1} = 0, \qquad \text{(I.25)} \\
\left(-i\omega\gamma_0^3 v_{x0} v_{y0} + B_z\right) v_{x1} + \left(-i\omega\gamma_0^3 v_{y0}^2 - i\omega\gamma_0\right) v_{y1} \\
+ \left(-i\omega\gamma_0^3 v_{y0} v_{z0} - B_x\right) v_{z1} = 0, \qquad \text{(I.26)} \\
\left(-i\omega\gamma_0^3 v_{x0} v_{z0} - B_y\right) v_{x1} + \left(-i\omega\gamma_0^3 v_{y0} v_{z0} + B_x\right) v_{y1} \\
+ \left(-i\omega\gamma_0^3 v_{z0}^2 - i\omega\gamma_0\right) v_{z1} = 0. \qquad \text{(I.27)}
\end{aligned}$$

The condition for a nontrivial solution of Eqs. (I.25) - (I.27) gives

$$
\begin{aligned}
&-\left(i\omega\gamma_0^3 v_{x0}^2 + i\omega\gamma_0\right)\left(i\omega\gamma_0^3 v_{y0}^2 + i\omega\gamma_0\right)\left(i\omega\gamma_0^3 v_{z0}^2 + i\omega\gamma_0\right) \\
&-\left(i\omega\gamma_0^3 v_{x0}v_{y0} + B_z\right)\left(i\omega\gamma_0^3 v_{y0}v_{z0} + B_x\right)\left(i\omega\gamma_0^3 v_{x0}v_{z0} + B_y\right) \\
&+\left(-i\omega\gamma_0^3 v_{x0}v_{z0} + B_y\right)\left(-i\omega\gamma_0^3 v_{x0}v_{y0} + B_z\right)\left(-i\omega\gamma_0^3 v_{y0}v_{z0} + B_x\right) \\
&-\left(\omega^2\gamma_0^6 v_{x0}^2 v_{z0}^2 + B_y^2\right)\left(i\omega\gamma_0^3 v_{y0}^2 + i\omega\gamma_0\right) - \left(\omega^2\gamma_0^6 v_{y0}^2 v_{z0}^2 + B_x^2\right)\left(i\omega\gamma_0^3 v_{x0}^2 + i\omega\gamma_0\right) \\
&-\left(\omega^2\gamma_0^6 v_{x0}^2 v_{y0}^2 + B_z^2\right)\left(i\omega\gamma_0^3 v_{z0}^2 + i\omega\gamma_0\right) = 0. \qquad \text{(I.28)}
\end{aligned}
$$

Using the relation $v_{x0}^2 + v_{y0}^2 + v_{z0}^2 = 1 - \gamma_0^{-2}$, we obtain the frequency,

$$\omega^2 = \gamma_0^{-4}[\gamma_0^2(\boldsymbol{B}\cdot\boldsymbol{v}_0)^2 + B^2], \qquad \text{(I.29)}$$

and the velocity,

$$v_{y1} = \frac{(\omega^2\gamma_0^4 v_{y0}v_{z0} + B_y B_z) - i\omega(\gamma_0^3 v_{x0}\boldsymbol{B}\cdot\boldsymbol{v}_0 + \gamma_0 B_x)}{(\omega^2\gamma_0^4 v_{x0}v_{z0} + B_x B_z) + i\omega(\gamma_0^3 v_{y0}\boldsymbol{B}\cdot\boldsymbol{v}_0 + \gamma_0 B_y)} v_{x1}, \qquad \text{(I.30)}$$

$$v_{z1} = \frac{(\omega^2\gamma_0^4 v_{y0}v_{z0} + B_y B_z) + i\omega(\gamma_0^3 v_{x0}\boldsymbol{B}\cdot\boldsymbol{v}_0 + \gamma_0 B_x)}{(\omega^2\gamma_0^4 v_{x0}v_{y0} + B_x B_y) - i\omega(\gamma_0^3 v_{z0}\boldsymbol{B}\cdot\boldsymbol{v}_0 + \gamma_0 B_z)} v_{x1}. \qquad \text{(I.31)}$$

This velocity satisfies the relation $\boldsymbol{U}\cdot\boldsymbol{v}_1 = 0$, which is consistent with Eq. (I.23). The unnormalized forms of these solutions are given by Eqs. (6.22)–(6.24) in Sec. 6.1.3.

This motion is elliptic, which can easily be seen in the coordinate system $(\tilde{x}, \tilde{y}, \tilde{z})$ in which the $\tilde{z}$ axis is parallel to $\boldsymbol{U}$ (Fig. I.1). Noting that the three vectors $\boldsymbol{B}$, $\boldsymbol{v}_0$, and $\boldsymbol{U}$ are coplanar, we take the $\tilde{x}$ axis in this plane, in the direction parallel to $\boldsymbol{v}_0 - (\boldsymbol{U}\cdot\boldsymbol{v}_0)\boldsymbol{U}/U^2$. We can then express $\boldsymbol{B}$ and $\boldsymbol{v}_0$ as $\boldsymbol{B} = (B_{\tilde{x}}, 0, B_{\tilde{z}})$ and $\boldsymbol{v}_0 = (v_{\tilde{x}0}, 0, v_{\tilde{z}0})$ with

$$v_{\tilde{x}0} = [v_0^2 - (\boldsymbol{U}\cdot\boldsymbol{v}_0)^2/U^2]^{1/2}. \qquad \text{(I.32)}$$

Since $\boldsymbol{U}$ is nearly parallel to $\boldsymbol{v}_0$, the magnitude of $v_{\tilde{x}0}$ is quite small: With the aid of Eq. (I.24), we see that $v_{\tilde{x}0} = [v_0^2 B^2 - (\boldsymbol{v}_0\cdot\boldsymbol{B})^2]^{1/2}/U \sim \gamma_0^{-2}$. Taking the scalar product of Eq. (I.24) with $\boldsymbol{B}$ and with $\boldsymbol{v}_0$, we have

$$UB_{\tilde{z}} = \gamma_0^2(\boldsymbol{v}_0\cdot\boldsymbol{B})^2 + B^2, \qquad \text{(I.33)}$$

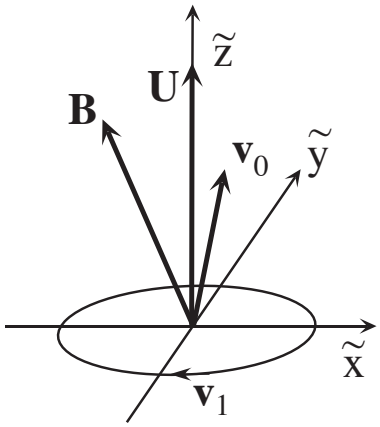

Figure I.1: Schematic diagram of the coordinate system $(\tilde{x}, \tilde{y}, \tilde{z})$. The $\tilde{z}$ axis is taken to be parallel to $\boldsymbol{U}$. The vectors $\boldsymbol{U}$, $\boldsymbol{B}$, and $\boldsymbol{v}_0$ are in the $(\tilde{x}, \tilde{z})$ plane, while $\boldsymbol{v}_1$ is in the $(\tilde{x}, \tilde{y})$ plane. The vectors in the figure do not show exact magnitudes.

$$U v_{\tilde{z}0} = \gamma_0^2 (\boldsymbol{v}_0 \cdot \boldsymbol{B}), \tag{I.34}$$

where use has been made of the relation $\gamma_0^2 = \gamma_0^2 v_0^2 + 1$. The $\tilde{x}$ component of Eq. (I.24) leads to

$$B_{\tilde{x}} = -\frac{\gamma_0^2 v_{\tilde{x}0} v_{\tilde{z}0}}{\gamma_0^2 v_{\tilde{x}0}^2 + 1} B_{\tilde{z}}. \tag{I.35}$$

Because of the relation (I.23), we take $v_{\tilde{z}1}$ to be zero. From Eq. (I.22), we then obtain equations for $(v_{\tilde{x}1}, v_{\tilde{y}1})$:

$$-i\omega\gamma_0(\gamma_0^2 v_{\tilde{x}0}^2 + 1) v_{\tilde{x}1} - B_{\tilde{z}} v_{\tilde{y}1} = 0, \tag{I.36}$$

$$B_{\tilde{z}} v_{\tilde{x}1} - i\omega\gamma_0 v_{\tilde{y}1} = 0, \tag{I.37}$$

$$-i\omega\gamma_0^3 v_{\tilde{x}0} v_{\tilde{z}0} v_{\tilde{x}1} + B_{\tilde{x}} v_{\tilde{y}1} = 0. \tag{I.38}$$

Substituting Eq. (I.35) in Eq. (I.38) yields the equation same as Eq. (I.36). Hence, the condition for a nontrivial solution of Eqs. (I.36)–(I.38) becomes

$$\omega^2 = \frac{B_{\tilde{z}}^2}{\gamma_0^2(\gamma_0^2 v_{\tilde{x}0}^2 + 1)}. \tag{I.39}$$

On account of Eqs. (I.24), (I.32), and (I.33), one can show that Eq. (I.39) is identical to Eq. (6.22) in the main text. The velocity component $v_{\tilde{y}1}$ is related to $v_{\tilde{x}1}$ as

$$v_{\tilde{y}1} = -i(\gamma_0^2 v_{\tilde{x}0}^2 + 1)^{1/2} v_{\tilde{x}1}, \tag{I.40}$$

which is an elliptic motion in the $(v_{\tilde{x}}, v_{\tilde{x}})$ plane.

I.2 Perturbations of ion motion

For the ions, we normalize the physical quantities using Ω_{i0}: $\hat{t} = \Omega_{i0}t$, $\hat{\boldsymbol{v}} = \boldsymbol{v}/c$, and $\hat{x} = x/(c/\Omega_{i0})$. As in the previous section, the hat is omitted below. We expand $\boldsymbol{x}$, $\boldsymbol{v}$, and the field quantities in the same way as Eqs. (I.1), (I.2), and (I.10), respectively, and use the ordering for Γ, dv_0/dt, and $d\gamma_0/dt$ same as Eqs. (I.3)–(I.5). Instead of Eq. (I.6), however, we assume that

$$d\boldsymbol{v}_1/dt \sim \Gamma^{-1/2}\boldsymbol{v}_1, \tag{I.41}$$

i.e., the characteristic frequency ω is higher than the relativistic ion gyrofrequency. As a result, Eq. (I.7) is replaced by

$$\epsilon' \sim \Gamma^{-1/2}\epsilon. \tag{I.42}$$

Assuming again that $\boldsymbol{v}_1$ is nearly perpendicular to $\boldsymbol{v}_0$, Eq. (I.8), we obtain

$$\epsilon'\boldsymbol{v}_0 \cdot \frac{d\boldsymbol{v}_1}{dt} \sim \epsilon'\Gamma^{-5/2}v_0v_1 \sim \epsilon\Gamma^{-3}. \tag{I.43}$$

Applying these expansions and orderings to the equation of motion, we find Eq. (I.18) in the first order of ϵ' (and ϵ). The magnitude of the Lorentz force is $v_{y1}B_z(\xi_0) - v_{z1}B_y(\xi_0) \sim \epsilon\Gamma^{-1/2}$, which is obviously smaller in magnitude than, for instance, $\epsilon'\gamma_0 d\boldsymbol{v}_1/dt$ ($\sim \epsilon$). We thereby find the equation in the order of ϵ as

$$\gamma_0^3\left(\boldsymbol{v}_0 \cdot \frac{d\boldsymbol{v}_1}{dt}\right)\boldsymbol{v}_0 + \gamma_0\frac{d\boldsymbol{v}_1}{dt} = \frac{d\boldsymbol{E}}{d\xi_0}x_1 + \boldsymbol{v}_0 \times \frac{d\boldsymbol{B}}{d\xi_0}x_1. \tag{I.44}$$

In the $O(\epsilon^2)$ equation, we have terms such as $3\gamma_0^5 v_{x0}^2 v_{x1}(dv_{x1}/dt)\boldsymbol{v}_0$, which is smaller than the terms of Eq. (I.44) if

$$\epsilon < \Gamma^{-7/2}. \tag{I.45}$$

We suppose that ϵ is so small that (I.45) is satisfied.

Now, assuming that the perturbed quantities vary with time as $\exp(-i\omega t)$, we find from Eq. (I.44) the frequency ω as

$$\omega^2 = -\frac{(1 - v_{\rm sh}^2)}{\gamma_0}\left(\frac{dE_x}{d\xi_0} + v_{y0}\frac{dB_z}{d\xi_0} - v_{z0}\frac{dB_y}{d\xi_0}\right). \tag{I.46}$$

Equation (I.46) is consistent with the ordering (I.41) and indicates that ω has real values if

$$\frac{dE_x}{d\xi_0} + v_{y0}\frac{dB_z}{d\xi_0} - v_{z0}\frac{dB_y}{d\xi_0} < 0. \tag{I.47}$$

If this condition is not met, then the oscillation would grow with time; the particle would quickly escape from the shock transition region.

The perturbed velocity $\boldsymbol{v}_1$ is given as

$$\boldsymbol{v}_1 = -i\omega x_1(1, -\gamma_{\rm sh}^2 v_{\rm sh} v_{y0}, -\gamma_{\rm sh}^2 v_{\rm sh} v_{z0}). \tag{I.48}$$

We thus find that

$$\boldsymbol{v}_0 \cdot \boldsymbol{v}_1 = -i\omega x_1 v_{\rm sh}\gamma_{\rm sh}^2/\gamma_0^2, \tag{I.49}$$

which is in agreement with the ordering (I.8), indicating that $\boldsymbol{v}_1$ is almost perpendicular to $\boldsymbol{v}_0$. Equation (I.48) also shows that the perturbation is one dimensional: $\boldsymbol{v}_1$ is parallel to the vector $(1, -\gamma_{\rm sh}^2 v_{\rm sh} v_{y0}, -\gamma_{\rm sh}^2 v_{\rm sh} v_{z0})$.

Appendix J

Electron motions inside and outside a compressive pulse

J.1 Elliptic orbits in the momentum space

To analyze the relativistic electron motion near a small compressive pulse behind a shock front, we assume, as in Sec. 7.1.1, that the electric and magnetic fields are $\boldsymbol{E}_{\rm I} = (0, E_{\rm I}, 0)$ and $\boldsymbol{B}_{\rm I} = (0, 0, B_{\rm I})$ inside the pulse and $\boldsymbol{E}_{\rm II} = (0, E_{\rm II}, 0)$ and $\boldsymbol{B}_{\rm II} = (0, 0, B_{\rm II})$ outside the pulse.

When an electron is inside the pulse, $x_{\rm bd} < x < x_{\rm bd} + \Delta$, it moves in an ellipse in the momentum space, which can be shown with use of the relativistic equation of motion:

$$m_e \frac{d}{dt}(\gamma v_x) = -\frac{e}{c} v_y B_{\rm I}, \tag{J.1}$$

$$m_e \frac{d}{dt}(\gamma v_y) = -eE_{\rm I} + \frac{e}{c} v_x B_{\rm I}. \tag{J.2}$$

The z component of the momentum is constant because $E_z = 0$,

$$p_z = p_{z0}. \tag{J.3}$$

From Eqs. (J.1) and (J.2), we obtain

$$m_e c^2 \left(\gamma - \gamma_{0\rm I}\right) = -eE_{\rm I}(y - y_{0\rm I}), \tag{J.4}$$

where the subscript 0 refers to initial values; $\gamma_{0\rm I}$ can be expressed as

$$\gamma_{0\rm I} = \left(1 + \frac{p_{x0}^2 + p_{y0}^2 + p_{z0}^2}{m_e^2 c^2}\right)^{1/2}. \tag{J.5}$$

Integrating Eq. (J.1) gives

$$m_e\gamma v_x - m_e\gamma_{0\mathrm{I}}v_{x0\mathrm{I}} = -\frac{eB_\mathrm{I}}{c}(y - y_{0\mathrm{I}}). \tag{J.6}$$

Combining Eqs. (J.4) and (J.6), and using the relation $\gamma = [1 + \boldsymbol{p}^2/(m_e^2c^2)]^{1/2}$, we obtain an elliptic equation for $\boldsymbol{p}$, Eqs. (7.4) and (7.5), where P_I and a_I are given as

$$P_\mathrm{I} = m_e\gamma_{\mathrm{dI}}^2 v_{\mathrm{dI}}\gamma_{0\mathrm{I}}(1 - v_{\mathrm{dI}}v_{x0\mathrm{I}}/c^2), \tag{J.7}$$

$$a_\mathrm{I}^2 = (c^2/v_{\mathrm{dI}}^2)P_\mathrm{I}^2 - (m_e^2c^2 + p_{z0}^2)\gamma_{\mathrm{dI}}^2. \tag{J.8}$$

Behind the pulse, $x < x_\mathrm{bd}$, electrons also make elliptic motions in the momentum space, which are shown by Eqs. (7.6) and (7.7) with

$$P_\mathrm{II} = m_e\gamma_{\mathrm{dII}}^2 v_{\mathrm{dII}}\gamma_{0\mathrm{II}}(1 - v_{\mathrm{dII}}v_{x0\mathrm{II}}/c^2), \tag{J.9}$$

$$a_\mathrm{II}^2 = (c^2/v_{\mathrm{dII}}^2)P_\mathrm{II}^2 - (m_e^2c^2 + p_{z0}^2)\gamma_{\mathrm{dII}}^2. \tag{J.10}$$

The quantities P_I and P_II are both positive because $v_{\mathrm{dI}} > 0$ and $v_{\mathrm{dII}} > 0$.

J.2 Sign of a_I^2

We prove here that a_I^2 and a_II^2 are also positive. Noting that

$$\gamma_{0\mathrm{I}} \geq \gamma_{xz}, \tag{J.11}$$

where

$$\gamma_{xz} = [1 + (p_{x0}^2 + p_{z0}^2)/(m_e^2c^2)]^{1/2}, \tag{J.12}$$

we find that

$$\frac{a_\mathrm{I}^2}{\gamma_{\mathrm{dI}}^2} \geq m_e^2c^2\gamma_{xz}^2\gamma_{\mathrm{dI}}^2\left(1 - \frac{v_{\mathrm{dI}}v_{x0}}{c^2}\right)^2 - (m_e^2c^2 + p_{z0}^2). \tag{J.13}$$

Substituting the relation

$$m_e^2c^2 + p_{z0}^2 = m_e^2c^2(\gamma_{xz}^2 - \gamma_{0\mathrm{I}}^2v_{x0}^2/c^2) \leq m_e^2c^2\gamma_{xz}^2(1 - v_{x0}^2/c^2), \tag{J.14}$$

in Eq. (J.13) yields

$$\frac{a_\mathrm{I}^2}{\gamma_{\mathrm{dI}}^2} \geq m_e^2c^2\gamma_{xz}^2F(v_{x0}), \tag{J.15}$$

where

$$F(v_{x0}) = \gamma_{\rm dI}^2 \left(1 - \frac{v_{\rm dI} v_{x0}}{c^2}\right)^2 - \left(1 - \frac{v_{x0}^2}{c^2}\right). \tag{J.16}$$

With the aid of the relation

$$\frac{dF}{dv_{x0}} = 2\frac{\gamma_{\rm dI}^2}{c^2}(v_{x0} - v_{\rm dI}), \tag{J.17}$$

we see that $F(v_{x0})$ has its minimum value $F(v_{x0}) = 0$ at $v_{x0} = v_{\rm dI}$. Hence, Eq. (J.15) indicates that $a_{\rm I}^2 \geq 0$. One can prove that $a_{\rm II}^2 \geq 0$ in the same way.

J.3 Sign of $\Delta P(t_0)$

When a particle goes out to the region behind the pulse at $t = t_0$ at point B with $p_y(t_0) = 0$ (Fig. 7.2), the center of the ellipse is shifted along the p_x axis by the amount given by Eq. (7.8). This section proves that it is positive, Eq. (7.9).

To connect the two ellipses at point B, we take the constants in Eqs. (J.7) and (J.9) to be

$$\gamma_{0\rm I} = \gamma_{0\rm II} = \gamma(t_0), \tag{J.18}$$

$$v_{x0\rm I} = v_{x0\rm II} = v_x(t_0). \tag{J.19}$$

We then find $\Delta P(t_0)$ as

$$\begin{aligned} \Delta P(t_0) &= m_e c \gamma(t_0)(\gamma_{\rm dI}^2 \beta_{\rm dI}^2 - \gamma_{\rm dII}^2 \beta_{\rm dII}^2) \\ &\times \left[\frac{v_x(t_0)}{c} - \left(1 + \frac{(1-\beta_{\rm dI})(1-\beta_{\rm dII})}{\beta_{\rm dII} + \beta_{\rm dI}}\right)\right], \end{aligned} \tag{J.20}$$

where $\beta_{\rm dI}$ and $\beta_{\rm dII}$ are defined as

$$\beta_{\rm dI} = v_{\rm dI}/c, \tag{J.21}$$

$$\beta_{\rm dII} = v_{\rm dII}/c. \tag{J.22}$$

By using Faraday's law, we can find the relation among the pulse and drift speeds. If the propagation of the compressive pulse is nearly stationary, integrating the z component of Faraday's law over a small region containing the rear boundary $x = x_{\rm bd}$, we obtain

$$\frac{v_{\rm cp}}{c}(B_{\rm I} - B_{\rm II}) = E_{\rm I} - E_{\rm II}, \tag{J.23}$$

where $v_{\rm cp}$ is the propagation speed of the compressive pulse. We then find the relation

$$v_{\rm dII} - v_{\rm dI} = \frac{(B_{\rm I} - B_{\rm II})}{B_{\rm I}}(v_{\rm dII} - v_{\rm cp}). \tag{J.24}$$

Since $B_{\rm I} > B_{\rm II}$, we have

$$v_{\rm dII} > v_{\rm dI} > v_{\rm cp}, \tag{J.25}$$

or

$$v_{\rm dII} < v_{\rm dI} < v_{\rm cp}. \tag{J.26}$$

If the compressive pulse is an ordinary nonlinear magnetosonic pulse propagating in the positive x direction in an equilibrium plasma, $v_{\rm dII}$ is zero in the laboratory frame where the plasma is at rest outside the pulse, and the relation (J.26) holds. If, however, a magnetosonic pulse behind a shock front propagates in the negative x direction relative to the downstream plasma, then Eq. (J.25) can be satisfied. In this case, the relation

$$\gamma_{\rm dI}^2\beta_{\rm dI}^2 - \gamma_{\rm dII}^2\beta_{\rm dII}^2 < 0, \tag{J.27}$$

and thus Eq. (7.9) hold: The shift $\Delta P(t_0)$ is positive.

In the same way, we obtain the shift of the ellipse center at $t = t_1$, $\Delta P(t_1) = P_{\rm I}(t_1) - P_{\rm II}(t_1)$, as

$$\begin{aligned} \Delta P(t_1) &= m_e c\gamma(t_1)(\gamma_{\rm dII}^2\beta_{\rm dII}^2 - \gamma_{\rm dI}^2\beta_{\rm dI}^2) \\ &\times \left[\frac{v_x(t_1)}{c} - \left(1 + \frac{(1-\beta_{\rm dII})(1-\beta_{\rm dI})}{\beta_{\rm dI} + \beta_{\rm dII}}\right)\right]. \end{aligned} \tag{J.28}$$

It is noted that $P_{\rm I}(t_1) \neq P_{\rm I}(t_0)$, while $P_{\rm II}(t_1) = P_{\rm II}(t_0)$. Under the condition (J.25), it is negative

$$\Delta P(t_1) < 0. \tag{J.29}$$